A Novel Approach to the High-Magnetisation Limit of Relativistic Magnetohydrodynamics

David Nicholas Huttly Phillips

27th October, 2023

Submitted in accordance with the requirements for the degree of Doctor of Philosophy

The University of Leeds
School of Mathematics

Declaration of Authorship

I confirm that the work submitted is my own and that appropriate credit has been given where reference has been made to the work of others.

Acknowledgments

I would first like to thank my supervisors Serguei Komissarov and Rainer Hollerbach for their continual guidance and invaluable feedback over the course of my work. In addition, I would like to thank the rest of the staff at the Maths department at Leeds who have been a great source of support. I would also like to thank my family, who have provided me with their constant support and encouragement, as well as some helpful suggestions in writing my thesis.

Abstract

Many astrophysical phenomena associated with black holes and neutron stars involve large-scale relativistic flows of magnetised plasma. Such flows are best described with the framework of relativistic magnetohydrodynamics (RMHD). Like many other fluid frameworks, RMHD allows analytical solutions only for highly simplified problems, and any more or less realistic problem requires computer simulations. Numerical techniques for RMHD have been developed for over two decades now, with shock-capturing conservative schemes having been particularly successful. But while they have allowed great advances in our understanding of many phenomena of relativistic astrophysics, they all share one major flaw: none of the current conservative schemes can handle the regime of relativistically high magnetisation, where the electromagnetic mass-energy dominates the mass-energy of the plasma. Often the problems start even when the two are comparable.

In this thesis, we describe a method to overcome this problem caused by the fact that the electromagnetic field becomes almost Force-Free and as a result the system of RMHD conservation laws become degenerate. In our approach we split the flow dynamics into the Force-Free evolution of the electromagnetic field and the interaction between this field with the plasma. This novel approach is similar in spirit to the operator-splitting methods for differential equations and can be applied even in the case of moderate- to low-magnetisation RMHD problems. In the high magnetisation regime, this approach is similar to a perturbation technique.

To test the approach, we have built a code for Special Relativistic RMHD and carried out a large number of one- and two-dimensional test simulations in Cartesian geometry. The simulations included the cases of both the strongly- and weakly-magnetised relativistic plasmas and compared against exact solutions, where known, and solutions obtained with other methods, or even frameworks, like Force-Free degenerate electrodynamics and plasma kinetics. The results are very promising.

Contents

List of Figures

List of Tables

Conventions, Notations and Special Relativity

Some notations in this thesis may be unfamiliar, and some conventions are ambiguous as well, so we will give a brief overview of these here.

In this work, we will use units (unless stated otherwise) such that the speed of light $c = 1$, 4π and μ_0 vanish from Maxwell's equations, and Boltzmann's constant $k_B = 1$ (in other words, the equations are nondimensionalised).

Greek indices such as α, β are assumed to range from 0 to 3 (where the 0 index refers to the time coordinate), while Latin indices such as i, j range from 1 to 3, or just the spatial coordinates. Unless otherwise specified, a number value is not an index but instead implies exponentiation, i.e. $r^2 = r \cdot r$. We also use Einstein summation notation, so that a repeated index has an implied sum

$$a^\alpha b_\alpha = \sum_{\alpha=0}^{3} a^\alpha b_\alpha .$$

We further choose the sign convention so that the metric signature is $(-,+,+,+)$. Thus vectors written with a Greek index such as a^α are 4-vectors, with four components. We further split these into time and space components via $a^\alpha = (a^0, \boldsymbol{a})$, where a^0 is the time component, and $\boldsymbol{a}$ are the spatial components. That is, a vector that is either written in bold or with Latin indices represents only the three spatial components.

$\boldsymbol{v}$ represents a 3-velocity. If $\boldsymbol{x}(t)$ is the position in space in Cartesian coordinates of an object at t in the laboratory frame, then $\boldsymbol{v} = \dfrac{d\boldsymbol{x}}{dt}$, so $\boldsymbol{v}$ is the velocity of an object as observed by someone in the laboratory frame.

$u^\alpha = (u^0, \boldsymbol{u})$ represents a 4-velocity. This is given by $u^\alpha = \dfrac{dx^\alpha}{d\tau}$, where $x^\alpha = (t, \boldsymbol{x})$ (the position of the object in spacetime) and τ is the proper time (the time as measured by the object that is moving). Given the Lorentz factor $\gamma = \dfrac{dt}{d\tau}$ we can write the 4-velocity in terms of the 3-velocity as $u^\alpha = (\gamma, \gamma \boldsymbol{v})$.

A vector a written without Latin or Greek indices and not in bold face is the magnitude of the full vector, whether it is a 4-vector or 3-vector. If it is a 3-vector like $\boldsymbol{v}$ this is $v^2 = v^i v_i = \boldsymbol{v} \cdot \boldsymbol{v}$, while if it is a 4-vector like a^α then this is $a^2 = a^\alpha a_\alpha$.

Thus for a 4-vector a is not the magnitude of the spatial components alone, but instead the magnitude of the entire 4-vector. However, this is with the sole exception of the 4-velocity u^α, where u instead represents the magnitude of the spatial components, $u^2 = \boldsymbol{u} \cdot \boldsymbol{u}$.

Chapter 1

Introduction

This chapter sets the thesis in the relevant astrophysical background, with a brief introduction and literature review of important application areas such as Jets, Black Holes, Pulsars and the recent developments of gravitational wave astronomy and the Event Horizon Telescope, as well as a review of some of the numerical techniques used to model them.

Numerical schemes for Relativistic Magnetohydrodynamics (RMHD) have come a long way since their inception, and there are now several such schemes. Among these, conservative schemes are used to capture discontinuities, like shocks and current sheets. However, in RMHD conservative schemes all exhibit stiffness in regions of high magnetisation, i.e. when the Stress-Energy tensor is dominated by the Electromagnetic components (Komissarov, 2006). We characterise this here by the ratio of magnetic pressure to plasma rest-enthalpy density, $\sigma = \dfrac{B^2 - E^2}{w}$, where w is the relativistic enthalpy density, $\boldsymbol{B}$ is the magnetic field and $\boldsymbol{E}$ is the electric field.

This parameter σ is a relativistic equivalent to the non-relativistic plasma beta, although now the ratio is inverted (so that high numbers indicate strong magnetic fields). For a high magnetisation plasma, we would thus have $\sigma \gg 1$. In this high magnetisation regime, errors in the calculations due to approximate integration methods become comparable to other important values, and so the solution becomes difficult to compute accurately, and non-physical tricks need to be employed to prevent codes from crashing, such as pumping extra plasma into the system if σ gets too high, e.g. Komissarov (2004b).

In order to simulate such situations accurately, we need a new code to deal with this regime. This project proposes a form of operator splitting model of the dynamics in this regime. We split the overall equations into a fully electromagnetic component, and an interaction component. The electromagnetic and interaction terms are then integrated separately each time step.

1.1 Astrophysical applications and Literature Review

It is widely held that at least 99.9% of (baryonic) matter in the universe is plasma (Bachynski, 1961). Therefore, as the quintessential example of a magnetised fluid, we can conclude that the motion of a large proportion of the universe's matter is governed by magnetohydrodynamics (MHD). The realm of relativistic magnetohydrodynamics (RMHD), however, is certainly more restrictive. Even if nearly all the matter is plasma, for relativity to be required in the model means extreme conditions, such as energy densities so high that it is comparable to the mass-energy of the particles, or particle velocities approaching the speed of light.

Although restrictive, these conditions do occur naturally in the universe, in some of the most extreme environments imaginable. These conditions include AGNs (Active Galactic Nuclei) and GRBs (Gamma Ray Bursts), jets from X-ray binaries, as well as Pulsars and their associated Pulsar Wind Nebulae (PWNs). A common feature of many such examples is a compact object such as a black hole or neutron star; this is an object so small relative to their mass that the treatment of gravity warrants a fully general relativistic description. Of course, other cases like supernovae do not feature a compact object — although one is typically expected to be formed from the stellar core during the supernova.

1.1.1 Black Holes, X-ray Binaries and Active Galactic Nuclei

Perhaps the most well known result to come out of general relativity, black holes have been of interest to Astronomers and many others since they were first theorised by Schwarzschild (1916) as an exact solution to the equations of general relativity, which had been published only a few months prior by Einstein (1915). These objects create some of the most extreme conditions in the universe since the Big Bang itself, with gravity so strong that not even light can escape from within the event horizon.

There are currently two categories of Black Holes known to exist: First, we have stellar mass black holes, with a mass of around 5 to 20 solar masses (McClintock and Remillard, 2006). These are the remnants of supernovae, from progenitor stars with masses above around 8 solar masses (Smartt, 2009).

These black holes are of particular interest when they are active, i.e. when they have infalling material. This most often occurs if black hole forms part of a binary system, such as when its progenitor star was already in a binary system. In this case, the black hole can leech material from its pair. The infalling material releases enormous amounts of gravitational potential energy as it falls in, causing it to heat up and emit X-rays. Thus this arrangement has become known as an X-ray binary (Tauris and van den Heuvel, 2006). Note that an X-ray binary may alternatively have a neutron star instead of a black hole for the compact object.

On the extreme end we have supermassive black holes, gigantic black holes that sit at the centre of galaxies. These black holes can have masses in excess of billions of solar masses (Shemmer *et al.*, 2004; Mortlock *et al.*, 2011; Wu *et al.*, 2015). When the supermassive black hole at the centre of a galaxy is active — i.e. when matter is falling in — it is known as an active galactic nucleus (AGN). The resulting accretion disc and associated magnetic fields often creates a magnetised, relativistic jet of plasma that blast out from the poles of the black hole, extending for thousands of parsecs out into intergalactic space (Kundt, 2016). This is in addition to the extreme temperature of the accretion disc itself, which thereby emits copious amounts of high energy electromagnetic radiation.

One of the most well known examples is the core of M87, a relatively nearby galaxy with a supermassive black hole of $6.5 \pm 0.7 \times 10^9$ solar masses (Akiyama *et al.*, 2019b) in its core, M87*. This black hole has generated a jet that extends 10 kiloparsecs out from the black hole (Biretta and Junor, 1995) — most likely with a twin on the other side hidden from us via relativistic beaming (Sparks *et al.*, 1992), a relativistic effect where matter looks brighter when moving towards the observer and dimmer when moving away.

The exact mechanism of these relativistic jets is still a subject of some debate. The current most popular candidate comes from Blandford and Znajek (1977). In that paper, the authors suggest that energy and angular momentum can be extracted from a rotating black hole by an externally supported magnetic field — for instance, a magnetised accretion disc. The magnetic fields lines are then twisted by the rotating black hole, which can then accelerate particles away from the black hole in two twin jets, in opposite directions.

Unfortunately, although there has been promising work in numerical modelling of black hole accretion discs and the Blandford-Znajek mechanism (Komissarov, 2001; De Villiers *et al.*, 2003; McKinney, 2006), current models of black holes have great difficulty with modelling the case accurately. This is because the magnetisation of the black hole can reach many orders of magnitude higher than what current codes can handle, especially near the black hole horizon.

For instance, Kino *et al.* (2015) used data from the Event Horizon telescope data of M87* (Akiyama *et al.*, 2019a) to estimate the magnetisation of the plasma near the event horizon the black hole. Due to uncertainty about the nature of the plasma around M87* the exact value is not certain, but generally they estimate magnetisation of at least

$\sigma > 10^3$, and potentially as high as $\sigma = 10^6$ or higher.

To get around this, some authors such as Komissarov (2001); McKinney (2006) used a force-free approach, i.e. neglecting the small inertial components entirely. This system is known as Force-Free Degenerate Electrodynamics, or FFDE. While this is able to handle high magnetisation better than RMHD codes, neglecting the plasma is obviously not ideal if it is important for the dynamics, such as if a current sheet forms. For the BZ mechanism in particular, matter is required since it works by accelerating charged particles.

Other authors have performed simulations of the BZ mechanism using a true RMHD code including the inertial components, but they had to use various means in order to avoid the high σ limitation. For instance, McKinney and Gammie (2004) and Qian *et al.* (2018) limited the initial ratio of gas pressure to magnetic pressure to 100 and 10 respectively (thus limiting σ to 0.01 and 0.1), while Komissarov (2004b) limited the maximum σ by "pumping" new plasma into the region near the black hole where the value of σ is highest.

In addition, isentropic flows can handle higher σ as the energy equation can be eliminated (Komissarov *et al.*, 2007a), while the adiabatic entropy transport equation can be integrated to bypass these errors as well. Of course, these will not be helpful for non-adiabatic flows, such as shocks and current sheets.

Given that we expect real black hole accretion discs to have far higher magnetisations and to have current sheets, these limitations are not desirable. However, with current codes potentially having difficulty with magnetisation as low as $\sigma \approx 1$ (Porth *et al.*, 2013), these magnetisations are well beyond current capabilities. Thus it is highly desirable to develop a numerical code that can handle these magnetisations.

1.1.2 Gamma Ray Bursts and Supernovae

Gamma Ray Bursts (GRBs) are extremely energetic bursts of Gamma Rays observed in other galaxies. These bursts are the brightest and most energetic events in the known universe (Burns *et al.*, 2023). GRBs can generally be sorted into two main categories, differing by duration and ultimately cause, although more categories have been proposed (Kouveliotou *et al.*, 1993).

Short GRBs, classified as those less than 2 seconds, account for around 30% of the GRBs detected. On average they last ~ 0.3s, and are thought to occur either when two neutron stars merge into a new black hole, or when a neutron star merges with a black hole to form a larger one — something which was confirmed to an extent when a short GRB was positively identified with the detection of a neutron star merger by LIGO, by identifying a short GRB with an associated gravitational wave of the form that models predicted such an event would emit (Abbott *et al.*, 2017b). The majority of the energy released during the inspiral is emitted as gravitational waves, and thus can be modelled without RMHD. However, if the GRB jets are powered magnetically then the system will require RMHD to simulate, and when the magnetic term becomes dominant we again need a simulator that can handle this regime.

Core Collapse

The remainder of GRBs are long GRBs. Long GRBs are emitted due to the core collapse of a relatively high-mass star, of at least around 10 solar masses (Woosley and Bloom, 2006). Core collapse has two main possible outcomes: either it can end in a supernova, or a long GRB.

Once a star runs out of Hydrogen in its core, it begins to contract from the loss of internal pressure as its main power source is lost. If the star has enough mass, the pressure in the core becomes high enough that Helium will begin fusing instead. This will run out eventually too, and so again if the star has enough mass the Lithium will begin to fuse.

With enough initial mass, this chain continues up the periodic table, until it reaches iron. At this point, there is no longer any energy to be released from fusion as the reaction is now endothermic for further elements (Woosley and Janka, 2005). The resultant drop in energy output in the core means that the core temperature begins to fall, and thus it can no longer hold up against the enormous gravity of the mass of the star above. The only factor that can hold it back now is the electron degeneracy pressure, whereby matter is so dense that to compress further would force electrons to occupy the same energy states, a situation forbidden by the Pauli exclusion principle (Lieb and Yau, 1987).

However, this too has a limit at the Chandrasekhar mass, of around 1.44 solar masses (Lieb and Yau, 1987). When the core finally exceeds this limit, the core begins to collapse rapidly (Burrows and Vartanyan, 2021). This collapse is very rapid, but is quickly halted by a second resisting pressure, that of neutron degeneracy pressure. Thus the rapidly contracting core comes to a sudden stop as it reaches nuclear densities, creating a shock wave that begins to propagate back out. However, this shock is soon stalled due energy losses from dissociating nuclei and neutrino emissions, thus it transforms into an accretion shock (Bethe, 1990). What happens next is dependent on several factors, most notably the initial mass of the star.

With a lower mass, the rapid contraction heats the core adiabatically, and so in the hot and dense core it becomes energetically favourable for protons and electrons to merge into neutrons via electron capture. This process of electron capture releases vast quantities of neutrinos, which rarely interact with normal matter and thus carry much of the energy out of the core. Through a process that is not currently well understood, some of these neutrinos are absorbed by the outer envelope of the star depositing large amounts of energy into these regions, restarting the shock and triggering the supernova explosion (Fryer and New, 2003). Meanwhile, the inner core converts into a compact object composed almost entirely of neutrons — i.e. it has become a neutron star.

Like the electron degeneracy pressure before, neutron degeneracy pressure also has a limit. Thus the mass of the neutron star is limited to between 2.01 ± 0.04 and 2.16 ± 0.17 solar masses (Rezzolla *et al.*, 2018). With a higher initial mass, this limit can be exceeded during the collapse of the inner core. Thus the neutron star formed above will then collapse further into a black hole. If a black hole forms, then the timing is key. If the collapse happens after the supernova explosion has been triggered, then the supernova will still occur leaving relatively little material to accrete onto the new black hole. However, if the core collapses into a black hole before the supernova has been triggered then the neutrinos will not be released. Thus we have a failed supernova, where the star does not explode.

Since the outer envelope has not been blasted away, it now begins to accrete into the new black hole. If there is enough initial angular momentum in the infalling material, it will form an accretion disc, which in turn will produce jets, either via the BZ mechanism (Komissarov and Barkov, 2009) or neutrino heating (Popham *et al.*, 1999; Kohri *et al.*, 2005). At some distance from the black hole, these jets will produce gamma rays, which thus forms a long GRB that continues until the accretion disc runs out of infalling material. This sequence of events is the current most popular model for the production of a long GRB from a collapsing star (Woosley, 1993; MacFadyen and Woosley, 1999).

Numerical models of supernovae have been performed for a long time (Gull and Longair, 1973; Xu *et al.*, 1985; Reinecke *et al.*, 2002), but even the more recent examples such as Nagakura *et al.* (2020); Burrows *et al.* (2023) still do not fully include important factors such as relativity. This is due partly to high magnetisation causing problems with RMHD — in particular high magnetisation is unavoidable for a BZ jet driving the GRB — but also because supernovae is a multi-physics problem, involving general relativity (especially if a compact object forms), neutrino-matter interactions, nuclear physics, radiation, and plasma dynamics. This complexity makes supernova modelling particularly difficult.

1.1.3 Astrophysical Jets

Astrophysical jets are beams of gasses and plasmas travelling relative into or through a background medium. While some jets have a low enough energy to be modelled in

Newtonian hydrodynamics (HD) — or magnetohydrodynamics (MHD) if magnetic fields are involved — some jets are energetic enough that the fluid is moving at relativistic speeds, and so the jet can only be modelled by relativistic models.

These jets can be powered by many different astrophysical phenomena, such as black holes as noted above. While modelling the power source and origin of the jet is of great interest, modelling just the jets themselves is also useful. Thanks to this as well as the fact that the jets alone are a simpler case to model, jets were among the first astrophysical phenomena to be modelled.

The first numerical model of a jet came from Rayburn (1977), in the form of a simple HD code. They studied the structure generated by a 2D, uniform, supersonic, cylindrical flow, with an external medium with density either uniform or decreasing with the distance from the injection nozzle. This code ran as a Particle-in-cell (PIC) model on a 2D grid of just 10 x 20 grid cells, with 16 particles per cell.

In spite of the small size of the model, it was still capable of producing two shocks – the bow shock of the jet entering the external medium, and the reverse shock of the termination of the jet. The model also generated a rarefied (less dense) region around the jet, as the external medium was heated by the shocks.

Later studies also utilised 2D HD codes, such as Norman *et al.* (1981) who used a finite difference code on a 40 x 40 grid to study if a hot gas inserted into a gravitationally bound cloud could escape in the form of jets. Notably, this numerical study did not quite agree with theoretical results. While the hot gas did create a cavity in the cloud and a de Laval nozzle through which hot gas escaped, the cavity developed a Rayleigh-Taylor instability (at the interface between the hot, rarefied gas in the cavity and the cooler, denser, exterior cloud) which could destroy the nozzle, in contrast to theoretical models. This clearly demonstrates the important place that numerical studies hold, as a form of confirmation (or refutation) for theoretical models. Given that traditional scientific experimentation is difficult if not impossible in relativistic astrophysics, with the closest to real data being astronomical observations, this is very useful to have.

Of course, given that most matter in the universe is a plasma where electric and magnetic fields are important, a simple HD model is not enough to capture the dynamics of most flows in astrophysics, not to mention jets. The first MHD model of jets came from Clarke *et al.* (1986). They used an axisymmetric scheme for MHD that was a simple extension of their earlier HD codes. While the setup of this model was identical to one of their earlier HD models, besides an azimuthal magnetic field which increased linearly with the distance from the axis, the results did not match the HD model, as we would expect.

The shocked plasma at the front of the jet did not flow backwards to create the cavity around the jet, and instead flowed forward to form a magnetically-pinched structure in front of the termination shock, known as a “nose-cone”, the development of which was determined by the parameter $\beta = \frac{p_g}{B^2/2}$, the ratio of inertial gas pressure to magnetic pressure. Later, fully 3D codes by Mignone *et al.* (2010a) showed that this formation was an artefact of the 2D model, as it suppressed non-axisymmetric instabilities that would have otherwise destroyed the nose-cone.

The first models of relativistic jets were more tests of codes, as opposed to realistic models of astrophysical jets. Some of the first realistic numerical models of 2D RMHD were done by Komissarov (1999b), who studied axisymmetric jets with a purely azimuthal magnetic field, and the same settings as with Clarke *et al.* (1986). Analysis of the jets showed that it was not the β of typical MHD that determined the nose-cone development, but instead the relativistic σ, the ratio of magnetic energy to rest-mass energy.

Unlike the previous cases of black holes and GRBs, jets are not expected to have exceptionally high magnetisations. For instance, Król *et al.* (2022) estimate that the magnetisation of a relativistic, current-carrying jet with radial velocity shear will likely only be $\sigma \sim \mathcal{O}(1)$ — although they do note it could get as high as $\sigma \lesssim \mathcal{O}(10)$ in the right circumstances. Even so, this moderate value of σ is still large enough to cause problems in some cases, as noted above. So a method to handle these cases is still warranted.

Moreover, the base of the jet (i.e. where it forms) such as a black hole can have much higher magnetisations. Thus one important question here is why the jet magnetisation is low, given that the magnetisation at its base can be very high. This could be due to a number of factors, such as mixing with low σ gasses such as winds from the accretion disc, and conversion of magnetic to kinetic energy. Clearly, to study this numerically we need a model that can handle low and high σ simultaneously.

1.1.4 Pulsars

First discovered by Hewish *et al.* (1968), pulsars are neutron stars characterised by the radio beams that are emitted from them. Since these beams are often misaligned with the axis of rotation, as the pulsar spins the beam sweeps across the sky in a cone shape. If the Earth happens to lie in this cone, then we can detect the beam sweeping across us as a regular pulse of radio waves. As the neutron star is very massive and spins at very high speeds, the large angular momentum in its rotation means that this pulse is very regular, and barely changes in frequency for each pulsar — although there are still means by which this frequency can change on longer time scales, especially from either energy loss via electromagnetic radiation and gravitational waves (Zhang *et al.*, 2016), or energy gain via accretion of material from a binary companion (Bhattacharya and van den Heuvel, 1991).

Although the radio pulses emanating from a pulsar are the most distinctive feature of one, in terms of energy extracted from the pulsar the radio beams represent only a tiny fraction of all the power output of a typical pulsar. The total energy loss of a pulsar can be quite accurately estimated from precise measurements of its rotation period P and time derivative $\dot{P}$. Using the known mass and radius of the pulsar, we can calculate the total rotational energy and the power output as a result of the loss of this energy, or “spindown” power (Cerutti and Beloborodov, 2017). Comparisons of the spindown power to the power in the radio beams shows a huge deficit (Pétri, 2016).

Early models of the magnetosphere near the surface of the pulsar reasoned that the intense surface gravity of the pulsar would prevent any particles from lifting from the surface and would prevent them from filling the magnetosphere, causing the magnetosphere of the pulsar to be a near vacuum (Pacini, 1967, 1968; Ostriker and Gunn, 1969). Combined with the dipole model of the pulsar itself, this led to the vacuum dipole magnetosphere models.

The strong dipole magnetic field of the pulsar means that particles in the field are restricted to the drift velocity $\boldsymbol{v}_D = \dfrac{\boldsymbol{E} \times \boldsymbol{B}}{B^2}$ for motion perpendicular to the magnetic field $\boldsymbol{B}$. However, particles are free to move unobstructed along the field lines, especially if there is a component of parallel electric field $\boldsymbol{E}_{||}$, so that $\boldsymbol{E} \cdot \boldsymbol{B} \neq 0$. The vacuum dipole solutions showed that there was indeed strong $\boldsymbol{E}_{||}$, and thus Goldreich and Julian (1969) pointed out that these electric fields in the equatorial region were in fact easily strong enough to lift particles from the surface of the neutron star and fill the magnetosphere with particles, eliminating the vacuum.

At least some part of this plasma near to the surface of this pulsar must be corotating with the pulsar, due to the boundary with the surface and due to the rotation mass of the star itself dragging around material with it via frame dragging. This corotation has a limit of course, as to remain corotating means faster and faster orbits as one goes further out; at its limit, the material would need to be moving at the speed of light. The corotational limit cylinder this indicates is called the light cylinder, the radius of which is therefore given by $r_L = \dfrac{1}{\Omega}$, where Ω is the angular frequency of the pulsar. For the most rapidly spinning “millisecond pulsars” the light cylinder can be only a few kilometres above the surface of the pulsar equator.

This therefore divides the pulsar magnetosphere into two regions, an inner corotational region within the light cylinder, and an outer pulsar wind region which is no longer corotating and leaves the pulsar at very high velocities.

Although electrons and ions lifted from the surface is one source of particles in the pulsar magnetosphere, this alone cannot fully explain the spindown of the pulsar. Later observation of the pulsar wind showed that this wind is an electron-positron ($e^{\pm}$) plasma. These positrons were not lifted from the surface, but are expected theoretically (Cerutti and Beloborodov, 2017).

Consider, as before, that we have a strong magnetic field $\boldsymbol{B}$ and a parallel electric field $\boldsymbol{E}_{\|}$. Charged particles such as electrons are forced to follow magnetic field lines and are accelerated along them by the electric field $\boldsymbol{E}_{\|}$ to relativistic speeds. If the magnetic field lines are curved, then these relativistic electrons will then emit synchrotron radiation as high energy γ-rays as they are forced to turn.

These high-energy photons will in turn interact with the strong magnetic fields to create a particle-antiparticle pair via pair production. The new particles are also accelerated along the magnetic field lines, and the result is that any region with $\boldsymbol{E} \cdot \boldsymbol{B} \neq 0$ will rapidly fill with an $e^{\pm}$ plasma (Erber, 1966; Harding and Lai, 2006).

This process does not proceed indefinitely however, as these charged particles then serve to increase the conductivity of the plasma, until it is high enough that $\boldsymbol{E} \cdot \boldsymbol{B} = 0$ and no more particles can be produced. Thus only the less dense, particle-poor regions termed “gaps” can produce more particles to fill the magnetosphere (Cerutti and Beloborodov, 2017).

Even though there is now an $e^{\pm}$ plasma filling the magnetosphere, the energy and momentum of the plasma is still dwarfed by that of the electromagnetic fields in the region (Philippov and Spitkovsky, 2014; Cerutti *et al.*, 2015). The dynamics of the plasma are thus dominated by the electromagnetic fields, and the plasma itself does little to affect the dynamics beside make the conductivity high enough that $\boldsymbol{E} \cdot \boldsymbol{B} = 0$ is nearly satisfied everywhere. There are only a few particular cases where the plasma inertia cannot be ignored — most notably current sheets.

Although gaps are required to fill the magnetosphere, it makes sense to consider models of so-called force-free solutions (so termed because the Lorentz force vanishes), where we assume that violations of $\boldsymbol{E} \cdot \boldsymbol{B} = 0$ necessary to create particles are minimal, and that the inertial mass of the plasma is much smaller than the energy density of the electromagnetic fields.

One common feature of all such force-free solutions is the presence of a current sheet separating the magnetic field of either pole (Spitkovsky, 2006; Kalapotharakos and Contopoulos, 2009). This is problematic because current sheets are regions where fully force-free models are not viable. Such solutions cannot exist in force-free models, as the current sheet heats up the plasma and makes neglecting the inertial terms no longer an accurate assumption.

More recently, numerical simulations have been performed using PIC models instead (Philippov and Spitkovsky, 2014; Cerutti *et al.*, 2015). Currently this is the only other method available that can handle the high magnetisation in this system. Unfortunately, although PIC models can be used this case is somewhat unsuitable for it since simulations must be global. This is due to the inherently non-local nature of the system, since activity near the light cylinder affects activity near the polar caps and vice versa (Cerutti and Beloborodov, 2017).

In practice, PIC models are limited to a few orders of magnitude of scale separation between the scale of the macroscopic (neutron star radius, light cylinder radius) and the microscopic (plasma skin depth) scales, which for real pulsars is huge (Cerutti and Beloborodov, 2017). This scale separation is still sufficient to capture the fundamentals of pulsars such as gap formation, but a different model for pulsar magnetospheres such as a true RMHD plasma model that can handle high σ is warranted.

Pulsar Wind Nebulae

Beyond the immediate magnetosphere region of the pulsar we enter the Pulsar Wind Nebula (PWN). These are formed of the outflow from the pulsar itself and are frequently found inside the supernova remnant of the progenitor.

As a result of the high magnetisation of the plasma and the high angular velocity of the pulsar, the magnetosphere emits a pulsar wind, similar to a stellar wind. This magnetised, relativistic wind then collides and interacts with the nearby interstellar medium and (typically) the outer supernova remnant, from when the pulsar originally went supernova. Once again, we need RMHD to simulate this system, as the winds are relativistic.

While not as extreme as the pulsar magnetosphere, the magnetisation in the pulsar wind can still be very high, at least close to the pulsar, and especially near the polar regions. Lyutikov *et al.* (2018) note that while the magnetisation at the boundary of the PWN and the outer supernova remnant is small with $\sigma \ll 1$, the magnetisation in the polar regions at the termination shock could be as high as $\sigma \approx 400$.

1.1.5 Notable Recent Developments

These extreme flows and the compact objects that drive them are quite difficult to observe. They are typically rare enough that finding one close enough to earth for good observation is unlikely. The compact objects themselves are also usually very small, many times smaller than the stars that formed them — with the notable exception of supermassive black holes, which can grow to the point that they have masses exceeding 10^{10} solar masses, and Schwarzschild radii beyond 1,000 AU (i.e. 1,000 times the distance from the Earth to the Sun) in the most extreme known cases (Shemmer *et al.*, 2004). However, since each galaxy is expected to usually only have one supermassive black hole, they are very rare and distant — and the closest known (Sagittarius A*, located at the centre of the Milky Way) is cloaked behind the dust in the galactic disc. While supernovae are also large and bright, they are also rare events and very difficult (if not impossible) to predict, and the same applies to mergers.

However, relatively recently there have been notable breakthroughs that have allowed for observations of these high energy scenarios, through two key methods: Gravitational wave astronomy, and the Event Horizon Telescope.

Gravitational Wave Astronomy

One of the predictions made by general relativity is that of the existence of gravitational waves, waves in spacetime itself that travel at the speed of light. These waves are radiated whenever mass-energy is accelerating, provided that the motion is not spherically or rotationally symmetric. One important case of this motion is any two-body system in orbit, and thus the energy carried by these waves causes even orbits in two-body systems to decay, in contrast to the Newtonian case (Misner *et al.*, 1973).

Gravitational waves are transverse waves and have the effect of stretching and compressing distances between objects as they pass. That is, if we imagine the simple case of a circular ring of test particles in flat spacetime and a single-frequency, polarised, small-amplitude (i.e. linearised) gravitational wave passing through perpendicular to the plane of the ring, then the wave will distort the shape of the ring into an ellipse. As the wave passes, the ellipse will pulsate and switch which dimensions are stretched and compressed. This distortion will not change the area inside the ring, so the product of the two axes of the ellipse is constant.

Fig. 1.1a gives a diagram of the passage of just such a polarised, pure frequency gravitational wave, passing perpendicular to the plane of the test particles. In this case, the displacement of each particle follows a straight line, and oscillates around its initial position in a sine wave. In this case, the wave is $\times$-polarised, meaning that the axes of the ellipse make a cross shape, as opposed to $+$-polarised waves, which are the same but rotated through $\pi/4$ radians.

Gravitational waves can also be circularly polarised. Such waves have the effect of rotating the ellipse instead of causing it to pulsate, see Fig. 1.1b. In this case the particles now follow small circular orbits around the unperturbed position; note that the particles

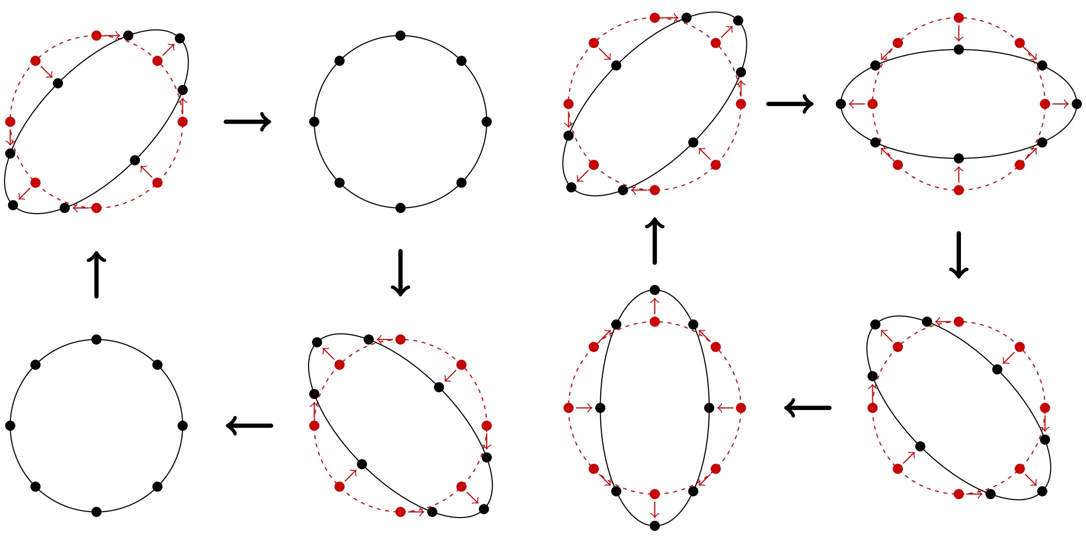

(a) *×-Polarised Wave.* ***(b)*** *Circularly Polarised Wave.*

Figure 1.1: *Effect of the passage of a ×-polarised (a) and a circularly polarised gravitational wave (b) on a circular ring of test particles, passing perpendicular to the plane of the particles. Shown are four states of the oscillation; each state progresses to the next in a clockwise fashion, following the black arrows. The red points and dashed circle indicate the original positions of the test particles, the black dots and ellipses/circles are the displaced positions, with the red arrows indicating the displacement vectors of each particle.*

themselves do not rotate around the centre with the ellipse, so there is no overall rotation of the system.

Note that the amplitude in these diagrams is heavily exaggerated. The amount of extra displacement Δs between two masses is proportional to the original displacement s between them, thus the amplitude of a gravitational wave is typically measured by the strain h, given by $h = 2\Delta s/s$. While the strain in this diagram is $h = 0.7$, the strain of waves that pass the Earth is extremely small. For example, the first detection of gravitational waves — originating from the merger of binary stellar mass black holes — by Abbott *et al.* (2016a) had a peak strain of just $h \approx 10^{-21}$. If the initial displacement of two test masses is 1 km, this gravitational wave would increase the displacement by around one ten thousandth the diameter of a proton.

While the energy lost by gravitational waves for a typical planet orbiting a star is too small to have a meaningful effect on its orbit, for massive objects orbiting rapidly in small orbits the energy loss is significant enough to mean that they will eventually collide. For instance, one of the first indirect pieces of evidence of the existence of gravitational waves came from Taylor and Weisberg (1982), who showed that the binary pulsar PSR 1913+16 was reducing in orbital period at a rate with excellent agreement to the calculated orbital decay due to gravitational radiation.

The amount of energy emitted as gravitational waves in some of these events can be enormous, in spite of how small the detected strain is here on Earth. For instance, Reisswig *et al.* (2009) performed numerical relativity models of the merger of equal-mass binary black holes with aligned spins. For the energy emitted as gravitational waves during the merger, they came to a value of around 2–10% of the total mass-energy of each black hole. Thus for a merger of two stellar-mass black holes with masses of (say) 40 solar masses, around 1–4 solar masses worth of mass-energy will be emitted as gravitational waves during the merger. This has since been confirmed by observations of gravitational waves from real mergers (Abbott *et al.*, 2016b).

The form of the gravitational wave packet produced by a merger is quite characteristic. Since the frequency of the waves is twice the orbital frequency and the energy emitted increases as the objects move faster in tighter orbits, as the objects inspiral they emit gravitational waves in a profile of increasing frequency and increasing energy, a signal known as a "chirp" (Boyle *et al.*, 2019).

Other notable scenarios that can emit gravitational waves of significant magnitude include supernovae, binaries of compact objects prior to the final inspiral, and fast rotating neutron stars with a non-spherical mass distribution (Misner *et al.*, 1973).

Detecting gravitational waves from these objects is of interest for a few reasons. First of all, they simply provide another means by which we can observe these scenarios; in some cases, they are the *only* means by which they can be observed. Furthermore, these waves can travel freely through dust clouds and other opaque objects unlike electromagnetic waves, allowing us the observe things that are otherwise hidden from view. Finally, the methods of detection used detect the wave amplitude, not the energy directly. The amplitude of a gravitational wave decays like r^{-1} where r is the distance to the emission location, unlike the energy which decays like r^{-2} (Ju *et al.*, 2000).

The same is also true of electromagnetic waves. For electromagnetic waves, detection in a telescope involves absorbing the light, and measuring the change in energy. However, the gravitational wave detectors (described below) are based on measuring the strain instead, and this decays slower than the energy. This makes gravitational waves better suited for the detection of distant objects — although the strain is so small no matter the distance that detection is typically easier for electromagnetic waves.

There are a handful of methods that can be used to detect these waves, depending on the frequency of the waves. For waves emitted by cases relevant to this project — e.g. compact object mergers, binaries, supernovae — the wave frequencies are of a range that can be detected using laser interferometry. Laser interferometry is a technique that uses lasers to detect minute changes in the distance between objects, in this case caused by the passage of a gravitational wave.

One of the main such methods used for current gravitational wave detectors is a Michelson Interferometer (Bond *et al.*, 2017). In this case, a laser is split into two beams at right angles and sent down two different arms that are as long as possible, and exactly the same length; these beams are then reflected back (typically multiple times to increase the effective length) and recombined. As a gravitational wave passes through, it will change the lengths of the arms. Since the arms are perpendicular to each other, as one arm is stretched the other will be compressed. As a result, the distance (and hence the time) the beam travels will be different between the two arms. The originally in-phase light beams will therefore be out of phase by the time they reach the detector, and so they will interfere with each other.

Since the difference is so slight, detecting these waves is a challenge and the detectors are very sensitive to other distortions, such as minor earthquakes for ground-based interferometers. In spite of this, in 2015 the two LIGO detectors (Laser Interferometer Gravitational-Wave Observatory) became the first interferometers detect a confirmed gravitational wave (Abbott *et al.*, 2016a). Since then, other detectors like Virgo in Italy, GEO600 in Germany and KAGRA (Kamioka Gravitational Wave Detector) in Japan have joined in and made many more observations of gravitational waves (Abbott *et al.*, 2017a, 2022). By comparing the exact detection times for the same gravitational waves at these different locations, it is possible to triangulate which direction the wave came from.

Ground-based interferometers are limited in the range of frequencies they can detect by their length and environmental factors. For instance, the LIGO detectors are restricted to the frequency range 10 Hz to 10 kHz (Martynov *et al.*, 2016), meaning they can only expect to detect rapid events, such as the final inspiral of compact object mergers and supernovae. However, space-based interferometers are currently being planned such as LISA (Laser Interferometer Space Antenna) and DECIGO (Deci-hertz Interferometer Gravitational wave Observatory).

These interferometers will use satellites in space instead of long arms on the ground, allowing for much longer interferometer arms and the elimination of factors like earthquakes. This in turn allows for the detection of lower frequency phenomena such as compact object binaries. For instance, LISA is planned to cover the range of frequencies from 100 µHz to 1 Hz (Amaro-Seoane *et al.*, 2012); this will be done with three separate spacecraft orbiting the Sun 2.5 million km apart, effectively creating an interferometer with arms of that length (Cornish and Robson, 2017).

Whether it is detected on Earth or in space, the data received from the interferometers consists of a shift in the phases of the two beams, and thus a distortion in the length of the interferometer arms. In order to identify the cause of these, we have two main methods: First, by comparing the exact time of detection at multiple detectors, it is possible to triangulate the location of the event that emitted the waves. Telescopes can then look nearby in that region and potentially identify a possible source for the event, such as an associated gamma ray burst from a neutron star merger.

For example, the gravitational wave emitted from a neutron star merger detected by Abbott *et al.* (2017b) arrived just 1.7 s ahead of a GRB from the same direction (Abbott *et al.*, 2017c), providing some of the first evidence that neutron star mergers can trigger GRBs.

Second (and more relevant to this thesis), the gravitational wave profile of numerical models of these events can be compared to real detections. This has made it possible to make positive identifications of various black hole-black hole and black hole-neutron star merger events; for instance, the first gravitational wave detection in Abbott *et al.* (2016a) was identified as a merger of two solar mass black holes by matching the “chirp” produced to numerical models like those of Reisswig *et al.* (2009).

There are now significant catalogues of numerical results to compare the detected gravitational waves against, such as those of Boyle *et al.* (2019); Healy and Lousto (2022) which now have thousands of different black hole-black hole, black hole-neutron star and neutron star-neutron star merger waveforms.

One thing to note about all those waveforms is that they are purely models of the compact objects themselves and neglect any plasma or electromagnetic fields. As discussed previously, complete models of these mergers requires plasma modelling of the magnetospheres of these objects during the merger. The main source of the gravitational waves is of course the compact objects themselves, however with more sensitive detectors the impacts of plasma and the electromagnetic fields will be important (Henry *et al.*, 2023). Including the plasma could also allow us to model the resulting GRB, to help connect gamma-ray burst observations to merger events.

For supernovae, plasma modelling is crucial to get the gravitational wave profile correct since there are no central compact objects (at least at first) to dominate the dynamics. Thus in this case we do need an accurate model of the plasma to get an accurate model of the gravitational wave profile.

Overall, gravitational wave astronomy provides a new source of data for matching against numerical models of the phenomena. In the flip side, modelling the emitted gravitational waves from these phenomena also helps us to identify the origin of these waves. For many of these cases, as we have noted above, high magnetisation is quite likely to occur and thus a numerical model which can handle this regime is necessary.

Event Horizon Telescope

Black holes are the smallest possible objects given their mass, which makes them quite difficult to observe directly (of course, we would be observing their accretion discs and jets, not the black holes themselves). Stellar mass black holes have radii of only a few kilometres — the Schwarzschild radius of the Sun (i.e. the radius of a black hole with the same mass) is just 3 km — so observing even nearby black holes is difficult.

On the other hand, supermassive black holes can be far larger. As noted above, the largest currently known have masses on the order of 10^{10} to 10^{11} solar masses (Shemmer *et al.*, 2004; Ge *et al.*, 2019); for example, the supermassive black hole TON 618 has a estimated mass of 4×10^{10} solar masses, making its Schwarzschild radius approximately 1,300 AU, i.e. 1,300 times the average distance from the Earth to the Sun, or more than 40 times the average distance of Neptune to the Sun.

However, these black holes are also much rarer, typically limited to just one per galaxy, and most are not that large either. The closest known is Sagittarius A* (located at the centre of our Milky Way galaxy) and has mass of "only" 4×10^6 solar masses, corresponding to a Schwarzschild radius of around 18 solar radii (Abuter *et al.*, 2023). However, even this nearby supermassive black hole is located 8.277 kiloparsecs away (26,996 light years), and it is also hidden behind dust in the galactic disc.

Due to this, identification of black holes has in the past been limited to the motion of stars and gas clouds near to the supposed black hole. For instance, stars nearby to Sagittarius A* have been observed in infrared orbiting a seemingly empty spot at extreme speeds (Eckart *et al.*, 2002).

However, a recent breakthrough has been made by the team behind the Event Horizon Telescope (EHT). By making multiple simultaneous observations of the same black hole with different telescopes across the globe, the data from the various telescopes was combined to create observations using what is effectively a telescope the size of the Earth. This allowed them to resolve far more distant objects than each telescope could alone.

Such arrays have been used before of course (Thompson *et al.*, 2017), but what is unique about the EHT is its very short, low-mm wavelength detection range.

In a series of papers starting with Akiyama *et al.* (2019a), they published their first results of observations of the supermassive black hole at the centre of M87, a relatively nearby galaxy. This black hole is much more massive and thus much larger than Sagittarius A*, and is responsible for a relativistic jet that extends out into intergalactic space.

They have also since come out with observations of Sagittarius A* (Akiyama *et al.*, 2022) as well as several other black holes, such as 3C 279 (Kim *et al.*, 2020) — which also included direct observations of a relativistic jet emerging from the AGN core.

Now that we have proper observational data, it is finally possible to match numerical models to observations. We also now have more accurate data for the numerical model conditions as well. Of particular relevance to this thesis is the fact that these black holes are commonly expected to have high values for σ — and indeed, observations from EHT indicate that the magnetisation of M87 is at least $\sigma > 10^3$, as noted above. Current models are unable to deal with this high magnetisation, especially when it interacts with low magnetisation plasma as well, and thus a new numerical scheme that can handle the high magnetisation regime is necessary.

1.2 Numerical Methods for Relativistic Plasmas

There are multiple ways of modelling a plasma; at its most basic level, we can try following every single particle in the plasma individually, a vast number of charged (and possibly uncharged) particles moving about and interacting either in the short-range via collisions, or in the long-range via electric and magnetic fields.

Although this would theoretically capture all the dynamics of the plasma accurately (provided a method for solving Maxwell's equations for the electric and magnetic fields as well), due to the enormous number of particles for even the smallest of cases modelling plasmas in this fashion is impractical. We can afford to drop this extreme level of accuracy to some extent in most situations, thus many different numerical techniques have been developed to model plasmas, each with their own strengths and weaknesses.

1.2.1 Particle-in-Cell Method

The first method to discuss is the particle-in-cell (PIC) method. Instead of evolving every particle in the plasma individually, this model represents the plasma particles as a set of "super-particles". Each super-particle then represents a distribution of individual particles (Birdsall and Langdon, 1985). The super-particles are then moved around the computational domain in accordance with their momentum and the forces acting on them (i.e. the Lorentz force), as if they were individual particles themselves.

Meanwhile, the electric and magnetic fields are solved for via Maxwell's equations. The method to solve these equations varies, but regardless of what method is used this requires values for the current density $\boldsymbol{J}$. This is of course dependent on the particles of the plasma, and thus must be calculated from the super-particles. This is done using a form of averaging scheme, which takes nearby super-particles and collects them into "cells" to calculate an average. This average is usually not uniform and takes into account the fact that each super-particle is in fact a distribution of many particles. If the integration scheme does not enforce exact adherence to Gauss' law, then the charge density is also needed in order to clean the errors in the divergence of the electric field.

Since this method models the particles themselves to an extent, PIC models are highly accurate and include much of the small-scale physics. In addition, PIC models are able to probe the high-σ regime that other models are unable to model. PIC models have been used successfully for various different cases of relativistic plasmas; for instance, Chen and Beloborodov (2014); Philippov and Spitkovsky (2014) use PIC codes to model neutron star magnetospheres, and Hirotani *et al.* (2021) use a PIC code to model a stellar black hole magnetosphere.

However, even with collecting particles into less numerous super-particles, PIC models still struggle with how many super-particles are needed to model cases properly. As we mentioned briefly in section 1.1.4, PIC models are limited to a few orders of magnitude of scale separation between the scale of the macroscopic and the microscopic (plasma skin depth) scales (Cerutti and Beloborodov, 2017). This means that these models are only capable of capturing some of the more basic phenomena in scenarios with large scale separations, such as black holes or pulsars.

1.2.2 Kinetic Models

The next category is that of kinetic models. These model the plasma as a distribution of particle positions and velocities (i.e. a distribution in phase-space) which is then evolved according to an equation — such as the Vlasov equation (e.g. Rasio *et al.* (1989)) or the more accurate Fokker-Planck equations (e.g. Stahl *et al.* (2017)) — which describes the evolution of such a statistical distribution.

So instead of discrete particles being moved around the domain, the plasma is instead represented as a continuum in phase space, which is updated according to partial differential equations. In addition to this distribution function, the electric and magnetic fields are evolved according to Maxwell's equations simultaneously, much like the PIC method.

As a result of working in phase space, the distribution function is six-dimensional, consisting of three velocity components and three positional components, plus time (Liu *et al.*, 2019). Since we cannot work numerically with a fully continuous distribution, the grid is discretised so that we are working with the value of the distribution function at a finite set of discrete points.

These methods often also treat different particle species as separate distribution functions; for instance, an electron-proton plasma may have a distribution function each for the electrons and protons. With this many variables defined at each point in space, these kinetic methods can also be quite demanding computationally.

1.2.3 RMHD

A simpler alternative to both kinetic models and a PIC method is a fluid model, which represents the plasma not by individual particles or by a distribution, but by macroscopic quantities like pressure or temperature. When applied to relativistic plasmas, this model is known as relativistic magnetohydrodynamics, or RMHD.

The fluid model of RMHD allows for a much easier time modelling plasmas, as the number of values needed to be tracked is far smaller. This does come at the cost of some major simplifying assumptions, however. For instance, we have assumed that the plasma is collisional, meaning that the particles collide often enough that a statistical, thermal equilibrium is reached (otherwise the plasma cannot be represented properly by a single temperature, since we no longer know the distribution the particles follow). For some cases like the accretion discs of supermassive black holes, it is expected that the plasma will be collisionless instead; for example, the accretion disc around M87 is expected to be collisionless (Ryan *et al.*, 2018). In this case a fluid model may not be appropriate.

However, even without significant collisions a weakly collisional the plasma may still achieve isotropy and reach a thermal equilibrium via other methods. For instance, instabilities in the plasma can exhibit collective plasma interactions (Kunz *et al.*, 2014, 2016), allowing the plasma to reach a statistical distribution.

One of the key strengths (or weaknesses) of a numerical method for fluid dynamics is its ability to handle discontinuities; in the context of relativistic plasmas, the principal examples are shock waves and current sheets. In most of the applications detailed above, we expect some of these discontinuities to appear. For example, as discussed in section 1.1.4, analytical models of pulsar magnetospheres typically expect at least one current sheet to appear that separates the magnetospheres of the northern and southern hemispheres of the pulsar. This means that it is necessary for the numerical method used to be able to handle discontinuities well.

The equations of RMHD are a system of partial differential equations, involving derivatives of the variables with respect to space and time. The derivatives in these equations are the key issue for discontinuities; they obviously do not exist at discontinuities, so this system will fail if one appears. This differential form of the equations is known as the strong form because it prohibits discontinuous (or non-differentiable) solutions. If we instead integrate the equations over an arbitrary volume and over time then these differential equations can be transformed into integral equations, in which these strict conditions on the solutions can be relaxed, allowing for discontinuous solutions. This integral form of the equations is known as the weak form.

Many numerical methods are based on solving the differential form of the equations. For instance, in the finite difference method we start with a grid of points in the computational domain where the exact value of the solution function is known. Using these known values, the time derivative of the solution at those points is calculated based on the system of equations, which is used to update the values by a time step. If there is a discontinuity, then this method will generally fail to compute the derivatives correctly.

Of course, with a finite grid of points with non-zero spacing between each point, a discontinuity in the data is indistinguishable from very high gradients. Thus discontinuities in the data do not necessarily lead automatically to failure of the integration scheme. Instead, other issues tend to occur such as spurious oscillations near the discontinuity.

In order to deal with discontinuities one of two methods is typically used: The first method is to add artificial numerical dissipation to smooth out discontinuities, for instance by adding artificial viscosity (Hartmann and Houston, 2002; Česenek *et al.*, 2013). Although this does allow these methods to handle discontinuities by smoothing them over multiple grid points, the extra dissipation is obviously not satisfactory if we are interested in resolving the discontinuities accurately.

The second method is to give special treatment to the discontinuities. This generally involves an extra procedure that identifies discontinuities (Zanotti *et al.*, 2015; Deppe *et al.*, 2022). After they have been identified, these specific points are then treated differently; for example, one may use an entirely different integration scheme that handles them properly.

Finite Volume Schemes

Alternatively, we can use a shock-capturing scheme. Unlike the previous methods described, a shock-capturing scheme can handle discontinuities without any special treatment. One such method, very common in RMHD modelling (and fluids more generally), is the finite volume (FV) method.

The FV method takes advantage of the fact that the equations of RMHD can be expressed as a system of conservation laws, such as conservation of momentum and conservation of energy. The computational domain is split into a grid of cells, in which the known quantities are cell averages of the conserved variables, instead of point values like a finite difference method.

Since the quantities are conserved, the dynamics of the system can be modelled by evaluating the flux of these quantities across cell boundaries cell averages. In some cases we may also have source terms, which are sources that produce (or remove) conserved quantities inside the cell itself; for example, for a resistive plasma the dissipation due to electrical resistance appears as source terms.

The finite volume method is based on solving the weak form of the equations instead of the strong form. As a result of using these integral equations instead of differential equations, these methods can capture discontinuities without special treatment, and thus are shock-capturing schemes.

Although the treatment of discontinuities in FV methods is superior to non shock-capturing schemes, these methods can still run into problems with discontinuities; in particular, for improved accuracy FV methods require spatial interpolation of variables during the calculation of the fluxes. If this interpolation crosses a discontinuity, then the result will be spurious oscillations.

There are now various methods for avoiding such issues, such as total variation diminishing (TVD) schemes (e.g. Balsara (2001)) or weighted essentially non-oscillatory (WENO) schemes (e.g. Tchekhovskoy *et al.* (2007)). Generally, these methods work by avoiding interpolation across the discontinuity, either by reducing the number of cells being interpolated over or by simply shifting the range of interpolated cells to avoid the discontinuity.

For RMHD, FV techniques (and other conservative techniques) are highly effective for modelling many cases, such as much of the scenarios above. They have proven very successful at modelling a great many cases, and several different codes have been developed for modelling RMHD — see for example HARM (Gammie *et al.*, 2003), ECHO (Del Zanna *et al.*, 2007), CAFE (Lora-Clavijo *et al.*, 2015), IllinoisGRMHD (Etienne *et al.*, 2015) and KORAL (Sądowski *et al.*, 2013), among others.

However, it is not without its issues. The most notable for us is that when the magnetic fields are too strong and σ is large, these methods can have difficulty modelling the system, since in the limit of $\sigma \to \infty$ the conservation equations of RMHD are degenerate and not independent. Since several of the astrophysical cases described above involve these strong magnetic fields, the current models of this type are insufficient.

The actual scheme that will be used later is a closely related method to the FV method, known as a conservative finite difference method (CFD). Generally speaking, FD schemes do not maintain conservation of variables like momentum, energy etc. down to numerical precision. As noted above, methods like an FD method which is based on the differential form should have issues near discontinuities.

However, our CFD method is an adaptation of an FV method, which allows it to avoid this problem. In this case, the gradients are computed as the difference between fluxes at the boundaries, which allows neighbouring cells to share fluxes again and maintain conservation. In practice, our CFD method is extremely similar to an FV method, and thus has similar advantages and drawbacks to such a method.

Force-Free Degenerate Electrodynamics

One of the most common methods of avoiding the issue at high magnetisation is to go to the extreme end and model the case of RMHD with $\sigma \to \infty$, a regime known as force-free degenerate electrodynamics (FFDE). In this regime, the components related to the inertia of the plasma (e.g. plasma pressure, rest-mass density etc.) are neglected entirely and only the magnetic and electric fields are retained. Thus this regime is essentially a vacuum solution of Maxwell's equations.

Ideal RMHD assumes that the condition of perfect conductivity is satisfied (embodied by the condition $\boldsymbol{E} = -\boldsymbol{v} \times \boldsymbol{B}$). The lack of $\boldsymbol{v}$ in this case (since the plasma is being neglected, the plasma velocity $\boldsymbol{v}$ has no meaning) means that this condition must become two separate constraints, $\boldsymbol{E} \cdot \boldsymbol{B} = 0$ and $B^2 - E^2 > 0$.

A key aspect of FFDE is that the equations are not independent, so it is not actually possible to ensure conservation of all conserved quantities, due to errors inherent to the integration scheme. In particular, the equations of energy and momentum conservation are not independent, and only have two independent equations.

This degeneracy makes numerical modelling of FFDE a little more tricky, since the techniques of finite volume methods and conservative finite difference methods that allow us to enforce conservation of the conserved variables to numerical precision can no longer enforce this for all the variables, because we are trying to conserve seven different variables with just five equations. If we try to evolve all of the equations, then truncation error will cause them to disagree after each time step, i.e. the integration will give inconsistent results.

Methods for solving FFDE can be effectively sorted into two types, based on the equations being solved. On the one hand, we have the $\boldsymbol{S}$-$\boldsymbol{B}$ formulation, i.e. where Poynting Flux $\boldsymbol{S} = \boldsymbol{E} \times \boldsymbol{B}$ and magnetic field $\boldsymbol{B}$ are the conserved variables. This method evolves the system using Faraday's law to evolve $\boldsymbol{B}$, and momentum conservation to evolve $\boldsymbol{S}$. Some of these methods also evolve the energy as well, in order to ensure energy conservation.

Komissarov (2002) presents an example of an $\boldsymbol{S}$-$\boldsymbol{B}$ formulation. The scheme follows a finite volume scheme, evolving $\boldsymbol{B}$ and $\boldsymbol{S}$ via conservation laws. This scheme differs however when it comes to calculate $\boldsymbol{E}$ from $\boldsymbol{S}$ and $\boldsymbol{B}$ (which is necessary to calculate fluxes).

To find $\boldsymbol{E}$, the simple provision $\boldsymbol{E} = (\boldsymbol{S} \times \boldsymbol{B})/B^2$ is used. This automatically enforces the two constraints $\boldsymbol{E} \cdot \boldsymbol{B} = 0$ and $B^2 - E^2 > 0$. However, the resultant $\boldsymbol{E}$ does not satisfy $\boldsymbol{S} = \boldsymbol{E} \times \boldsymbol{B}$. This condition is generally impossible to satisfy, as we would require $\boldsymbol{S} \cdot \boldsymbol{B} = 0$ in order for this to be possible, which will be violated by errors in the integration. In effect, this method eliminates the component of $\boldsymbol{S}$ parallel to $\boldsymbol{B}$.

Besides not fully conserving momentum, the previous method also completely neglects energy conservation, which McKinney (2006) points out may be the most important to enforce due to the fact that the energy has larger non-linearity compared to the momenta. Thus they suggest also evolving energy conservation. When it comes to calculate $\boldsymbol{E}$, they suggest using the same method for calculating $\boldsymbol{E}$ as before, except after calculating $\boldsymbol{E}$ as above they alter the magnitude of $\boldsymbol{E}$ to match the energy as determined by integrating the energy conservation equation. In this way energy conservation is conserved exactly, but momentum conservation is even less accurate than before.

The second formulation for FFDE is the $\boldsymbol{E}$-$\boldsymbol{B}$ formulation, which evolves $\boldsymbol{B}$ and $\boldsymbol{E}$ directly using Faraday's law for $\boldsymbol{B}$ and Ampères law (including the displacement current) for $\boldsymbol{E}$ (Mahlmann *et al.*, 2021). Ampères law requires the current density $\boldsymbol{J}$, and thus requires an Ohm's law to relate the current to the electric and magnetic fields.

Although it is possible to evolve the system with just this, Gauss' law applies a constraint on the electric field. Munz *et al.* (1999) point out that if this constraint is ignored, the difference $|\boldsymbol{\nabla} \cdot \boldsymbol{E} - \rho_c|$ may grow unbounded, thus this formulation also requires an estimate for the charge density ρ_c for Gauss' law, which itself requires the inclusion of charge conservation as another evolution equation.

This method also requires a scheme to enforce the two constraints $\boldsymbol{E} \cdot \boldsymbol{B} = 0$ and $B^2 - E^2 > 0$, as otherwise these conditions can be violated. Various methods have been proposed for this as well. For instance, Palenzuela *et al.* (2010) change $\boldsymbol{E}$ to enforce the two conditions; first they project $\boldsymbol{E}$ into the subspace of vectors orthogonal to $\boldsymbol{B}$ to enforce $\boldsymbol{B} \cdot \boldsymbol{E} = 0$, and then if $B^2 - E^2 < 0$ they reduce the magnitude of $\boldsymbol{E}$ until $B^2 = E^2$.

Other authors instead use driver terms to enforce these conditions (Alic *et al.*, 2012; Parfrey *et al.*, 2017). Effectively, this means artificial currents which act to correct the violation of the conditions. This of course means that these conditions are not enforced exactly and will be violated to some extent. However, the violations are significantly reduced from what they would be without any correction.

Unfortunately, however it is modelled, FFDE suffers from a major drawback in that some scenarios at high magnetisation cannot be modelled. In particular, current sheets require full modelling of the plasma, as plasma heating means that the plasma cannot be ignored, so the inertia of the plasma pressure becomes significant (Mahlmann *et al.*, 2021). Since there are important high-σ cases where current sheets appear, such as pulsar magnetospheres, this flaw is a major problem in modelling these cases.

Smoothed Particle Hydrodynamics

The RMHD fluid models described above are all Eulerian descriptions of the flow, meaning that we have discretised the domain into a grid of discrete points where the flow parameters such as velocity, pressure etc. are known. This mesh of grid points moves independently of the fluid (if they move at all), and thus the fluid flows independently of the gird, through these points.

However, it is also possible to model fluids from a Lagrangian description. In this case, the locations of known quantities follow individual fluid parcels. In this sense, this method is similar to a PIC method since we are following particles through the domain — although in this case the forces acting on the particles are macroscopic parameters like pressure.

One of the first Lagrangian numerical methods is that of Smoothed Particle Hydrodynamics (SPH). As a Lagrangian method, it follows a discrete, finite set of fluid parcels around the domain as they are affected by various forces, e.g. gas pressure and the Lorentz force. Each parcel has its own values for the macroscopic quantities of pressure, density etc., and this means that instead of having these quantities known at a specific set of grid points, we know them at a complex distribution of points.

However, like a finite volume method, each particle does not represent the quantities at a particular location but instead a region surrounding it. The SPH method then calculates the actual values of quantities like density, gas pressure etc. at each parcel location by considering the smoothing length of each particle — essentially, these are calculated as weighted averages of nearby particles, with more weight given to closer particles (Monaghan, 1992; Martí and Müller, 2003; Price, 2012). This is quite similar to the averaging scheme used in a PIC method to calculate the macroscopic quantities of the current and charge densities.

This method has several unique advantages. The fact that the parcels will have a tendency to be concentrated in regions of high density means that these regions will automatically receive higher accuracy, as the grid has effectively been refined automatically. In addition, the meshless nature of a Lagrangian method means that this scheme is well-suited to cases with complex geometries, as there is no preferred grid (Liptai and Price, 2019).

Unfortunately, this method is not without its drawbacks. Most notably, just like with finite difference methods artificial viscosity is required to handle shocks (Martí and Müller, 2003), which is not desirable for accurate resolution of shocks. Moreover, for relativistic

SPH it is not clear what form this viscosity should take to be begin with (Liptai and Price, 2019). Viscosity can also be required to damp unphysical oscillations as well (Rosswog, 2010).

SPH models have been used to model various systems in the realm of RMHD. For example, Diener *et al.* (2022) used it to model a neutron star merger, while Barai *et al.* (2011) used it to model accretion onto a supermassive black hole. Meanwhile, Huško and Lacey (2023) used SPH to model an AGN jet interacting with the intra-cluster medium.

1.3 Structure of this Thesis

Altogether, we see that there are multiple astrophysical scenarios in which the magnetisation σ is high enough to cause problems. Although some methods such as FFDE and PIC codes are able to make some progress in modelling these scenarios, these both have major drawbacks that make them unsuitable for modelling these cases properly. Thus it is highly desirable to develop a code that can handle the high magnetisations properly, and it is this task that we will attempt in this thesis.

This Chapter gave a brief discussion of the placement of this project within the wider field of RMHD.

Chapter 2 will introduce and briefly analyse the governing equations of RMHD as well as the high magnetisation limit of RMHD, Force-free electrodynamics. This will include a discussion of various exact solutions to the equations, to be used later for testing.

Next, Chapter 3 will go into detail regarding the numerical methods used to model the system — both those which were previously considered and those which have been settled on — before moving on to a discussion of our novel approach itself.

Chapters 4 and 5 will give results for 1D and 2D tests respectively, going into detail regarding the strengths and shortcomings of the novel technique, and comparing results for different alterations of the method.

Finally, Chapter 6 will conclude the project with a summation of the results, as well as a discussion of further improvements and/or progress that may be possible.

Chapter 2

RMHD & FFDE

This chapter will be an in depth look at RMHD, in particular a discussion of the equations of RMHD and their basic properties, such as phase speeds of waves and hyperbolicity. It will also discuss a few exact solutions of the equations, for use later in testing. The same will also be done for the high-magnetisation limit of RMHD, known as Force-Free Degenerate Electrodynamics (FFDE).

2.1 Ideal Relativistic Magnetohydrodynamics

Ideal RMHD concerns the dynamics of a relativistic plasma. This means that we are dealing with an inviscid, compressible fluid with electromagnetic components and no resistivity. Resistive plasmas *are* of interest in the study of astrophysical plasmas; for instance, consider the "gaps" in the models of pulsar magnetospheres, where charged particles are not abundant enough to render the plasma (almost) perfectly conducting. However, in this project we will only be considering the ideal case of a perfectly conducting plasma.

This project will also only go as far as Special Relativity, not General Relativity. General relativity is of course important — it is absolutely necessary to model black holes, pulsars and supernovae — there was not sufficient time to include these effects as well. This means we will not be including gravity, and greatly simplifies the equations, as instead of a general metric tensor $g^{\alpha\beta}$ we will be using the Minkowski metric tensor of flat spacetime

$$g^{\alpha\beta} = \eta^{\alpha\beta} = \begin{pmatrix} -1 & 0 & 0 & 0 \\ 0 & 1 & 0 & 0 \\ 0 & 0 & 1 & 0 \\ 0 & 0 & 0 & 1 \end{pmatrix}, \tag{2.1}$$

(written here in Cartesian coordinates), which is of course much easier to deal with.

Many authors have already developed several different conservative codes for modelling RMHD in special and general relativity, such as Komissarov (1999a); Gammie *et al.* (2003); Del Zanna *et al.* (2007); Lora-Clavijo *et al.* (2015). While these codes are very successful in many areas, they all have one problem in common: they cannot handle high magnetisations well (Komissarov, 2006), sometimes having difficulty with magnetisation as low as $\sigma \approx 1$. For instance, Porth *et al.* (2013) had to cap $\sigma \leq 3$ for numerical stability in their model of a pulsar wind.

There are couple of methods to get around this issue. One method employed by Komissarov (2004b) is to simply pump extra plasma into regions where σ climbs too high. Although this prevents the issue with high magnetisation, this is clearly unsatisfactory if one wishes to study a case where high magnetisation is important.

Higher values of σ can be handled for isentropic flows, as the energy equation can be eliminated (Komissarov *et al.*, 2007a). In addition, Noble *et al.* (2009) used a fix for the GRMHD code HARM (Gammie *et al.*, 2003) based on parallel integration of the adiabatic entropy transport equation. If high magnetisations ever caused a problem, this conservation law could be substituted for the conservation of energy and avoid the problems with high magnetisation. However, since shocks and current sheets are not adiabatic and therefore violate entropy conservation, this is not helpful for cases involving shocks, such as termination shocks in pulsar winds (Porth *et al.*, 2013), or involving current sheets such as pulsar magnetospheres (Spitkovsky, 2006).

In light of these issues, a model that can handle high-σ accurately is highly desirable.

2.1.1 Governing Equations

In covariant form, the conservation of energy and momentum can be concisely written (Dixon, 1978; Anile, 1989)

$$\nabla_\alpha T^{\alpha\beta} = 0, \tag{2.2}$$

where $T^{\alpha\beta}$ is the stress-energy tensor, expressing the flux of the α component of 4-momentum through the β-coordinate. In other words, $T^{\alpha\beta}$ describes the flux of energy and momentum through space and time.

This equation simply enforces energy and momentum conservation, corresponding to $\beta = 0$ and $\beta = (1, 2, 3)$ respectively. Since we are working only in special relativity, the covariant derivative ∇_α is greatly simplified, and effectively equivalent to ∂_α in Cartesian coordinates, the partial derivative with respect to the α coordinate.

In RMHD, $T^{\alpha\beta}$ consists of two components: an inertial component $T^{\alpha\beta}_{(m)}$ corresponding to the stress-energy of the fluid itself (i.e. in the mass and internal energy of the fluid), and an electromagnetic component $T^{\alpha\beta}_{(e)}$ corresponding to the stress-energy of the electromagnetic fields. This is such that $T^{\alpha\beta} = T^{\alpha\beta}_{(m)} + T^{\alpha\beta}_{(e)}$.

If we assume that the fluid is inviscid and that there is no heat flux, the inertial component $T^{\alpha\beta}_{(m)}$ can be written in terms of the fluid properties as (Lichnerowicz, 1967; Schutz, 2009)

$$T^{\alpha\beta}_{(m)} = wu^{\alpha}u^{\beta} + \eta^{\alpha\beta}p_g, \tag{2.3}$$

where u^{α} is the fluid 4-velocity, p_g is the gas pressure, $w(\rho, p_g)$ is the enthalpy density. Note that in relativity, the enthalpy density is given by $w(\rho, p_g) = \rho + \rho\epsilon + p_g$, where ϵ is the specific internal energy, and so includes the rest-mass energy in addition to the typical non-relativistic enthalpy.

Meanwhile, the electromagnetic component $T^{\alpha\beta}_{(e)}$ can be written in terms of the Faraday tensor $F^{\alpha\beta}$ as (Misner *et al.*, 1973)

$$T^{\alpha\beta}_{(e)} = F^{\alpha\mu}F^{\beta}_{\mu} - \frac{1}{4}\eta^{\alpha\beta}F_{\mu\nu}F^{\mu\nu}. \tag{2.4}$$

With Eq. (2.2) and these two components, we now have a set of four conservation laws, corresponding to the four rows of the $T^{\alpha\beta}$ tensor. In addition to these equations, we also have Maxwell's equations for the electromagnetic fields,

$$\nabla_{\alpha}{}^{*}F^{\alpha\beta} = 0, \tag{2.5}$$

and

$$\nabla_{\alpha}F^{\alpha\beta} = J^{\beta}, \tag{2.6}$$

where $J^{\beta} = (\rho_c, \boldsymbol{J})$ is the 4-current with ρ_c the electric charge density and $\boldsymbol{J}$ the conventional current density, while ${}^{*}F^{\alpha\beta} = \frac{1}{2}\epsilon^{\alpha\beta\mu\nu}F_{\mu\nu}$ is the dual of the Faraday tensor with $\epsilon^{\alpha\beta\mu\nu}$ the four-dimensional Levi-Civita Symbol. Although both of these are evolution equations (except for $\beta = 0$ where $F^{00} = {}^{*}F^{00} = 0$ means there is no time derivative in either case), Eq. (2.6) is not used to evolve $F^{\alpha\beta}$ and is only used in order to determine the 4-current J^{β} (if desired), just like in non-relativistic MHD. This is because Eq. (2.6) gives us the evolution of the electric field, but the perfect conductivity condition below in Eq. (2.8) gives us the electric field in terms of the velocity and magnetic field. In resistive RMHD models, these equations can no longer be dropped; see for example Mattia *et al.* (2023).

The final evolution equation we need expresses the conservation of mass (Komissarov, 1999a),

$$\nabla_{\alpha}(\rho u^{\alpha}) = 0. \tag{2.7}$$

Of course, in some conditions these quantities are not conserved, for instance if there is significant pair production generating new plasma. This would add source terms to right of Eq. (2.7), expressing this change in plasma density. These cases will not be considered here.

In addition to these three evolution equations, we also need equation to make this ideal RMHD: the perfect conductivity (PC) condition (Del Zanna *et al.*, 2007)

$$F^{\alpha\beta}u_\alpha = 0, \tag{2.8}$$

which expresses the lack of electrical resistance in the fluid. If the fluid is not perfectly conducting, then we would need to include the relativistic Ohm's law. We will not be considering a resistive plasma here, but a discussion of Ohm's law is helpful to understand where Eq. (2.8) comes from.

The simplest case of Ohm's law is that of a scalar law, but in a sufficiently strong magnetic field the resistivity becomes anisotropic. The key here is the ratio between Larmor radius r_l and mean free path λ (Petschek, 1958). The mean free path gives the average distance a particle travels before a collision, while the Larmor radius is the radius of the curved path the particle follows in a given magnetic field. That is, given that the magnetic component of the Lorentz force acts perpendicular to the velocity of a charged particle and the magnetic field, the magnetic field acts to cause to particle to follow a curved path — either circular if the particle has no velocity parallel to the magnetic field, or helical otherwise. This is given by

$$r_l = \frac{mv_\perp}{B|q|},$$

where m is the mass of the particle, $v_\perp$ is the velocity of the particle orthogonal to $\boldsymbol{B}$, and q is the charge of the particle.

If $r_l \gg \lambda$, i.e. the Larmor radius is significantly larger than the mean free path, then the particles will follow approximately straight paths between collisions, thus meaning that the conductivity will be isotropic and therefore scalar. However, if r_l becomes comparable to λ then particle paths will be curved. Thus the travel of charged particles orthogonal to the magnetic field is suppressed, hence conductivity in this direction is also suppressed. Meanwhile, particles can still travel freely along the magnetic field lines. In this more general case, a tensor formulation of Ohm's law is thus more appropriate.

If we stick to a scalar law here, then Ohm's law takes the form (Lyutikov and Uzdensky, 2003)

$$J^\beta = \rho_c^0 u^\beta + \sigma_c F^{\alpha\beta}u_\alpha, \tag{2.9}$$

where σ_c is the fluid conductivity, and $\rho_c^0 = -J_\alpha u^\alpha$ is the electric charge density in the fluid frame.

This law can be understood as having two components; the first term denotes current due to advection of charges with the fluid, while the second is current forced by the electric and magnetic fields. If we assume that the current J^β is finite, then since the second term must remain finite also, as $\sigma_c \to \infty$ we must have the condition Eq. (2.8).

Another aspect worth mentioning is entropy conservation. Entropy can be defined using Gibbs' equation (Eckart, 1940)

$$T ds = d\epsilon + p d\left(\frac{1}{\rho}\right), \tag{2.10}$$

where T is the absolute temperature of the fluid, ϵ is the specific internal energy of the fluid and s is the specific rest entropy, i.e. the specific entropy as measured by an observer moving with the fluid.

Taub (1948) showed that if we use this equation with Eqs. (2.2) and (2.7) and let $\boldsymbol{B} = \boldsymbol{E} = 0$ (i.e. an unmagnetised gas), then conservation of energy for an ideal fluid can be written as

$$\rho T u^\alpha \nabla_\alpha s = 0, \tag{2.11}$$

so conservation of mass, momentum and energy implies constant entropy along streamlines, much like the non-relativistic case. This means that entropy is conserved, provided that the flow is continuous. If the flow has discontinuities, then when the streamlines intersect them the variables can have a discontinuity and overall entropy conservation can thus be violated.

Harris (1957) further showed that similar arguments can be applied to a relativistic, *magnetised* plasma with $\boldsymbol{B}$ and $\boldsymbol{E}$ non-zero to obtain

$$\rho T u^\alpha \nabla_\alpha s = \boldsymbol{J}_c \cdot \boldsymbol{E}', \tag{2.12}$$

where $\boldsymbol{J}_c = \boldsymbol{J} - \rho_c \boldsymbol{v}$ is the conduction current (the electric current minus the advection current, the current due to advection of charged particles), and $\boldsymbol{E}'$ is the electric field as measured by an observer moving with the fluid,

$$\boldsymbol{E}' = \gamma \left(\boldsymbol{E} + \boldsymbol{v} \times \boldsymbol{B} \right). \tag{2.13}$$

The assumption of perfect conductivity Eq. (2.8) implies that $\boldsymbol{E}' = 0$, and therefore entropy is also constant along streamlines for an ideal, magnetised plasma as well. Naturally, for a resistive plasma $\boldsymbol{E}' = 0$ is generally not true and so entropy is not conserved, even for continuous cases.

Equation of State

The final key we need to close this system is an equation of state, relating the relativistic enthalpy density w (or alternatively specific internal energy ϵ) to the rest mass density

ρ and gas pressure p_g, i.e. we need a relation of the form $w = w(\rho, p_g)$. The form of this equation depends on the properties of the plasma being described; the most common assumption is that of an ideal gas, a gas in which all the particles are randomly moving point particles without inter-particle interactions. In the non-relativistic case this reduces very simply as the ratio of specific heats in this case is constant, independent of the density and pressure and dependent only on the degrees of freedom of the individual molecules. This means we can write the internal energy for the non-relativistic case of an ideal gas as

$$e = \frac{\Gamma}{\Gamma - 1} p_g,$$

where $\Gamma = \dfrac{C_p}{C_v}$ is the ratio of specific heats, and e is the internal energy of the gas (notably not including the rest-mass energy of the fluid in the non-relativistic case). Unfortunately, Γ is not constant for a relativistic perfect gas, so the equation of state for a perfect gas is much more complicated in this case.

Suppose a gas is made of N particle species which are all individually conserved, so that

$$\nabla_\alpha D_I^\alpha = 0, \tag{2.14}$$

where $D_I^\alpha = n_I u^\alpha$ is the 4-particle flux of species I, and n_I is the number density of species I in the rest frame. Although generally we could use a multi-fluid description of the fluid, where each particle species is represented by a separate fluid and has its own velocity, here we will only consider the simplified case where all N species share the same 4-velocity u^α, the fluid velocity. The total particle number density is given by

$$n = \sum_{I=1}^{N} n_I, \tag{2.15}$$

so given the particle rest mass of each species m_I we must have

$$\rho = \sum_{I=1}^{N} n_I m_I, \tag{2.16}$$

for the fluid rest mass density.

Synge (1957) gives the following equation of state for a perfect gas

$$w = \sum_{I=1}^{N} n_I m_I G(\xi_I)\,, \tag{2.17}$$

$$p_g = \sum_{I=1}^{N} \frac{n_I m_I}{\xi_I}, \tag{2.18}$$

where $\xi_I = \dfrac{m_I}{T}$, with T the gas temperature, and

$$G(\xi) = \frac{K_3(\xi)}{K_2(\xi)}, \tag{2.19}$$

where the $K_\nu(\cdot)$ are the modified Bessel functions of the second kind. The plasma temperature T is assumed to be the same for all particle species at any given location, and can be calculated from the ideal gas law

$$p_g V = NT, \tag{2.20}$$

where V is a given volume and N is the number of particles in said volume. Since the number density $n = N/V$, we can rearrange for temperature as

$$T = \frac{p_g}{n}, \tag{2.21}$$

so we can calculate the temperature from the gas pressure p_g and the particle number density n. Eqs. (2.17) and (2.18) therefore constitute the required equation of state for a relativistic ideal gas.

The adiabatic sound speed a_s is given by

$$a_s^2 = \left(\frac{\partial p}{\partial \epsilon}\right)_s, \tag{2.22}$$

where s is the entropy. We can also calculate the ratio of specific heats for this relativistic gas as

$$\Gamma = \frac{\sum_{I=1}^{N} n_I G'(\xi_I)\, \xi_I^2}{\sum_{I=1}^{N} n_I \left(G'(\xi_I)\, \xi_I^2 + 1\right)}, \tag{2.23}$$

which we can then use to write Eq. (2.22) as

$$a_s^2 = \frac{\Gamma p_g}{w}. \tag{2.24}$$

Using Eqs. (2.17), (2.18) and (2.23) we can then show that for an ultra-relativistic gas with $p_g \gg \rho$ (i.e. plasma internal energy density much larger than rest-mass energy density), we have that

$$\Gamma \to \frac{4}{3}, \quad a_s^2 \to \frac{1}{3}. \tag{2.25}$$

Since the speed of sound a_s is an increasing function of p_g, the speed of sound for a relativistic ideal gas is therefore limited to $a_s = c/\sqrt{3} \approx 0.577c$, a little more than half the speed of light.

Analogy with the non-relativistic case would lead one to search for a ratio $\Gamma_\star$ as

$$w = \rho + \frac{\Gamma_\star}{\Gamma_\star - 1} p_g, \tag{2.26}$$

and we can then use Eqs. (2.17) and (2.18) to write this as (Falle and Komissarov, 1996)

$$\frac{\Gamma_\star}{\Gamma_\star - 1} = \frac{\sum_{I=1}^{N} n_I m_I \left(G(\xi_I) - 1\right)}{\sum_{I=1}^{N} n_I m_I \xi_I^{-1}}. \tag{2.27}$$

In non-relativistic, ideal gases these two ratios Γ and $\Gamma_\star$ are the same. However, it is important to note that in the relativistic case the two are no longer necessarily the

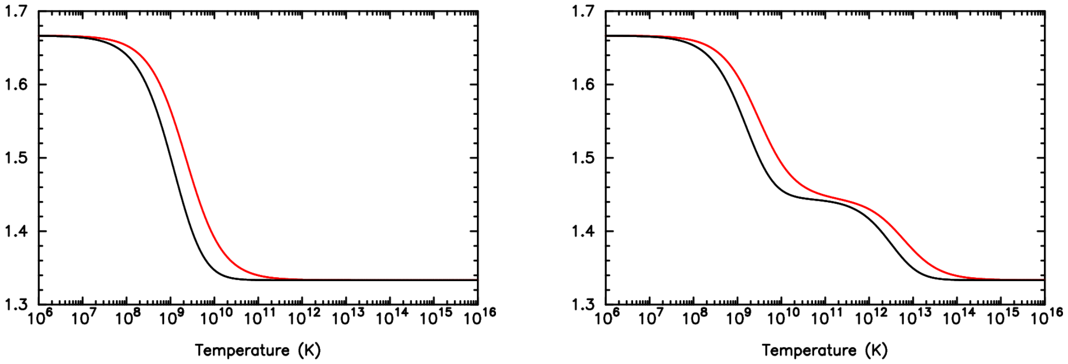

(a) *(b)*

Figure 2.1: Γ *(black) and* Γ^* *(red) for an Electron-Positron (a) and an Electron-Proton gas (b), with equal ratios of particle species in both cases.*

same, so that generally $\Gamma \neq \Gamma_\star$. These two are generally only equal if the gas is either non-relativistic so that $p_g \ll \rho$, or if the gas is ultra-relativistic so that $p_g \gg \rho$. Although they are asymptotically equal for the non-relativistic and ultrarelativistic cases, in the transition between these extremes their values diverge.

Fig. 2.1 shows a comparison of Γ and $\Gamma_\star$ for an electron-positron gas and an electron-proton gas (with equal number densities of each particle species), the most common types of plasma in astrophysical situations. Note how the electron-proton gas appears two have two regions where increased temperature leads to decreased $\Gamma/\Gamma_\star$. This is a product of the fact that such a plasma consists of particles of two different masses.

The temperature of the particles can be related to the average kinetic energy per particle. Since we have assumed that at any given location all particle species have the same temperature, each particle species gave the same average energy per particle. Thus the particles with less mass reach the relativistic regime — where the particles are moving at significant fractions of the speed of light — before the more massive particles.

Although for accuracy's sake we should be using the above equation of state described in Eqs. (2.17) and (2.18), for the purposes of testing our numerical model it is unnecessary to use this full equation of state; we can see from Fig. 2.1 that although there are relativistic corrections to be made, they are not particularly significant, and only serve to change the ratio of specific heats (for a monatomic gas) from $\frac{5}{3}$ in the non-relativistic regime to $\frac{4}{3}$ in the ultrarelativistic regime.

Furthermore, this inclusion also makes the calculation of some exact solutions much more cumbersome, especially considering the presence of Bessel functions in Eq. (2.17). We would also need to include Eq. (2.14) for all N species, unless there is only one species $N = 1$ (in which case conservation of particle number is equivalent to Eq. (2.7), mass conservation).

For the purposes of testing our new numerical scheme this therefore adds an unnecessary complication, and as such for the remainder of this thesis we will assume a constant-Γ gas law

$$w(\rho, p_g) = \rho + \frac{\Gamma}{\Gamma - 1} p_g, \tag{2.28}$$

and use the ultra-relativistic value for $\Gamma = \frac{4}{3}$. For this value of Γ, the gas law reduces to $w(\rho, p_g) = \rho + 4p_g$, and the speed of sound retains the limit of $a_s^2 \to \frac{1}{3}$.

2.1.2 Special Relativistic 3+1 Splitting

While the covariant forms of the equations of RMHD (Eqs. (2.2), (2.5), (2.7) and (2.8)) are concise and often convenient to work with analytically due to all the tools of tensor calculus, for the purposes of numerical integration it is more convenient to express these in the form of conservation laws in terms of primitive properties of the fluid, such as density ρ, gas pressure p_g etc.

First of all we can start with Eq. (2.7), conservation of mass. Under special relativistic splitting and in Cartesian coordinates this becomes

$$\partial_t \left(\rho u^0 \right) + \boldsymbol{\nabla} \cdot (\rho \boldsymbol{u}) = 0, \tag{2.29}$$

where we recall that $\boldsymbol{u}$ the three spatial components of the 4-velocity, and $u^0 = \gamma$ is the fluid Lorentz factor, given by

$$\gamma^2 = u^2 + 1 = \frac{1}{1 - v^2}. \tag{2.30}$$

Next we have Eq. (2.2), the conservation of energy and momentum. We can write out the Electromagnetic component $T^{\alpha\beta}_{(e)}$ in Minkowski coordinates by first defining the Maxwell stress tensor

$$\sigma_{ij} = E_i E_j + B_i B_j - \frac{1}{2} \left(E^2 + B^2 \right) \delta_{ij}, \tag{2.31}$$

where δ_{ij} is the Kronecker delta, i.e.

$$\delta_{ij} = \begin{cases} 1 & \text{if } i = j \\ 0 & \text{if } i \neq j \end{cases}. \tag{2.32}$$

Now we can write out the electromagnetic component of the stress-energy tensor $T^{\alpha\beta}_{(e)}$ as (Misner *et al.*, 1973)

$$T^{\alpha\beta}_{(e)} = \begin{pmatrix} \frac{1}{2}(E^2 + B^2) & (\boldsymbol{E} \times \boldsymbol{B})_x & (\boldsymbol{E} \times \boldsymbol{B})_y & (\boldsymbol{E} \times \boldsymbol{B})_z \\ (\boldsymbol{E} \times \boldsymbol{B})_x & -\sigma_{xx} & -\sigma_{xy} & -\sigma_{xz} \\ (\boldsymbol{E} \times \boldsymbol{B})_y & -\sigma_{yx} & -\sigma_{yy} & -\sigma_{yz} \\ (\boldsymbol{E} \times \boldsymbol{B})_z & -\sigma_{zx} & -\sigma_{zy} & -\sigma_{zz} \end{pmatrix}. \tag{2.33}$$

With this expression for $T_{(e)}^{\alpha\beta}$ we are ready to write out the equations; Eq. (2.2) splits separately into the conservation of energy

$$\partial_t\Big(wu^0u^0 - p_g + \frac{1}{2}\big(E^2 + B^2\big)\Big) + \boldsymbol{\nabla}\cdot\Big(wu^0\boldsymbol{u} + \boldsymbol{E}\times\boldsymbol{B}\Big) = 0, \tag{2.34}$$

and the conservation of momentum

$$\partial_t\Big(wu^0\boldsymbol{u} + \boldsymbol{E}\times\boldsymbol{B}\Big) + \boldsymbol{\nabla}\cdot\left(w\boldsymbol{u}\boldsymbol{u} - \boldsymbol{E}\boldsymbol{E} - \boldsymbol{B}\boldsymbol{B} + \Big(p_g + \frac{1}{2}\big(E^2 + B^2\big)\Big)\,\delta^{ij}\right) = 0, \tag{2.35}$$

which is a vector equation, consisting of three equations in one, one for each dimension of space.

The final set of evolution equations is in Eq. (2.5), Gauss' law for magnetism and Faraday's law. We can write out the Faraday tensor in Minkowski coordinates in terms of the magnetic field $\boldsymbol{B}$ and electric field $\boldsymbol{E}$ as

$$F^{\alpha\beta} = \begin{pmatrix} 0 & -E_x & -E_y & -E_z \\ E_x & 0 & -B_z & B_y \\ E_y & B_z & 0 & -B_x \\ E_z & -B_y & B_x & 0 \end{pmatrix}, \tag{2.36}$$

so the time component of Eq. (2.5) gives us Gauss' law for magnetism, the divergence-free condition on $\boldsymbol{B}$

$$\boldsymbol{\nabla}\cdot\boldsymbol{B} = 0, \tag{2.37}$$

while the space components give Faraday's law

$$\partial_t\boldsymbol{B} - \boldsymbol{\nabla}\times\boldsymbol{E} = 0. \tag{2.38}$$

Of particular note here is how the divergence-free condition is not an evolution equation, and instead acts as a constraint on $\boldsymbol{B}$. This is of particular importance in 2D and higher models, as particular care needs to be taken to ensure that this constraint remains satisfied.

We can also write out the remaining two of Maxwell's laws, although as noted previously with perfect conductivity these equations are not used for the evolution of the system. From the time component of Eq. (2.6) we have Gauss' law

$$\boldsymbol{\nabla}\cdot\boldsymbol{E} = \rho_c, \tag{2.39}$$

while the space components give Ampères' law

$$\partial_t\boldsymbol{E} - \boldsymbol{\nabla}\times\boldsymbol{B} = -\boldsymbol{J}. \tag{2.40}$$

Note that unlike non-relativistic MHD we can not neglect the displacement current $\partial_t\boldsymbol{E}$ here.

The time component of the PC condition Eq. (2.8) gives

$$\boldsymbol{E} \cdot \boldsymbol{u} = 0. \tag{2.41}$$

Since $\boldsymbol{u}$ is parallel to $\boldsymbol{v}$ with only a factor of $\gamma \neq 0$, we can also write this as $\boldsymbol{E} \cdot \boldsymbol{v} = 0$.

Finally, the spatial components of Eq. (2.8) give

$$\boldsymbol{E} = -\boldsymbol{v} \times \boldsymbol{B}. \tag{2.42}$$

This perfect conductivity condition implies several other conditions on $\boldsymbol{E}$: First, it clearly implies Eq. (2.41), making that equation superfluous. Second, it implies that $\boldsymbol{E} = 0$ in the fluid frame, where $\boldsymbol{v} = 0$. Third, it implies $\boldsymbol{B} \cdot \boldsymbol{E} = 0$. Finally fourth, with the condition that the fluid is not superluminal $v < 1$ it implies that $B^2 > E^2$. For the latter two, the expressions $\boldsymbol{B} \cdot \boldsymbol{E}$ and $B^2 - E^2$ are both Lorentz invariants, and therefore true in any frame, as we would expect.

Eqs. (2.29) to (2.42) constitute the complete equations of RMHD, after we include the equation of state Eq. (2.28). We could substitute for $\boldsymbol{E}$ in these equations using Eq. (2.42), although for our purposes this only serves to make the equations even more complex. In order to study the system analytically, we can change the equations into another form. Following Anile (1989), we now define the magnetic 4-vector

$$b_\alpha = \frac{1}{2}\epsilon_{\alpha\beta\gamma\delta} u^\beta F^{\gamma\delta}. \tag{2.43}$$

In the fluid frame $b^\alpha = (0, \boldsymbol{B})$, so since b^2 is a Lorentz invariant we find that in any frame, the value of b^2 is equal to the value of B^2 in the fluid frame. In the laboratory frame, the components of b^α are related to $\boldsymbol{B}$ and $\boldsymbol{E}$ via

$$b^0 = \boldsymbol{B} \cdot \boldsymbol{u}, \quad \boldsymbol{b} = \frac{\boldsymbol{B} + b^0 \boldsymbol{u}}{u^0}, \quad b^2 = B^2 - E^2,$$

$$\boldsymbol{B} = \boldsymbol{b} u^0 - \boldsymbol{u} b^0, \quad \boldsymbol{E} = -\boldsymbol{u} \times \boldsymbol{b},$$

where we have used the PC condition to get $\boldsymbol{E}$ in terms of $\boldsymbol{u}$ and $\boldsymbol{b}$.

Given b^α, the covariant form of the RMHD equations is simpler, as the two tensors $T^{\alpha\beta}$ and $F^{\alpha\beta}$ can be written

$$T^{\alpha\beta} = \left(w + b^2\right) u^\alpha u^\beta + \left(p_g + \frac{1}{2} b^2\right) \eta^{\alpha\beta} - b^\alpha b^\beta, \tag{2.44}$$

$$F^{\alpha\beta} = b^\alpha u^\beta - b^\beta u^\alpha. \tag{2.45}$$

Note that this vector b^α is only useful due to the PC condition Eq. (2.8), as otherwise we cannot cancel the electric field.

We can thus rewrite the equations of RMHD using this to obtain (Anile, 1989; Komissarov, 1999a)

$$\partial_t\Big(\left(w+b^2\right)u^0u^0-\left(p_g+\frac{1}{2}b^2\right)-b^0b^0\Big)+\boldsymbol{\nabla}\cdot\Big(\left(w+b^2\right)u^0\boldsymbol{u}-b^0\boldsymbol{b}\Big)=0, \tag{2.46}$$

for energy conservation,

$$\partial_t\Big(\left(w+b^2\right)u^0\boldsymbol{u}-b^0\boldsymbol{b}\Big)+\boldsymbol{\nabla}\cdot\Big(\left(w+b^2\right)\boldsymbol{u}\boldsymbol{u}-\boldsymbol{b}\boldsymbol{b}+\left(p_g+\frac{1}{2}b^2\right)\delta^{ij}\Big)=0, \tag{2.47}$$

for momentum conservation, and

$$\partial_t\boldsymbol{B}+\boldsymbol{\nabla}\times(\boldsymbol{u}\times\boldsymbol{b})=0, \tag{2.48}$$

for Faraday's law (this form with $\boldsymbol{E}$ eliminated is often called the induction equation). Mass conservation is unchanged of course, given that there is no input from the electromagnetic fields.

Note how $b^2=B^2-E^2$ appears together with the gas pressure p_g in Eq. (2.44), and thus also appears with it in Eqs. (2.46) and (2.47). This term (with a factor of 1/2, so $\frac{1}{2}b^2$) is called the magnetic pressure p_m, and acts similar to the gas pressure. It is equivalent to the magnetic pressure in the non-relativistic case. As the magnitude of a 4-vector, this value is a Lorentz invariant, much like the gas pressure p_g, the rest-mass density ρ, and the enthalpy density w.

After applying condition Eq. (2.42), these equations are altogether a total of eight differential equations with eight unknowns and one constraint, Eq. (2.37). In 1D this system reduces to seven differential equations, as Eq. (2.37) reduces to $\partial_x B_x=0$, while the x-component of Faraday's law Eq. (2.48) reduces to $\partial_t B_x=0$. So in 1D these two equations enforce that B_x is constant in both space and time, and we have no need to deal further with the divergence-free condition.

2.1.3 Linear Theory

To help understand the dynamics of RMHD, we will look into the behaviour of linear waves. Non-linear phenomena like shock waves and rarefaction waves can also be related to small-amplitude, linear counterparts (Toro, 1997), thus this will be helpful for constructing exact solutions for testing the code. In addition, the linearisation is also of great interest for numerical methods based on Riemann solvers, such as the numerical method used in this project discussed later in section 3.1.2.

We are looking for small amplitude, plane wave solutions of the equations Eqs. (2.29) to (2.42). In the most general case (but neglecting source terms), we are working with a system of equations of the form

$$\frac{\partial\boldsymbol{Q}}{\partial t}+\frac{\partial\boldsymbol{F}^x}{\partial x}=0, \tag{2.49}$$

where $\boldsymbol{Q}$ is a vector of conserved quantities, and $\boldsymbol{F}^x = \boldsymbol{F}^x(\boldsymbol{Q})$ is a vector of x-fluxes. Note that we have assumed the plane wave is parallel to the y-z plane, so we can drop y- and z-derivatives. A non-parallel plane wave can easily be transformed into a parallel one by rotation, so we have not lost any details.

We now look for plane wave solutions of the form

$$\boldsymbol{Q}(x,t) = \boldsymbol{Q}_0 + \boldsymbol{Q}_1 e^{i(kx-\omega t)}, \tag{2.50}$$

where $\boldsymbol{Q}_0$ is a constant background state, $\boldsymbol{Q}_1$ is a small perturbation and k, ω are the angular wave-number and angular frequency of the wave respectively.

Inserting this into Eq. (2.49), we obtain

$$\frac{\partial}{\partial t}\left(\boldsymbol{Q}_0 + \boldsymbol{Q}_1 e^{i(kx-\omega t)}\right) + \frac{\partial}{\partial x}\boldsymbol{F}^x\left(\boldsymbol{Q}_0 + \boldsymbol{Q}_1 e^{i(kx-\omega t)}\right) = 0, \tag{2.51}$$

which comes out to

$$-i\omega \boldsymbol{Q}_1 e^{i(kx-\omega t)} + \boldsymbol{A}\Big(\boldsymbol{Q}_0 + \boldsymbol{Q}_1 e^{i(kx-\omega t)}\Big)\, ik\boldsymbol{Q}_1 e^{i(kx-\omega t)} = 0, \tag{2.52}$$

where $\boldsymbol{A} = \dfrac{\partial \boldsymbol{F}^x}{\partial \boldsymbol{Q}}$ is the Jacobian of $\boldsymbol{F}^x$ with respect to $\boldsymbol{Q}$. If we use the assumption that $\boldsymbol{Q}_1$ is small compared to $\boldsymbol{Q}_0$, then the $\boldsymbol{Q}_1$-dependence of $\boldsymbol{A}$ can be dropped so that after rearranging we have

$$\left(\boldsymbol{A}(\boldsymbol{Q}_0) - \frac{\omega}{k}\boldsymbol{I}\right)\boldsymbol{Q}_1 = 0, \tag{2.53}$$

where $\boldsymbol{I}$ is the identity matrix.

In other words, the plane waves have phase velocity $\mu = \omega/k$ given by the eigenvalues of $\boldsymbol{A}(\boldsymbol{Q}_0)$, and the perturbation vectors $\boldsymbol{Q}_1$ of each wave are the eigenvectors.

Thus we need to find the eigenvalues and eigenvectors of $\boldsymbol{A}$ for our system. Performing this analysis on our system however is easier said than done, given its complexity. One way of doing this is to solve the system in the fluid frame with $u^\alpha = (1,0,0,0)$, a far simpler case, and then use Lorentz transformations to find the solution in the general case.

Alternatively, we could greatly simplify the problem if the system were written in covariant form, since then we would have access to the powerful tools of tensor calculus. For this, the vector of unknowns must be constructed of 4-vectors and 4-scalars. For RMHD, these could be $u^\alpha, b^\alpha, p_g, s$, where s is specific entropy. However, we have ten unknowns here, so this requires ten evolution equations instead of the seven we have in 1D.

To overcome this problem, Anile and Pennisi (1986) used an ingenious method to construct three more evolution equations by transforming the three constraints we have into evolution equations; these constraints being the divergence-free condition Eq. (2.37), as well as two more constraints on the 4-vectors u^α and b^α: $u_\alpha u^\alpha = -1$ and $u_\alpha b^\alpha = 0$. This allows us to write the system in terms of the primitive vector $\boldsymbol{U} = (u^\alpha, b^\alpha, p_g, s)$.

As a consequence of adding three extra evolution equations to the system, three new unphysical waves appear in the solution. These waves can easily be identified as the only three waves which break the constraints these extra equations were derived from.

We will first present the results of Anile and Pennisi (1986) in covariant form; however, before that we need to introduce a covariant wavevector following from Friedrichs (1954, 1974).

First, suppose that the position of a wavefront is given by

$$\phi(x^\alpha) = 0, \tag{2.54}$$

where ϕ is a 4-scalar and a function of position x^α, so that the wavefront is on a level curve of ϕ.

Let μ be the wave speed and $\boldsymbol{n}$ the unit vector in the direction of travel of the wavefront in the Laboratory frame Σ. Now define a covariant vector ϕ_α such that in the frame Σ we have

$$\phi_\alpha = (-\mu, \boldsymbol{n}), \tag{2.55}$$

which is of course related to $\phi(x^\alpha)$ as the wavevector $\partial_\alpha \phi$ normalised to $\phi_\alpha \phi^\alpha = 1 - \mu^2$.

Now further introduce the unit vectors $\xi_\alpha = (-1, \boldsymbol{0})$ and $\chi_\alpha = (0, \boldsymbol{n})$. These vectors therefore satisfy

$$\phi_\alpha = \mu \xi_\alpha + \chi_\alpha, \quad \xi_\alpha \xi^\alpha = -1, \quad \chi_\alpha \chi^\alpha = 1, \quad \xi_\alpha \chi^\alpha = 0, \quad G = \phi_\alpha \phi^\alpha = 1 - \mu^2. \tag{2.56}$$

In our case we are only interested in waves travelling along the x-axis in the frame Σ, so we have

$$\xi^\alpha = (1, 0, 0, 0), \quad \chi^\alpha = (0, 1, 0, 0), \quad \phi^\alpha = (\mu, 1, 0, 0). \tag{2.57}$$

This vector ϕ^α was introduced by Friedrichs (1954, 1974) in order to formulate hyperbolic laws in covariant form.

Eigenvalues

Anile and Pennisi (1986) derived from their augmented model the following expression for the eigenvalues

$$\mathcal{E} a^2 \mathcal{A}^2 \mathcal{N} = 0, \tag{2.58}$$

where

$$\mathcal{A} = \mathcal{E} a^2 - \mathcal{B}^2, \tag{2.59}$$

$$\mathcal{N} = w\left(e'_p - 1\right)a^4 - \left(w + e'_p b^2\right)a^2 G + B^2 G, \tag{2.60}$$

$$a = \phi_\alpha u^\alpha, \quad \mathcal{B} = \phi_\alpha b^\alpha, \quad \mathcal{E} = w + b^2, \quad e'_p = \left(\frac{\partial e}{\partial p}\right)_s = \frac{1}{a_s^2}.$$

With Eq. (2.57) we have that

$$a = u^x - \mu u^0, \quad \mathcal{B} = b^x - \mu b^0. \tag{2.61}$$

Since $\mathcal{E} > 0$, Eq. (2.58) generally has the following solutions:

1. One solution for $a^2 = 0$, a repeated root,
2. Two solutions for $\mathcal{A}^2 = 0$, both repeated roots,
3. Four solutions for $\mathcal{N} = 0$.

We can now obtain the phase speeds,

$$\mu_m = v_x = \frac{u^x}{u^0}, \tag{2.62}$$

for material waves advecting with the fluid and corresponding to $a = 0$,

$$\mu_a = \frac{b^x \pm u^x\sqrt{\mathcal{E}}}{b^0 \pm u^0\sqrt{\mathcal{E}}}, \tag{2.63}$$

for Alfvén waves, corresponding to $\mathcal{A} = 0$, and

$$u_0^4\left(\mu_{ms} - v_x\right)^4\left(1 - \epsilon^2\right) + \left(1 - \mu_{ms}^2\right)\left(\frac{a_s^2}{\mathcal{E}}\left(b^x - \mu_{ms}b^0\right)^2 - u_0^2\left(\mu_{ms} - v_x\right)^2\epsilon^2\right) = 0, \tag{2.64}$$

for Magneto-Sonic waves, corresponding to $\mathcal{N} = 0$ and where

$$\epsilon^2 = a_s^2 + s^2 - a_s^2 s^2, \quad s^2 = \frac{b^2}{\mathcal{E}}. \tag{2.65}$$

Unfortunately, Eq. (2.64) is a quartic polynomial in μ_{ms} and does not generally permit separate expressions for the fast and slow magneto-sonic waves, unlike MHD (Lichnerowicz, 1967; Keppens and Meliani, 2008). If calculating these speeds is necessary in the model then we need to be able to solve a quartic polynomial — fortunately, this is possible analytically.

As it turns out, just like in the non-relativistic case of MHD these seven types of waves always appear in the same order of phase speed. That is, the phase speeds always satisfy the following (Keppens and Meliani, 2008)

$$-1 \le \mu_f^- \le \mu_a^- \le \mu_s^- \le \mu_m \le \mu_s^+ \le \mu_a^+ \le \mu_f^+ \le 1, \tag{2.66}$$

where $\mu_f^\pm$ and $\mu_s^\pm$ are the fast and slow MS phase speeds respectively, and where the sign of ± indicates left-going waves for $-$ and right-going waves for $+$. Note that these are left

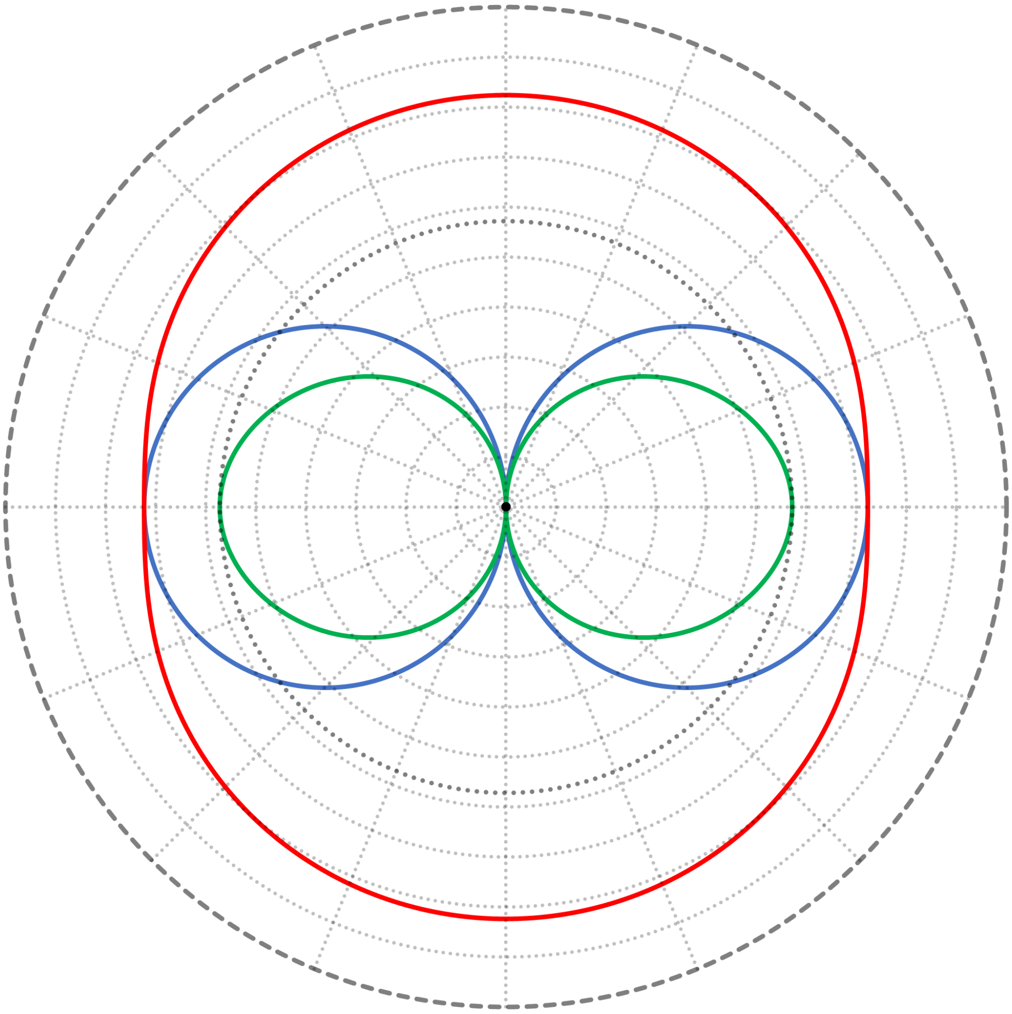

Figure 2.2: *Phase speeds in the fluid frame. The phase speeds are calculated for the state* $\boldsymbol{B} = (3, 0, 0)$, $\rho = 1$, $p_g = 2$. *In this plot, the red line indicates fast speed, the blue line is Alfvén speed, and the green line is the slow speed. The outermost dashed circle is the speed of light, and the dotted circle tangent to the slow speed is at the adiabatic sound speed* a_s. *The remaining dotted circles are at constant velocities of* $0.1, 0.2, ..., 0.9$.

or right going in the fluid frame; in an arbitrary frame, the fluid may have a high enough velocity that $\mu_s^- > 0$ or even $\mu_f^+ < 0$, for example.

From comparison to non-relativistic MHD we expect one material wave and two Alfvén waves, and as such we expect that the three additional waves introduced by the augmented system are an extra wave travelling with the material wave, and two additional waves travelling with the Alfvén waves, and this is exactly the case (Anile and Pennisi, 1986). We can thereby refer to the additional material wave the "pseudo-material" wave and the additional Alfvén waves the "pseudo-Alfvén" waves.

The group speed of each wave behaves similarly to MHD (Keppens and Meliani, 2008); fast waves are roughly the same between phase and group speed in all direction and Alfvén waves follow the magnetic field lines advected by the fluid flow. Slow waves follow magnetic

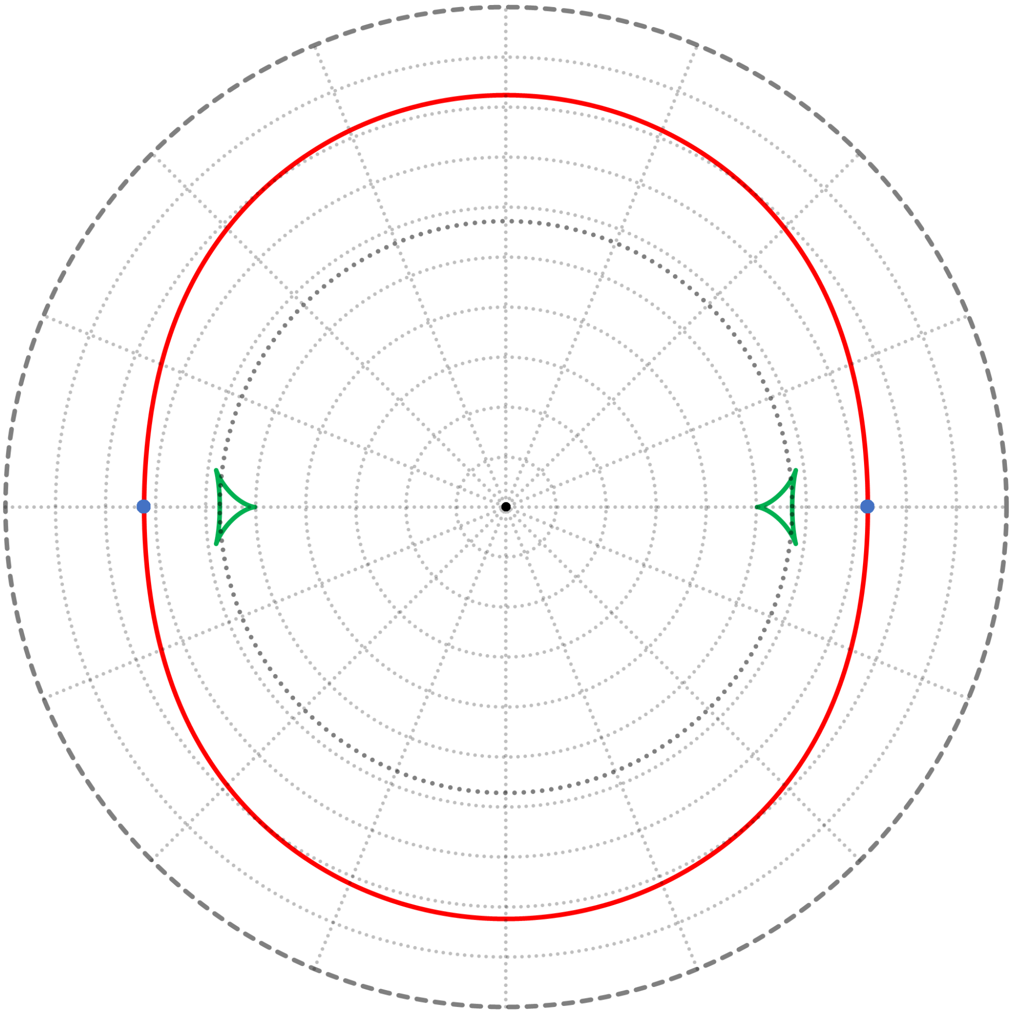

Figure 2.3: *Group speeds in the fluid frame. The plot has the same state and plot description as Fig. 2.2.*

field lines to an extent, although not exactly. To help visualise these, see Figs. 2.2 and 2.3 for a plot of the phase and group speeds in the fluid frame.

In these plots, we are showing the phase or group speeds of each of the three wave types in each direction. For the phase speed plot, this represents the phase speed of a plane wave in each direction. For the group speed plot, this represents the speed and direction in which energy is carried from the system. That is, if energy is inserted into the system at the centre of the plot, the group speed plot shows the speed and direction in which the energy is carried by each wave type. The group speeds for these plots are calculated from the phase speeds via a Huygens construction (Keppens and Meliani, 2008).

For a low magnetisation $\sigma \ll 1$ plasma, the fast phase and group speeds approach the speed of sound a_s in all directions, since the fast wave in the limit of no magnetisation turns into a normal sound wave in RHD (Relativistic Hydrodynamics). Meanwhile, the slow and Alfvén waves travel together at the same speed down field lines, with their speed approaching 0 as $\sigma \to 0$, effectively disappearing in RHD.

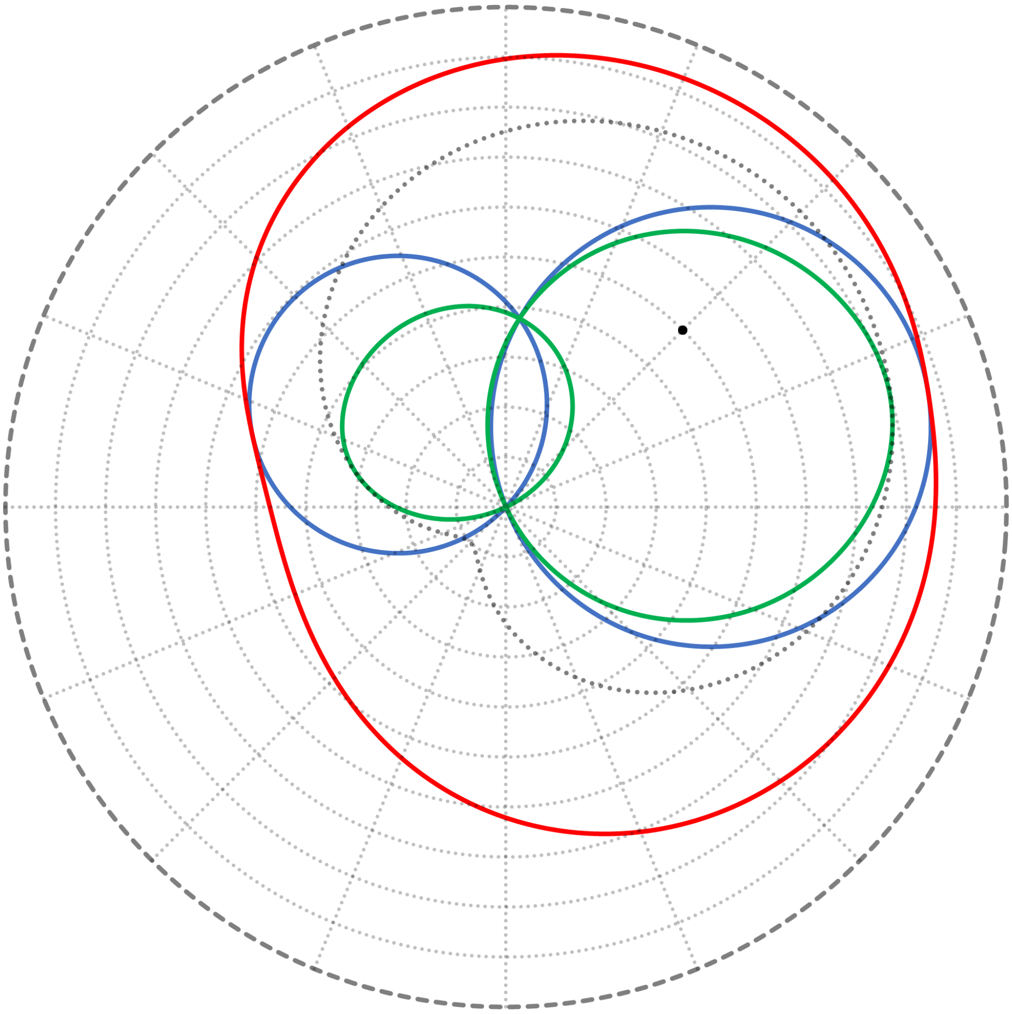

Figure 2.4: *Phase speeds in the laboratory frame. The phase speeds are calculated for the same state as Fig. 2.2, after a Lorentz boost of* $0.5c$ *towards the lower right. In this frame* $\boldsymbol{B} = (3.232, -0.2321, 0)$ *and the 4-velocity is* $\boldsymbol{u} = (0.408, 0.408, 0)$ *(indicated by the black dot), while* ρ *and* p_g *are unchanged by the Lorentz boost. The plot setup is otherwise the same as in Fig. 2.2.*

As magnetisation increases, the fast speed begins to approach the speed of light, except exactly down field lines where it retains the speed of sound, a_s. The Alfvén and slow speeds come up to meet it, until the slow and Alfvén speeds also reach the speed of sound down field lines.

At this point, a transition occurs, and as magnetisation increases the fast Alfvén speed continues to increase as the fast speed down field lines begins to increase beyond a_s. Meanwhile, the sound speed is no stuck to a_s along field lines.

As magnetisation increases further to $\sigma \gg 1$, the fast speed approaches the speed of light in all directions, while the Alfvén wave approaches a wave travelling at the speed of light down magnetic field lines. Meanwhile, the slow wave approaches a wave travelling at a_s down field lines instead.

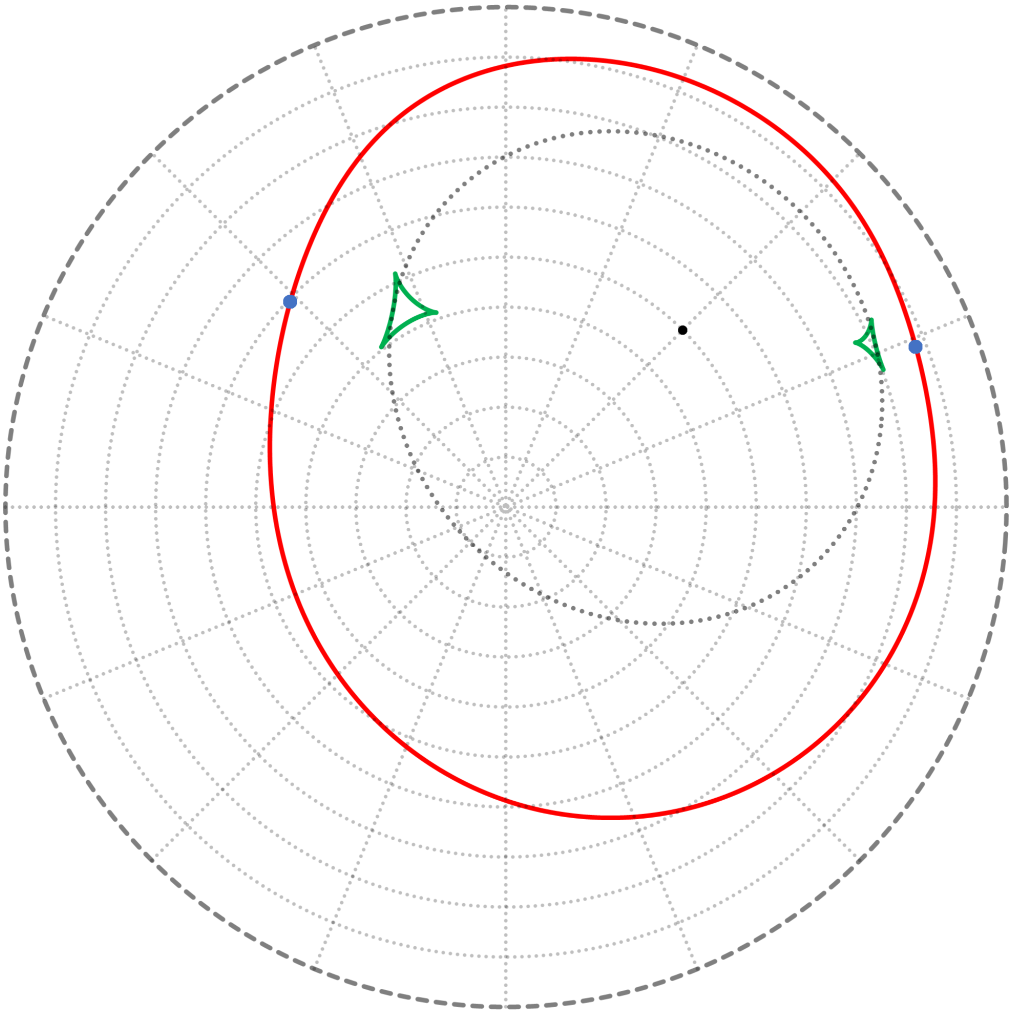

Figure 2.5: *Group speeds in the laboratory frame. The plot has the same state and plot setup as Fig. 2.4. Compare this case to the fluid frame in Fig. 2.3; note how relativistic effects compress speeds that are closer to the speed of light in this frame and expands speeds that are closer to* 0*.*

Thus besides the limit of the speed of light c, phase and groups speeds in RMHD are quite similar to that of MHD (Keppens and Meliani, 2008). The main differences are in the specifics of the degeneracies (i.e. where multiple waves have the same phase speed), as we will discuss in section 2.1.3.

Eigenvectors

As the non-physical waves have the same eigenvalues as some of the physical waves, we need a way to find a basis of these eigenspaces, such that the required eigenvectors are physical. As noted above, physical waves should not change the constraints that we included in the augmented system, and we can use these to separate out the non-physical waves. From this, we obtain the following eigenvectors, in $\boldsymbol{U} = (u^\alpha, b^\alpha, p_g, s)$ space (Anile and Pennisi, 1986):

The material wave:

$$\boldsymbol{r}_m = (0^\alpha, 0^\alpha, 0, 1)\,. \tag{2.67}$$

The Alfvén waves:

$$\boldsymbol{r}_a = \left(\zeta^\alpha, \frac{\mathcal{B}}{a}\zeta^\alpha, 0, 0\right)^T, \tag{2.68}$$

where $\zeta_\alpha = \epsilon_{\alpha\beta\gamma\delta}\phi^\beta u^\gamma b^\delta$.

The magnetosonic waves:

$$\boldsymbol{r}_{ms} = (\kappa^\alpha, \tau^\alpha, \mathcal{A}a, 0)^T\,, \tag{2.69}$$

where

$$\kappa^\alpha = \frac{a_s^2 - 1}{a_s^2}\left(\frac{a^4}{G}(\phi^\alpha + a u^\alpha) - \frac{a^2\mathcal{B}}{w}b^\alpha\right), \quad \tau^\alpha = \frac{\mathcal{B}}{a}\kappa^\alpha + \frac{\mathcal{A}}{w}\left(\frac{a}{a_s^2}b^\alpha - \mathcal{B}u^\alpha\right).$$

The pseudo-material wave:

$$\boldsymbol{r}_{pm} = (0^\alpha, \phi^\alpha, 0, 0)^T\,. \tag{2.70}$$

The pseudo-Alfvén waves:

$$\boldsymbol{r}_{pa} = \left(\theta^\alpha, \frac{\mathcal{B}}{a}\theta^\alpha, 0, 0\right)^T, \tag{2.71}$$

where $\theta^\alpha = \epsilon_{\alpha\beta\gamma\delta}\zeta^\beta\phi^\gamma b^\delta$

Thus we have expressions for the eigenvectors in $\boldsymbol{U}$-space, which can easily be transformed into expressions for the variation of the magnetic field $\boldsymbol{B}$ instead of b^α, or other variables such as density ρ and 3-velocity $\boldsymbol{v}$ as desired.

These eigenvectors are fairly complex and difficult to understand — although we can point out to things. First, the material wave is the only wave that has a change in entropy, so in the linear regime only material waves change entropy. Second, for the Alfvén waves the variation in magnetic field and 4-velocity is parallel, and they do not change the pressure. Since they also do not change entropy, the density must also be constant.

To help visualise these eigenvectors further we can write them in the fluid frame, and we can also give the variation in other variables in this frame too. In the fluid frame, the phase speeds of each wave are given by (Komissarov, 1999a)

$$\mu_m = 0, \quad \mu_a^2 = \frac{B_x^2}{\mathcal{E}}, \quad \mu_{ms}^4 - \left(a_s^2\mu_a^2 + \epsilon^2\right)\mu_{ms}^2 + a_s^2\mu_a^2 = 0, \tag{2.72}$$

where we note that it is now possible to separate the magnetosonic waves into slow and fast modes as

$$\mu_f^2 = \frac{a_s^2\mu_a^2 + \epsilon^2 + \sqrt{(a_s^2\mu_a^2 + \epsilon^2)^2 - 4a_s^2\mu_a^2}}{2}, \tag{2.73}$$

$$\mu_s^2 = \frac{a_s^2\mu_a^2 + \epsilon^2 - \sqrt{\left(a_s^2\mu_a^2 + \epsilon^2\right)^2 - 4a_s^2\mu_a^2}}{2}. \tag{2.74}$$

We can also discuss the eigenvectors in this frame; for the following, we will discuss only the right-going waves, $\mu \geq 0$. In the case of the material wave this is very simple with only a variation in entropy — thus corresponding to a variation in only density. All other variables (i.e. $p_g, \boldsymbol{u}, \boldsymbol{B}$ and $\boldsymbol{E}$) are constant, and the phase speed is $\mu_m = 0$ as well, so this is simply advected by the fluid.

Alfvén waves feature no variation in pressure or entropy, and therefore density is constant as well. For other variables we have

$$d\boldsymbol{u} = \frac{\operatorname{sgn} B_x}{\sqrt{\mathcal{E}}}\begin{pmatrix} 0 \\ B_z \\ -B_y \end{pmatrix}, \quad d\boldsymbol{B} = \begin{pmatrix} 0 \\ -B_z \\ B_y \end{pmatrix}, \quad d\boldsymbol{E} = \frac{\operatorname{sgn} B_x}{\sqrt{\mathcal{E}}}\begin{pmatrix} -\left(B_y^2 + B_z^2\right) \\ B_xB_y \\ B_xB_z \end{pmatrix}. \tag{2.75}$$

Here we can see that in the fluid frame, the magnetic variation $d\boldsymbol{B}$ is orthogonal to the component of $\boldsymbol{B}$ perpendicular to the x-axis, $\boldsymbol{B}_\perp$.

By contrast, magnetosonic waves have variation in all variables besides entropy. For these remaining variables, the variation in the fluid frame is

$$\begin{gathered} d\boldsymbol{u} = \begin{pmatrix} \mu_{ms}^2 - \mu_a^2 \\ \frac{B_xB_y}{\mathcal{E}}\left(a_s^2 - 1\right) \\ \frac{B_xB_z}{\mathcal{E}}\left(a_s^2 - 1\right) \end{pmatrix}, \quad d\boldsymbol{B} = \frac{\eta^2}{\mu_{ms}}\begin{pmatrix} 0 \\ B_y \\ B_z \end{pmatrix}, \quad d\boldsymbol{E} = \eta^2\begin{pmatrix} 0 \\ B_z \\ -B_y \end{pmatrix}, \\ dp_g = \frac{wa_s^2}{\mu_{ms}}\left(\mu_{ms}^2 - \mu_a^2\right), \quad d\rho = \frac{\rho dp_g}{wa_s^2} = \frac{\rho}{\mu_{ms}}\left(\mu_{ms}^2 - \mu_a^2\right), \end{gathered} \tag{2.76}$$

where $\eta^2 = \mu_{ms}^2 - a_s^2\mu_a^2$.

In this case we can see that in the fluid frame, the variation in magnetic field $d\boldsymbol{B}$ is now parallel to $\boldsymbol{B}_\perp$ instead, with the tangential velocity component $\boldsymbol{u}_\perp$ parallel to that as well. However, there is a longitudinal component of $d\boldsymbol{u}$ provided $\mu_{ms}^2 \neq \mu_a^2$. The compression in gas pressure and density is naturally proportional to this longitudinal component. We can also see that there is no variation in E_x as well, meaning that at least in this frame only Alfvén waves can change E_x.

Another point to note is that if we insert the expressions for μ_{ms}^2 from Eqs. (2.73) and (2.74) into η^2, the factor of $d\boldsymbol{B}$ and $d\boldsymbol{E}$, then we find that this expression is only zero if: $B_x = 0$, the degenerate case with $\mu_a = \mu_s = 0$; $a_s^2 = 1$, which is not possible with our equation of state; or $w = 0$, in which case there is no plasma. Thus there is always a magnetic and electric component to this eigenvector.

The difference between fast and slow modes is subtle, but we can see from Eq. (2.66) that the sign of $\mu_{ms}^2 - \mu_a^2$ will flip. So the longitudinal variation of $\boldsymbol{u}$ as well as the variations of p_g and ρ will all change sign, even as the variation of other components such as $\boldsymbol{u}_\perp$ retain their sign.

Degeneracies

A system of PDEs with all eigenvalues real and a diagonalisable Jacobian is called hyperbolic, and a hyperbolic system with all eigenvalues distinct is called strictly hyperbolic (LeVeque, 2002). While RMHD and the augmented system are both hyperbolic, the augmented system of RMHD is never strictly hyperbolic, as the non-physical waves match the phase speeds of some of the physical waves. As these waves are artificial and not present in the original RMHD, we will no longer discuss them.

But unaugmented RMHD is also not strictly hyperbolic; just like in MHD the eigenvalues are repeated in a few specific cases, although in the general case all the eigenvalues are distinct (Anile and Pennisi, 1986). In the degenerate cases where they are not distinct, while the expressions for the eigenvalues given above are functional, the expressions for the eigenvectors either diverge or are not linearly independent of the eigenvector expressions at the same phase speed.

So in these degenerate cases we require different expressions for the eigenvectors with the same phase speeds. The remaining distinct eigenvectors do not require correction.

To start with, it is easier to understand the degeneracies if we begin in the fluid frame. The same degeneracies should be present in all frames, so this will describe all possible degeneracies. Using the phase speeds given for this frame in Eqs. (2.72) to (2.74), we find that RMHD has the same degeneracies as MHD (Komissarov, 1999a):

$$\begin{aligned}
&\textit{Case 1}\text{: if } B_x = 0, && \text{then}\quad \mu_m = \mu_s^\pm = \mu_a^\pm = 0\\
&\textit{Case 2}\text{: if } B_\perp = 0, && \text{then}\quad \begin{cases} \mu_f^\pm = \mu_a^\pm & \text{if } s > a_s, \\ \mu_s^\pm = \mu_a^\pm & \text{if } s < a_s, \end{cases}\\
&\textit{Case 2a}\text{: if } B_\perp = 0 \text{ and } s = a_s, && \text{then}\quad \mu_s^\pm = \mu_a^\pm = \mu_f^\pm,
\end{aligned}$$

where $B_\perp$ is the component of $\boldsymbol{B}$ perpendicular to the x-axis, and where $s^2 = b^2/\mathcal{E}$.

To identify these degeneracies in the Laboratory frame it is convenient to find the covariant form of these conditions.

Case 1: We are looking for a solution μ of both $a(\mu) = 0$ and $\mathcal{N}(\mu) = 0$. Since $a = 0$ in this case, we can insert $a = 0$ into Eq. (2.60) which tells us that μ_m is a solution of $\mathcal{N}(\mu) = 0$ if and only if $\mathcal{B} = 0$. In the fluid frame this is equivalent to $B_x = 0$ as before. In the laboratory frame, this reads (Komissarov, 1999a)

$$0 = \mathcal{B} = b^x - v^x b^0 = \frac{B_x}{u^0}.$$

Since $u^0 \geq 1$, in the Laboratory frame the condition still reads $B_x = 0$.

Case 2: In this case we are looking for a solution of both $\mathcal{A}(\mu) = 0$ and $\mathcal{N}(\mu) = 0$. Inserting $\mathcal{B}^2 = \mathcal{E}a^2$ from Eq. (2.59) into Eq. (2.60) easily gives us that provided $a \neq 0$ the solution of $\mathcal{A}(\mu) = 0$ satisfies $\mathcal{N}(\mu) = 0$ if and only if

$$b^2 = \frac{\mathcal{B}^2}{a^2 + G},$$

In the fluid frame this reduces to $B_\perp = 0$. However, the fact that $B_\perp = 0$ in the fluid frame does not necessarily indicate that it is degenerate in the laboratory frame. In fact, it is not even the case that both left and right going waves will be degenerate at the same time; unlike the MHD case, it is now possible to have $\mu_a^+ = \mu_s^+ \ or\ \mu_f^+$ without $\mu_a^- = \mu_s^- \ or\ \mu_f^-$ and vice versa (Komissarov, 1999a).

Case 2a: Both s and a_s are 4-scalars so the condition $s = a_s$ is covariant. Therefore whether we have $\mu_s^\pm = \mu_a^\pm$ or $\mu_f^\pm = \mu_a^\pm$ or even $\mu_s^\pm = \mu_f^\pm = \mu_a^\pm$ is easily determined from s and a_s.

Figs. 2.4 and 2.5 shows the phase and group speeds in an arbitrary frame; degeneracies correspond to points where the phase speeds of different waves are equal. Note how the points where $\mu_f^\pm$ and $\mu_a^\pm$ are equal (where the red and blue lines are tangent) are not opposite each other with respect to the centre of the plot. This shows how it is possible to have only one direction degenerate at once.

2.1.4 Non-relativistic MHD

Now that we have an understanding of relativistic MHD, it is worth contrasting it to the non-relativistic case. Having split the covariant equations into time and space derivatives and rewritten the equations of RMHD (Eqs. (2.29), (2.34), (2.35), (2.37), (2.38) and (2.42)) into the alternate forms using $\boldsymbol{b}$ (Eqs. (2.29), (2.37) and (2.46) to (2.48)), the equations of RMHD now bear a clearer resemblance to the equations of non-relativistic MHD in conservation form. Those equations are (Goedbloed and Poedts, 2004): mass conservation

$$\partial_t \rho + \boldsymbol{\nabla} \cdot (\rho \boldsymbol{u}) = 0; \tag{2.77}$$

energy conservation

$$\partial_t e + \boldsymbol{\nabla} \cdot \left(\left(e + p_g + \frac{1}{2} B^2 \right) \boldsymbol{v} - \boldsymbol{B} \left(\boldsymbol{v} \cdot \boldsymbol{B} \right) \right) = 0, \tag{2.78}$$

where $e = \dfrac{p_g}{\Gamma - 1} + \frac{1}{2}B^2 + \frac{1}{2}\rho v^2$, the total energy density; momentum conservation

$$\partial_t \left(\rho \boldsymbol{v} \right) = \boldsymbol{\nabla} \cdot \left(\rho \boldsymbol{v}\boldsymbol{v} - \boldsymbol{B}\boldsymbol{B} + \left(p_g + \frac{1}{2} B^2 \right) \right) = 0; \tag{2.79}$$

as well as Gauss' law for magnetism and Faraday's law, which are unchanged from Eqs. (2.37) and (2.38).

These equations will naturally bear a strong resemblance because we expect to recover the MHD equations in the non-relativistic limit of RMHD. In this limit, we have

$$b^2 \to B^2, \quad w \to \rho, \quad u^0 \to 1, \quad \boldsymbol{u} \to \boldsymbol{v}, \quad b^0 \to 0.$$

If we insert these into Eqs. (2.29), (2.37) and (2.46) to (2.48) then we recover the equations of MHD as expected, except for energy conservation. Since RMHD energy includes mass-energy, this conservation law reduces to mass conservation instead. To recover Eq. (2.78) we must first subtract RMHD mass conservation Eq. (2.29) from energy conservation Eq. (2.46) before taking the limit.

However, in spite of this close resemblance RMHD has some major difficulties that MHD does not. First and most obviously, the magnetic field in RMHD is now involved in the conserved variables outside of Faraday's law. Thus variable conversion algorithms to calculate primitive variables from conservatives is significantly more difficult — in fact, it now requires an iterative algorithm, instead of analytic formulae; see for example Newman and Hamlin (2014).

Another difficulty unique to modelling relativistic MHD (and relativistic HD) is that the fluid 3-velocity now has a cap at the speed of light. If we are working with the 3-velocity, then we need to be sure that its magnitude is less than the speed of light at all times, and frequently we find that exceeding this limit will immediately cause major problems for the code wherever it occurs, since this makes the Lorentz factor γ imaginary.

In many cases this can be avoided by using the 4-velocity, which also has the advantage of being more sensitive at high Lorentz factors. Since the 3-velocity is capped at the speed of light, at high Lorentz factors the 3-velocity becomes insensitive to changes in velocity that would otherwise be very large. While working with the 4-velocity can avoid many of these, in some instances it is necessary to use the 3-velocity; for instance, if two states have 4-velocity $\boldsymbol{u}$ and $\boldsymbol{u}'$, then $u_x = u'_x$ does *not* imply that they have the no relative velocity in the x-direction. There is no relative velocity in the x-direction if and only if the 3-velocities match, $v_x = v'_x$.

2.2 Force-Free Degenerate Electrodynamics

Force-Free Degenerate Electrodynamics (FFDE) (also known as Force Free Electrodynamics (FFE) and Magnetodynamics (MD)), is the case of RMHD in the limit of high σ, i.e. the massless approximation of RMHD. Initially, it was used as a simplified set of equations, to analyse the condition near compact objects, such as pulsars (Goldreich and Julian, 1969; Ingraham, 1973; Mestel, 1973), black holes (Blandford and Znajek, 1977; MacDonald and Thorne, 1982; Okamoto, 1992) and accretion discs (Blandford, 1977), where in all such cases the value of σ can be large enough to warrant this approximation, as it is too large for current RMHD models. These applications were all generally stationary, and in most cases axisymmetric configurations.

Ushida (1997); Gruzinov (1999) and Komissarov (2002) extended the description to a full time-dependent, non-axisymmetric formulation of the system — the latter of which in particular with a view toward numerical modelling. Here we will follow Komissarov (2002) and describe the system in much the same way as we have previously for RMHD by first describing the equations in a covariant framework, before transitioning to special relativistic 3+1 splitting for the equations in conservation form. We will also give an alternative form, in terms of the derivatives of $\boldsymbol{B}$ and $\boldsymbol{E}$ directly. Both of these forms of the equations are commonly used in numerical applications.

As the limit of high σ, FFDE is simply RMHD without the inertial terms. Naturally, just as with RMHD the basic energy-momentum conservation laws Eq. (2.2) and Maxwell's equations Eq. (2.5) still hold. Maxwell's equations are completely unaffected by the absence of the inertial components; the difference with RMHD lies in the conservation laws, where the stress-energy Tensor $T^{\alpha\beta}$ no longer includes the stress-energy of the inertial fluid, so that we simply have (Komissarov, 2002)

$$T^{\alpha\beta} = T^{\alpha\beta}_{(e)} = F^{\alpha\mu}F^{\beta}_{\mu} - \frac{1}{4}\eta^{\alpha\beta}F_{\mu\nu}F^{\mu\nu}. \tag{2.80}$$

Thus the covariant evolution equations of FFDE are

$$\nabla_\beta T^{\alpha\beta} = 0, \tag{2.81}$$

$$\nabla_\alpha {}^*F^{\alpha\beta} = 0; \tag{2.82}$$

naturally mass conservation Eq. (2.7) is dropped since there is no mass to conserve.

From the Lorentz Force (Jackson, 1999) we have

$$\nabla_\beta T^{\alpha\beta}_{(e)} = -F_{\alpha\beta}J^\beta, \tag{2.83}$$

where J^α is the 4-current, satisfying the remaining Maxwell equations

$$\nabla_\beta F^{\alpha\beta} = J^\alpha,$$

and it therefore follows from Eqs. (2.81) and (2.83) that we must have

$$0 = \nabla_\beta T^{\alpha\beta} = -F_{\alpha\beta}J^\beta, \tag{2.84}$$

so that FFDE therefore requires the vanishing of the Lorentz force, hence why it is known as “force-free”. This also implies that $\det F_{\alpha\beta} = 0$ (Ushida, 1997).

The biggest difference between FFDE and RMHD lies in the PC condition; if we recall from Eq. (2.8) the PC condition in covariant form is

$$F^{\alpha\beta}u_\alpha = 0,$$

but without the fluid description u_α is undefined, thus an alternate version of the PC condition is required. If we consider Eq. (2.8) we can derive two conditions on only the Faraday Tensor F^α as (Komissarov, 2002)

$$F_{\alpha\beta}{}^*F^{\alpha\beta} = 0, \tag{2.85}$$

$$F_{\alpha\beta}F^{\alpha\beta} > 0, \tag{2.86}$$

which turn out to be sufficient.

Writing out the equations under $3+1$ splitting we can put the equations in a more familiar form. Without u^α there is no reason to use b^α — moreover, we need to keep the electric field $\boldsymbol{E}$ in the equations as we can no longer cancel it with $\boldsymbol{E} = -\boldsymbol{v} \times \boldsymbol{B}$.

Energy conservation of Eq. (2.81) becomes (Komissarov, 2002)

$$\partial_t\left(\frac{1}{2}\left(E^2 + B^2\right)\right) + \boldsymbol{\nabla}\cdot(\boldsymbol{E}\times\boldsymbol{B}) = 0, \tag{2.87}$$

while momentum conservation of Eq. (2.81) becomes

$$\partial_t(\boldsymbol{E}\times\boldsymbol{B}) + \boldsymbol{\nabla}\cdot\left(-\boldsymbol{E}\boldsymbol{E} - \boldsymbol{B}\boldsymbol{B} + \left(\frac{1}{2}\left(E^2 + B^2\right)\right)\delta^{ij}\right) = 0. \tag{2.88}$$

Meanwhile, Faraday’s law Eq. (2.38) is unchanged

$$\partial_t\boldsymbol{B} - \boldsymbol{\nabla}\times\boldsymbol{E} = 0,$$

as is the divergence-free condition Eq. (2.37)

$$\boldsymbol{\nabla}\cdot\boldsymbol{B} = 0.$$

Finally, the two PC conditions (2.85) and (2.86) are now

$$\boldsymbol{B}\cdot\boldsymbol{E} = 0, \tag{2.89}$$

and

$$B^2 - E^2 > 0. \tag{2.90}$$

Note that both of these values $\boldsymbol{B}\cdot\boldsymbol{E}$ and $B^2 - E^2$ are Lorentz invariant (naturally, given that they are 4-scalars derived directly from $F^{\alpha\beta}$). Thus we do not need to worry about the potential existence of Lorentz frames in which one (or both) of these conditions are violated. Moreover, these two constraints also guarantee the existence of a Lorentz frame in which the electric field $\boldsymbol{E} = 0$ (Komissarov, 2002). Since a boost in the direction of $\boldsymbol{B}$ would then leave $\boldsymbol{B}$ and $\boldsymbol{E}$ unchanged in this case, this guarantees the existence of a 1-parameter family of such frames. One such frame can be found by a Lorentz boost by the drift velocity $\boldsymbol{v}_D = \dfrac{\boldsymbol{E} \times \boldsymbol{B}}{B^2}$, which is the Lorentz boost of minimum velocity magnitude needed to reach such a frame.

Both of these conditions also hold in RMHD, and therefore the same reasoning implies the existence of a 1-parameter family of frames with $\boldsymbol{E} = 0$ in these frames as well. In RMHD, one of these frames is the fluid frame, where the PC condition Eq. (2.42) clearly shows that $\boldsymbol{E} = 0$ if $\boldsymbol{v} = 0$. This means that in RMHD, one of the 1-parameter family of frames is unique. FFDE has no unique frames since it does not have the fluid velocity $\boldsymbol{v}$, and therefore this information is lost when we take the high-σ limit of RMHD.

Alternate Derivation

Besides the two PC conditions (2.89) and (2.90) these conservation equations are identical to vacuum electromagnetics. This indicates an interpretation of FFDE as the dynamics of some kind of perfectly conducting vacuum. The derivation given above describes FFDE as the high-σ limit of RMHD, but the fact that the equations are identical to electromagnetism in a vacuum plus the PC condition suggests an alternate derivation:

We start with Maxwell's equations

$$\frac{\partial \boldsymbol{B}}{\partial t} = -\boldsymbol{\nabla} \times \boldsymbol{E}, \tag{2.91}$$

$$\boldsymbol{\nabla} \cdot \boldsymbol{B} = 0, \tag{2.92}$$

$$\frac{\partial \boldsymbol{E}}{\partial t} = -\boldsymbol{\nabla} \times \boldsymbol{B} - \boldsymbol{J}, \tag{2.93}$$

$$\boldsymbol{\nabla} \cdot \boldsymbol{E} = \rho_c, \tag{2.94}$$

where $\boldsymbol{J}$ is the current density and ρ_c the charge density. If we take the time and space components of the Lorentz force Eq. (2.83) and enforce the force-free condition by setting them equal to zero, then we also get the conditions

$$\boldsymbol{E} \cdot \boldsymbol{J} = 0, \tag{2.95}$$

$$\rho_c \boldsymbol{E} + \boldsymbol{J} \times \boldsymbol{B} = 0. \tag{2.96}$$

Note that we can easily derive $\boldsymbol{E} \cdot \boldsymbol{B} = 0$ and $B^2 > E^2$ from Eq. (2.96), provided $\rho_c \neq 0$.

We want to eliminate the current $\boldsymbol{J}$ and charge density ρ_c, so first taking the cross product of Eq. (2.96) with $\boldsymbol{E}$ and rearranging gives us the current perpendicular to $\boldsymbol{B}$

$$\boldsymbol{J}_{\perp} = \frac{\rho_c}{B^2}\boldsymbol{E}\times\boldsymbol{B} = \frac{\boldsymbol{\nabla}\cdot\boldsymbol{E}}{B^2}\boldsymbol{E}\times\boldsymbol{B}, \tag{2.97}$$

where we have used Gauss' law Eq. (2.94) to eliminate ρ_c.

Now we take the time derivative of the Force-free condition $\boldsymbol{E}\cdot\boldsymbol{B} = 0$

$$\boldsymbol{E}\cdot\frac{\partial\boldsymbol{B}}{\partial t} + \boldsymbol{B}\cdot\frac{\partial\boldsymbol{E}}{\partial t} = 0,$$

and substitute in the equations for $\partial_t\boldsymbol{B}$ and $\partial_t\boldsymbol{E}$ and rearrange to obtain

$$\boldsymbol{B}\cdot\boldsymbol{J} = \boldsymbol{B}\cdot\boldsymbol{\nabla}\times\boldsymbol{B} - \boldsymbol{E}\cdot\boldsymbol{\nabla}\times\boldsymbol{E},$$

so therefore we have for the current parallel to $\boldsymbol{B}$ (Mahlmann *et al.*, 2021)

$$\boldsymbol{J}_{\parallel} = \frac{\boldsymbol{B}}{B^2}\left(\boldsymbol{B}\cdot\boldsymbol{\nabla}\times\boldsymbol{B} - \boldsymbol{E}\cdot\boldsymbol{\nabla}\times\boldsymbol{E}\right),$$

which combined with Eq. (2.97) gives us an expression for the current $\boldsymbol{J}$ as (McKinney, 2006)

$$\boldsymbol{J} = \frac{1}{B^2}\left[\left(\boldsymbol{\nabla}\cdot\boldsymbol{E}\right)\boldsymbol{E}\times\boldsymbol{B} + \boldsymbol{B}\left(\boldsymbol{B}\cdot\boldsymbol{\nabla}\times\boldsymbol{B} - \boldsymbol{E}\cdot\boldsymbol{\nabla}\times\boldsymbol{E}\right)\right]. \tag{2.98}$$

Finally, we can substitute this expression for $\boldsymbol{J}$ back into Eq. (2.93) to gain

$$\frac{\partial\boldsymbol{E}}{\partial t} = -\boldsymbol{\nabla}\times\boldsymbol{B} - \frac{1}{B^2}\left[\left(\boldsymbol{\nabla}\cdot\boldsymbol{E}\right)\boldsymbol{E}\times\boldsymbol{B} + \boldsymbol{B}\left(\boldsymbol{B}\cdot\boldsymbol{\nabla}\times\boldsymbol{B} - \boldsymbol{E}\cdot\boldsymbol{\nabla}\times\boldsymbol{E}\right)\right], \tag{2.99}$$

which taken together with Faraday's law Eq. (2.37), the divergence-free condition on $\boldsymbol{B}$ Eq. (2.38), and the PC conditions (2.89) and (2.90) gives an alternate formulation for the equations of FFDE, this time not in conservative form, but rather directly in terms of the time derivatives of $\boldsymbol{E}$ and $\boldsymbol{B}$.

2.2.1 Degeneracy

The two formulations of FFDE are equivalent, but comparing these two formulations of FFDE, we note that there is a discrepancy in the number of equations between them. The conservative formulation has:

- Seven evolution equations: Eqs. (2.38), (2.87) and (2.88),
- Two equality constraints: Eqs. (2.37) and (2.89),
- One inequality constraint: Eq. (2.90).

Meanwhile, the direct formulation has:

- Six evolution equations: Eqs. (2.38), (2.88) and (2.99),

- Two equality constraints: Eqs. (2.37) and (2.89),
- One inequality constraint: Eq. (2.90).

So the conservative formulation has one more evolution equation in comparison. This is indicative of the fact that some of the equations in the conservative formulation are not independent of each other. In fact, taking into account all the constraints there are actually only really four independent evolution equations (Komissarov, 2002).

This can be shown more explicitly using the covariant formulation. Ushida (1997) notes that the fact that $F_{\alpha\beta}$ is an antisymmetric tensor with $\det F_{\alpha\beta} = 0$ implies that $F_{\alpha\beta}$ is an even rank matrix. Thus since $\boldsymbol{B}$ is not a zero vector by Eq. (2.90), it follows that $F_{\alpha\beta}$ has non-zero elements, and therefore $\det F_{\alpha\beta} = 0$ implies that $F_{\alpha\beta}$ has a two-dimensional eigenspace of zero eigenvalues. That is, there are two vectors a^α for which

$$F_{\alpha\beta} a^\alpha = 0.$$

Following Komissarov (2002), we let a^α be one of them. Since we have Eq. (2.85), the second zero eigenvector b^α can then be introduced via

$$b^\alpha = {}^*F^{\beta\alpha} a_\beta.$$

So in terms of a^α and b^α we can write

$$F_{\alpha\beta} = \epsilon_{\alpha\beta\gamma\delta} a^\gamma b^\delta, \quad {}^*F^{\alpha\beta} = b^\alpha a^\beta - a^\alpha b^\beta,$$

thus it follows from the latter (Komissarov, 2002) that a unit space-like vector c^α orthogonal to a^α and b^α is a zero eigenvector of ${}^*F^{\alpha\beta}$. Once again, another zero eigenvector d^α of ${}^*F^{\alpha\beta}$ is given by

$$d^\alpha = F^{\beta\alpha} c_\beta,$$

and again we can write in terms of c^α and d^α

$${}^*F_{\alpha\beta} = \epsilon_{\alpha\beta\gamma\delta} c^\gamma d^\delta, \quad F^{\alpha\beta} = c^\alpha d^\beta - d^\alpha c^\beta.$$

Taken together with the Lorentz force Eq. (2.83) it follows that the vector $\nabla_\alpha T^{\alpha\beta}$ always lies in the 2D plane described by c^α and d^α, and thus it follows that only two components of Eq. (2.2) are independent in FFDE (Komissarov, 2002).

2.2.2 Linear Theory

Just as with RMHD in section 2.1.3 we can study the dynamics of linear FFDE via the eigenvalues and eigenvectors of the Jacobian. Since FFDE is the limit of RMHD as

$\sigma \to \infty$, we can derive the eigenvalues and eigenvectors of FFDE either directly from the Jacobian, or as the limit of those from RMHD. However, the reduced degrees of freedom limits the number of possible eigenvectors to just four, which clearly means that some of the eigenvectors of RMHD cannot have counterparts.

Limit of RMHD

We naturally will not expect to have a material wave in FFDE; both because the phase speed μ_m is the fluid 3-velocity v_x — a variable not present in the formulation of FFDE — as well as the simple fact that there is no material in FFDE.

For the remaining eigenvalues we can consider μ_a and μ_{ms} as $\sigma \to \infty$. First, we begin with Eq. (2.72) so that in the fluid frame, Alfvén wave phase speeds are given by

$$\mu_a = \pm\frac{B^x}{\sqrt{w+B^2}} = \pm\frac{B^x}{|\boldsymbol{B}|\sqrt{1+\sigma^{-1}}}, \tag{2.100}$$

where we have taken $|\boldsymbol{B}|$ out of the square root, and substituted $w/B^2 = \sigma^{-1}$. If we now further define $B^x/|\boldsymbol{B}| = \cos\theta$, where θ is the angle between $\boldsymbol{B}$ and the x-axis, then we can take the limit as $\sigma \to \infty$ as

$$\lim_{\sigma\to\infty} \mu_a = \pm\cos\theta. \tag{2.101}$$

Similarly, the MS phase speeds in the fluid frame from Eq. (2.72) are

$$\mu_{ms}^{\pm} = \sqrt{\frac{1}{2}\left(d^2 \pm \sqrt{d^4 - 4a_s^2\mu_a^2}\right)}, \quad d^2 = \epsilon^2 + a_s^2\mu_a^2 = a_s^2 + s^2 + a_s^2\left(\mu_a^2 - s^2\right),$$

$$s^2 = \frac{B^2}{w+B^2} = \frac{1}{1+\sigma^{-1}}.$$

We already know the limit of μ_a, so for s^2 and d^2 we have that

$$\lim_{\sigma\to\infty} s^2 = 1, \quad \lim_{\sigma\to\infty} d^2 = a_s^2 + 1 + a_s^2\left(\cos^2\theta - 1\right) = 1 + a_s^2\cos^2\theta,$$

hence the limit of $\mu_{ms}^{\pm}$ is

$$\begin{aligned}\lim_{\sigma\to\infty} \mu_{ms}^{\pm} &= \pm\sqrt{\frac{1}{2}\left(1 + a_s^2\cos^2\theta \pm \sqrt{(1 + a_s^2\cos^2\theta)^2 - 4a_s^2\cos^2\theta}\right)} \\ &= \pm\sqrt{\frac{1}{2}(1 + a_s^2\cos^2\theta \pm (1 - a_s^2\cos^2\theta))},\end{aligned}$$

and so we obtain

$$\lim_{\sigma\to\infty} \mu_s^{\pm} = \pm a_s\cos\theta, \quad \lim_{\sigma\to\infty} \mu_f^{\pm} = \pm 1. \tag{2.102}$$

Thus in summary, the fast waves travel at the speed of light in all directions, Alfvén waves travel at the speed of light down magnetic field lines, and slow waves travel at the speed of sound down magnetic field lines. However, the adiabatic sound speed a_s is obviously dependent on the neglected inertial terms, thus it should have no meaning in FFDE. As the only wave still dependent on a_s, slow waves are the odd one out here, and their presence would appear to be an issue as they have no meaning in FFDE. We will show that these slow waves do not appear at all if we derive the eigenvalues directly from the FFDE system itself in the next section.

Direct derivation

Besides deriving them as the limit of RMHD, we can also study these waves as a direct derivation from the equations of FFDE themselves. If we start with the conservation law form, then written in the form

$$\frac{\partial \boldsymbol{Q}}{\partial t} + \frac{\partial \boldsymbol{F}}{\partial x} = 0, \tag{2.103}$$

we have

$$\boldsymbol{Q} = \begin{pmatrix} B_y \\ B_z \\ E_y B_z - E_z B_y \\ E_z B_x - E_x B_z \\ E_x B_y - E_y B_x \\ \frac{1}{2}(E^2 + B^2) \end{pmatrix}, \quad \boldsymbol{F} = \begin{pmatrix} E_z \\ -E_y \\ -E_x E_x - B_x B_x + \frac{1}{2}(E^2 + B^2) \\ -E_x E_y - B_x B_y \\ -E_x E_z - B_x B_z \\ E_y B_z - E_z B_y \end{pmatrix}, \tag{2.104}$$

where we have dropped the $\partial_t B_x$ term since we have the same conditions on B_x as with RMHD; in 1D, $\partial_t B_x = 0$ and $\partial_x B_x = 0$, hence B_x is constant.

Calculating $\partial \boldsymbol{F} / \partial \boldsymbol{Q}$ directly from this is quite complex since the components of $\boldsymbol{F}$ are not easily calculated from those of $\boldsymbol{Q}$. It is more convenient to find another vector $\boldsymbol{P}$ such that we can write both $\boldsymbol{Q}(\boldsymbol{P})$ and $\boldsymbol{F}(\boldsymbol{P})$. With this we could write Eq. (2.103) in the form

$$\boldsymbol{A} \frac{\partial \boldsymbol{P}}{\partial t} + \boldsymbol{C} \frac{\partial \boldsymbol{P}}{\partial x} = 0, \tag{2.105}$$

where

$$\boldsymbol{A} = \frac{\partial \boldsymbol{Q}}{\partial \boldsymbol{P}}, \quad \boldsymbol{C} = \frac{\partial \boldsymbol{F}}{\partial \boldsymbol{P}},$$

so we are looking for solutions of the generalised eigenvalue problem

$$(\boldsymbol{C} - \mu \boldsymbol{A})\, \boldsymbol{r} = \boldsymbol{0}, \tag{2.106}$$

for eigenvalues μ and eigenvectors $\boldsymbol{r}$.

We are now left with choosing the variables in $\boldsymbol{P}$; selecting from $\boldsymbol{B}$ and $\boldsymbol{E}$ suggests itself since we have already written $\boldsymbol{Q}$ and $\boldsymbol{F}$ in terms of these variables. First, we already know that B_x is not necessary since this variable cannot change. Furthermore, two of the conservative variables above involve only B_y and B_z, so we must choose these two.

We know that there are only four independent equations, so we only have two choices left, so we select two of the components of $\boldsymbol{E}$. Unfortunately, the choice of these depends on the direction of the magnetic field. If $B_x = 0$ then we must choose E_x and similarly for y and z, so no choice will cover all possibilities.

Komissarov (2002) suggests augmenting the equations by relaxing the PC condition in Eq. (2.89), similar to the method above for finding the eigenvalues of RMHD. We then modify the equations such that the condition is automatically satisfied if the condition is satisfied by the initial data.

Komissarov (2002) selects all three space components of energy-momentum conservation in Eq. (2.81) and adds the extra term $B_i \partial_t (\boldsymbol{B} \cdot \boldsymbol{E})$ to these equations to gain

$$\nabla_\alpha T^{i\alpha} + B_i \frac{\partial (\boldsymbol{B} \cdot \boldsymbol{E})}{\partial t} = 0. \tag{2.107}$$

Clearly, if our initial data satisfies the PC condition Eq. (2.89), then as we have $\boldsymbol{B} \cdot \boldsymbol{E} = 0$ the equations are unchanged. Moreover, if we take Eq. (2.107) and use Eqs. (2.6) and (2.83) we can rewrite the first term in terms of the Faraday Tensor as (Komissarov, 2002)

$$F_{i\alpha} \frac{\partial F^{\alpha t}}{\partial t} + F_{i\alpha} \frac{\partial F^{\alpha x}}{\partial x} + B_i \frac{\partial (\boldsymbol{B} \cdot \boldsymbol{E})}{\partial t} = 0, \tag{2.108}$$

which we can then contract with B^i to get

$$(\boldsymbol{B} \cdot \boldsymbol{E}) \frac{\partial E_x}{\partial x} + B^2 \frac{\partial (\boldsymbol{B} \cdot \boldsymbol{E})}{\partial t} = 0,$$

which shows that provided $B^2 > 0$ (which is guaranteed by Eq. (2.90)), if $\boldsymbol{B} \cdot \boldsymbol{E} = 0$ at time $t = 0$ then $\boldsymbol{B} \cdot \boldsymbol{E} = 0$ for all future times $t > 0$ as well. Therefore, if the initial data satisfies the PC condition Eq. (2.89) then the augmented system will have the same dynamics as the unaugmented system.

With this augmented system we can now safely select

$$\boldsymbol{P} = (B_y, B_z, E_x, E_y, E_z)\,, \tag{2.109}$$

and with this we can write out the two Jacobians $\boldsymbol{A}$ and $\boldsymbol{C}$; using Eq. (2.107) we find

$$\boldsymbol{A} = \begin{pmatrix} 1 & 0 & 0 & 0 & 0 \\ 0 & 1 & 0 & 0 & 0 \\ B_x E_y + E_z & B_x E_z - E_y & B_x^2 & B_x B_y - B_z & B_x B_z + B_y \\ B_y E_y & B_y E_z + E_x & B_x B_y + B_z & B_y^2 & B_y B_z - B_x \\ B_z E_y - E_x & B_z E_z & B_x B_z - B_y & B_y B_z + B_x & B_z^2 \end{pmatrix} \tag{2.110}$$

$$\boldsymbol{C} = \begin{pmatrix} 0 & 0 & 0 & 0 & -1 \\ 0 & 0 & 0 & 1 & 0 \\ -B_y & -B_z & E_x & -E_y & -E_z \\ B_x & 0 & E_y & E_x & 0 \\ 0 & B_x & E_z & 0 & E_x \end{pmatrix}. \tag{2.111}$$

Thus the solutions of the generalised eigenvalue problem Eq. (2.106) are (Komissarov, 2002)

$$\mu_f^\pm = \pm 1, \tag{2.112}$$

$$\mu_a^\pm = \frac{B_z E_y - B_y E_z \pm \sqrt{B_x^2(B^2 - E^2)}}{B^2}, \tag{2.113}$$

$$\mu_n = 0.$$

Note that the augmented system naturally includes an extra solution compared to the unaugmented system, so we have five solutions instead of four.

Comparison of Eqs. (2.112) and (2.113) to Eqs. (2.101) and (2.102) tells us that $\mu_n = 0$ must be the unphysical extra solution, and that the slow waves are the solutions that disappear for FFDE as expected (Komissarov, 2002).

Eigenvectors

With the eigenvalues given by Eqs. (2.112) and (2.113) we then can obtain the eigenvectors. The eigenvectors of the fast waves are (Komissarov, 2002)

$$\boldsymbol{r}_f^\pm = \left(-\eta_f, \nu_f, 0, \pm\nu_f, \pm\eta_f\right)^T, \tag{2.114}$$

where the sign of ± indicates the wave direction, and

$$\eta_f = E_z \pm B_y, \quad \nu_f = E_y - \mp B_z.$$

Meanwhile, the eigenvectors of the Alfvén waves are

$$\boldsymbol{r}_a^\pm = \left(\nu_a, \eta_a, -\frac{\eta_a^2 + \nu_a^2}{B_x}, \mu_a^\pm \eta_a, -\mu_a^\pm \nu_a\right)^T, \tag{2.115}$$

where we assume $B_x \neq 0$ and

$$\eta_a = E_z + \mu_a^\pm B_y, \quad \nu_a = E_y - \mu_a^\pm B_z.$$

Just as with RMHD, there are degenerate cases for these eigenvectors, where two or more phase speeds are equal.

Case 1a: If we have

$$\boldsymbol{E}_\perp = -\boldsymbol{i} \times \boldsymbol{B}, \tag{2.116}$$

where $\boldsymbol{E}_\perp$ is the component of $\boldsymbol{E}$ perpendicular to the x-axis, and $\boldsymbol{i}$ is the unit vector in the positive x-direction.

Given this condition then we will have

$$\mu_a^+ = \mu_f^+,$$

so the right-going Alfvén and fast waves have the same phase speed (Komissarov, 2002). This is of course equivalent to the Case 2 degeneracy of RMHD.

In this case we can use the eigenvectors

$$\boldsymbol{r}_1 = (0,1,0,1,0)^T, \quad \boldsymbol{r}_2 = (-1,0,0,0,1)^T,$$

as a basis for the eigenspace.

Case 1b: If we have

$$\boldsymbol{E}_\perp = \boldsymbol{i} \times \boldsymbol{B}, \tag{2.117}$$

then we will have

$$\mu_a^- = \mu_f^-,$$

so now the left-going Alfvén and fast waves have the same phase speed (Komissarov, 2002).

For this eigenspace we can use the eigenvectors

$$\boldsymbol{r}_1 = (0,1,0,-1,0)^T, \quad \boldsymbol{r}_2 = (1,0,0,0,1)^T.$$

Case 1c: Just as in RMHD, it is possible to have only one of Cases 1a and 1b true at once, i.e. we could have $\mu_a^+ = \mu_f^+, \mu_a^- \neq \mu_f^-$ and vice versa. However, it is still also possible for both conditions in Eqs. (2.116) and (2.117) to be true at once; if we consider the implications of both conditions and the PC condition Eq. (2.89) together then it is clear that we must have (Komissarov, 2002)

$$\boldsymbol{E} = 0, \quad \boldsymbol{B}_\perp = 0,$$

which is of course also a sufficient condition for this degeneracy. In this case, the eigenvectors given for Cases 1a and 1b are already linearly independent and are therefore sufficient.

Case 2: We again also have the tangential degeneracy for $B_x = 0$. In this case, we have (Komissarov, 2002)

$$\mu_a^\pm = \mu_a = \frac{E_y}{B_z} = -\frac{E_z}{B_y}, \tag{2.118}$$

again forming a 2D eigenspace. In this case we can use the eigenvectors

$$\boldsymbol{r}_1 = \left(1, 0, \frac{B_y\left(1-\mu_a^2\right)}{E_x}, 0, -\mu_a\right)^T, \quad \boldsymbol{r}_2 = \left(0, 1, \frac{B_z\left(1-\mu_a^2\right)}{E_x}, \mu_a, 0\right)^T,$$

as the basis provided that $E_x \neq 0$; if we do have that $E_x = 0$, then instead we can use

$$\boldsymbol{r}_1 = (0, 0, 1, 0, 0)^T , \quad \boldsymbol{r}_2 = (B_z, -B_y, 0, -\mu_a B_y, \mu_a B_z)^T .$$

We might be concerned that it may be possible to have both Case 2 and one of the Case 1 conditions simultaneously, but if we consider the implications of $\mu_a = \pm 1$ with Eq. (2.118) (i.e. $E_y = B_z$ and $E_z = -B_y$) then it is clear that in order to satisfy one of Eqs. (2.116) and (2.117) in addition to Eq. (2.118), then we must have $B^2 \leq E^2$, violating the second PC condition in Eq. (2.90).

2.3 1D Exact Solutions in RMHD

In order to test the accuracy of our code, we will need some method to check the results against. We could of course compare the results to previous authors, or even against our own non-split RMHD code on the same conditions. These cases of course depend on these codes being able to handle the regime being modelled, and hence are mostly limited to low-σ regimes — except for models performed using FFDE or PIC schemes which are able to handle the high-σ regime, although the FFDE tests will not include any plasma of course.

Besides this though, we can also test the code against known exact solutions to the equations. Clearly, if we know exactly what the results the code should achieve are, then we get an excellent test of the accuracy of the code. In this section we will describe various known exact, 1D solutions for RMHD which will later be used in chapter 4 for testing.

Provided that the wave amplitude is small relative to the background state, the eigenvectors above for RMHD (section 2.1.3) and FFDE (section 2.2.2) can be used to construct linear, exact solutions of RMHD and FFDE. This particular case will be discussed in section 2.3.2. However, the fact that these cases all have sufficiently small amplitude to remain in the linear regime severely limits their utility for testing purposes. Although the code should be able to handle linear waves, this is the simplest possible test besides a constant state.

Besides the basic linear solutions we found above, we can also look for non-linear solutions, where the variation of $\boldsymbol{Q}$ is no longer small relative to the magnitude of $\boldsymbol{Q}$. These exact solutions are of particular use for testing the code, as a working code should match the exact results, or at least approach them as the resolution increases.

The equations being solved can be written in the conservation form and in Cartesian coordinates as (LeVeque, 2002)

$$\frac{\partial \boldsymbol{Q}}{\partial t} + \frac{\partial \boldsymbol{F}}{\partial x} + \frac{\partial \boldsymbol{G}}{\partial y} + \frac{\partial \boldsymbol{H}}{\partial z} = \boldsymbol{S}, \tag{2.119}$$

where $\boldsymbol{Q}$ is a vector of conserved variables; for RMHD these are the conserved mass $\rho\gamma$ (Eq. (2.29)), the conserved energy $w\gamma^2 - p + \frac{1}{2}(E^2 + B^2)$ (Eq. (2.34)), the conserved momentum $w\gamma\boldsymbol{u} + \boldsymbol{E} \times \boldsymbol{B}$ (Eq. (2.35)), and the magnetic field $\boldsymbol{B}$ (Eq. (2.38)). $\boldsymbol{F}, \boldsymbol{G}$ and $\boldsymbol{H}$ are vectors of the corresponding x-fluxes, y-fluxes and z-fluxes respectively, and $\boldsymbol{S}$ is a vector of source terms — for which we have $\boldsymbol{S} = 0$ for both RMHD and FFDE in Cartesian coordinates.

Calculating exact solutions for RMHD for 2D or 3D models is a very difficult task, so to simplify the discussion we will assume planar symmetry in the y and z planes (i.e. $\boldsymbol{Q}(x, y, z, t) = \boldsymbol{Q}(x, y + a, z + b, t)$ for any $a, b \in \mathbb{R}$), so that the system reduces to 1D as y and z-derivatives vanish. In this way, the derivatives of $\boldsymbol{F}_y$ and $\boldsymbol{F}_z$ in Eq. (2.119) both vanish, and we are left with

$$\frac{\partial \boldsymbol{Q}}{\partial t} + \frac{\partial \boldsymbol{F}_x}{\partial x} = 0. \tag{2.120}$$

This has a particularly profound effect on the x-component of the magnetic field, B_x. For this component, Faraday's law (2.38) reduces to $\dfrac{\partial B_x}{\partial t} = 0$; meanwhile, Gauss' law (2.94) reduces to $\dfrac{\partial B_x}{\partial t} = 0$. Taken together then, this means that $B_x =$ constant, and thus allows us to eliminate B_x from the unknowns, reducing the system to seven equations with seven unknowns.

Even reducing the system to just 1D still retains much of the complexity of RMHD. An arbitrary initial condition may have a solution, but that by no means allows us to calculate it analytically. So in order to find some solutions we must simplify further.

Eq. (2.120) is the strong form of the equations, and so assumes continuity and differentiability, much like the rest of our discussion above in this chapter. Thus all legitimate solutions are differentiable solutions, in which all the variables and their derivatives are continuous across the whole domain at the initial time $t = 0$, and at least up to some non-zero time $t = t_1 > 0$.

However, it is generally the case for hyperbolic problems — including RMHD — that discontinuities like shocks can form via methods like nonlinear steepening, which is a nonlinear effect where the back of a wave travels faster than its front, causing it to catch up and eventually form a discontinuity. In such cases, the model will break at some finite time $t > 0$ in the future. Alternatively, we may be interested in cases that start with a discontinuity.

Since cases like these are of interest in modelling, and even beyond the point where the discontinuity forms, we relax the conditions of continuity and differentiability, and consider cases with discontinuities as well. Indeed, the very reason one would use a conservative numerical scheme like we do, as described later in chapter 3, is because that method can capture discontinuities more effectively than other methods. Systems like Eq. (2.120) can easily be converted into a weak form by putting into an integral form, i.e. integrating the equations over some volume V and time interval T. In this weak form, discontinuities in the variables as well as discontinuities in their derivatives (weak discontinuities) are still valid solutions.

2.3.1 Discontinuities

Since we are modelling discontinuities, it is useful to also look for discontinuous solutions of the weak form of the equations. The simplest case of a discontinuity consists of a constant left state $\boldsymbol{Q}_l$ and a constant right state $\boldsymbol{Q}_r$, with a discontinuity of zero width separating them and moving at velocity v. This system would not evolve over time besides the constant movement of the discontinuity.

An arbitrary choice of $\boldsymbol{Q}_l$ and $\boldsymbol{Q}_r$ in a hyperbolic PDE the system matches the conditions described in section 3.1.2 for a Riemann problem. As we will discuss in that section, this generally does not remain as a single discontinuity and instead splits into a collection of up to n distinct waves travelling at different speeds, where n is the number of distinct eigenvalues of the hyperbolic system.

We must therefore look for specific choices of $\boldsymbol{Q}_l$ and $\boldsymbol{Q}_r$ that remain as a single discontinuity with constant velocity. If we consider a general 1D system of conservation laws Eq. (2.120), then using our assumption of a single discontinuity of constant velocity v we can integrate this system over the discontinuity and over a small time interval to obtain

$$v\left(\boldsymbol{Q}_l - \boldsymbol{Q}_r\right) = \boldsymbol{F}_l - \boldsymbol{F}_r, \tag{2.121}$$

which is thus the general equation that any discontinuous solution of a system of conservation laws must satisfy.

Note that if the change at the discontinuity is small (i.e. $\boldsymbol{Q}_l - \boldsymbol{Q}_r \sim \mathcal{O}(\Delta q)$ with $\Delta q \ll 1$) then this reduces to a small perturbation of Eq. (2.49) — in other words, the solutions of Eq. (2.121) reduce to the solutions found in section 2.1.3 for the linear case. Therefore, all the solutions for this equation found subsequently can be considered non-linear discontinuous extensions of the linear waves given there, and by examining the low amplitude limit of each solution these discontinuities can be identified with their linear counterparts.

Analysis of Eq. (2.121) further tells us that if μ_l and μ_r are the phase speeds of the corresponding linear waves in the left and right regions, then one of the following inequalities must hold (Webb *et al.*, 1987)

$$\mu_l \leq v \leq \mu_r \quad \text{or} \quad \mu_l \geq v \geq \mu_r.$$

That is, the velocity of the discontinuity is between the phase velocities of the corresponding linear waves in the adjacent regions.

RMHD is a fully relativistic system of equations, and thus we can use a Lorentz transformation to change reference frame to one in which v is any value we like — including $v = 0$ and vice versa. So if we have a solution in a frame where the discontinuity has velocity $v = 0$, then we can Lorentz boost this solution into another solution with any desired velocity v. Furthermore, provided that $v \neq \pm 1$ so that the discontinuity is not moving at the speed of light, any solution has a Lorentz frame in which it is stationary with $v = 0$. Since in RMHD all discontinuities have $|v| < 1$, any solution can be calculated in this way.

However, fast waves in FFDE do have velocity $v = \pm 1$. In relativity, there is no Lorentz frame in which such a wave is stationary; it will always be moving at the speed of light for all observers. Although such solutions do exist in the high-σ limit FFDE, below this limit all discontinuities have $|v| < 1$, since they are all non-linear extensions of the linear waves — the phase speeds of which are all $\mu < 1$. The fact that a Lorentz frame exists in which fast waves are stationary in RMHD but not FFDE is a major difference between the two systems.

In the frame of the discontinuity, Eq. (2.121) reduces to

$$\boldsymbol{F}_l = \boldsymbol{F}_r, \tag{2.122}$$

which is of course a much more manageable problem — although the complexity of RMHD makes this by no means easy.

Thus if we insert the form of the flux $\boldsymbol{F}$ in RMHD from Eqs. (2.29), (2.34), (2.35) and (2.38) into this equation, then we are looking for solutions of the following system

$$\rho_l u_l^x = \rho_r u_r^x, \tag{2.123}$$

$$w_l u_l^0 u_l^x + E_l^y B_l^z - E_l^z B_l^y = w_r u_r^0 u_r^x + E_r^y B_r^z - E_r^z B_r^y, \tag{2.124}$$

$$w_l u_l^x u_l^x - E_l^x E_l^x + p_l + \frac{1}{2}\left(E_l^2 + B_l^2\right) = w_r u_r^x u_r^x - E_r^x E_r^x + p_r + \frac{1}{2}\left(E_r^2 + B_r^2\right), \tag{2.125}$$

$$w_l u_l^x u_l^y - E_l^x E_l^y - B^x B_l^y = w_r u_r^x u_r^y - E_r^x E_r^y - B^x B_r^y, \tag{2.126}$$

$$w_l u_l^x u_l^z - E_l^x E_l^z - B^x B_l^z = w_r u_r^x u_r^z - E_r^x E_r^z - B^x B_r^z, \tag{2.127}$$

$$E_l^z = E_r^z, \tag{2.128}$$

$$E_l^y = E_r^y, \tag{2.129}$$

with the PC condition (2.42) determining $\boldsymbol{E}$ in terms of $\boldsymbol{B}$ and $\boldsymbol{u}$ on both sides. Since B^x is constant, we have $B^x_l = B^x_r = B^x$.

In general these equations do not look particularly easy to solve, although we can take pointers from MHD as we expect the known solutions from MHD to appear at low velocities, temperatures and magnetic field strengths. In particular, we expect to find contact discontinuities, current sheets, Alfvén (rotational) discontinuities, and fast and slow Magneto-Sonic Shocks. They will likely not behave identically, but they should approach their non-relativistic counterparts as the plasma velocity, temperature and magnetic field strength are reduced. We can also note that these solutions are extensions of the linear solutions, and so we may expect to find analogues of each linear wave as discontinuities and no extra solutions that do not correspond to any linear waves.

We can make some headway with solving these equations by assuming some of the components are constant, or even equal to zero, in order to cancel terms and reduce the complexity.

Stationary Discontinuities

To start with, we can first take the simple case of assuming $\boldsymbol{u} = 0$ on both sides, which cancels many of the components. This would correspond to a discontinuity that advects with the fluid. Cancelling Eqs. (2.123) to (2.129) gives us

$$p_l + \frac{1}{2}B_l^2 = p_r + \frac{1}{2}B_r^2, \tag{2.130}$$

$$B^x B^y_l = B^x B^y_r, \tag{2.131}$$

$$B^x B^z_l = B^x B^z_r, \tag{2.132}$$

where Eqs. (2.123), (2.124), (2.128) and (2.129) have been dropped entirely since all their terms cancelled.

The first point to note here is that the density ρ has disappeared entirely, thus the density can change freely here, we can have $\rho_l \neq \rho_r$ regardless of what the other components are doing. The simple case where only ρ changes is known as a contact discontinuity, and is one of the simplest exact solutions we can find; moreover, this case extends identically into higher dimensions and into the continuous case. Since the discontinuity is stationary in the fluid frame, this solution implies that any variation in only the density should be advected by the fluid velocity.

The first of these three conditions Eq. (2.130) specifies that the total pressure of gas pressure plus magnetic pressure must be constant. So any drop in gas pressure must be compensated by a rise in magnetic pressure and vice versa.

Now consider Eqs. (2.131) and (2.132). There are two possibilities: first, $B^x \neq 0$ implies $B^y_l = B^y_r$ and $B^z_l = B^z_r$, and so all three components of $\boldsymbol{B}$ are constant, hence Eq. (2.130) means that $p_l = p_r$. So in this case all the components besides ρ must be constant. So if there is non-zero B^x only the density can change for a stationary discontinuity. Such a solution is of course an extension of material waves from section 2.1.3, as these waves are stationary relative to the fluid and only change the density.

The second possibility is $B^x = 0$. In this case (2.131, 2.132) no longer restrict B^y and B^z, so the only remaining condition is Eq. (2.130)), that the total pressure remains constant. Hence in this case, if $B^x = 0$ then the equations are solved so long as this total pressure remains constant; there are clearly many choices for this, but one of the most important is to keep gas pressure constant $p_l = p_r$ and then rotate the magnetic field, $B^y_r = B^y_l \cos\theta - B^z_l \sin\theta$ and $B^z_r = B^y_l \sin\theta + B^z_l \cos\theta$. This case is known as a current sheet, since for a change of non-zero thickness this implies the existence of a sheet of current in the region of rotation. In the most extreme case, $\theta = \pi$ and the magnetic field completely flips direction, $\boldsymbol{B}_l = -\boldsymbol{B}_r$ This test is of particular importance because it does not work in FFDE models, since it tends to violate $B^2 - E^2 > 0$ in the sheet, as the plasma is heated by the current (Komissarov, 2002).

These stationary solutions correspond to the stationary linear waves with $B^x = 0$; if we recall from section 2.1.3, Alfvén waves and slow waves both have $\mu = 0$ in the fluid frame in addition to entropy waves, and so these discontinuities therefore correspond to this combination of three different waves in this degenerate case. For our current sheet that merely rotates the magnetic field, it is purely an Alfvén wave.

The de Hoffmann-Teller Frame

So far we have already Lorentz boosted to a frame in which the discontinuity is stationary, so that we only need to solve $\boldsymbol{F}_l = \boldsymbol{F}_r$. But there are many such frames, since from this frame any boost parallel to the discontinuity is still a stationary frame.

One such stationary frame is quite special, known as the de Hoffmann-Teller frame, first noted in de Hoffmann and Teller (1950). In this frame, the velocity on one side $\boldsymbol{u}_l$ is parallel to the magnetic field $\boldsymbol{B}_l$ so that $\boldsymbol{B}_l \times \boldsymbol{v}_l = \boldsymbol{E}_l = 0$. Moreover, the balance of fluxes in Faraday's law in Eqs. (2.128) and (2.129) tells us that $\boldsymbol{E}_r = 0$ also, and hence the velocity $\boldsymbol{u}$ is parallel to the magnetic field $\boldsymbol{B}$ on both sides in this frame. Thus in this frame, there is no electric field on either side of the discontinuity. Note however that this frame exists if and only if $B^x \neq 0$.

In this frame Eqs. (2.123) to (2.129) are considerably simplified due to the annihilation of $\boldsymbol{E}$; moreover the last two Eqs. (2.128) and (2.129) are eliminated entirely, so the equations we are left with are

$$\rho_l u_l^x = \rho_r u_r^x, \tag{2.133}$$

$$w_l u_l^0 u_l^x = w_r u_r^0 u_r^x, \tag{2.134}$$

$$w_l u_l^x u_l^x + p_l + \frac{1}{2} B_l^2 = w_r u_r^x u_r^x + p_r + \frac{1}{2} B_r^2, \tag{2.135}$$

$$w_l u_l^x u_l^y - B^x B_l^y = w_r u_r^x u_r^y - B^x B_r^y, \tag{2.136}$$

$$w_l u_l^x u_l^z - B^x B_l^z = w_r u_r^x u_r^z - B^x B_r^z. \tag{2.137}$$

Alfvén Discontinuities

Now let us consider a case where both u^x and u^0 is constant; this therefore corresponds to a case where the velocity can only rotate around the x-axis (Komissarov, 1997). With u^x constant we immediately have $\rho_l = \rho_r$ from Eq. (2.133), and Eq. (2.134) further gives us $w_l = w_r$, which taken together tells us that $p_l = p_r$.

Plugging these into Eq. (2.135) tells us that $B_l^2 = B_r^2$, and therefore the magnetic field is also restricted to rotations about the x-axis. Hence we have that the only available changes are rotations of $\boldsymbol{u}$ and $\boldsymbol{B}$ about the x-axis, with all other components constant.

So we can re-parametrise the system as a rotation of the perpendicular components of $\boldsymbol{u}$ and $\boldsymbol{B}$. We still have the freedom to rotate the entire system, so we choose to rotate such that $u_l^z = 0$, which implies $B_l^z = 0$ since $\boldsymbol{u}$ and $\boldsymbol{B}$ are parallel. With this, we have

$$u_l^y = u_\perp, \quad u_l^z = 0, \quad B_l^y = B_\perp, \quad B_l^z = 0,$$

$$u_r^y = u_\perp \cos(\theta)\,, \quad u_r^z = u_\perp \sin(\theta)\,, \quad B_r^y = B_\perp \cos(\theta)\,, \quad B_r^z = B_\perp \sin(\theta)\,,$$

where $u_\perp$ and $B_\perp$ are the magnitudes of the perpendicular components of $\boldsymbol{u}$ and $\boldsymbol{B}$, and θ is the rotation of $\boldsymbol{u}$. Note that since $\boldsymbol{u}$ and $\boldsymbol{B}$ are parallel after the rotation as well, the rotation of $\boldsymbol{B}$ is also θ. Finally, inserting these into Eq. (2.137) and cancelling gives us

$$w u^x u_\perp = B^x B_\perp, \tag{2.138}$$

which gives us a condition the discontinuity must satisfy.

This kind of discontinuity is known as an Alfvén discontinuity (Komissarov, 1997), or alternatively a rotational discontinuity (since the main effect is to rotate the magnetic field and velocity).

In an arbitrary frame, this discontinuity moves at the local Alfvén speed. In fact, it is notable because the Alfvén speed is an invariant across the discontinuity as well. It is also no longer a simple rotation of the magnetic field and velocity, and in fact "rotates" the velocity and magnetic field through an ellipse. Furthermore, in an arbitrary frame the normal components u^x and E^x are no longer constant — although v^x is constant.

We noted before that the de Hoffmann-Teller frame that we are using only exists so long as $B^x \neq 0$. In the case that $B^x = 0$, the equivalent Alfvén discontinuity is in fact the current sheet we discussed previously; note how for both cases the magnetic field is rotated about the x-axis in the frame of the discontinuity.

Magnetosonic Shocks

The final type of discontinuity to discuss is that of Magnetosonic shocks. These are discontinuities that feature movement of plasma material across the shock, and form via non-linear steepening of continuous waves, unlike other discontinuities which generally either only form due to boundary conditions, or were already present in the initial conditions. Magnetosonic shocks are the extensions of the Magnetosonic waves from section 2.1.3, and thus can be sorted into fast shocks and slow shocks.

Solving the shock equations Eqs. (2.123) to (2.129) in the most general case for shocks is a fairly involved affair. We shall instead first derive results for some special cases before describing the solution for the general case.

It is common to describe shocks in terms of "upstream" and "downstream" states. These are defined such that fluid flows across the shock from the upstream state to the downstream state.

Parallel Shocks The first case we shall investigate is parallel shocks, where the Magnetic field $\boldsymbol{B}$ lies in the plane of the shock in the shock frame, i.e. so that $B^x = 0$. This choice means that the shock can only be a fast shock, as slow shocks do not exist in this state.

As noted previously, this scenario does not permit the de Hoffmann-Teller frame, so instead we will follow Komissarov and Lyutikov (2011) and choose a frame where $\boldsymbol{u}$ is in the x-y plane so that $u^z = 0$, and the magnetic field $\boldsymbol{B}$ parallel to the z-axis so that $B^y = B^x = 0$, so $\boldsymbol{u}$ and $\boldsymbol{B}$ are orthogonal. Furthermore, we will orient the shock so that the left state is the upstream state.

Since this gives us $b^0 = 0$, it is more convenient to insert these assumptions into the version of the RMHD equations in terms of b^α instead of $\boldsymbol{B}$ and $\boldsymbol{E}$ in Eqs. (2.46) to (2.48); doing so gives us

$$\rho_l \gamma_l v_l^x = \rho_r \gamma_r v_r^x, \tag{2.139}$$

$$\left(w_l + b_l^2\right) \gamma_l^2 v_l^x = \left(w_r + b_r^2\right) \gamma_r^2 v_r^x, \tag{2.140}$$

$$\left(w_l + b_l^2\right) \gamma_l^2 v_l^x v_l^x + p_l + \frac{1}{2} b_l^2 = \left(w_r + b_r^2\right) \gamma_r^2 v_r^x v_r^x + p_r + \frac{1}{2} b_r^2, \tag{2.141}$$

$$\left(w_l + b_l^2\right) \gamma_l^2 v_l^x v_l^y = \left(w_r + b_r^2\right) \gamma_r^2 v_r^x v_r^y, \tag{2.142}$$

$$\gamma_l v_l^x b_l^z = \gamma_r v_r^x b_r^z, \tag{2.143}$$

where we have written this in terms of the 3-velocity $\boldsymbol{v}$ and Lorentz factor γ (given by Eq. (2.30)) as it makes some things simpler. Note that $b^z = \dfrac{B^z}{u^0}$ on both sides and is the only non-zero component of b^α, so from here on we will drop the z superscript.

Taking Eqs. (2.140) and (2.142) gives us $v_l^y = v_r^y$, meanwhile Eqs. (2.139), (2.140) and (2.143) yields

$$\frac{\rho_r}{\rho_l} = \frac{b_r}{b_l} = \frac{\sigma_r}{\sigma_l} = \frac{\eta}{\chi}, \quad a_r^2 = \frac{1}{\kappa}\left(\eta\left(1 + \kappa a_l^2 + \frac{B_l^2}{\rho_l}\right) - \frac{B_l^2}{\rho_l}\left(\frac{\eta}{\chi}\right) - 1\right), \tag{2.144}$$

where $\kappa = \dfrac{\Gamma}{\Gamma - 1}$ with Γ the ratio of specific heats, $a^2 = p/\rho$ is the temperature of the plasma, $\chi = v_r^x / v_l^x$, and

$$\eta = \frac{\gamma_l}{\gamma_r} = \sqrt{1 + u_{xl}^2\left(1 - \chi^2\right)}. \tag{2.145}$$

So given the downstream state and the parameter χ we can calculate the corresponding upstream state.

To determine χ we need the final equation we have not yet used, Eq. (2.141), into which we can substitute all the above expressions for the downstream state. Doing so gives a rather difficult algebraic equation to solve, but we can simplify it with some assumptions to reduce the complexity, as in Komissarov and Lyutikov (2011). In particular, we can assume that the upstream flow is cold ($a_l \to 0$) and highly relativistic ($\gamma_l \gg 1$). In this case, the equation for χ reduces to

$$\begin{aligned}
&\chi^3\left(\left(1 + \sigma_l\right) u_{xl}^2 \left(\kappa - 1\right)\right) + \chi^2\left(-\sigma_l u_{xl}^2 \left(\frac{\kappa - 2}{2}\right) - \kappa\left(1 + \sigma_l\right) u_{xl}^2 - \frac{\kappa \sigma_l}{2}\right) \\
&+ \chi\left(\left(1 + \sigma_l\right)\left(1 + u_{xl}^2\right) - \eta\right) + \left(\sigma_l \left(\frac{\kappa - 2}{2}\right)\left(1 + u_{xl}^2\right)\right) = 0.
\end{aligned} \tag{2.146}$$

This is still difficult to deal with, since η is a function of χ, so this is not truly a cubic function in χ. To deal with this, we can further assume that $u_{xl} \gg 1$. If we denote the angle between the upstream fluid velocity $\boldsymbol{u}_l$ and the shock front by θ_l, then this condition implies $\sin\theta_l \gg 1/\gamma_l$. The above cubic equation then reduces further to

$$\chi^3\left(1 + \sigma_l\right)\left(\kappa - 1\right) - \chi^2\left(\sigma_l\left(\frac{3\kappa - 2}{2}\right) + \kappa\right) + \chi\left(1 + \sigma_l\right) + \sigma_l\left(\frac{\kappa - 2}{2}\right) = 0. \tag{2.147}$$

Given its definition, there is of course a root $\chi = 1$ corresponding to the continuous solution, $\boldsymbol{P}_l = \boldsymbol{P}_r$. For the remaining two solutions only one is physical

$$\chi = \frac{2 + 6\sigma_l + \sqrt{D}}{4\left(1 + \sigma_l\right)\left(\kappa - 1\right)}, \tag{2.148}$$

where

$$D = \left(2 + \sigma_l \kappa\right)^2 - 8\left(1 + \sigma_l\right)\sigma_l\left(\kappa - 1\right)\left(2 - \kappa\right). \tag{2.149}$$

With the ultrarelativistic plasma condition $\Gamma = 4/3 \implies \kappa = 4$ we therefore have

$$\chi = \frac{1 + 2\sigma_l + \sqrt{16\sigma_l^2 + 16\sigma_l + 1}}{6\left(1 + \sigma_l\right)}. \tag{2.150}$$

This means that the corresponding downstream Lorentz factor is

$$\gamma_r = \frac{1}{\sqrt{1 - \chi^2}} \frac{1}{\sin\theta_l}. \tag{2.151}$$

Although this may appear to imply that small θ_l causes the downstream Lorentz factor to diverge, this would violate the earlier assumption that $u_{xl} \gg 1$.

For low upstream magnetisation $\sigma_l \ll 1$ this gives us

$$\gamma_r = \frac{3}{2\sqrt{2}} \left(1 + \frac{1}{2}\sigma_l\right) \frac{1}{\sin\theta_l}, \tag{2.152}$$

while for high upstream magnetisation $\sigma_l \gg 1$ we instead have

$$\gamma_r = \frac{\sqrt{\sigma_l}}{\sin\theta_l}, \tag{2.153}$$

so the downstream Lorentz factor increases with upstream magnetisation σ_l, at first linearly and later with the square root.

Perpendicular Shocks The opposite extreme of the parallel shock, perpendicular shocks feature $\boldsymbol{B}_\perp = 0$ on both sides of the shock front. Since B^x must be constant, this therefore means that the magnetic field cannot change at all.

Returning to the de Hoffmann-Teller frame in Eqs. (2.133) to (2.137), the magnetic contributions vanish from these conditions; since the magnetic field is constant across the shock it cancels from all of the jump conditions. Moreover, since the fluid velocity is parallel to the magnetic field on both sides of the shock we can cancel the latter two equations from this system entirely, and thus the system can be reduced to the following three jump conditions

$$\rho_l u_l^x = \rho_r u_r^x, \tag{2.154}$$

$$w_l u_l^0 u_l^x = w_r u_r^0 u_r^x, \tag{2.155}$$

$$w_l u_l^x u_l^x + p_l = w_r u_r^x u_r^x + p_r. \tag{2.156}$$

Since the magnetic contributions have cancelled, the shock is effectively a purely hydrodynamic shock (Webb *et al.*, 1987)

Oblique Shocks In the general case, the magnetic field will be neither parallel nor perpendicular to the shock front and will instead be oblique on at least one side of the shock. Solving this system here is quite complex, so instead we will simply describe the results.

Webb *et al.* (1987) showed that besides a few special cases (including the parallel and perpendicular cases discussed above), the shock equations reduce to a polynomial of degree seven, which must be solved to find shock solutions. For any given state, there can only be at most four physical shock solutions corresponding to two fast shocks and two slow shocks (one each for either direction) — and one each of these will violate the entropy condition, as entropy will be reduced across the shock — and thus most of these solutions will be non-physical, and only two of the solutions at the most will correspond to physical solutions.

In terms of general results for oblique shocks, Webb *et al.* (1987) showed that density and gas pressure always increases across the shock, for both fast and slow shocks. However, in the shock frame the tangential magnetic field $\boldsymbol{B}_\perp$ is reduced downstream for a slow shock, while it is increased for a fast shock (Webb *et al.*, 1987).

2.3.2 Continuous Solutions

For continuous solutions, we are looking for solutions of the equations with all variables varying continuously across the domain, at least at $t = 0$ if not for all future times $t > 0$. Note that we are not necessarily requiring smooth variables, so first and higher derivatives can feature discontinuities; such discontinuities are known as weak discontinuities.

Small Amplitude Waves

Perhaps the simplest type of continuous wave solutions is that of small amplitude waves. These are waves with sufficiently small amplitude such that they do not appreciably change the background state, and so do not self-interact nor interact with other waves, and the system becomes fully linear.

These waves are given by the eigenvalue and eigenvector solutions we found in section 2.1.3, wherein the eigenvalues correspond to the phase speeds, and the eigenvectors to the "shape" of the wave perturbation in $\boldsymbol{P}$-space, i.e., the relative change in each variable across each wave.

We therefore have seven different types of waves to choose from, and we can also freely choose the waveform; for instance, we could use a sine wave, or a sawtooth wave. Moreover, we can also superpose these seven different waves onto each other, giving us a huge number of different solutions to choose from. In fact, we could even rotate the wave vectors, allowing us to construct a fully multi-dimensional test case.

The only limitation is that the amplitude needs to be small, to avoid non-linear effects. Unfortunately, this limitation means that these solutions are not particularly useful as tests; a model which can't handle these tests likely has significant problems, but they are by far the easiest solutions to model correctly (besides a uniform state). The only real use such a solution would have been for testing stability; that is, if the amplitude grows in time instead of staying constant (or more typically shrinking due to numerical dissipation) then the numerical model is unstable.

Simple Waves

Beyond these small amplitude waves, a common way of finding continuous solutions is to look for simple waves. These can be defined as *"one-dimensional unsteady motion in which the hydrodynamic and electrodynamic variables in some inertial system of reference depend upon the x-coordinate along a direction of propagation and upon t through any combination $\phi(x,t)$"* (Shikin (1969), p. 348). In other words, all the variables can be described as functions of a single variable $\phi(x,t)$, so the degrees of freedom have been reduced.

To help explain, we first define characteristics. We start with a general 1D conservation law in the form of Eq. (2.49). To reiterate, that is

$$\frac{\partial \boldsymbol{Q}}{\partial t} + \boldsymbol{A}(\boldsymbol{Q})\,\frac{\partial \boldsymbol{Q}}{\partial x} = 0,$$

where $\boldsymbol{A}(\boldsymbol{Q})$ is an $n \times n$ matrix. Now, let $\boldsymbol{l}_i(\boldsymbol{Q})$ and $\boldsymbol{r}_i(\boldsymbol{Q})$, $i = 1, \dots, n$ be left and right eigenvectors of $\boldsymbol{A}(\boldsymbol{Q})$, so that

$$\boldsymbol{l}_i(\boldsymbol{Q})\,\boldsymbol{A}(\boldsymbol{Q}) = \lambda_i \boldsymbol{l}_i(\boldsymbol{Q})\,, \quad \text{and} \quad \boldsymbol{A}(\boldsymbol{Q})\,\boldsymbol{r}_i(\boldsymbol{Q}) = \lambda_i \boldsymbol{r}_i(\boldsymbol{Q})\,. \tag{2.157}$$

This then further means that

$$\boldsymbol{l}_i \cdot \boldsymbol{r}_j = 0 \quad \text{for} \quad i \neq j, \tag{2.158}$$

provided the $\boldsymbol{r}_j$ are linearly independent, and the same for the $\boldsymbol{l}_i$. It is always possible to find such eigenvectors for RMHD, even in the degenerate cases with repeated eigenvalues.

If we take $\boldsymbol{Q}(x,t)$ and now consider the differential $d\boldsymbol{Q}$ then we have

$$d\boldsymbol{Q} = \partial_t \boldsymbol{Q} dt + \partial_x \boldsymbol{Q} dx = -\boldsymbol{A}\partial_x \boldsymbol{Q} dt + \partial_x \boldsymbol{Q} dx. \tag{2.159}$$

We can now left-multiply by the left eigenvectors $\boldsymbol{l}_i$ to obtain

$$\boldsymbol{l}_i \cdot d\boldsymbol{Q} = -\left(\boldsymbol{l}_i \boldsymbol{A}\right) \partial_x \boldsymbol{Q} dt + \boldsymbol{l}_i \cdot \partial_x \boldsymbol{Q} dx = \left(dx - \lambda_i dt\right) \boldsymbol{l}_i \cdot \partial_x \boldsymbol{Q}. \tag{2.160}$$

Therefore along the curves defined by $dx/dt = \lambda_i(\boldsymbol{Q})$, we must have $\boldsymbol{l}_i \cdot d\boldsymbol{Q} = 0$; these curves are known as characteristics (Courant and Hilber, 1989). Since the eigenvalues λ_i

are the phase velocities μ of the hyperbolic system, they can also be understood as curves that follow their corresponding waves through the (x, t) plane.

With this definition, simple waves can be understood as the case where all the characteristics for the same i are straight lines and do not self-intersect. Note that the other characteristics need not be straight.

Since it reduces the description to functions of a single variable, the case of a simple wave clearly greatly simplifies the problem. We can further impose one of two further constraints to simplify further; we can impose either:

A. The characteristics all come from the same point, an initial discontinuity. In this case we can describe all variables of the wave as $\boldsymbol{Q}(x,t) = \boldsymbol{U}(x/t)$ (where we have placed the initial discontinuity at $(0,0)$). See Fig. 2.6a for a plot of the characteristics of a case of this type.

B. The characteristics are all parallel, and therefore the wave does not change over time and instead moves in the domain (and so assuming it is not moving at the speed of light, there must be a frame in which it is stationary). This wave can then be described as $\boldsymbol{Q}(x,t) = \boldsymbol{U}(x - \mu t)$, where μ is the phase speed of the wave. See Fig. 2.6b for a plot of the characteristics of a case of this type.

Outside of the ends of these waves we will then have a constant region, as with the discontinuities above. Generally this will mean that the ends of the waves will feature weak discontinuities.

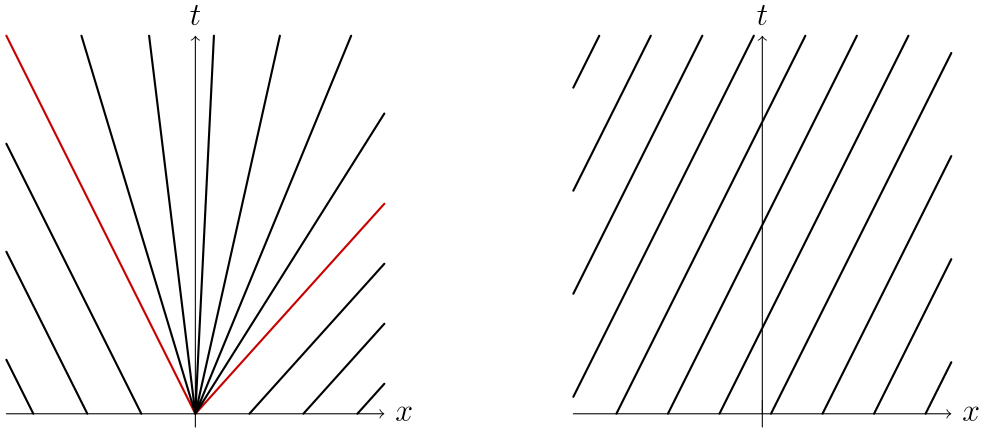

(a) *(b)*

Figure 2.6: *Simple wave characteristics for cases A (a) and B (b). In case A the red characteristics indicate the edges of the expansion fan. The straight lines are the characteristics of the eigenvalue corresponding to this particular wave mode; other characteristics will generally not be straight.*

Case A If we use the condition of case A from above then we can substitute $\boldsymbol{Q}(x,t) = \boldsymbol{U}(x/t)$ into the general equation for a 1D conservation law, Eq. (2.49), then we have

$$\frac{\partial}{\partial t}\boldsymbol{U}\left(\frac{x}{t}\right) + \frac{\partial}{\partial x}\boldsymbol{F}^x\left(\boldsymbol{U}\left(\frac{x}{t}\right)\right) = 0,$$

which we can easily differentiate to get

$$-\frac{x}{t^2}\boldsymbol{U}'\left(\frac{x}{t}\right) + \boldsymbol{A}\left(\boldsymbol{U}\left(\frac{x}{t}\right)\right)\frac{1}{t}\boldsymbol{U}'\left(\frac{x}{t}\right) = 0,$$

where $\boldsymbol{A} = \dfrac{\partial \boldsymbol{F}^x}{\partial \boldsymbol{Q}}$ is again the Jacobian of $\boldsymbol{F}^x$ with respect to $\boldsymbol{Q}$. We can further rearrange this to obtain (Landau and Lifshitz, 1959)

$$\left(\boldsymbol{A}\left(\boldsymbol{U}\left(\frac{x}{t}\right)\right) - \frac{x}{t}\boldsymbol{I}\right)\boldsymbol{U}'\left(\frac{x}{t}\right) = 0, \tag{2.161}$$

where $\boldsymbol{I}$ is the identity matrix.

Note how Eq. (2.161) is an eigenvalue problem for the Jacobian $\boldsymbol{A}$. This of course means that solutions are exactly the same as those found in section 2.1.3, and so it follows that each point in the wave moves with the same speed as one of the phase speeds of the linear waves. Since these phase speeds are different in the general case, a particular wave will use only one of the phase speeds, and so the simple wave can be identified with this linear wave.

Moreover, the shape of the wave given by $\boldsymbol{U}'\left(\dfrac{x}{t}\right)$ must then be the eigenvector of corresponding wave so we can find the shape of the wave simply by integrating, and therefore system must solve the differential equation (Falle *et al.*, 1998)

$$\frac{d\boldsymbol{Q}}{d\nu} = \boldsymbol{r}_i(\boldsymbol{Q}), \tag{2.162}$$

for some parameter ν and where $\boldsymbol{r}_i$ is the eigenvector.

Case B Now, if we use case B from above then we can instead write $\boldsymbol{Q}(x,t) = \boldsymbol{U}(x - \mu t)$, where μ is the speed of the wave, which must be constant. If we once again insert this into Eq. (2.49) and reduce as above, then we will obtain

$$\left(\boldsymbol{A}(\boldsymbol{U}(x-\mu_i t)) - \mu_i\right)\boldsymbol{U}'(x-\mu_i t) = 0. \tag{2.163}$$

So once again the system has been reduced to an eigenvalue problem for $\boldsymbol{A}$. The solution is therefore the same as before, but with one caveat: We have assumed that the phase speed μ is constant, so μ cannot change over the form of the wave. In other words, we require the condition

$$\boldsymbol{r}_i \cdot \boldsymbol{\nabla}_U \mu_i = 0, \tag{2.164}$$

to hold, where $\boldsymbol{r}_i$ is the corresponding eigenvector.

Rarefactions

Rarefaction waves are travelling continuous waves for which the density drops over the wave. They can be considered the continuous non-linear counterpart of the MS shocks from before, since they also correspond to linear MS waves. Unlike the shock case however these waves are isentropic, which can be clearly seen from how the eigenvectors in section 2.1.3 have no entropy component.

Since the phase speed of the wave is not constant across the wave, these waves correspond to the case A type of simple waves discussed above. Unfortunately, the eigenvectors are complex enough that integrating Eq. (2.162) for this case is not possible analytically, so we must find these solutions via numerical integration instead.

Since we are following case A, rarefaction waves must spread out as time increases, since the phase speed at each end of the wave is different. However, since these waves are isentropic the time reverse is also a physical wave, as this does not violate the second law of thermodynamics. In this case, this wave is a so-called compression wave which compresses the plasma as it travels. If a rarefaction spreads out from an initial discontinuity as in case A, a compression wave would then collapse towards a final discontinuity in finite time, after which the solution is no longer correct. Note that since the overall difference between the left and right states of MS shocks is different from that of rarefaction waves — after all, rarefaction and compression waves are isentropic, while shocks are not — this “final discontinuity” that a compression wave collapses into is not generally a shock solution.

Alfvén Waves

Closely related to the Alfvén discontinuous discussed in section 2.3.1, continuous Alfvén waves are effectively identical to the discontinuous case except with non-zero width (Komissarov, 1997). Just like the discontinuities, these waves will (in the de Hoffmann-Teller frame) rotate the magnetic field and the 4-velocity.

An important detail is that since the corresponding Alfvén phase velocity is constant across the wave, the wave is not compressed nor stretched over time. That is, unlike rarefaction and compression waves each point in the wave travels at the same velocity, and so the shape of the wave is unchanged as it travels.

Outside of the de-Hoffmann-Teller frame, the magnetic field vector traces out an ellipse in the $\boldsymbol{B}_y - \boldsymbol{B}_z$ plane instead of a circle, thus generally this wave also changes the magnitude of $\boldsymbol{B}$. However, since b^2 is constant like in the discontinuous case the magnetic pressure does not change.

Unlike rarefactions, Alfvén waves do satisfy Eq. (2.164) and so we can use case B.

Moreover, since the phase speed is constant, for case A an Alfvén wave would in fact be a discontinuity, identical to that calculated above. Thus to construct an Alfvén wave, we need only start in the de Hoffmann-Teller frame and then rotate the magnetic field and velocity together around the x-axis (i.e. keeping them parallel) by a different angle for each point on the x-axis. If the angle smoothly changes in x then we have an Alfvén wave, otherwise it is an Alfvén discontinuity.

Since this is the case, it is possible to rotate the magnetic field back to the initial state. This means we can start and end at the same state, which is quite convenient as it means we can use periodic boundary conditions, unlike rarefactions which do not start and end in the same state. Periodic boundaries are convenient because it means the case we are modelling cannot leave the computation domain, and so we can run the test for as long as we like. For discontinuous tests it is possible to follow the discontinuity, but rarefactions spread out over time so eventually it will escape the domain.

2.4 1D Exact Solutions in FFDE

We can also consider exact solutions in the reduced system of FFDE; these are naturally going to be extensions of results from section 2.3 in the limit of $\sigma \to \infty$, and as such these solutions are limited to Alfvén waves and fast waves. For reasons that will become clear, it is sufficient to consider only continuous solutions.

2.4.1 Fast Waves

The continuous solutions in FFDE will of course satisfy the same conditions as in RMHD; as such, using the form of the eigenvectors from Eq. (2.114) we find that FFDE fast waves must satisfy the following differential equations (Komissarov, 2002)

$$\frac{dE_x}{0} = \frac{dB_y}{-\left(E_z \pm B_y\right)} = \frac{dB_z}{E_y \mp B_z} = \frac{dE_y}{\pm\left(E_y \mp B_z\right)} = \frac{dE_z}{\pm\left(E_z \pm B_y\right)}, \tag{2.165}$$

where the sign of ± again indicates the direction of the fast wave. These equations can then be easily integrated to obtain (Komissarov, 2002)

$$\mu_f = \pm 1 = \text{constant}, \tag{2.166}$$

$$E_x = \text{constant}, \tag{2.167}$$

$$\eta_f = E_z \pm B_y = \text{constant}, \tag{2.168}$$

$$\nu_f = E_y \mp B_z = \text{constant}. \tag{2.169}$$

Naturally $\boldsymbol{B} \cdot \boldsymbol{E}$ is also invariant, as a constraint of FFDE.

If we now introduce the vector

$$\boldsymbol{t}_f = (0, \nu_f, \eta_f)^T\,,$$

then it follows that

$$d\boldsymbol{B}_\perp \cdot \boldsymbol{t}_f = 0, \quad d\boldsymbol{E}_\perp \parallel \boldsymbol{t}_f, \tag{2.170}$$

where $d\boldsymbol{B}_\perp$ and $d\boldsymbol{E}_\perp$ are the variation of the components of $\boldsymbol{B}$ and $\boldsymbol{E}$ perpendicular to the x-axis (and therefore, the wave direction). Thus these waves are transverse waves and have the same properties as linearly polarised electromagnetic waves in a vacuum.

A point to bear in mind is the fact that while FFDE fast waves have phase speeds at the speed of light, in RMHD these waves are slightly slower than the speed of light. This has significant consequences, because while there is a Lorentz frame in which any RMHD fast wave will be stationary, there are no frames in which a wave travelling at the speed of light is stationary. This is therefore a significant divergence between FFDE and RMHD, even at high values of σ.

We note that the inertial terms of RMHD generally include a factor γ, the Lorentz factor of the plasma. Both energy and momentum conservation, Eqs. (2.34) and (2.35), have the term $w\gamma^2$; meanwhile, mass conservation, Eq. (2.29), has the smaller term $\rho\gamma$. Since the fast wave speeds in the fluid frame will be near the speed of light, a Lorentz boost to a frame where one of these waves is stationary will result in a very high γ for the plasma, meaning that the inertial terms are no longer small, despite the high value of σ. This may suggest that the alternate parameter

$$\sigma^* = \frac{\sigma}{\gamma^2} = \frac{b^2}{w\gamma^2} = \frac{B^2 - E^2}{w\gamma^2}, \tag{2.171}$$

may be more appropriate for determining the relative magnitudes of the electromagnetic and inertial components of the system. Unfortunately, this new parameter is not a Lorentz invariant.

In order to determine the relative sizes of the electromagnetic and inertial components in the fast wave frame, we can calculate the value of this parameter σ^* in the frame of a fast wave. Starting from the fluid frame, we can use the phase speeds of MS modes calculated previously in Eq. (2.73), where thanks to the simplified case of the fluid frame we can separate out the fast and slow modes.

Since we want to find the solutions for $\sigma \to \infty$, it is convenient to rewrite Eq. (2.73) in terms of σ. To this end we take out a factor of w from each appearance of b^2, so that

$$s^2 = \frac{\sigma}{1+\sigma},$$

and Eq. (2.73) becomes

$$\mu_f^2 = \frac{\frac{\sigma_x}{1+\sigma}a_s^2 + \epsilon^2 + \sqrt{\left(\frac{\sigma_x}{1+\sigma}a_s^2 + \epsilon^2\right)^2 - 4\frac{\sigma_x}{1+\sigma}a_s^2}}{2}, \tag{2.172}$$

where we have defined σ_x in analogy to the definition of σ as

$$\sigma_x = \frac{B_x^2}{w}.$$

Since we are currently in the fluid frame, a Lorentz boost to the fast wave frame would have a fluid Lorentz factor γ given by

$$\gamma^2 = \frac{1}{1-\mu_f^2}, \tag{2.173}$$

therefore the parameter σ^* in this frame is

$$\sigma^* = \sigma\left(1-\mu_f^2\right). \tag{2.174}$$

Given Eqs. (2.172) and (2.174) we can find the limit of σ^* as

$$\lim_{\sigma\to\infty} \sigma^* = \frac{1-a_s^2}{1-a_s^2\cos^2\phi}, \tag{2.175}$$

where ϕ is given by

$$\cos^2\phi = \frac{\sigma_x}{\sigma} = \frac{B_x^2}{B^2},$$

i.e. ϕ is the cosine of the angle between B_x and the x-axis in the fluid frame.

Eq. (2.175) thus tells us that provided that the adiabatic sound speed does not approach the speed of light, then $\sigma^* \sim \mathcal{O}(1)$ in the fast wave frame. For the equation of state we are using, discussed in section 2.1.1, we have that a_s is capped at $a_s^2 = 1/3$ and so therefore Eq. (2.175) is

$$\lim_{\sigma\to\infty} \sigma^* = \frac{2}{3-\cos^2\phi},$$

for a sufficiently hot plasma. So for a hot plasma, in the limit of large σ, the value of σ^* is such that $2/3 \leq \sigma^* \leq 1$ in the fast wave frame. For colder plasmas $a_s^2 < 1/3$ and so the lower limit $> 2/3$ in this case, while the upper limit is unchanged. In either case, $\sigma^* \leq 1$ in the fast wave frame and in the limit of high magnetisation, in spite of the fact that σ is large.

2.4.2 Alfvén Waves

For Alfvén waves we can use the eigenvectors from Eq. (2.115), so the wave must satisfy the differential equations (Komissarov, 2002)

$$\frac{dB_y}{E_y - \mu_a B_z} = \frac{dB_z}{E_z + \mu_a B_y} = -\frac{B_x dE_x}{\eta_a^2 + \nu_a^2} = \frac{dE_y}{\mu_a(E_z + \mu_a B_y)} = -\frac{dE_z}{\mu_a(E_y - \mu_a B_z)}, \tag{2.176}$$

where μ_a is the phase speed of the Alfvén wave, so $\mu_a = \mu_a^+$ or $\mu_a = \mu_a^-$, and

$$\eta_a = E_z + \mu_a B_y, \quad \nu_a = E_y - \mu_a B_z,$$

as before.

These equations can then be solved to find the following invariants

$$B^2 - E^2 = \text{constant}, \tag{2.177}$$

$$\mu_a = \text{constant}, \tag{2.178}$$

$$\eta_a = E_z + \mu_a B_y = \text{constant}, \tag{2.179}$$

$$\nu_a = E_y - \mu_a B_z = \text{constant}, \tag{2.180}$$

and again $\boldsymbol{B} \cdot \boldsymbol{E}$ is also invariant.

Since the component of E_x is not constant, Alfvén waves are not fully transverse, unlike fast waves. But like fast waves, these waves can still be characterised as linearly polarised; if we introduce the vector

$$\boldsymbol{t}_a = (0, \nu_a, \eta_a)^T,$$

then

$$d\boldsymbol{B}_\perp \cdot \boldsymbol{t}_a = 0, \quad d\boldsymbol{E}_\perp \parallel \boldsymbol{t}_a, \tag{2.181}$$

and so comparing Eqs. (2.170) and (2.181) indicates that while both waves are linearly polarised, they are not generally mutually orthogonal.

Eqs. (2.166) and (2.178) indicate that all waves of FFDE are linearly degenerate; that is, just like Alfvén waves in RMHD the phase speed of every wave is constant across the wave, and so they simply travel without changing shape. This also means that shocks cannot form via non-linear steepening (since the back of the wave is not able to "catch up" to the front), although they may appear due to initial or boundary conditions. As a result, in the high-σ regime of RMHD fast waves will steepen very slowly. This also means that fast shocks do not have strong non-linear steepening keeping them thin and non-diffuse; this will have consequences later on for simulations of fast shocks. This also means that the jump conditions of shocks in FFDE are equivalent to that of simple waves, i.e. discontinuous solutions are equivalent to continuous waves with zero width.

2.5 The Equations of RMHD and FFDE

To finish up, we will summarise the equations of RMHD and FFDE being solved in our scheme. Although the scheme is aimed at solving only the equations of RMHD, the equations of FFDE are relevant as they form part of our new scheme we will introduce in the next chapter.

2.5.1 RMHD

The equations of ideal RMHD consist of eight evolution equations: Mass conservation Eq. (2.29)

$$\partial_t\Big(\rho u^0\Big) + \boldsymbol{\nabla}\cdot(\rho\boldsymbol{u}) = 0,$$

momentum conservation Eq. (2.47)

$$\partial_t\Big(wu^0\boldsymbol{u} + \boldsymbol{E}\times\boldsymbol{B}\Big) + \boldsymbol{\nabla}\cdot\left(w\boldsymbol{u}\boldsymbol{u} - \boldsymbol{E}\boldsymbol{E} - \boldsymbol{B}\boldsymbol{B} + \left(p_g + \frac{1}{2}\Big(E^2+B^2\Big)\right)\delta^{ij}\right) = 0,$$

energy conservation Eq. (2.34)

$$\partial_t\left(wu^0u^0 - p_g + \frac{1}{2}\Big(E^2+B^2\Big)\right) + \boldsymbol{\nabla}\cdot\Big(wu^0\boldsymbol{u} + \boldsymbol{E}\times\boldsymbol{B}\Big) = 0,$$

and Faraday's Law Eq. (2.38)

$$\partial_t\boldsymbol{B} - \boldsymbol{\nabla}\times\boldsymbol{E} = 0.$$

There are also two constraints, Eqs. (2.37) and (2.42)

$$\boldsymbol{\nabla}\cdot\boldsymbol{B} = 0, \quad \boldsymbol{E} = -\boldsymbol{v}\times\boldsymbol{B}.$$

In addition to these equations, we also need an equation of state, for which we use the simple Eq. (2.28)

$$w(\rho,p_g) = \rho + \frac{\Gamma}{\Gamma-1}p_g,$$

with $\Gamma = 4/3$.

Taken together, this is the entire system that we are attempting solve.

2.5.2 FFDE

The equations of FFDE consist of seven different evolution equations: Energy conservation Eq. (2.87)

$$\partial_t\left(\frac{1}{2}\Big(E^2+B^2\Big)\right) + \boldsymbol{\nabla}\cdot(\boldsymbol{E}\times\boldsymbol{B}) = 0,$$

momentum conservation Eq. (2.88)

$$\partial_t(\boldsymbol{E}\times\boldsymbol{B}) + \boldsymbol{\nabla}\cdot\left(-\boldsymbol{E}\boldsymbol{E} - \boldsymbol{B}\boldsymbol{B} + \left(\frac{1}{2}\Big(E^2+B^2\Big)\right)\delta^{ij}\right) = 0,$$

and Faraday's law again Eq. (2.38)

$$\partial_t\boldsymbol{B} - \boldsymbol{\nabla}\times\boldsymbol{E} = 0.$$

Meanwhile, we have three constraints, Eqs. (2.37), (2.89) and (2.90)

$$\boldsymbol{\nabla}\cdot\boldsymbol{B} = 0, \quad \boldsymbol{B}\cdot\boldsymbol{E} = 0, \quad B^2 - E^2 > 0.$$

Chapter 3

Numerical Schemes

This chapter will introduce the fundamental numerical schemes integral to the project. It will first introduce the numerical integration scheme, including a discussion of the finite difference method used, as well as discussion of the methods used to obtain higher-order accuracy integration. The chapter will then move on to introduce the novel approach at the heart of this thesis.

3.1 Integration Method

As we discussed in section 1.2, there are a multitude of different methods for solving hyperbolic systems of conservation laws; one of the most important categorisations of which are non-conservative versus conservative schemes.

These two categories differ in how they treat the conservative variables, e.g. mass and momentum. Obviously, the exact solution of a system of conservation laws will keep them conserved, with the exception of boundary conditions and source terms. However, numerical methods generally have sources of error that cause this conservation to be invalidated.

There are two main sources of error in a numerical scheme. The first is numerical error, which is error that arises from the imprecision with which values are stored in the computation. It most frequently becomes an issue if we take the difference between two similar values, as the number of significant figures of the difference will be limited. For example, if we have $x = 4.61344$ and $y = 4.61334$ so that both x and y are stored to six significant figures, then their difference will be $x - y = 0.00009$, and therefore reduced to just one significant figure. This error can be reduced by increasing the precision of the stored values or avoiding points which require taking the difference of similar values, but it is otherwise difficult to avoid.

The other main source is truncation error, arising from the discretisation and approximation of the system. For example, a time integration scheme will step forward a non-zero time Δt each time step. The solution at each iteration is an approximation of the true solution given the state at the previous step.

Consider a simple ODE, for example,

$$\frac{dx}{dt} = f(x, t)\,, \tag{3.1}$$

with initial data $x(t_0) = x_0$. Now let us suppose that the exact solution to this equation can be expressed as a Taylor series

$$x(t - t_0) = x_0 + (t - t_0)\, x'(t_0) + \frac{1}{2}\,(t - t_0)^2\, x''(t_0) + \mathcal{O}\Big((t - t_0)^3\Big)\,. \tag{3.2}$$

After evolving the system k iterations to some $t = k\Delta t$, since the numerical method is an approximate solution this numerical solution will only match the exact solution up to a finite number of terms. That is, the Taylor series is truncated. The error due to this truncation (i.e. the difference between exact and numerical solutions) is thus known as truncation error (Süli and Mayers, 2003). For partial derivative equations, we can also incur truncation error from spatial discretisation as well.

If the truncation error is $\mathcal{E}_T \sim \mathcal{O}(\Delta x^n) + \mathcal{O}(\Delta t^m)$ then we say that the method is n^{th}-order in space and m^{th}-order in time, because if we halve Δx then the error due to the spatial discretisation will decrease by Δx^n, while if we halve Δt then the error due to temporal discretisation will decrease by Δt^m. Clearly a higher order code is more accurate, but this will generally come at the cost of increased complexity in implementation and computation.

In this case, the equations being solved here are conservation laws. If we integrate such an equation over a given volume V and over a time interval t_0 to t_1 (and ignore source terms), then we will find that the change in the total of a conserved variable inside the volume is equal to the flux of that quantity across the volume boundaries.

Therefore, if we have two volumes sharing a boundary, the flux across that boundary is shared by both volumes, and thus a change in one volume across that boundary is exactly balanced by the change in the other volume. Overall, the variables are conserved.

Conservative schemes exploit this fact by splitting the integration domain into small cells; see Fig. 3.1. Each cell represents a volume, and the change of the conservative variables inside each cell us given by the flux over its boundaries. Since these fluxes are shared (equal but opposite) by neighbouring cells, by updating the cell values using these fluxes we can guarantee that the total of the conserved variables across the entire domain remains constant to numerical precision instead of truncation precision, besides boundary conditions and source terms.

Both conservative and non-conservative schemes have been applied to RMHD. Among non-conservative schemes, some examples include Dumbser *et al.* (2008); Zanotti and Dumbser (2015); Zanotti *et al.* (2015) who developed a discontinuous Galerkin method for RMHD; meanwhile, De Villiers and Hawley (2003) developed a scheme similar to the popular ZEUS solver for non-relativistic HD and MHD (Stone and Norman, 1992).

However, as with all non-conservative schemes, both of these schemes have difficulties with discontinuities. The former of the two implemented an algorithm that detects discontinuities, to which an alternative conservative solver is applied to find a solution in the vicinity of the discontinuity. Although this method is effective, it still requires a conservative solver anyway.

Meanwhile, the latter applied artificial viscosity to smear out the discontinuities to enable the finite difference scheme to handle them. This method, first introduced by Von-Neumann and Richtmyer (1950) is common among non-conservative schemes for handling discontinuities, such as Hartmann and Houston (2002); Česenek *et al.* (2013). However, since it causes shocks to be smeared over multiple grid points, this method is not satisfactory for accurate evaluation of shocks.

Thus if the case one is attempting to model is dependent on resolving discontinuities accurately, then a conservative solver that can handle them without artificial viscosity or special treatments will be very useful. As such, we seek to create a conservative method.

The basic method we are using to integrate the system of RMHD is that of a conservative finite difference scheme. If we work here in three dimensions and Cartesian coordinates, then we have the general conservation law Eq. (2.119)

$$\frac{\partial \boldsymbol{Q}}{\partial t} + \frac{\partial \boldsymbol{F}}{\partial x} + \frac{\partial \boldsymbol{G}}{\partial y} + \frac{\partial \boldsymbol{H}}{\partial z} = \boldsymbol{S}.$$

These equations are then split into two parts

$$\frac{\partial \boldsymbol{Q}}{\partial t} + \frac{\partial \boldsymbol{F}}{\partial x} + \frac{\partial \boldsymbol{G}}{\partial y} + \frac{\partial \boldsymbol{H}}{\partial z} = 0 \quad \text{and} \quad \frac{\partial \boldsymbol{Q}}{\partial t} = \boldsymbol{S}, \tag{3.3}$$

i.e. a homogeneous system, and an inhomogeneous system containing the source terms. These two systems are then integrated separately (if there are any source terms at all).

The computation domain is split into a Cartesian grid of cells $C_{i,j,k}$; see Fig. 3.1 for a 2D representation. Each iteration starts with the known values of the conservative variables $\boldsymbol{Q}$ at the centre of each cell, $\boldsymbol{Q}_{i,j,k}$ (in fewer dimensions we simply have fewer subscripts) — in Fig. 3.1 these are the points at the centre of each cell, located on the lines $x = x_{i-1}, x_i, x_{i+1}$ and $y = y_{i-1}, y_i, y_{i+1}$. We then start by integrating the homogeneous system, the left equation in Eq. (3.3). Starting with the $\boldsymbol{Q}_{i,j,k}$, the basic steps of a single iteration of this scheme are as follows:

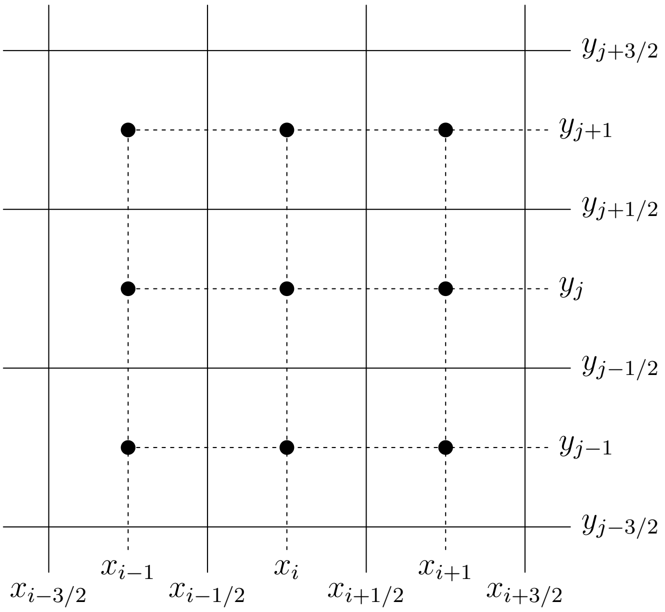

Figure 3.1: *The discretised computational domain for the 2D case. Known cell values are located on the lines with integer subscript,* $x = x_{i-1}, x_i, x_{i+1}$ *and similar for* y*. Cell boundaries where fluxes are calculated are located on the half-integer lines* $x = x_{i-3/2}, ..., x_{i+3/2}$ *and similar for* y*.*

First, the known cell values are interpolated within each cell to its boundaries, using nearby cell values. Since each boundary is a boundary of two cells, each boundary has two different interpolated values for $\boldsymbol{Q}$, from either side of the boundary. Thus the interpolated result at each boundary consists of a state on the "left" in one cell $\boldsymbol{Q}_l$ and a state on the "right" in its neighbour $\boldsymbol{Q}_r$.

These interpolations can be any functions that interpolates the data. We now simplify by asserting that these states are both constant at the boundary, giving us what is known as a Riemann problem at each cell boundary. We now solve each Riemann problem at every boundary with an approximate Riemann solver, to obtain the fluxes $\boldsymbol{F}_{i+1/2,j,k}, \boldsymbol{G}_{i,j+1/2,k}$ and $\boldsymbol{H}_{i,j,k+1/2}$ at each boundary $x = x_{i+1/2}$, $y = y_{j+1/2}$ and $z = z_{k+1/2}$ respectively.

These fluxes are then corrected to $\hat{\boldsymbol{F}}_{i+1/2,j,k}$ and similar for $\boldsymbol{G}$ and $\boldsymbol{H}$ so that the gradients of the fluxes in each cell can be approximated to a high degree of accuracy via

$$\frac{\partial \boldsymbol{F}_{i,j,k}}{\partial x} = \frac{1}{\Delta x}\left(\hat{\boldsymbol{F}}_{i+1/2,j,k} - \hat{\boldsymbol{F}}_{i-1/2,j,k}\right), \tag{3.4}$$

where Δx is the cell width in the x-dimension, and the same for $\boldsymbol{G}$ and $\boldsymbol{H}$.

With these gradients, we can integrate the homogeneous system and update the $\boldsymbol{Q}_{i,j,k}$ by a time step. Since every cell shares each boundary with another cell, the flux $\hat{\boldsymbol{F}}_{i+1/2,j,k}$ etc. at these boundaries appear in the gradient of both neighbouring cells with opposite sign. Thus the total of the conserved quantities $\boldsymbol{Q}_{i,j,k}$ remains constant over the computation domain down to numerical precision, besides flux across the boundary and source terms. For accurate time integration we use a Runge-Kutta scheme, so in this case we update the $\boldsymbol{Q}_{i,j,k}$ to multiple points within the full time step, to get estimates of the gradients at multiple points and therefore construct a more accurate overall gradient to update the system over the full time step.

We have now fully integrated the homogeneous system of Eq. (3.3), so we now integrate the source terms separately. In our case, the source terms are simple enough that this can be done analytically; the equations of RMHD detailed in the previous chapter have no source terms, and in 1D this is also true of our method. However, in 2D and above the method we use to remove the divergence of $\boldsymbol{B}$ resulting from truncation errors requires the addition of a source term — although the form of this source term is so simple that the system can be solved analytically with ease.

With this, a single time step is complete. Now that we have completed an overview of the method, we shall now go into more technical detail of the method.

3.1.1 Finite Difference and Finite Volume Schemes

Among conservative schemes, there are two main approaches, via either finite difference or finite volume schemes. Both types of schemes have been developed extensively for RMHD. For finite volume schemes, we have examples like the CAFE code (Lora-Clavijo *et al.*, 2015), the IllinoisGRMHD code (Etienne *et al.*, 2015) and the GENESIS code (Aloy *et al.*, 1999; Leismann *et al.*, 2005), while for finite difference schemes we have the ECHO code (Del Zanna *et al.*, 2007), and the KORAL code (Sądowski *et al.*, 2013), among others.

The main difference between finite volume and conservative finite difference methods is what the known values represent. For FV schemes, the known values are cell averages, the average of each conservative variable inside each cell. For CFD schemes (and more generally any finite difference scheme), the known values are instead point values, i.e. the exact value of the conservative variables at the given position in the domain.

The main integration method we will use to solve the equations of RMHD presented in chapter 2 is a conservative third order finite difference scheme, based on Godunov's scheme (Godunov, 1959). The basic scheme is the same as that of the ECHO code of Del Zanna *et al.* (2007).

Finite Volume Methods

In order to understand the CFD method, it is helpful to first describe the similar finite volume (FV) method.

We first discretise the computational domain into a grid of cells $C_{i,j,k}$. This works just as above; see Fig. 3.1 for a grid in 2D. We can integrate Eq. (2.119) over each cell $C_{i,j,k}$ and over the time step $[t_n, t_{n+1}]$. Since we can easily cancel each derivative with its respective integral, this gives us

$$\begin{aligned}
&\int_{x_{i-1/2}}^{x_{i+1/2}} \int_{y_{j-1/2}}^{y_{j+1/2}} \int_{z_{k-1/2}}^{z_{k+1/2}} \left(\boldsymbol{Q}(x,y,z,t_{n+1}) - \boldsymbol{Q}(x,y,z,t_n)\right) dxdydz \\
&\quad + \int_{t_n}^{t_{n+1}} \int_{y_{j-1/2}}^{y_{j+1/2}} \int_{z_{k-1/2}}^{z_{k+1/2}} \left(\boldsymbol{F}\left(x_{i+1/2}, y, z, t\right) - \boldsymbol{F}\left(x_{i-1/2}, y, z, t\right)\right) dydzdt \\
&\quad + \int_{t_n}^{t_{n+1}} \int_{x_{i-1/2}}^{x_{i+1/2}} \int_{z_{k-1/2}}^{z_{k+1/2}} \left(\boldsymbol{G}\left(x, y_{j+1/2}, z, t\right) - \boldsymbol{G}\left(x, y_{j-1/2}, z, t\right)\right) dxdzdt \\
&\quad + \int_{t_n}^{t_{n+1}} \int_{x_{i-1/2}}^{x_{i+1/2}} \int_{y_{j-1/2}}^{y_{j+1/2}} \left(\boldsymbol{H}\left(x, y, z_{k+1/2}, t\right) - \boldsymbol{H}\left(x, y, z_{k-1/2}, t\right)\right) dxdydt \\
&\qquad\qquad = \int_{t_n}^{t_{n+1}} \int_{x_{i-1/2}}^{x_{i+1/2}} \int_{y_{j-1/2}}^{y_{j+1/2}} \int_{z_{k-1/2}}^{z_{k+1/2}} \boldsymbol{S}\, dxdydzdt. \qquad (3.5)
\end{aligned}$$

We now define

$$\bar{\boldsymbol{Q}}^n_{i,j,k} = \frac{1}{\Delta x \Delta y \Delta z} \int_{x_{i-1/2}}^{x_{i+1/2}} \int_{y_{j-1/2}}^{y_{j+1/2}} \int_{z_{k-1/2}}^{z_{k+1/2}} \left(\boldsymbol{Q}(x,y,z,t_n)\right) dxdydz, \qquad (3.6)$$

where $\Delta x, \Delta y$ and Δz are the grid spacings in the x, y and z-coordinates respectively, i.e. $\Delta x = x_{i+1/2} - x_{i-1/2}$ etc. This definition means that $\bar{\boldsymbol{Q}}^n_{i,j,k}$ is the average of $\boldsymbol{Q}(\boldsymbol{x}, t)$ over the cell $C_{i,j,k}$ at time t_n. We further define

$$\bar{\boldsymbol{F}}^{n+1/2}_{i+1/2,j,k} = \frac{1}{\Delta y \Delta z \Delta t} \int_{t_n}^{t_{n+1}} \int_{y_{j-1/2}}^{y_{j+1/2}} \int_{z_{k-1/2}}^{z_{k+1/2}} \boldsymbol{F}\left(x_{i+1/2}, y, z, t\right) dydzdt, \qquad (3.7)$$

where Δt is the time interval, $\Delta t = t_{n+1} - t_n$. Again, this is defined so that $\bar{\boldsymbol{F}}^{n+1/2}_{i+1/2,j,k}$ is the average of $\boldsymbol{F}(\boldsymbol{x}, t)$ over the upper x-boundary of cell $C_{i,j,k}$ (located in the y-z plane at $x = x_{i+1/2}$) and over the time interval $[t_n, t_{n+1}]$. We also define $\bar{\boldsymbol{G}}^{n+1/2}_{i,j+1/2,k}$ and $\bar{\boldsymbol{H}}^{n+1/2}_{i,j,k+1/2}$ similarly, as averages of the flux over the y and z boundaries respectively. Finally, we define

$$\bar{\boldsymbol{S}}^{n+1/2}_{i,j,k} = \frac{1}{\Delta x \Delta y \Delta z \Delta t} \int_{t_n}^{t_{n+1}} \int_{x_{i-1/2}}^{x_{i+1/2}} \int_{y_{j-1/2}}^{y_{j+1/2}} \int_{z_{k-1/2}}^{z_{k+1/2}} \boldsymbol{S}\, dxdydtdt, \qquad (3.8)$$

so that $\bar{\boldsymbol{S}}^{n+1/2}_{i,j,k}$ is the average of $\boldsymbol{S}$ over $C_{i,j,k}$ and over $[t_n, t_{n+1}]$.

With these new definitions, we can rewrite Eq. (3.5) as an equation in terms of these averages as

$$\begin{aligned}
&\frac{1}{\Delta t}\left(\bar{\boldsymbol{Q}}^{n+1}_{i,j,k} - \bar{\boldsymbol{Q}}^{n}_{i,j,k}\right) + \frac{1}{\Delta x}\left(\bar{\boldsymbol{F}}^{n+1/2}_{i+1/2,j,k} - \bar{\boldsymbol{F}}^{n+1/2}_{i-1/2,j,k}\right) \\
&\quad + \frac{1}{\Delta y}\left(\bar{\boldsymbol{G}}^{n+1/2}_{i,j+1/2,k} - \bar{\boldsymbol{G}}^{n+1/2}_{i,j-1/2,k}\right) + \frac{1}{\Delta z}\left(\bar{\boldsymbol{H}}^{n+1/2}_{i,j,k+1/2} - \bar{\boldsymbol{H}}^{n+1/2}_{i,j,k-1/2}\right) = \bar{\boldsymbol{S}}^{n+1/2}_{i,j,k}. \qquad (3.9)
\end{aligned}$$

By calculating the average boundary fluxes $\bar{\boldsymbol{F}}^{n+1/2}_{i\pm1/2,j,k}$ etc. as well as the average source terms $\bar{\boldsymbol{S}}^{n+1/2}_{i,j,k}$, we can therefore calculate the change in $\bar{\boldsymbol{Q}}^n_{i,j,k}$ in the cell over the time step.

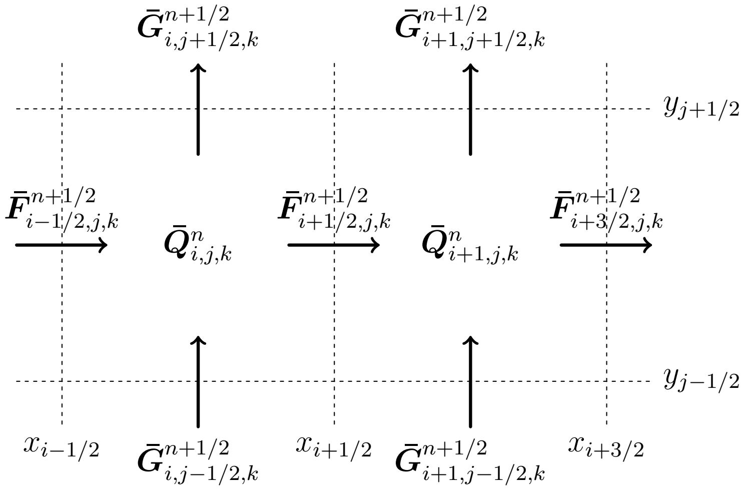

Figure 3.2: *Two neighbouring cells in a 2D finite volume scheme. The average of each cell $\bar{\boldsymbol{Q}}^n_{i,j,k}$ is updated by the total average flux over the entire boundary. Since the two cells share the boundary $x = x_{i+1/2}$, the total of $\boldsymbol{Q}$ between both cells is not affected by the flux over this boundary $\boldsymbol{F}^{n+1/2}_{i+1/2,j,k}$.*

Note how the flux $\bar{\boldsymbol{F}}^{n+1/2}_{i+1/2,j,k}$ will also be present in the update of $\bar{\boldsymbol{Q}}^n_{i+1,j,k}$, with a minus sign, see also Fig. 3.2 for an illustration of this in 2D. This is also true of the other fluxes $\bar{\boldsymbol{G}}$ and $\bar{\boldsymbol{H}}$ as well. Thus like a telescoping sum, these will cancel out for the total of $\boldsymbol{Q}$ over the entire domain (i.e. the integral over the entire domain), leaving only fluxes at the domain boundaries and source terms. This is the key to conservative schemes, and what allows them to ensure conservation, since this guarantees that $\boldsymbol{Q}$ must be conserved down to numerical precision.

Eq. (3.9) is the fundamental equation of a finite volume scheme. All we have left is to evaluate the average fluxes $\bar{\boldsymbol{F}}$. There are many different methods of doing this, and many of the RMHD codes mentioned at the start of section 3.1.1 can implement more than one of them.

Reducing Eq. (3.9) to 1D and neglecting source terms, the basic numerical method is thus

$$\bar{\boldsymbol{Q}}^{n+1}_i = \bar{\boldsymbol{Q}}^n_i - \frac{\Delta t}{\Delta x}\left(\boldsymbol{F}^{n+1/2}_{i+1/2} - \boldsymbol{F}^{n+1/2}_{i-1/2}\right), \tag{3.10}$$

where $\boldsymbol{F}^{n+1/2}_{i+1/2}$ is some approximation of the average flux at the given boundary, i.e.

$$\boldsymbol{F}^{n+1/2}_{i+1/2} \approx \bar{\boldsymbol{F}}^{n+1/2}_{i+1/2} = \frac{1}{\Delta t}\int_{t_n}^{t_{n+1}} \boldsymbol{F}\Big(x_{i+1/2}, t\Big)\, dt. \tag{3.11}$$

Thus we now must find a way to approximate the average boundary fluxes. Perhaps the simplest method would be to use the simple average

$$\boldsymbol{F}^{n+1/2}_{i+1/2} = \frac{1}{2}\left(\boldsymbol{F}(\bar{\boldsymbol{Q}}^n_i) + \boldsymbol{F}(\bar{\boldsymbol{Q}}^n_{i+1})\right), \tag{3.12}$$

so that $\boldsymbol{F}(\bar{\boldsymbol{Q}}_i^n)$ is the flux $\boldsymbol{F}$ associated with the average of cell C_i; inserting this into Eq. (3.10) gives

$$\bar{\boldsymbol{Q}}_i^{n+1} = \bar{\boldsymbol{Q}}_i^n - \frac{\Delta t}{2\Delta x} \left(\boldsymbol{F}(\bar{\boldsymbol{Q}}_{i+1}^n) - \boldsymbol{F}(\bar{\boldsymbol{Q}}_{i-1}^n) \right). \tag{3.13}$$

Unfortunately, this is unstable for hyperbolic methods (LeVeque, 2002).

One simple method of avoiding this instability is via the classic Lax-Friedrichs method, which instead has the form

$$\bar{\boldsymbol{Q}}_i^{n+1} = \frac{1}{2} \left(\bar{\boldsymbol{Q}}_{i-1}^n + \bar{\boldsymbol{Q}}_{i+1}^n \right) - \frac{\Delta t}{2\Delta x} \left(\boldsymbol{F}(\bar{\boldsymbol{Q}}_{i+1}^n) - \boldsymbol{F}(\bar{\boldsymbol{Q}}_{i-1}^n) \right). \tag{3.14}$$

This is very similar to the previous method, except that the initial state $\bar{\boldsymbol{Q}}_i^n$ has been replaced by the average of the two neighbouring states. This may seem to contradict the form Eq. (3.10), but this method can be recast in this form (LeVeque, 2002). Doing so makes it clear that this method has introduced an extra diffusive term to the simple averaging method, which has the effect of suppressing its instability. Although in the limit $\Delta x \to 0$ this method does solve the original equations, this artificial viscosity is quite significant.

This method is known as a central method, because the update to the cell values is symmetric in space about the point where we are updating the solution (LeVeque, 2002). This is a property shared by a number of different schemes, some of which have been applied to RMHD, such as a Lax-Wendroff scheme, as used by (for example) Del Zanna *et al.* (2003); or a Rusanov scheme (also known as local Lax-Freidrichs), as used by HARM (Gammie *et al.*, 2003) and KORAL (Sądowski *et al.*, 2013).

However, for hyperbolic systems we expect information to travel down characteristics at specific velocities, given by the eigenvalues of the Jacobian Eq. (2.53). In our case, this means the two fast, slow and Alfvén phase velocities, as well as the advection speed v_x. Given this, it makes sense to try to take advantage of this fact to better integrate the system, by biasing the integration; after all, in the extreme case where all the characteristics velocities have the same sign (i.e. travelling in the same direction), any cells in the downwind direction cannot possibly have any effect on the solution.

One of the most common such approaches that of Godunov (1959). In this case, the known cell averages are interpolated to the cell boundaries — in Godunov's original scheme, this was done by simply assuming each cell was constant, with each cell having a constant value equal to its cell average.

From this point, the entire system is evolved together at once for a time step. Each cell boundary consists of two constant states with a discontinuity at the boundary. This is a well-known problem known as a Riemann problem, which has a relatively simple solution compared to the general case. After evolving the system for a time step (assumed short enough that neighbouring Riemann problems do not interact), the cell averages are recalculated from the new state. This scheme is upwind because it takes into account the direction of the characteristics — for each Riemann problem, the characteristics with $\lambda < 0$ move into the left cell, while those with $\lambda > 0$ move into the right.

Thanks to a convenient property of Riemann problems that the state at the initial discontinuity (i.e. the boundary in our case) is constant in time after the initial state, this is equivalent to finding the flux of this location in each Riemann problem individually and using that as the boundary fluxes.

The final remaining task to complete the method is to find a Riemann solver, a method that can solve any given Riemann problem. Ideally this would be done via an exact solver, i.e. a method that outputs the exact solution to the given Riemann problem. However, in most cases such a solver is impractical in both implementation and computational complexity. Thus most methods will use an approximate solver of some kind. There are many different such methods, of which we will discuss a few later in section 3.1.2.

Godunov's original scheme is first order in space, because the method assumes that the value of the initial data in each cell is constant and equal to the cell average, so the initial data is piecewise constant. We can improve this accuracy by instead interpolating in each cell by a more complex function; the simplest example would be a linear interpolation, which would allow each cell to have a non-zero gradient.

This would mean that each Riemann problem now has non-constant states, and so is in fact now a generalised Riemann problem, with the two left and right states being some arbitrary function. While methods that use generalised Riemann solvers have been proposed, such as Ben-Artzi and Falcovitz (1984) who developed such a method for the Euler equations, these generalised Riemann solvers will be exceedingly complicated, especially if we allow for higher order interpolations such as quadratic or higher polynomial functions.

However, an approximate solution is all that is really needed, thus most schemes opt for a simplification and assume that the Riemann problem still has constant states, equal to the value of the inter-cell interpolations at the boundary (Toro, 1997).

For Godunov-type schemes, it is clear that in order for the results to be reasonable we must have that Riemann problem between (for instance) cell C_{i-1} and C_i and that between C_i and C_{i+1} cannot interact. This means that the time step Δt must be small enough that the fastest wave modes neighbouring cells do not have enough time to cross the full width of the cell, Δx. Therefore, if we denote the fastest wave mode in the whole computational domain by v then this generates the Courant-Friedrichs-Lewy (CFL) condition (Courant *et al.*, 1928)

$$C_u = \frac{v\Delta t}{\Delta x}, \tag{3.15}$$

where C_u is a dimensionless number called the Courant number.

This condition is a condition for the stability of the scheme, when the time stepping is explicit. Although our justification above applies only to Godunov-type schemes, this condition in fact applies to all explicit finite volume schemes (LeVeque, 2002). Notably however, this condition does not apply for an implicit scheme, which is unconditionally stable (Fernández-Pato *et al.*, 2018), thus these methods can use larger values of C_u. This stability and larger potential time steps is one of the main reasons why one would use an implicit scheme, in spite of the increased complexity both of implementation and calculation. However, this does not mean we can increase C_u to any value we like in that case, as an increase in step size still results in a loss of accuracy, even if the scheme is stable.

Godunov-type schemes are very popular in RMHD, and have been implemented in many different codes, such as that of Komissarov (1999a), as well as the Athena++ (White *et al.*, 2016), ECHO (Del Zanna *et al.*, 2007), KORAL (Sądowski *et al.*, 2013), and CAFE (Lora-Clavijo *et al.*, 2015) codes, among others. These schemes all differ in the exact implementation however, in particular the choice of Riemann solvers used.

The basic method detailed above is a finite volume method, which describes cell values in terms of the averages inside each cell. Although very effective, this method does have a fairly significant issue with implementing it easily: In one of the steps of the finite volume scheme above, we interpolated the known cell averages to the cell boundaries to set up the Riemann problem. In one dimension this is a relatively simple task — although there are complications we will discuss in section 3.1.3. In higher dimensions however, this interpolation must take into account the full multidimensionality of the problem and interpolate values using all nearby cells. This scheme can thus be quite difficult to implement.

Conservative Finite Difference Methods

Another major class of numerical methods is that of a finite difference (FD) method. Unlike finite volume schemes which use cell averages, finite difference schemes discretise the system using exact cell values instead. These methods therefore use the differential form of the equations Eq. (2.119) instead of the integral form Eq. (3.9). Thus we are searching for an estimate of the derivatives of the fluxes are the cell centres, instead of the averages over the cell boundaries. These schemes have a major advantage in that the interpolations to boundaries along one dimension need only take into account the cell values in that dimension, and can ignore the other cell values nearby. Thus the interpolation scheme in higher dimensions can be the same as that of one dimension.

However, since we are trying to evaluate derivatives, we may have difficulty with discontinuities, since this is the strong form of the equations that enforces continuity and differentiability. In addition, while finite volume schemes automatically conserve the variables, finite difference schemes need not satisfy this condition.

However, there is a way to get around this problem, by adapting the finite volume scheme above for a finite difference framework. Like other finite difference schemes, this scheme still needs an estimate for the gradients $\partial_x \boldsymbol{F}$ etc. at the grid points, but the method used to obtain these is very similar to a finite volume scheme — and is designed specifically to maintain conservation like a finite volume scheme — and thus it can handle discontinuous cases. In fact, if we stick to just using first derivatives for interpolations (i.e. second order) this scheme is *identical* to a finite volume scheme. However, while this method avoids multidimensional interpolations, this method also introduces an extra step not previously necessary, that we will discuss in section 3.1.4.

This method has been applied to non-relativistic MHD codes, such as Mignone *et al.* (2010b); Minoshima *et al.* (2019), as well as relativistic MHD codes like Del Zanna *et al.* (2007). Our own scheme will use this method, generally following the scheme as set out in Del Zanna *et al.* (2007), and works as follows:

To simplify the discussion, we will again assume planar symmetry in the y and z planes, so that the system reduces to 1D as y and z-derivatives vanish. Thus we are updating $\boldsymbol{Q}_{i,n}$ (the value at the centre of cell C_i at time $t = t_n$), using an estimate of the gradient $\partial_x \boldsymbol{F} = \boldsymbol{\mathcal{F}}_i$ at this location.

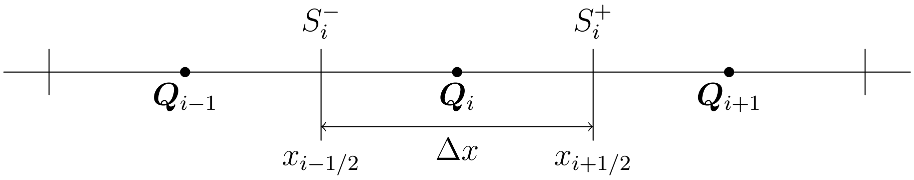

Figure 3.3: *Diagram of the cells in a 1D Conservative Finite Difference Scheme.*

The basic idea is to calculate fluxes $\boldsymbol{F}_i^+$ and $\boldsymbol{F}_i^-$ at the upper and lower boundaries of the cell (S_i^+ and S_i^-, located at $x = x_{i-1/2}$ and $x = x_{i+1/2}$ respectively) so that $\frac{1}{\Delta x}\left(\boldsymbol{F}_i^+ - \boldsymbol{F}_i^-\right)$ is an estimate for the gradient $\partial_x \boldsymbol{F}$ at the cell centre (where Δx is the grid spacing). See Fig. 3.3 for a diagram of a 1D scheme.

If these fluxes are again shared by neighbouring cells like a finite volume scheme, i.e. $\boldsymbol{F}_i^+ = \boldsymbol{F}_{i+1}^-$, then when we update the values of $\boldsymbol{Q}_{i,j,k}^n$ using these fluxes, the quantities are once again conserved to numerical error.

Following a finite volume scheme up to this point, the fluxes we have calculated $\boldsymbol{F}_i^\pm$ at each cell boundary are the exact values of the fluxes at these points. It is important to note however, that the estimate $\frac{1}{\Delta x}\left(\boldsymbol{F}_i^+ - \boldsymbol{F}_i^-\right)$ for the gradient of $\boldsymbol{F}$ at the cell centre is at most second order accurate (Del Zanna *et al.*, 2007). See Fig. 3.4 for a diagram of this estimate.

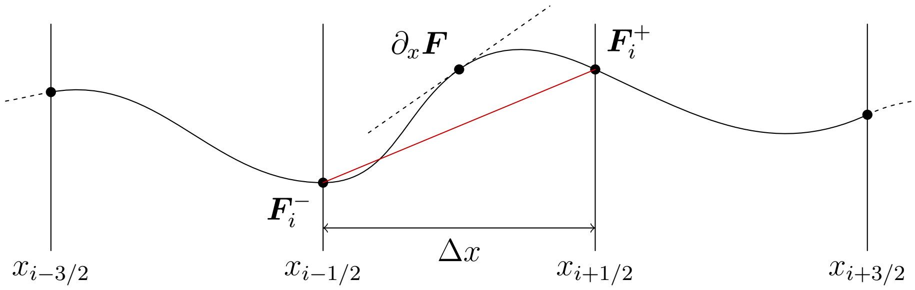

Figure 3.4: *Diagram of the uncorrected fluxes in a 1D Conservative Finite Difference Scheme. The curve is the exact flux at each point, the known solutions at the boundaries are $\boldsymbol{F}_i^+$ and $\boldsymbol{F}_i^-$ (it should be noted that these are actually approximations of the exact solution). The second-order accurate estimate of $\partial_x \boldsymbol{F}$ at $x = x_i$ is the estimate $\frac{1}{\Delta x}\left(\boldsymbol{F}_i^+ - \boldsymbol{F}_i^-\right)$, here represented by the gradient of the red line connecting $\boldsymbol{F}_i^+$ to $\boldsymbol{F}_i^-$.*

If we wish to create a scheme with higher order accuracy, then we must apply a correction to these exact fluxes to get the corrected fluxes $\hat{\boldsymbol{F}}_i^\pm$, for which $\frac{1}{\Delta x}\left(\hat{\boldsymbol{F}}_i^+ - \hat{\boldsymbol{F}}_i^-\right)$ is a higher order accurate approximation to the gradient $\partial_x \boldsymbol{F}$.

Thus we wish to calculate an approximation to these $\hat{\boldsymbol{F}}_i^\pm$. We can then use these in the semi-discrete equation (Del Zanna *et al.*, 2007)

$$\frac{d\boldsymbol{Q}_i}{dt} + \frac{1}{\Delta x}\left(\hat{\boldsymbol{F}}_i^+ - \hat{\boldsymbol{F}}_i^-\right) = \boldsymbol{S}, \tag{3.16}$$

to integrate the $\boldsymbol{Q}_i$.

There are two key properties that we want these flux approximations $\hat{\boldsymbol{F}}_i^\pm$ to satisfy:

1. To maintain conservation of the $\boldsymbol{Q}_i$, we require

   $$\hat{\boldsymbol{F}}_i^+ = \hat{\boldsymbol{F}}_{i+1}^-, \tag{3.17}$$

   for all i, so that the change in $\boldsymbol{Q}_i$ is matched by a change in neighbouring cells (besides boundaries and source terms).

2. To achieve n^{th} order spatial accuracy, we require that $\frac{1}{\Delta x}\left(\hat{\boldsymbol{F}}_i^+ - \hat{\boldsymbol{F}}_i^-\right)$ be an n^{th} order accurate approximation of $\left.\frac{\partial \boldsymbol{F}}{\partial x}\right|_{x=x_i}$. That is, they must satisfy

$$\frac{1}{\Delta x}\left(\hat{\boldsymbol{F}}_i^+ - \hat{\boldsymbol{F}}_i^-\right) = \left.\frac{\partial \boldsymbol{F}}{\partial x}\right|_{x=x_i} + \mathcal{O}(\Delta x^n)\,. \tag{3.18}$$

These fluxes $\hat{\boldsymbol{F}}_i^\pm$ must be calculated from the known data that is the exact flux at the boundaries, $\boldsymbol{F}_i^p m$.

Thus overall, the CFD scheme calculates $\hat{\boldsymbol{F}}_i^{\pm}$ based on the cell values $\boldsymbol{Q}_i$ in each cell works as follows. Here we follow the scheme laid out in Del Zanna *et al.* (2007).

To start with, we calculate the exact flux at the boundaries $\boldsymbol{F}_i^{\pm}$. The method here is the same as with an FV scheme, except we are interpolating exact cell values instead of averages, thus the interpolation scheme can be one dimensional instead of multidimensional.

Thus we first reconstruct the cell value at the upper and lower boundaries of each cell, using an approach which will be discussed in section 3.1.3. This gives us the interpolated value inside within the cell C_i at the start of the time step for the S_i^+ and S_i^- boundaries, i.e. $\boldsymbol{Q}_i^+$ and $\boldsymbol{Q}_i^-$. Although S_i^+ and S_{i+1}^- represent the same cell boundary, because the $\boldsymbol{Q}_i^+$ and $\boldsymbol{Q}_{i+1}^-$ were reconstructed using different cells they will generally not be equal.

Given the $\boldsymbol{Q}_i^+$ and $\boldsymbol{Q}_{i+1}^-$ on the same boundary we then solve the resulting Riemann problem using a Riemann solver which will be discussed in section 3.1.2. This will then give us the exact flux at the boundary $\boldsymbol{F}_i^{\pm}$, where now these do satisfy $\boldsymbol{F}_i^+ = \boldsymbol{F}_{i+1}^-$. Again, these exact values do not satisfy Eq. (3.18) for spatial accuracy > 2, and therefore for these higher order schemes we now require an extra step to calculate the $\hat{\boldsymbol{F}}_i^{\pm}$ from the $\boldsymbol{F}_i^{\pm}$; this is the so-called “DER” step in Del Zanna *et al.* (2007), discussed in more detail below.

This method may seem more complicated since it includes an extra DER step that is not necessary in an FV method, but as mentioned previously it is used because unlike the FV methods, multidimensional schemes only require 1D reconstruction algorithms for higher spatial order, as opposed to FV methods based on cell averages, which require multidimensional reconstruction to calculate fluxes on cell faces (Shu, 2020). Effectively, adding another dimension to the finite difference scheme just means using the exact same algorithm on the new dimension as well, and so the computational cost is exactly the same, per grid point per direction. This is much more efficient that finite volume methods (Casper *et al.*, 1994).

For the value of C_u that we use, we theoretically should use a value for C_u that is as large as possible, since the smaller C_u, the more time steps we need to perform to reach the same time point in the simulation. However, reducing C_u a little can be necessary to suppress some numerical instabilities which generate non-physical artefacts in the solution.

In our case, the fastest wave modes are always the fast waves, and at high σ these approach the speed of light, therefore we can use $v = 1$ for simplicity. Meanwhile, for C_u we use $C_u = 0.4$ for all tests in chapters 4 and 5, in order to suppress some numerical artefacts.

Both conservative finite difference methods and finite volume methods use the conservative variables $\boldsymbol{Q}$ as the integration variables, since these are the variables being conserved. In order to calculate important values like the fluxes we need to be able to calculate the fluxes from the conservative values. Unfortunately, for many systems including RMHD, the fluxes have no simple form in terms of the conservative variables. The typical remedy is to specify a set of intermediate variables called the primitive variables $\boldsymbol{P}$. These variables are chosen so that both the conservative variables and fluxes can be calculated from them easily. This makes it easier to calculate the fluxes, and also easier to apply boundary conditions, which are often not simple expressions in terms of the conservative variables either.

Calculating the primitives from the conservatives is often one of the most complex and slowest parts of a scheme, since the conservatives are often very complicated variables; RMHD is one such case, and several conversion methods have been developed (Del Zanna *et al.*, 2007; Newman and Hamlin, 2014).

3.1.2 Riemann Solvers

The Riemann solver is one of the most important parts of any method of Godunov-type, and as such many different types of Riemann solver have been proposed over the years. Riemann solvers are used to solve so-called Riemann problems, which are a particular class of initial conditions with a constant left state $\boldsymbol{Q}_l$, a constant right state $\boldsymbol{Q}_r$, and a discontinuity between. From here on, we will assume that the discontinuity is located at $x = 0$ at time $t = 0$, so therefore our Riemann problems are all of the form (Toro, 1997)

$$\boldsymbol{Q}(x, 0) = \begin{cases} \boldsymbol{Q}_l & \text{if} \quad x < 0, \\ \boldsymbol{Q}_r & \text{if} \quad x > 0. \end{cases} \tag{3.19}$$

Riemann problems are classic problems for hyperbolic systems as they will often exhibit all the most fundamental aspects of a particular system. For hyperbolic systems, this setup results in a solution which involves only discontinuities and centred rarefactions (Landau and Lifshitz, 1959; Jeffrey and Taniuti, 1984). Generally, a Riemann problem will decompose into a series of n distinct waves (either discontinuities or rarefactions), where n represents the number of distinct eigenvalues of a given hyperbolic system (Toro, 1997).

For instance, a Riemann problem in RMHD (just like in MHD) will typically decompose into seven separate waves, each corresponding to one of the seven distinct eigenvalues of the system; from the outside in, there will be a pair of fast waves, a pair of Alfvén waves, a pair of slow waves, and finally in the middle a contact discontinuity (Komissarov, 1999a). In between each wave is a region where all values are constant. This is unless one of the degeneracies is present, in which case some of the waves will move together and there will effectively be fewer waves.

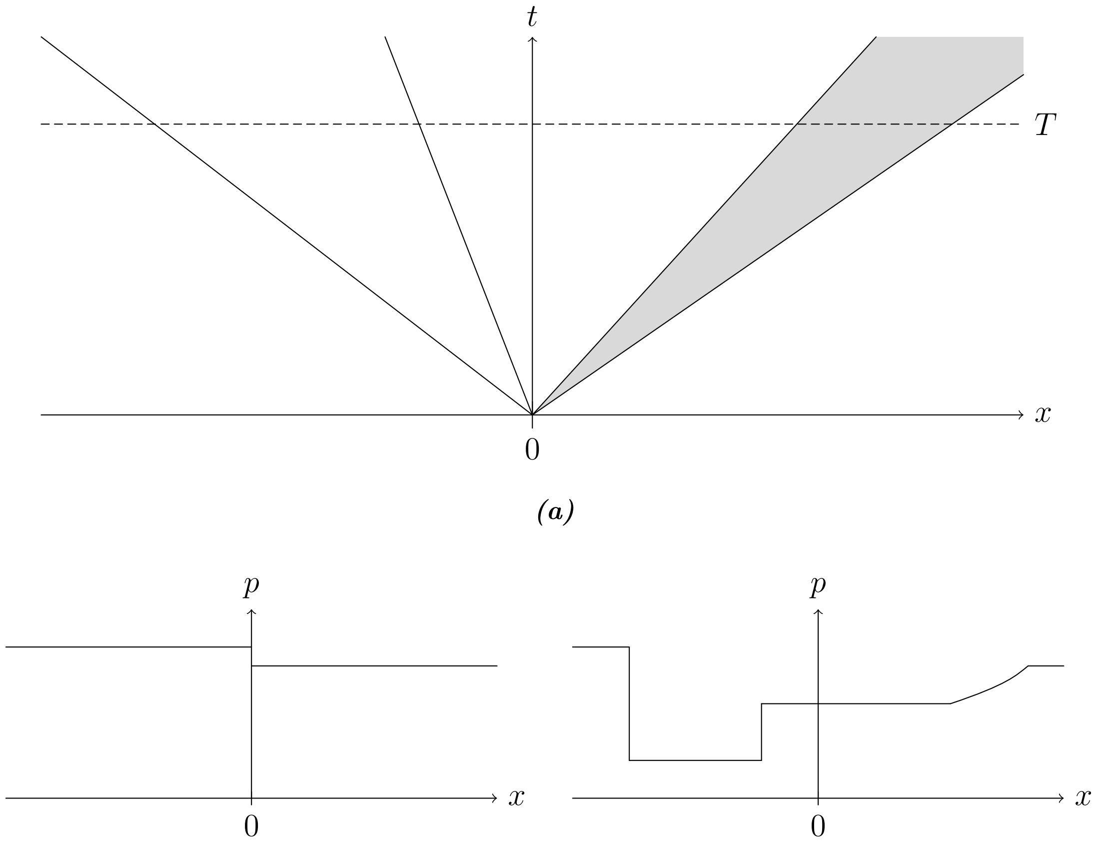

(a)

(b)

(c)

Figure 3.5: *An arbitrary Riemann fan for a variable* $p(x,t)$ *in a system with three wave modes, in this case splitting into two discontinuities with phase speeds* $\mu < 0$ *and a rarefaction with phase speed* $\mu > 0$ *over the full wave. (a) The Riemann fan in the* x*-*t *plane. The two slanted lines in the* $x < 0$ *half of the plane represents a discontinuity; the shaded region on the right indicates that it is a continuous wave (and thus a rarefaction), and is bounded by two weak discontinuities. Also shown here is the Riemann fan in the* x*-*p *plane at* $t = 0$ *(b) and* $t = T$ *(c).*

The exact form of the waves will depend on the initial discontinuity; in particular, the fast and slow waves can either be continuous rarefaction waves or discontinuous shock waves. The Alfvén and contact discontinuities will always be discontinuities however, as neither spread out over time since their own phase speed is constant across them.

In Fig. 3.5a we have an example of a Riemann fan for a variable $p(x,t)$, in the x-t plane, and with two slices in the p-x plane at $t = 0$ and $t = T$. The original Riemann problem in Fig. 3.5b has split into three separate waves, a left-going discontinuity, a slower left-going discontinuity, and a right-going rarefaction. This is a simplified case, as typically

RMHD will have seven separate waves — although this situation could occur in the $B_x = 0$ degeneracy case, as in that case five of the waves have the same phase speed.

Riemann problems (or to be more precise, their solutions) have a useful property of self-similarity. Consider a general system of equations

$$\frac{\partial \boldsymbol{Q}}{\partial t} + \frac{\partial \boldsymbol{F}}{\partial x} = \frac{\partial \boldsymbol{Q}}{\partial t} + \frac{\partial \boldsymbol{F}}{\partial \boldsymbol{Q}} \frac{\partial \boldsymbol{Q}}{\partial x} = 0, \tag{3.20}$$

coupled with the initial conditions Eq. (3.19).

Now consider $\boldsymbol{Q}_\lambda(x, t) = \boldsymbol{Q}(\lambda x, \lambda t)$, a scaled version of the solution $\boldsymbol{Q}$. If we substitute $\boldsymbol{Q}_\lambda$ into Eq. (3.20) then we obtain

$$\begin{aligned} \frac{\partial \boldsymbol{Q}_\lambda}{\partial t} + \frac{\partial \boldsymbol{F}}{\partial \boldsymbol{Q}_\lambda} \frac{\partial \boldsymbol{Q}_\lambda}{\partial x} &= 0, \\ \lambda \frac{\partial \boldsymbol{Q}}{\partial t}(\lambda x, \lambda t) + \lambda \frac{\partial \boldsymbol{F}}{\partial \boldsymbol{Q}}(\lambda x, \lambda t) \, \frac{\partial \boldsymbol{Q}}{\partial x}(\lambda x, \lambda t) &= 0, \end{aligned} \tag{3.21}$$

hence $\boldsymbol{Q}_\lambda$ is also a solution of the system, with initial conditions $\boldsymbol{Q}_\lambda(x, 0) = \boldsymbol{Q}(\lambda x, 0)$. Given the initial conditions Eq. (3.19) we find that $\boldsymbol{Q}_\lambda(x, 0) = \boldsymbol{Q}(x, 0)$, and thus $\boldsymbol{Q}_\lambda$ is a solution for the same initial conditions.

Therefore if we have the solution at some time $t_i > 0$ then we can find another at any other future time $t_j > 0$ by simply scaling appropriately. Equivalently, we can write our solution as a function of a single variable $\boldsymbol{Q}(x, t) = \boldsymbol{U}(x/t)$ where x/t is the similarity parameter. x/t of course represents a straight line from the origin that all features of the solution must follow, so that the derivative of $\boldsymbol{Q}$ along these lines is zero.

For the purposes of a Riemann solver in the numerical method, all that is actually needed is the solution at $x = 0$ at some time $t > 0$. Since all points on this line (besides at $t = 0$) have the same similarity parameter $x/t = 0$, this solution is in fact independent of t; for all future times $t > 0$ the exact result is constant. Thus the Riemann solver does not need to consider the time at all — provided of course that the CFL condition is fulfilled.

The most obvious method for solving such a problem is likely the exact solver, which given the Riemann problem supplied outputs the exact solution for the given initial condition. This type of solver is typically used for simple systems, where the solution of the Riemann problem can be found easily and with little computational overhead. For a system as complex as RMHD an exact solver is less useful due to the high complexity of such a solver, and the high computational costs.

After all, there will generally be seven separate waves of the types described in section 2.3 which were complex enough on their own. For instance, a shock wave (as discussed in section 2.3.1) generally requires solving a seventh order polynomial, which cannot be done analytically. Giacomazzo and Rezzolla (2006) have created a method for finding the exact solution, however their method uses an iterative procedure and is impractical for use in an actual numerical scheme, besides generating exact solutions for testing purposes.

Fortunately, numerical results typically do not suffer significantly with more approximate solutions (Toro, 1997). There can be negative effects, such as more diffuse discontinuities (spread over more cells) or numerical artefacts, but these can often be remedied in one way or another. In fact, it can be quite surprising how little the approximation needs to match the exact solution; as we will see later with the HLL solver in section 3.1.2, the numerical method can be reasonably accurate even if we reduce the number of waves down to just two.

There are multiple simplifications that can be applied to the Riemann solution to reduce the complexity. The first would be to collapse the continuous rarefaction waves into discontinuities, so that each component of the Riemann fan is reduced to a single velocity. This velocity should ideally be chosen such that the new discontinuity lies inside the original rarefaction wave, i.e. if v_l and v_r are the velocities of the left and right ends of the rarefaction respectively, then the velocity of the new discontinuity v_d should be $v_l < v_d < v_r$. Of course, this leaves us with some freedom over what velocity v_d we should choose.

Using this simplification, we would therefore only need to calculate the velocities of each wave, and the constant states between them. The solution we want at $x = 0$ then simply corresponds to the state between the wave with largest velocity $v < 0$ and the wave with smallest velocity $v > 0$ — unless all waves have $v > 0$ or $v < 0$, in which case the solution is simply one of the initial states $\boldsymbol{Q}_l$ or $\boldsymbol{Q}_r$ respectively.

Although this simplification is helpful, the difficulty of the problem has not been reduced very significantly, as the calculation of the constant states and of the velocities is still a highly intractable non-linear system of equations. Multiple further reductions have been proposed, but here we will only consider two.

Linear Riemann Solvers

The first method we will consider is that of a Linear solver (Roe, 1981; Powell, 1994; Toro, 1997). In section 2.1.3 we discussed the linearisation of RMHD, finding the eigenvalues and eigenvectors of the Jacobian $\boldsymbol{A}(\boldsymbol{Q})$. For a given state $\boldsymbol{Q}$, the eigenvalues correspond to the velocities of each wave, and the eigenvectors correspond to the direction of the jump in $\boldsymbol{Q}$-space.

As the amplitude of the waves increases the eigenvalues and eigenvectors no longer match the exact results, as non-linear effects become relevant. However, for a sufficiently small amplitude of the initial discontinuity this linearisation will give accurate results as these non-linear effects vanish.

Linear Riemann solvers simply assume that this is still an appropriate approximation, even for initial discontinuities of much higher amplitudes. In other words, to solve the Riemann problem we choose a base state $\boldsymbol{Q}_b$ and calculate the n eigenvalues λ_i and eigenvectors $\boldsymbol{v}_i$ of the Jacobian $\boldsymbol{A}(\boldsymbol{Q}_b)$. Since we know that the left state is $\boldsymbol{Q}_l$ and the right state is $\boldsymbol{Q}_r$, we then can find the amplitudes a_i of each wave by solving the linear system

$$\sum_{i=1}^{n} a_i \boldsymbol{v}_i = \boldsymbol{Q}_r - \boldsymbol{Q}_l, \tag{3.22}$$

for the a_i, which will have a unique solution provided the $\boldsymbol{v}_i$ are all linearly independent.

Then each of the $n-1$ in-between states $\boldsymbol{Q}_i$ must satisfy

$$\boldsymbol{Q}_i = \boldsymbol{Q}_l + \sum_{j=1}^{i} a_j \boldsymbol{v}_j, \tag{3.23}$$

or from the other side

$$\boldsymbol{Q}_i = \boldsymbol{Q}_r - \sum_{j=i+1}^{n} a_j \boldsymbol{v}_j. \tag{3.24}$$

This gives us a chain of states connecting $\boldsymbol{Q}_l$ and $\boldsymbol{Q}_r$. We can therefore derive the internal states $\boldsymbol{Q}_i$ from either direction, given $\boldsymbol{Q}_l$, $\boldsymbol{Q}_r$ and the $a_j \boldsymbol{v}_j$. Since this is the case, one of the waves $a_j \boldsymbol{v}_j$ can be neglected, as even if a link in the chain is missing, we can still calculate all of the $\boldsymbol{Q}_i$ by starting from the appropriate side of the Riemann problem.

Since we only need $n-1$ of the a_j, we can therefore drop one of the equations in Eq. (3.22) and reduce the number of unknowns of the linear problem by one. For RMHD, it is natural and simplest to neglect the amplitude of the contact wave as it is the simplest wave, only changing the density. Since this wave is always at the centre, this also maintains the symmetry of the system. Symmetry is useful because if we were to take the mirror image of our Riemann problem — i.e. swap $\boldsymbol{Q}_l$ and $\boldsymbol{Q}_r$ and reflect the vectors $\boldsymbol{u}$ and $\boldsymbol{B}$ — then we should get the exact same results (with mirrored vectors) because of the symmetry in the equations of RMHD. If the Riemann solver is not symmetric, then this property would be broken.

This also means we can neglect density from Eq. (3.22) and reduce the system down to six equations in six unknowns, reducing the computational cost of the Riemann solver.

All that remains here is to choose the base state $\boldsymbol{Q}_b$ from which we find the eigenvalues and eigenvectors. We have a lot of choice here of course, and in fact we might even use a different $\boldsymbol{Q}_b$ for some of the eigenvalues and eigenvectors. Using a different $\boldsymbol{Q}_b$ could have significant consequences though, since using the same base state generally guarantees that the eigenvectors are all linearly independent, which is not guaranteed otherwise.

One basic choice is to simply use the average $\boldsymbol{Q}_b = (\boldsymbol{Q}_l + \boldsymbol{Q}_r)/2$ as the base state (e.g. Riemann Solver B in Falle and Komissarov (1996), p. 589). In many situations this works well, although for some systems the average state might not be physical; for instance, with FFDE even if we have $\boldsymbol{B}_l \cdot \boldsymbol{E}_l = 0$ and $\boldsymbol{B}_r \cdot \boldsymbol{E}_r = 0$, generally speaking the averages of these $\boldsymbol{B}_a = \frac{1}{2}(\boldsymbol{B}_l + \boldsymbol{B}_r)$ and $\boldsymbol{E}_a = \frac{1}{2}(\boldsymbol{E}_l + \boldsymbol{E}_r)$ do not satisfy $\boldsymbol{B}_a \cdot \boldsymbol{E}_a = 0$, and so these averages are non-physical states.

Another simple choice for RMHD (and similar systems) is to use $\boldsymbol{Q}_l$ for the three fast, Alfvén and slow left waves and $\boldsymbol{Q}_r$ for the three fast, Alfvén and slow right waves (e.g. Riemann Solver A in Falle and Komissarov (1996), p. 588). Regardless of what base state we use, the contact wave only has a jump in density, so the choice of $\boldsymbol{Q}_b$ for that wave does not matter.

Instead of choosing a base state $\boldsymbol{Q}_b$ for the Jacobian, the Roe-type Riemann solver looks instead for an averaged Jacobian $\bar{\boldsymbol{A}}(\boldsymbol{Q}_l, \boldsymbol{Q}_r)$ from which all eigenvalues and eigenvectors are derived. This averaged Jacobian is required to satisfy three conditions; first, that it has n real eigenvectors. Second, that it satisfies the consistency condition $\bar{\boldsymbol{A}}(\boldsymbol{Q}, \boldsymbol{Q}) = \boldsymbol{A}(\boldsymbol{Q})$ for all $\boldsymbol{Q}$. Third, that

$$\boldsymbol{F}_r - \boldsymbol{F}_l = \bar{\boldsymbol{A}}\left(\boldsymbol{Q}_r - \boldsymbol{Q}_l\right). \tag{3.25}$$

(Roe, 1981) showed an averaged Jacobian satisfying these conditions is guaranteed to exist by the mean value theorem.

This third condition ensures that the Riemann solver is able to resolve even non-linear discontinuities accurately, since if $\boldsymbol{Q}_l$ and $\boldsymbol{Q}_r$ satisfy the jump conditions Eq. (2.53), then they satisfy

$$\boldsymbol{F}_l - \boldsymbol{F}_r = \lambda\left(\boldsymbol{Q}_l - \boldsymbol{Q}_r\right), \tag{3.26}$$

where λ is therefore both the shock speed *and* an eigenvalue of the averaged Jacobian. Thus in this specific case, the Roe solver gives an exact solution of the equations. Unfortunately, finding this averaged Jacobian can be quite difficult for complex systems.

Linear Riemann solvers have been used in various codes, such as for non-relativistic gas dynamics (Brio *et al.*, 2001) and MHD (Dai and Woodward, 1994). Some RMHD codes also use linear Riemann solvers, such as Komissarov (1999a); Koldoba *et al.* (2002).

A significant issue with linear solvers is degenerate cases. If a particular choice of $\boldsymbol{Q}_b$ produces repeated eigenvalues (i.e. waves travelling at the same velocity) then these cases must be treated separately, since we need to ensure that the eigenvectors chosen for these repeated eigenvalues are linearly independent (Falle *et al.*, 1998). Therefore this method can become quite complex as the algorithm evaluates which (if any) degenerate case we are in.

Another problem is that the in-between states $\boldsymbol{Q}_i$ found may not be physical. For instance, in RMHD we must have density $\rho > 0$ and gas pressure $p_g > 0$, however the linear solver may find that these values drop below 0, particularly in the presence of strong rarefactions. Generally the only method to deal with this is to set a minimum value to the density and gas pressure to prevent them from becoming negative, a clearly unsatisfactory and artificial solution.

HLL Solver

An alternative solver is the HLL solver, first proposed in Harten *et al.* (1983) and developed further in Einfeldt (1988). This method simplifies the system even further into just two waves, the waves with the highest and lowest velocity (i.e. the outermost signals from the Riemann problem). In the case of RMHD, this of course corresponds to the two fast waves. The remaining interior states are then averaged together into a single, constant interior state. The scheme works as follows (Toro, 1997):

Define v_r and v_l as the highest and lowest velocities of all waves respectively. If we have $v_r v_l > 0$ then the velocities have the same sign, and therefore the Riemann fan is entirely on one side of $x = 0$. Thus in this case, the solution for the flux can immediately be found as $\boldsymbol{F}_l$ if $v_l, v_r > 0$ or $\boldsymbol{F}_r$ if $v_l, v_r < 0$. For the remaining case with $v_r v_l < 0$ we need to find the flux inside the Riemann fan.

First, we choose an arbitrary $x_l < 0$ and $x_r > 0$ and a time $t = T$ such that $x_l \leq T v_l$ and $x_r \geq T v_r$. This setup means that the points where the lines $x = x_l$ and $x = x_r$ intersect the line $t = T$ lie beyond the intersection of the highest and lowest velocity waves, which at this time would be at $x = T v_l$ and $x = T v_r$ — in other words, we choose $x_l < T v_l$ and $x_r > T v_r$. Fig. 3.6 shows the general idea behind this set up; we can see that the interval $[T v_l, T v_r]$ is inside the interval $[x_l, x_r]$.

The equations for a general 1D homogeneous system are given by Eq. (2.119), dropping y and z derivatives and the source terms so that

$$\frac{\partial \boldsymbol{Q}}{\partial t} + \frac{\partial \boldsymbol{F}}{\partial x} = 0.$$

If we now integrate these equations over $[x_l, x_r] \times [0, T]$, then we obtain

$$\int_{x_l}^{x_r} \boldsymbol{Q}(x, T)\, dx - \int_{x_l}^{x_r} \boldsymbol{Q}(x, 0)\, dx = \int_0^T \boldsymbol{F}(\boldsymbol{Q}(x_l, t))\, dt - \int_0^T \boldsymbol{F}(\boldsymbol{Q}(x_r, t))\, dt. \tag{3.27}$$

Since we chose T such that the line from $(x_l, 0)$ to (x_l, T) lies entirely outside the Riemann fan, the state $\boldsymbol{Q}$ is constant along the line and therefore we have that the integral

$$\int_0^T \boldsymbol{F}(\boldsymbol{Q}(x_l, t))\, dt = T \boldsymbol{F}_l, \tag{3.28}$$

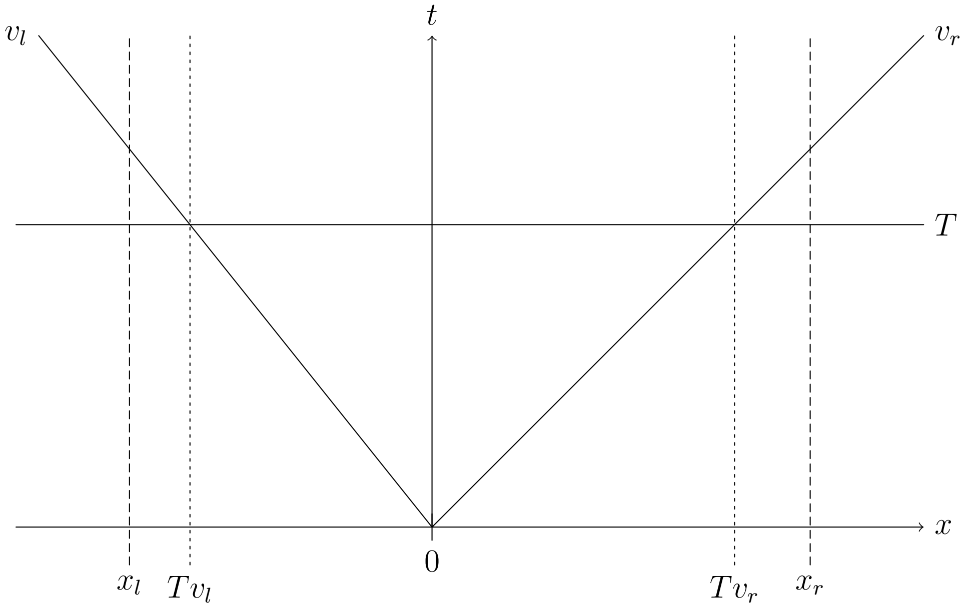

Figure 3.6: *A Riemann fan as reduced by the HLL scheme. v_l represents the fastest signal to the left, and v_r represents the fastest signal to the right.*

and similarly on the other side the same reasoning gives

$$\int_0^T \boldsymbol{F}(\boldsymbol{Q}(x_r,t))\,dt = T\boldsymbol{F}_r. \tag{3.29}$$

The integral along $t = 0$ is not completely constant, and instead has a single jump discontinuity at $x = 0$. Therefore the integral here is

$$\int_{x_l}^{x_r} \boldsymbol{Q}(x,0)\,dx = x_l\boldsymbol{Q}_l - x_r\boldsymbol{Q}_r, \tag{3.30}$$

we can therefore put Eqs. (3.28) to (3.30) into Eq. (3.27) to find

$$\int_{x_l}^{x_r} \boldsymbol{Q}(x,T)\,dx = x_r\boldsymbol{Q}_r - x_l\boldsymbol{Q}_l + T(\boldsymbol{F}_l - \boldsymbol{F}_r)\,, \tag{3.31}$$

so we know the exact result for the integral of $\boldsymbol{Q}$ at time $t = T$, provided the velocities v_l and v_r. Since we allowed the integral to extend slightly into the constant regions, we can further split this integral into

$$\int_{x_l}^{x_r} \boldsymbol{Q}(x,T)\,dx = \int_{x_l}^{Tv_l} \boldsymbol{Q}(x,T)\,dx + \int_{Tv_l}^{Tv_r} \boldsymbol{Q}(x,T)\,dx + \int_{Tv_r}^{x_r} \boldsymbol{Q}(x,T)\,dx, \tag{3.32}$$

where the first and third integrals on the right hand side can be evaluated to give us

$$\int_{x_l}^{x_r} \boldsymbol{Q}(x,T)\,dx = \int_{Tv_l}^{Tv_r} \boldsymbol{Q}(x,T)\,dx + (Tv_l - x_l)\,\boldsymbol{Q}_l + (x_r - Tv_r)\,\boldsymbol{Q}_r, \tag{3.33}$$

which we can now substitute this into Eq. (3.31) and rearrange to obtain

$$\frac{1}{T\,(v_r - v_l)}\int_{Tv_l}^{Tv_r} \boldsymbol{Q}(x,T)\,dx = \boldsymbol{Q}_{HLL} = \frac{v_r\boldsymbol{Q}_r - v_r\boldsymbol{Q}_l + \boldsymbol{F}_l - \boldsymbol{F}_r}{v_r - v_l}, \tag{3.34}$$

where $\boldsymbol{Q}_{HLL}$ is the average of $\boldsymbol{Q}$ in the Riemann fan at time $t = T$.

Although we could use this $\boldsymbol{Q}_{HLL}$ as our solution to the Riemann problem, we can do better by calculating the fluxes directly.

Now we can once again integrate the conservation laws in section 3.1.2 over the reduced area of $[x_l, 0] \times [0, T]$, to obtain

$$\int_{x_l}^{0} \boldsymbol{Q}(x,T)\,dx - \int_{x_l}^{0} \boldsymbol{Q}(x,0)\,dx = \int_{0}^{T} \boldsymbol{F}(\boldsymbol{Q}(x_l,t))\,dt - \int_{0}^{T} \boldsymbol{F}(\boldsymbol{Q}(0,t))\,dt. \tag{3.35}$$

The second integral on the left and the first integral on the right have already appeared before in Eq. (3.27). For the second integral on the right, the state $\boldsymbol{F}(\boldsymbol{Q})$ at $x = 0$ is also constant despite being inside the Riemann fan, as discussed previously. This flux is the value we are looking for, which we will call $\boldsymbol{F}_{HLL}$. With this, Eq. (3.35) reduces to

$$\int_{Tv_l}^{0} \boldsymbol{Q}(x,T)\,dx = -Tv_l\boldsymbol{Q}_l + T\left(\boldsymbol{F}_l - \boldsymbol{F}_{HLL}\right). \tag{3.36}$$

Using the initial simplifying approximation that the interior state between the two fastest signal velocities is constant, i.e. $\boldsymbol{Q}$ is constant inside the Riemann fan, $\boldsymbol{Q}$ inside the fan must be equal to the average, $\boldsymbol{Q}_{HLL}$. Therefore Eq. (3.36) further reduces to

$$\boldsymbol{F}_{HLL} = \boldsymbol{F}_l + v_l\left(\boldsymbol{Q}_{HLL} - \boldsymbol{Q}_l\right), \tag{3.37}$$

and finally we can substitute for $\boldsymbol{Q}_{HLL}$ using Eq. (3.34) to obtain

$$\boldsymbol{F}_{HLL} = \frac{v_r\boldsymbol{F}_l - v_l\boldsymbol{F}_r + v_l v_r\left(\boldsymbol{Q}_r - \boldsymbol{Q}_l\right)}{v_r - v_l}, \tag{3.38}$$

So we can calculate an estimate of the flux at the boundary using only the conserved variables and fluxes in the two initial states, and the maximal velocities of the waves in the Riemann fan.

We still need to calculate two of the phase speeds, which would generally depend on the solution; in order to maintain validity of this method we require that these phase speeds be at least as fast as the exact values, or at the very least close enough to not be an issue.

One method would be to use the eigenvalues of the left and right initial states for these phase velocities. If we write l_- and l_+ as the maximal phase velocities for the left state, and r_- and r_+ as the same for the right state, then we could use l_- as the maximal left phase velocity v_l, and r_+ for the maximal right phase velocity v_r.

However, depending on the initial states $\boldsymbol{Q}_l$ and $\boldsymbol{Q}_r$ we could either have $l_- < r_-$ or $l_- > r_-$, and similarly for the positive case. In the latter case, with $l_- > r_-$, it may be better to use r_- for v_l instead, in order to help ensure that the velocity v_l we are using is smaller than the true value, as suggested by Davis (1988). This is the choice that we decided to use for the HLL phase speeds.

In summary, given signal velocities v_l and v_r this scheme outputs the flux at the boundary for a given Riemann problem as

$$\boldsymbol{F}_{out} = \begin{cases} \boldsymbol{F}_l & \text{if} \quad v_l, v_r > 0 \\ \boldsymbol{F}_{HLL} & \text{if} \quad v_l v_r \leq 0 \\ \boldsymbol{F}_r & \text{if} \quad v_l, v_r < 0 \end{cases}, \tag{3.39}$$

with $\boldsymbol{F}_{HLL}$ given as above in Eq. (3.38).

The main advantage of the HLL method over other methods is its simplicity. In comparison to the Linear method previously discussed, all we need here is two of the phase velocities, and the conservative variables and fluxes for the initial states, which are generally quite simple to calculate.

Another advantage is that this method generally avoids the problem with linear methods wherein the resultant state can be non-physical; with this method that cannot happen, because we do not evaluate the actual state and directly output the flux at the boundary instead.

This method is not without its own drawbacks, however. neglecting all but two of the waves means that although the method can resolve the remaining waves, these waves tend to be quite diffusive, spreading these waves over more grid points (Toro, 1997). Various authors have suggested methods to combat this by using an alteration of the scheme to resolve these waves, at the cost of higher computational cost; for instance, the HLLC method developed in Toro *et al.* (1994) for non-relativistic Hydrodynamics restores the contact wave to reduce the diffusivity, and in Mignone *et al.* (2009) a five-wave version of the HLL scheme for RMHD is developed.

HLL solvers (and related solvers e.g. HLLC) are quite popular in RMHD, and have been used in various codes, such as Athena++ (White *et al.*, 2016), ECHO (Del Zanna *et al.*, 2007), IllinoisGRMHD (Etienne *et al.*, 2015) and CAFE (Lora-Clavijo *et al.*, 2015). The most significant factor in their popularity is likely their simplicity, and the fact that we only need the eigenvalues of the Jacobian to calculate the resultant Flux. For this reason, we will also use the HLL solver described above for our code.

3.1.3 Reconstruction

At the start of each time step, the known values in our scheme are the point values of $\boldsymbol{Q}$ at the centre of each cell $C_{i,j,k}$. To set up the Riemann problems to be solved via a method described in the previous section, we must interpolate the value of $\boldsymbol{Q}$ at the cell boundaries, in a step known as the reconstruction step. Generally speaking, the more accurate this interpolation is the more accurate the overall numerical solution will be. In particular, we seek to increase the spatial order of the code, as discussed at the start of this chapter.

Interpolating to first order is quite simple; in this case the interpolation can simply assume that $\boldsymbol{Q}$ is constant in each cell, and equal to the known value at the centre. At each boundary, the value of $\boldsymbol{Q}$ in one cell is matched next to the (generally different) value of $\boldsymbol{Q}$ in the next cell, and thus we have a Riemann problem that can be solved as above.

In order to obtain higher orders, we can use the known values of nearby cells as well to improve the interpolation of $\boldsymbol{Q}$ in each cell. We thus try to fit different functions to the known values as interpolating functions. We then interpolate to the boundaries of each cell from both directions (from the cell to the left and to the right). These two interpolations will generally give a different result, and thus we again have a Riemann problem that can be solved using the previous methods.

Most authors tend to use the simplest choice of polynomial interpolation (Liu *et al.*, 1994; Jiang and Shu, 1996), although other types such as trigonometric polynomial (Wang and Zhu, 2020) and exponential polynomial (Ha *et al.*, 2016) interpolation have also been proposed. For a polynomial fit however, the method is quite simple. Given any n consecutive known values, there is a unique $n-1$ order polynomial that passes through all n points exactly, the so-called Lagrange polynomial. This polynomial then serves as an n^{th}-order accurate approximation for the given variable in all n cells from which the interpolation was derived.

Thus each cell has a choice of n different polynomial interpolations which are all n^{th}-order accurate. Naively, we may assume that we can simply choose any of these polynomials for the approximation in a given cell. Unfortunately, things are not so simple.

Godunov's Theorem

Godunov (1959) proved a very important theorem related to numerical solutions of partial differential equations (PDEs). This theorem states that linear numerical schemes for solving PDEs, having the property of not generating new extrema (a monotone scheme), can be at most first order accurate. This theorem has come to be known as Godunov's theorem.

This problem can be understood as related to the Gibbs phenomenon in the Fourier series of data with a jump discontinuity. In that case, the Fourier series exhibits large overshoots and undershoots at the discontinuity, i.e. new extrema. While these new extrema become thinner as higher order sines and cosines are included, and thus the Fourier series converges to the data almost everywhere (except for the discontinuities), their am-

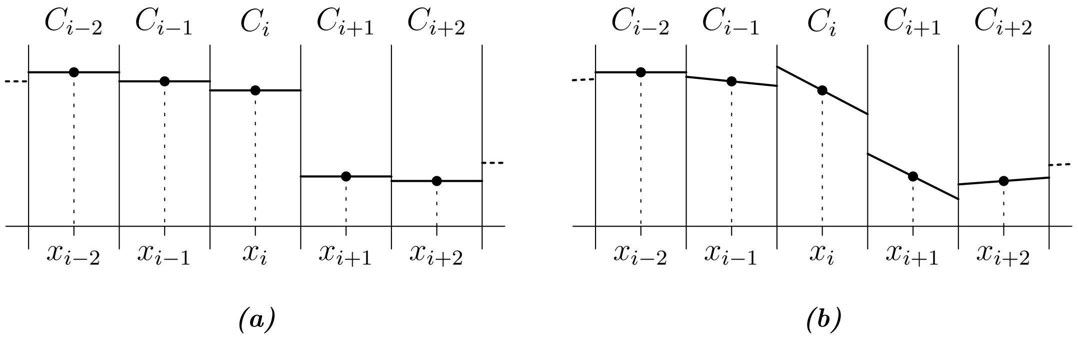

Figure 3.7: *First (a) and Second order (b) linear interpolation of the same data. This data has a discontinuity between C_i to C_{i+1}.*

plitude does not approach 0. Instead, it approaches a limit of about 9% the scale of the discontinuity itself (Bocher, 1906).

In our case, a polynomial approximation over a discontinuity will also exhibit a similar phenomenon near the discontinuity, and it is this which underlies Godunov's theorem. The only way we can guarantee avoiding new extrema is through the use of a first order approximation. That is, we assume the function is constant, and therefore we cannot exceed the known values of the function.

Fig. 3.7 gives an illustration of this issue. Here we have a first and second order interpolation of the same data. The gradient in the second order interpolation is set to the average of the gradient between itself and its two neighbours, i.e. the gradient in C_i is set to the average of the gradient between C_{i-1} and C_i, and the gradient between C_i and C_{i+1}.

We can see that while the first order interpolation has no problems at the discontinuity, the second order interpolation overshoots and introduces new extrema. For example, at the right boundary of C_{i+1} located at $x = x_{i+3/2}$ the interpolated value is now larger than the value in both C_{i+1} and C_{i+2}. However, the interpolation elsewhere does not have these issues, and so away from discontinuities it is still desirable to use a higher order interpolation.

Since these problems are caused specifically by discontinuities in the variables, if we can create a scheme that reduces the order near these discontinuities then we can obtain higher order approximations outside of these cases without issue. There are many different ways of obtaining higher order interpolations; a popular example is the piecewise parabolic method. This method is used in various RMHD codes such as ECHO (Del Zanna *et al.*, 2007), IllinoisGRMHD (Etienne *et al.*, 2015) and KORAL (Sądowski *et al.*, 2013).

In our case, we have used two different methods of achieving higher order code, for second and third order interpolation respectively.

Second order method

The second order method is the first method we used to improve the accuracy of the code. This particular method is based on the method from Komissarov (1999a).

Given the primitives $\boldsymbol{P}$ at the centre of cell C_i at time n, we use these $\boldsymbol{P}_{i,n}$ to calculate the gradient in each C_i as

$$\left(\frac{\partial \boldsymbol{P}}{\partial x}\right)_{i,n} = \frac{1}{\Delta x}\mathrm{av}\left(\Delta \boldsymbol{P}_{i-\frac{1}{2},n}, \Delta \boldsymbol{P}_{i+\frac{1}{2},n}\right), \tag{3.40}$$

where Δx is the cell width, $\mathrm{av}\left(\cdot,\cdot\right)$ is a non-linear averaging function and

$$\Delta \boldsymbol{P}_{i-\frac{1}{2},n} = \boldsymbol{P}_{i,n} - \boldsymbol{P}_{i-1,n}, \tag{3.41}$$

and so we can then use these gradients to calculate the cell value at the boundary as

$$\boldsymbol{P}^{l}_{i,n} = \boldsymbol{P}_{i,n} - \frac{1}{2}\Delta x\left(\frac{\partial \boldsymbol{P}}{\partial x}\right)_{i,n} \quad \text{and} \quad \boldsymbol{P}^{r}_{i,n} = \boldsymbol{P}_{i,n} + \frac{1}{2}\Delta x\left(\frac{\partial \boldsymbol{P}}{\partial x}\right)_{i,n}, \tag{3.42}$$

for the left and right boundaries of C_i respectively.

Given the boundary between C_i and C_{i-1} this gives two interpolations for this same boundary as the right boundary of the lower cell $\boldsymbol{P}^{r}_{i-1,n}$ and the left boundary of the upper cell $\boldsymbol{P}^{l}_{i,n}$. Generally these are not equal and so we then solve the resultant Riemann Problem, now neglecting the gradients within the cell.

All that remains is the averaging function $\mathrm{av}\left(\cdot,\cdot\right)$. For each cell, there are two different second order polynomial interpolations within the cell; the interpolation of the left and current cells, and the interpolation of the right and current cells. In both cases, the interpolation is just a straight line connecting the two known cell values at the cell centres, giving a gradient of $\Delta \boldsymbol{P}_{i-1/2,n}$ for the left interpolation and $\Delta \boldsymbol{P}_{i+1/2,n}$ for the right. In both cases, the interpolation at the cell boundary is simply the cell value at the centre plus this gradient over half the cell width.

The averaging function then simply finds an average between these two gradients, to find an interpolation that is balanced between the two, since left or right biased interpolations tend to have unwanted effects on the model results. Moreover, this non-linear average can be tuned so that the gradient of interpolations containing a discontinuity are dropped, in order to avoid the problem of Godunov's theorem.

We find then that a function $\mathrm{av}\left(\cdot,\cdot\right)$ which is homogeneous of degree one and has the following properties

$$\mathrm{av}(a,b) = 0 \quad \text{if } ab < 0,$$

$$\mathrm{av}(a,b) \to \begin{cases} \frac{1}{2}(a+b) & \text{as} \quad a \to b, \\ a & \text{as} \quad |a|/|b| \to 0, \\ b & \text{as} \quad |b|/|a| \to 0, \end{cases}$$

will have the desired behaviour. That is, if $a \approx b$ then the average approaches the usual average of the gradients, while are if $|a| \gg |b|$ or vice versa, so that one of the gradients a or b is much larger than the other, then the average defaults to the smaller of the two gradients, thus neglecting the interpolation of larger absolute gradient. If there is a discontinuity, then this should be the side with the larger absolute gradient and therefore the averaging function neglects this side, avoiding the issues associated with interpolation over a discontinuity. Finally, in the case where the gradient changes sign (so a minimum or maximum) the function outputs a gradient of 0, thereby eliminating the possibility of introducing new extrema.

Clearly there is a lot of freedom in the choice of function here, and no general agreement on which is best. Following van Leer (1977) and Komissarov (1999a), we choose

$$\mathrm{av}(a,b) = \begin{cases} \dfrac{a^2b + ab^2}{a^2+b^2} & \text{if } ab \geq 0 \text{ and } a^2+b^2 \neq 0, \\ 0 & \text{if } ab < 0 \text{ or } a^2+b^2 = 0, \end{cases}$$

which has all the correct properties, in addition to being quite simple.

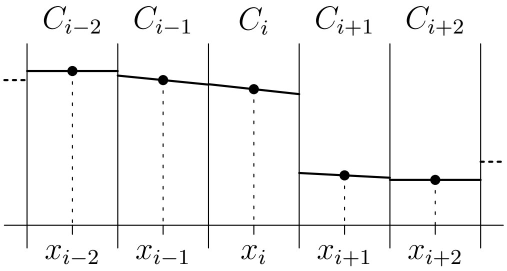

Figure 3.8: *Second order interpolation using the nonlinear averaging method, using the same data as in Fig. 3.7.*

Fig. 3.8 shows the results of this interpolation method, using the same data as before in Fig. 3.7. Comparing to the second order interpolation in Fig. 3.7b that uses a linear average, we can clearly see that this method has eliminated the issue with interpolations near the discontinuity.

One may note that this method does not in fact reduce to first order near discontinuities, unless at least one of the gradients is zero or the gradient changes sign. If this is not the case, then the averaging function gives a non-linear average of the two gradients, and still retains second order convergence. Thus this method does not actually reduce the order at all, and simply biases the interpolation to the side that does not contain any discontinuities. However, as noted previously the issue above was with interpolating over a discontinuity, and so this method should still serve to remove this issue.

Third order WENO method

Although in many circumstances a second order method is sufficient, we will see later that the reduction of truncation error is more important for this code than would generally be the case. In addition to this, the near-lack of non-linear steepening at high σ for fast shocks means that there are few factors to counteract numerical diffusion and keep shocks sharp, thus these shocks can spread over many cells with a low-accuracy integration scheme. We therefore decided to improve the method to third order so that we could reduce this error further.

Every n consecutive cells (called a stencil) provides an n^{th} order interpolation within these n cells. Each cell is a member of n different stencils, and therefore has n different n^{th} order interpolations for the value of $\boldsymbol{P}$ inside the cell, including both cell boundaries.

The essentially non-oscillatory or ENO method, first proposed in Harten *et al.* (1987), uses this fact to avoid the problem of oscillatory solutions. In its basic form, this method evaluates the “smoothness” of all n stencils, and then chooses the smoothest stencil for the interpolation. Since a stencil that contains a discontinuity should not be smooth, this method naturally selects a stencil that has none.

This method is known as essentially non-oscillatory, because even though it does not reduce to first order, it still avoids the oscillations induced by interpolating over a discontinuity, and therefore avoids this problem, for the most part.

Unfortunately, the basic ENO method will often be biased left or right, as in many conditions one can find that the smoothness of the stencils is itself biased, regardless of the presence of actual discontinuities. Many suggestions have been proposed to combat this, including trying to bias the selection process centrally, so that in smooth regions it tends to select central interpolations.

Importantly, any weighted average of the n difference interpolations is also an n^{th} order interpolation over the same domain. That is, if $\boldsymbol{P}_1(x)\,, \boldsymbol{P}_2(x)\,, \ldots, \boldsymbol{P}_n(x)$ are the n different interpolation functions within the cell, any weighted average

$$\bar{\boldsymbol{P}}(x) = \sum_{i=1}^{n} a_i \boldsymbol{P}_i(x)\,, \quad \text{with} \quad \sum_{i=1}^{n} a_i, \tag{3.43}$$

is also an n^{th} order interpolation of $\boldsymbol{P}$ inside the cell. This fact can also be used to try to bias the stencil selection more smoothly; we may note that the previous second order method can in fact be interpreted in this way, as an averaged ENO method.

However, rather than an arbitrary choice of weights, Liu *et al.* (1994) developed the so-called WENO method (Weighted essentially non-oscillatory) and showed that by averaging with a convex combination of all the stencils with a particular choice of weights, it can actually allow us to increase the order of the interpolation. A particular cell is contained in n different stencils, therefore an average of all these n interpolants contains data from $2n-1$ different cells in total. So it is not unreasonable to think that combining this data in a particular manner could increase the order of the method somehow, up to a maximum of $2n-1$.

While Liu *et al.* (1994) originally only showed that the order of the method could be increased by one, Jiang and Shu (1996) showed further that a particular method of averaging allows us to increase the order of the method up to the theoretical maximum of $2n-1$. That is, with all $2n-1$ cells involved there is a unique $2n-2$ order interpolation polynomial, and they showed that one can average all n interpolations to match this unique polynomial. The weights needed are independent of the actual values in the cells so long as the cell size is constant and only depends on the location we are interpolating to inside the cell, so we can always use the same weights. Since the full set of $2n-1$ cells are centred on the cell we are interpolating, this method is also naturally a central interpolation, so there is no bias.

However, we have of course been ignoring the problem of discontinuities in some cells. If we simply interpolate like the $2n-2$ order polynomial, then this is no different than just using this interpolation to begin with. The advantage of a WENO scheme is that we can modify the weights of the average so that if a discontinuity is in one (or more) of the stencils, then these interpolations are dropped from the average, avoiding the discontinuities — and also dropping the order of the interpolation, generally to the order of interpolation of a single stencil, n.

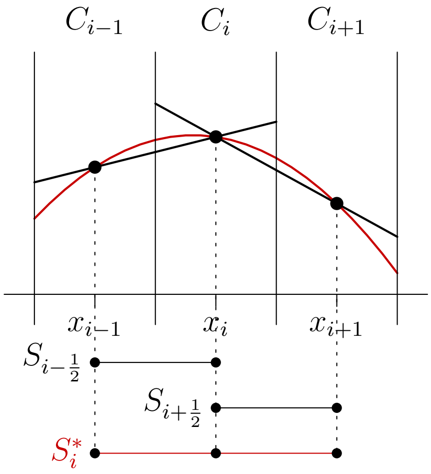

Figure 3.9: *Illustration of a third order WENO scheme. The second order interpolations of the sub-stencils $S_{i-1/2}$ and $S_{i+1/2}$ are in black, while the third order interpolation over the full stencil S_i^* is in red. Each stencil range is annotated below the plot.*

In our case, we are using a third order WENO scheme. An illustration of our set up can be seen in Fig. 3.9. The two linear interpolations have stencils $S_{i-1/2}$ over C_{i-1} to C_i and $S_{i+1/2}$ over C_i to $C_{i+1/2}$, with linear interpolations drawn in black. These two interpolations are both valid second order interpolations of the value of $\boldsymbol{P}$ inside the common cell C_i (assuming no discontinuities are present, of course). This therefore means that any weighted average of these two interpolations is also a second (or higher) interpolation of $\boldsymbol{P}$, including the specific choice of weights which match the interpolation over the stencil S_i^*, i.e. all three cells.

Both smaller stencils have unique linear interpolations for the left and right boundaries of C_i, so we write $\boldsymbol{P}_{i,-}^l$ as the interpolation of the left boundary at $x_{i-1/2}$ of C_i via stencil $S_{i-1/2}$, and similarly for the right boundary at $x_{i+1/2}$ we have $\boldsymbol{P}_{i,-}^r$, while the interpolations of stencil $S_{i+1/2}$ are given by $\boldsymbol{P}_{i,+}^l$ for the left boundary and $\boldsymbol{P}_{i,+}^r$ for the right. With these definitions, we can write these in terms of the known values at the cell centres $\boldsymbol{P}_i$ as

$$\begin{aligned} \boldsymbol{P}_{i,-}^l &= \frac{1}{2}\boldsymbol{P}_{i-1} + \frac{1}{2}\boldsymbol{P}_i \quad \text{and} \quad \boldsymbol{P}_{i,-}^r = -\frac{1}{2}\boldsymbol{P}_{i-1} + \frac{3}{2}\boldsymbol{P}_i, \\ \boldsymbol{P}_{i,+}^l &= \frac{3}{2}\boldsymbol{P}_i - \frac{1}{2}\boldsymbol{P}_{i+1} \quad \text{and} \quad \boldsymbol{P}_{i,+}^r = \frac{1}{2}\boldsymbol{P}_i + \frac{1}{2}\boldsymbol{P}_{i+1}. \end{aligned} \tag{3.44}$$

Meanwhile, the third order interpolations for the left and right boundaries using all three cells ${}^*\boldsymbol{P}_i^l$ and ${}^*\boldsymbol{P}_i^r$ are given by

$${}^*\boldsymbol{P}_i^l = \frac{3}{8}\boldsymbol{P}_{i-1} + \frac{3}{4}\boldsymbol{P}_i - \frac{1}{8}\boldsymbol{P}_{i+1} \quad \text{and} \quad {}^*\boldsymbol{P}_i^l = -\frac{1}{8}\boldsymbol{P}_{i-1} + \frac{3}{4}\boldsymbol{P}_i + \frac{3}{8}\boldsymbol{P}_{i+1}. \tag{3.45}$$

Comparing Eq. (3.44) to Eq. (3.45), we find that we can write the third order interpolations in terms of the second order interpolations as weighted averages

$$\boldsymbol{P}_i^l = \gamma_-\boldsymbol{P}_{i,-}^l + \gamma_+\boldsymbol{P}_{i,+}^l \quad \text{and} \quad \boldsymbol{P}_i^r = \gamma_+\boldsymbol{P}_{i,-}^r + \gamma_-\boldsymbol{P}_{i,+}^r, \tag{3.46}$$

if we use the weights $\gamma_- = 3/4$ and $\gamma_+ = 1/4$. Note how the weights for the left and right boundaries are not the same but instead swapped due to symmetry.

The weights $\gamma_\pm$ are known as the linear weights. They are the optimal choice of weights to achieve third order convergence, and in smooth regions these are the weights we want to use. However, if we were to simply use these weights everywhere the method would be no different from simply using a third order central scheme directly. It is when there are discontinuities that the advantages of a WENO method make themselves known; if a particular stencil contains a discontinuity, then we can reduce the weight of this stencil to ignore its impact.

We therefore require some method of identifying discontinuities. Unfortunately, with the only data we have being the values at the cell centres, it is impossible to perfectly separate cases of discontinuities to cases with merely very large gradients etc. — at least until the grid spacing Δx is small enough to fully resolve these features.

We must settle for a method that can identify where discontinuities *probably* are instead. To do this, we require some method of evaluating the "smoothness" of each stencil, much like an ENO method, which we can then use to calculate the so-called "non-linear weights"$w_\pm$, from which we can calculate our final interpolation result as

$$\boldsymbol{P}_i^l = w_- \boldsymbol{P}_{i,-}^l + w_+ \boldsymbol{P}_{i,+}^l \quad \text{and} \quad \boldsymbol{P}_i^r = w_+ \boldsymbol{P}_{i,-}^r + w_- \boldsymbol{P}_{i,+}^r. \tag{3.47}$$

We require two properties of these non-linear weights:

1. In smooth regions they should approach the linear weights, $w_\pm \to \gamma_\pm$ as $\Delta x \to 0$.
2. If stencil S_r contains a discontinuity then the associated weight should be small $w_r \to 0$.

For this purpose, we first need some way of measuring the smoothness of each stencil. Jiang and Shu (1996) originally suggested the following for these so-called "smoothness indicators"

$$\beta_i^k = \sum_{r=1}^{n} \Delta x^{2r-1} \int_{x_{i-1/2}}^{x_{i+1/2}} \left(\frac{d^r}{dx^r} p^{(k)}(x) \right)^2 dx, \tag{3.48}$$

where $\beta_i^k \geq 0$, with k ranging $1 \leq k \leq n$, represents the smoothness of the interpolation in the current cell C_i by the k^{th} interpolating function $p^{(k)}(x)$.

In other words, the smoothness β_i^k of a particular interpolating function $p^{(k)}(x)$ is the squared sum of the L^2-norms over the current cell C_i of its first n derivatives.

With this definition it is clear that functions with smaller derivatives will have smaller smoothness (given that smoother interpolations give smaller smoothness indicators, it is perhaps more accurate to call them roughness indicators). By comparing smoothness of each interpolation in the current cell, we can identify discontinuities by particularly large β_i^k.

In our case of a third order WENO scheme, the interpolating polynomials are all linear functions so all but then $r = 1$ derivative is 0. On a uniform grid, it is therefore very simple to evaluate the smoothness exactly in terms of the cell values; in this case it reduces very simply to

$$\beta_- = (p_i - p_{i-1})^2, \quad \beta_+ = (p_{i+1} - p_i)^2, \tag{3.49}$$

where the $\beta_\pm$ are the smoothness of the interpolation in stencil $S_{i\pm1/2}$ in the current cell. The smoothness indicators in this case are thus simply the squared differences.

With these smoothness indicators, Jiang and Shu (1996) then define the non-linear weights as

$$w_l = \frac{\tilde{w}_l}{\sum_{r=1}^{n} \tilde{w}_r}, \quad \text{with} \quad \tilde{w}_r = \frac{\gamma_r}{(\epsilon + \beta_r)^2}, \tag{3.50}$$

where $\epsilon > 0$ is a small number used to prevent the denominator from reaching 0 when $\beta_r = 0$. Generally this is chosen such that ϵ^2 is close to the numerical precision. Note that ϵ also serves as a minimum cut-off to the smoothness β_r; if $0 \leq \beta_r \ll \epsilon$ then these small smoothness values will effectively be ignored.

It is worth noting that it is not the absolute values of the β_r that matters, but rather their relative magnitudes to each other, since the non-linear weights only match the linear weights if all the smoothness scores β_r are equal. For our third order, two-stencil scheme then, the smoothness should have the following properties

1. $\beta_-/\beta_+ \to 0$ if the left stencil contains a discontinuity.
2. $\beta_+/\beta_- \to 0$ if the right stencil contains a discontinuity.
3. $\beta_-/\beta_+ \to 1$ if both stencils are smooth.

In most cases the non-linear weights w_l in Eq. (3.50) have the desired properties of reducing to 0 when containing a discontinuity, and approaching $w_l \to \gamma_l$ when both are smooth. However, there is a specific scenario in which the weights find smooth regions to be non-smooth: If the smooth region contains a critical point where the derivative of the variable being interpolated is zero, then the method only converges at second order.

This is because if there is no critical point in a given smooth stencil, then the smoothness is $\beta_r \sim \mathcal{O}(\Delta x)$, while if there is a critical point in the smooth stencil then the smoothness is $\beta_r \sim \mathcal{O}(\Delta x^2)$. So even if all the stencils are smooth, the smoothness of stencils containing the critical point converges to 0 faster than those that do not, and the result is these stencils appear smoother by this calculation, causing the scheme to neglect the other apparently less smooth stencils.

This issue was first recognised by Henrick *et al.* (2005). They also proposed a mapping method for fifth order WENO that preserves fifth order convergence even in the presence of critical points, by mapping the non-linear weights to new values. Unfortunately, this particular map is ineffective at avoiding the issue for third order WENO schemes.

Novel Smoothness Indicator

Several methods have been proposed to improve third order WENO. For instance, Don and Borges (2013) propose including a global smoothness indicator, which takes into account the overall smoothness over all three cells involved in each interpolation. The global smoothness $\tau = |\beta_- + \beta_+|$ is combined with the smoothness of the sub-stencils $\beta_\pm$ by altering Eq. (3.50) with

$$\tilde{w_r} = \gamma_r \left(1 + \frac{\tau}{\epsilon + \beta_r}\right), \tag{3.51}$$

to reduce dissipation.

To improve things further, Xiaoshuai and Yuxin (2015) suggest redefining this global smoothness to

$$\tau = \left| \frac{1}{2} \left(\beta_- + \beta_+ \right) - \beta_0 \right|, \tag{3.52}$$

where β_0 is the overall smoothness of the full 3-cell stencil as given by Eq. (3.48), and is therefore

$$\beta_0 = \frac{13}{12} \left(p_{i-1} - 2p_i + p_{i+1} \right) + \frac{1}{4} \left(p_{i-1} - p_{i+1} \right)^2 . \tag{3.53}$$

Xu and Wu (2018) suggest another redefinition of the global smoothness with the slightly simpler definition of

$$\tau = \left| \frac{1}{2} \left(\beta_- + \beta_+ \right) - \frac{1}{4} \left(p_{i-1} - p_{i+1} \right)^2 \right|, \tag{3.54}$$

and also suggest modifying Eqs. (3.50) and (3.51) further to

$$\tilde{w}_r = \gamma_r \left(1 + \frac{\tau}{\epsilon + \beta_r} + \lambda \frac{\beta_r + \epsilon}{\tau + \epsilon} \right), \tag{3.55}$$

where $\lambda = \Delta x^{1/6}$ if chosen for better results.

All of these methods show some improvements in the dissipation of the method, but none are able to deal with the issues near critical points. Although some methods do show promise in this regard (e.g. Ha *et al.* (2020)), for this thesis we opted for a novel method we developed that utilises an estimate of the magnitude of the interpolated variable to identify discontinuities, and thereby avoids reducing the order due to misidentified critical points. In the interest of simplicity, we will also not be using any of the above improved third order methods, although none are incompatible.

In order to prevent the reduction of order near critical points then, we propose the following novel adjustment to Eq. (3.48):

$$\beta_- = \left(u_i - u_{i-1} \right)^2 + AU_-^2 \Delta x^2 \quad \text{and} \quad \beta_+ = \left(u_{i+1} - u_i \right)^2 + AU_+^2 \Delta x^2, \tag{3.56}$$

where $U_\pm$ is the typical magnitude of the variable u over the stencils, for which we can use $U_-^2 = \left(u_i^2 + u_{i-1}^2 \right)/2$ and $U_+^2 = \left(u_{i+1}^2 + u_i^2 \right)/2$, and $A = 1/L^2$ where $L \gg \Delta x$ is the minimal length scale of a "smooth" solution. That is, the minimum width for what we can consider a smooth state of the system. For our numerical method the choice of $L = n_s \Delta x$ with $5 \leq n_s \leq 10$ works well. With this choice, the extra component of $AU_\pm^2 \Delta x^2$ becomes $U_\pm^2 / n_s^2$, so this component has no dependence on the grid spacing with this choice of L.

In smooth regions, we generally expect the magnitudes $U_\pm$ to dominate, so that

$$\left(u_{i+1} - u_i \right)^2 \approx \left(\frac{\partial u}{\partial x} \right)_i^2 \Delta x^2 \ll AU^2 \Delta x^2, \tag{3.57}$$

so with these new smoothness indicators and weights, unless the gradients $u_i - u_{i-1}$ or $u_{i+1} - u_i$ are large (suggesting the presence of a discontinuity), the $\beta_\pm$ will be dominated by the magnitude of the variables themselves. So we should have $\beta_-/\beta_+ \to 1$ in smooth regions, even if there is a critical point.

Meanwhile, in the presence of a discontinuity

$$(u_{i+1} - u_i)^2 \approx U^2 \gg \frac{U^2}{n_s^2} = AU^2\Delta x^2, \tag{3.58}$$

so the new terms are small, and the original smoothness indicators in Eq. (3.49) are recovered.

This method thus avoids the problems near critical points, without causing problems at discontinuities; this is of course with the sole exception of the case where the magnitude of the variables U is also small. That is, if the interpolated variable $u(x)$ happens to have a critical point where $u(x) = 0$ (i.e. a point $x = a$ where we have $u(a) = 0$ and $u'(a) = 0$). In this case, our assertion that the magnitudes $U_\pm$ will dominate is no longer valid, and Eq. (3.57) does not hold.

If this condition does not hold exactly then we expect that Eq. (3.57) will only hold at sufficiently small Δx. However, even if the condition need not be satisfied exactly, they are likely rare enough that they do not need to be dealt with. At the very least, these new smoothness indicators $\beta_\pm$ are clearly superior to the originals in Eq. (3.49) since those will also have the same problem.

The novel smoothness indicators in Eq. (3.56) can be inserted directly into Eq. (3.50) as a substitution for the original smoothness indicators of Eq. (3.49). With this adjustment, the third order interpolation is once again able to achieve third order convergence, even in the presence of critical points, besides the special case noted above.

Therefore, for all tests in chapters 4 and 5 we use a third-order WENO scheme using these novel smoothness indicators.

3.1.4 DER step

After reconstructing the variables at the boundaries and subsequently solving the Riemann problems at each boundary, we then have the exact values of the flux function at these boundaries $\boldsymbol{F}_{i+1/2}$. As noted previously, these values do not generally satisfy both Eqs. (3.17) and (3.18), at least for the case of a finite difference scheme. We can demonstrate this if we take a Taylor Series about x_i.

We can work with a single-equation PDE for simplicity

$$\frac{\partial q}{\partial t} + \frac{\partial f}{\partial x} = 0, \tag{3.59}$$

where the extension to systems of PDEs is the natural method, i.e. keeping each component of $\boldsymbol{Q}$ separate. Using the exact values at the boundaries, $f_{i+1/2}$, the finite difference approximation of the derivative is given by

$$\Delta x f'(x_i) \approx f_{i+1/2} - f_{i-1/2}, \tag{3.60}$$

where $f_{i+n/2}$ is the exact flux at $x = x_i + n\Delta x/2$. If we now take the Taylor series of $f(x)$ about x_i and insert $x = x_i \pm \Delta x/2$, then we obtain

$$f(x \pm \Delta x/2) = f_{i\pm 1/2} = f_i \pm \Delta x \frac{1}{2} f_i^{(1)} + \Delta x^2 \frac{1}{6} f_i^{(2)} \pm \Delta x^3 \frac{1}{24} f_i^{(3)} + \mathcal{O}\left(\Delta x^4\right), \tag{3.61}$$

where $f_i^{(k)}$ is the k^{th} derivative of $f(x)$ at x_i. Inserting into Eq. (3.60), we find

$$\Delta x f'(x_i) \approx \Delta x f_i^{(1)} + \Delta x^3 \frac{1}{12} f_i^{(3)} + \mathcal{O}\left(\Delta x^4\right). \tag{3.62}$$

Cancelling the first derivative from both sides, we find that the error of this approximation is $\frac{1}{12}\Delta x^3 f_i^{(3)} + \mathcal{O}(\Delta x^4)$, and therefore the approximation is only accurate up to second order. We thus need to calculate some $\hat{f}_{i+1/2}$ from these such that

$$\Delta x f'(x_i) \approx \hat{f}_{i+1/2} - \hat{f}_{i-1/2}, \tag{3.63}$$

is at least third order accurate; that is, the $\hat{f}_{i+1/2}$ satisfy Eq. (3.18).

In Del Zanna *et al.* (2007), they begin with a finite difference approximation of the derivative

$$\Delta x f'(x_i) \approx \hat{f}_{i+1/2} - \hat{f}_{i-1/2} = a\left(f_{i+1/2} - f_{i-1/2}\right) + b\left(f_{i+3/2} - f_{i-3/2}\right), \tag{3.64}$$

here based on a 4-point stencil. If we once again take the Taylor series of $f(x)$ about x_i and insert all the points

$$x = x_i - \frac{3}{2}\Delta x, \quad x = x_i - \frac{1}{2}\Delta x, \quad x = x_i + \frac{1}{2}\Delta x, \quad x = x_i + \frac{3}{2}\Delta x,$$

then after substituting for the $f_{i\pm 1/2}$ and $f_{i\pm 3/2}$ and collecting terms we get

$$\Delta x f_i^{(1)} = \sum_{k=0}^{\infty} f_i^{(k)} \frac{\Delta x^k}{k! 2^k} \left(1 - (-1)^k\right)\left(a + 3^k b\right) + \mathcal{O}\left(\Delta x^5\right). \tag{3.65}$$

Clearly the terms with even k cancel. In order to match the left hand side, we require a pair of values a and b such that the coefficient of the Δx term is 1, and the Δx^3 term is eliminated. After expanding, these conditions become

$$a + 3b = 1 \quad \text{and} \quad a + 27b = 0, \tag{3.66}$$

and it is easy to find that the solution to these equations is $a = 9/8$ and $b = -1/24$.

With these values of a and b we can calculate $\Delta x f'(x_i)$ directly from the $f_{i+1/2}$ etc. using Eq. (3.64). However, we require the values of the $\hat{f}_{i\pm1/2}$ specifically, so that we can share these fluxes between neighbouring cells and thus maintain conservation. So now we write

$$\begin{aligned} \hat{f}_{i+1/2} &= d_0 f_{i+1/2} + d_1 \left(f_{i-1/2} + f_{i+3/2}\right), \\ \hat{f}_{i-1/2} &= d_0 f_{i-1/2} + d_1 \left(f_{i+1/2} + f_{i-3/2}\right), \end{aligned} \tag{3.67}$$

and comparison with the values of a and b in Eq. (3.64) above tells us that we have $d_0 = 13/12$ and $d_1 = -1/24$. Using these values we can now derive the $\hat{f}_{i\pm1/2}$ and hence obtain a higher-order method.

Note that we could alternatively interpret this as a correction to the original flux $f_{i\pm1/2}$ by

$$\begin{aligned} \hat{f}_{i+1/2} &= f_{i+1/2} - \frac{1}{24}\left(f_{i-1/2} - 2f_{i+1/2} + f_{i-3/2}\right), \\ \hat{f}_{i-1/2} &= f_{i-1/2} - \frac{1}{24}\left(f_{i-3/2} - 2f_{i-1/2} + f_{i+1/2}\right), \end{aligned} \tag{3.68}$$

where we can identify the components in brackets as an estimate of the second derivative at that point. Indeed, Jiang and Shu (1996) give an alternative view of the DER correction as

$$\hat{f}_{i\pm1/2} = f_{i\pm1/2} + \sum_{k=1}^{m-1} a_{2k} \Delta x^{2k} f^{(2k)}_{i\pm1/2} + \mathcal{O}\left(\Delta x^{2m+1}\right), \tag{3.69}$$

making the DER correction a correction based on the even derivatives of $f(x)$. We could therefore potentially apply the DER step using a different approximation for the second derivative. In our case, $m = 2$ and so only the second derivative $f^{(2)}(x)$ is needed, which we calculate based on a centred, symmetric stencil.

The corrections given in Eq. (3.68) are quite small (being only of order Δx^2), so the oscillations induced by this correction are likely to be quite small. For this reason, Del Zanna *et al.* (2007) did not use a more costly WENO method (or otherwise), since this would seem unlikely to confer much benefit.

However, it is not impossible to conceive of a scenario in which this would cause problems. Consider a sharp, strong discontinuity in a conserved variable that on at least one side of the discontinuity is close to the limit of physical values. For instance, in RMHD we could have a value of the conserved energy from Eq. (2.34) that is very close to zero on one side of the discontinuity, next to a much larger value on the other side. Such a scenario is very common in — for instance — a fast shock spread over very few cells.

In this scenario, the flux in the interior of the shock could be of comparable value to that of the larger value of the conserved variable, and therefore potentially orders of magnitude larger than the smaller value. Thus any oscillations induced by using this central stencil may be enough to push the energy into the negatives and therefore break the simulation, despite the fact that the oscillations would be quite small. Indeed, in practice we have observed this very phenomenon when using initial conditions that are too sharp. Since we desire sharper discontinuities, it may be advantageous to use a method of some description to allow the model to handle these sharp discontinuities.

Since this is another case of an interpolation scheme having difficulty near discontinuities, it is tempting to try another WENO method. However, given that the oscillations are already small, problems with the DER method tend to only manifest like the suggested case above with the system being pushed out of the set of physical states. Given how close the system already is to failing in these cases, we have found in practice that implementing a non-oscillatory method like WENO does not help prevent these problems.

Instead, the only way we have found to prevent failure in those cases is to forgo the DER step entirely, and simply use the fluxes $f_{i\pm 1/2}$ prior to correction. This of course causes the code to reduce to third order, but ideally this would only be done in specific cases, when necessary.

With that said, we have also found other ways of preventing these failure cases by altering other parts of the code. As such, in all tests in chapters 4 and 5 (except where stated otherwise) we use the normal DER step in all cases with a central, symmetric stencil and do not skip it.

3.1.5 Runge-Kutta Methods

With the previous steps of reconstruction, Riemann solver and DER we have constructed inter-cell fluxes that we can insert into the semi-discrete system Eq. (3.16). Thus our system of partial differential equations has now become a system of ODEs for time integration, of the form

$$\frac{d\boldsymbol{Q}}{dt} = \boldsymbol{\mathcal{L}}(\boldsymbol{Q})\,, \tag{3.70}$$

where $\boldsymbol{Q}$ is the vector of conserved variables, and $\boldsymbol{\mathcal{L}}(\boldsymbol{Q})$ is a vector-valued differential operator which outputs the corresponding flux gradients (with an extra minus sign as we have moved this term to the other side of the equation). In other words, $\boldsymbol{\mathcal{L}}(\boldsymbol{Q})$ is an operator representing the previous three steps, which takes as an input a state $\boldsymbol{Q}$ and outputs an approximation to the flux gradient (or gradients, in the multidimensional case) of this state.

We thus now need a method of time integration. The most basic such method is the Euler method, which simply uses the gradient of $\boldsymbol{Q}$ at the beginning of the time step over the full time step. In other words, it uses a linear approximation of the solution, so the solution at the next step is

$$\boldsymbol{Q}_{n+1} = \boldsymbol{Q}_n + \Delta t \boldsymbol{\mathcal{L}}(\boldsymbol{Q}_n)\,. \tag{3.71}$$

However, this method is first order in time (i.e. the truncation error is $\mathcal{E}_T \sim \mathcal{O}(\Delta t)$), and as such it is quite inaccurate.

The CFL condition Eq. (3.15) means that Δt is proportional to Δx, provided we keep the C_u constant. Since the truncation error of the numerical scheme is $\mathcal{E}_T \sim \mathcal{O}(\Delta x^n) + \mathcal{O}(\Delta t^m)$, this error is dominated by the spatial error if $n < m$ and time stepping error if $n > m$, for sufficiently small Δx and Δt. Thus the higher order reconstruction scheme and DER step detailed above are not especially useful unless we also use a higher order time integration scheme.

There are different ways of creating a higher order time integration method, but the method we chose is an explicit Runge-Kutta method. The "explicit" term means that each step in the integration method only depends on currently known values, unlike implicit schemes where the next state can also be dependent on itself.

For instance, the simplest implicit method is the backwards Euler method; in this case (in contrast the to the Euler method) this method uses the gradient at the end of the time step. Thus for our system, the next time step as given by the backward Euler method is

$$\boldsymbol{Q}_{n+1} = \boldsymbol{Q}_n + \Delta t \boldsymbol{\mathcal{L}}(\boldsymbol{Q}_{n+1})\,. \tag{3.72}$$

Since the next step $\boldsymbol{Q}_{n+1}$ depends on itself, it is defined implicitly. This method is still first order, but it is more stable and in the case of FV/CFD methods it allows the CFL condition to be relaxed. However, calculating the next step is significantly more complex in both computation and implementation, since it requires more than just calculating the flux gradients $\boldsymbol{\mathcal{L}}$ at a given time step.

Thus most RMHD schemes use explicit time integration — although some schemes use implicit integration for just the source terms, as these terms can be stiff such as with resistive plasmas. This kind of mixed scheme is known as an implicit-explicit (IMEX) scheme, and has been used in some RMHD codes, such as Palenzuela *et al.* (2009); Ripperda *et al.* (2019). In our case, the only source terms we have can be solved analytically, so this is unnecessary.

For both the second order and third order code we used an explicit Runge-Kutta method of the respective order. For an explicit Runge-Kutta method, the solution for the next time step is then given by

$$\boldsymbol{Q}_{n+1} = \boldsymbol{Q}_n + \Delta t \sum_{i=1}^{s} b_i \boldsymbol{K}_i, \tag{3.73}$$

where

$$\boldsymbol{K}_i = \boldsymbol{\mathcal{L}}(\boldsymbol{S}_i)\,, \quad \text{and} \quad \boldsymbol{S}_i = \boldsymbol{Q}_n + \Delta t \sum_{j=1}^{i-1} a_{ij}\boldsymbol{K}_j. \tag{3.74}$$

Essentially, we step to various sub-steps $\boldsymbol{S}_i$ by a weighted sum of the currently known gradients $\boldsymbol{K}_i$. At these sub-steps, we calculate the gradient $\boldsymbol{K}_i$ via the operator $\boldsymbol{\mathcal{L}}(\boldsymbol{S}_i)$, then use this new gradient together with those of previous sub-steps in a weighted sum to step forward again to another point. Finally, we use all s of these known gradients to step forward the full step by Eq. (3.73).

The b_i are the weights of the gradients $\boldsymbol{K}_i$ for the full time step, and the a_{ij} are the weights of each gradient $\boldsymbol{K}_j$ for the i^{th} sub-step. It is easy to see why this could achieve a more accurate integration; by using the gradients from other points in the time step we get a better approximation for the true gradient from start to end of the time step. The values of these parameters are key to RK methods; various conditions are needed to make the method truly higher order. Even so, there is generally a lot of freedom in choosing these parameters exact values, and thus many different RK schemes we can choose from, even for the same order.

Generally speaking, RK methods need at least n sub-steps to achieve an n^{th} order code (Ascher and Petzold, 1998). It is therefore desirable to minimise the order of the method at at most the order of the spatial discretisation, to minimise wasteful calculations.

For our second order code, we used the second order midpoint method (Ascher and Petzold, 1998). In this case there is a single sub-step so that $s = 2$, and we have

$$\begin{aligned} \boldsymbol{K}_1 &= \boldsymbol{\mathcal{L}}(\boldsymbol{Q}_n)\,, \\ \boldsymbol{K}_2 &= \boldsymbol{\mathcal{L}}\Big(\boldsymbol{Q}_n + \frac{1}{2}\Delta t \boldsymbol{K}_j\Big)\,, \end{aligned} \tag{3.75}$$

so that $\boldsymbol{K}1$ is the gradient at the initial state t_n, and using $\boldsymbol{K}_1$ to reach the estimate of $\boldsymbol{Q}$ we have $\boldsymbol{K}_2$ as the gradient at the midpoint. With this, the full step is then

$$\boldsymbol{Q}_{n+1} = \boldsymbol{Q}_n + \Delta t \boldsymbol{K}_2, \tag{3.76}$$

so we simply use the gradient at the midpoint.

Meanwhile, for our third order code, we used Kutta's third order method (Ascher and Petzold, 1998), so we have

$$\begin{aligned} \boldsymbol{K}_1 &= \boldsymbol{\mathcal{L}}(\boldsymbol{Q}_n)\,, \\ \boldsymbol{K}_2 &= \boldsymbol{\mathcal{L}}\Big(\boldsymbol{Q}_n + \frac{1}{2}\Delta t \boldsymbol{K}_j\Big)\,, \\ \boldsymbol{K}_3 &= \boldsymbol{\mathcal{L}}(\boldsymbol{Q}_n + \Delta t\,(2\boldsymbol{K}_2 - \boldsymbol{K}_1))\,. \end{aligned} \tag{3.77}$$

Here $\boldsymbol{K}_1$ and $\boldsymbol{K}_2$ are the same as before, while $\boldsymbol{K}_3$ is an estimate for the gradient at the end point using the two previous $\boldsymbol{K}_1$ and $\boldsymbol{K}_2$. With these, we can calculate the full time

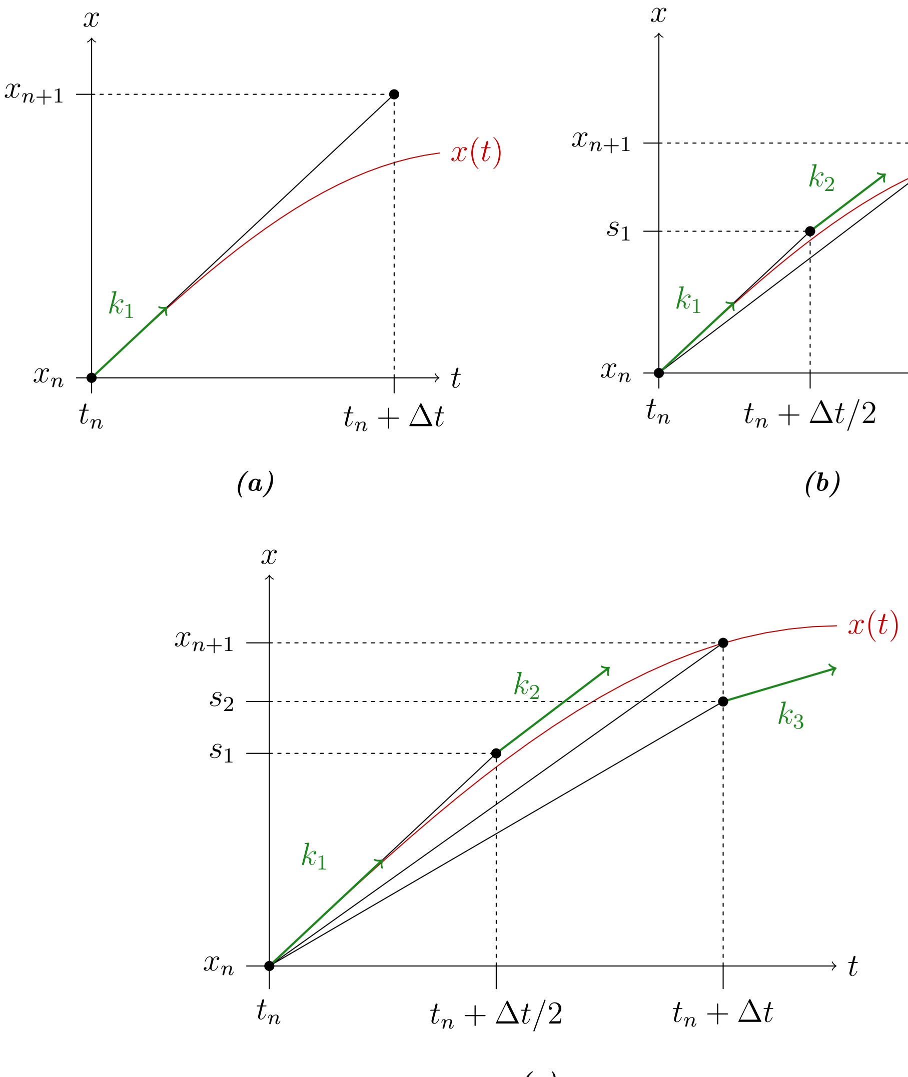

(a) ***(b)***

(c)

Figure 3.10: *Diagrams of Runge-Kutta stepping for the differential equation Eq.* (3.79) *with exact solution $x(t)$ via the Euler method (a), midpoint method (b) and Kutta's third order method (c). The initial state is $x = x_n$ at time $t = t_n$, the state after the time step Δt is x_{n+1}, the $x = s_i$ are the mid-steps and the k_i are the gradients as calculated at the s_i. There is a clear improvement in accuracy as the order is increased.*

step as

$$\boldsymbol{Q}_{n+1} = \boldsymbol{Q}_n + \Delta t \left(\frac{1}{6}\boldsymbol{K}_1 + \frac{2}{3}\boldsymbol{K}_2 + \frac{1}{6}\boldsymbol{K}_3 \right) = \boldsymbol{Q}_n + \frac{1}{6}\Delta t \left(\boldsymbol{K}_1 + 4\boldsymbol{K}_2 + \boldsymbol{K}_3 \right), \qquad (3.78)$$

so this time we have a weighted average, biased towards the midpoint estimate. Since this method requires an extra time step, it is slower to evaluate than the second order method.

Diagrams for the Euler method, midpoint method and our third order method can be seen in Fig. 3.10, for the scalar differential equation

$$\frac{dx}{dt} = f(x, t)\,. \qquad (3.79)$$

As we can see from this example, the third order method is significantly more accurate than the midpoint method, which is itself more accurate than the Euler method.

3.2 Novel Operator Splitting Method

High-Magnetisation RMHD

As we have noted previously, conservative numerical methods like the one described in section 3.1 are known to work for RMHD only so long as $\sigma = \left(B^2 - E^2\right)/w$ is small, so that the electromagnetic terms are relatively small. These methods can have difficulties even for relatively small values of $\sigma \sim \mathcal{O}(1)$. Dealing with this problem is the main crux of this thesis, but first we must seek a better understanding of the cause of this issue.

These problems have the form of large errors for the recovered key (primitive) parameters of plasma, e.g. its thermodynamic pressure and Lorentz factor, and ultimately the non-existence of physically meaningful values for such parameters consistent with the computed conserved quantities, such as mass, energy and momentum densities.

The fact that the equations of FFDE are degenerate (Komissarov, 2002) indicates that the system of RMHD should be *close* to degenerate for high-magnetisation flows. That is, with $\sigma \gg 1$ the energy (Eq. (2.34)) and momentum (Eq. (2.35)) conservation laws of RMHD should be close to linearly dependent. It has been suggested previously in Komissarov (2006) that this may be the fundamental cause behind the problems with conservative RMHD codes.

In the limit of high σ, the vector $\nabla_\alpha T^{\alpha\beta}$ should be restricted to a two dimensional plane as shown by Komissarov (2002) and reiterated in section 2.2.1. When σ is large but finite in RMHD, $\nabla_\alpha T^{\alpha\beta}$ is not restricted to a plane, but it should be close to a force-free configuration.

That is, if the vector $\nabla_\alpha T^{\alpha\beta}$ is far from this plane, then σ cannot be small, and the reverse is also true so that σ large implies that the vector must be close to the plane. Thus at high σ this vector is restricted in the value it can take, and so the range of physically realistic values for the conservative variables at the given magnetisation shrinks.

During the computation of the model, the computed values for the conservative variables in each iteration will incur some numerical and truncation error. Because the range of $\nabla_\alpha T^{\alpha\beta}$ for the given magnetisation has become quite small, this error can easily push the vector $\nabla_\alpha T^{\alpha\beta}$ into a range inconsistent with the given magnetisation. In this state, there may be no physically meaningful values for the gas pressure, density or Lorentz factor consistent with the given conservative variables, since the required values may be negative, or greater than 1 (for the Lorentz factor). Thus the numerical method fails in this instance.

In other words, since a force-free component of $\nabla_\alpha T^{\alpha\beta}$ is restricted to a 2D plane, any deviation from this restriction must be dealt with by a component that is not force-free, i.e. inertial terms such as density and gas pressure. But these terms should be $\mathcal{O}(\sigma^{-1})$, and so as σ increases the ability of these terms to deal with such deviation diminishes.

Operator Splitting

Now that we have an understanding of the numerical methods we will use, we can move on to the new method of modelling RMHD presented in this thesis, a kind of operator splitting method. The objective is to adapt an asymptotic method, and separate the RMHD system into two components: One of order $\sim \mathcal{O}(1)$, and one of order $\sim \mathcal{O}(\sigma^{-1})$.

To this end, we take Eq. (3.70) and we now split $\boldsymbol{Q}$ into $\boldsymbol{Q} = \boldsymbol{Q}_0 + \boldsymbol{Q}_1$, with $\boldsymbol{Q}_0 \sim \mathcal{O}(1)$ and $\boldsymbol{Q}_1 \sim \mathcal{O}(\sigma^{-1})$. Thus Eq. (3.70) splits into the two sub-equations

$$\frac{\partial \boldsymbol{Q}_0}{\partial t} + \boldsymbol{\mathcal{L}}_0(\boldsymbol{Q}_0, \boldsymbol{Q}_1) = 0, \tag{3.80}$$

$$\frac{\partial \boldsymbol{Q}_1}{\partial t} + \boldsymbol{\mathcal{L}}_1(\boldsymbol{Q}_0, \boldsymbol{Q}_1) = 0. \tag{3.81}$$

Thus the $\boldsymbol{Q}_0$ and $\boldsymbol{Q}_1$ individually satisfy their own conservation laws but are coupled to each other (although we will split the equations such that the operator $\boldsymbol{\mathcal{L}}_0$ does not depend on $\boldsymbol{Q}_1$). We can therefore step forward Eq. (3.70) in time by stepping forward Eqs. (3.80) and (3.81) separately.

RMHD

If we recall from the chapter 2, for the evolution equations for RMHD after special relativistic splitting, we have Eq. (2.29) which governs mass conservation

$$\partial_t\Big(\rho u^0\Big) + \boldsymbol{\nabla}\cdot(\rho\boldsymbol{u}) = 0,$$

Eq. (2.35) which governs momentum conservation

$$\partial_t\Big(wu^0\boldsymbol{u} + \boldsymbol{E}\times\boldsymbol{B}\Big) + \boldsymbol{\nabla}\cdot\left(w\boldsymbol{u}\boldsymbol{u} - \boldsymbol{E}\boldsymbol{E} - \boldsymbol{B}\boldsymbol{B} + \left(p_g + \frac{1}{2}\Big(E^2 + B^2\Big)\right)\delta^{ij}\right) = 0,$$

Eq. (2.34) which governs energy conservation

$$\partial_t\left(wu^0u^0 - p_g + \frac{1}{2}\Big(E^2 + B^2\Big)\right) + \boldsymbol{\nabla}\cdot\Big(wu^0\boldsymbol{u} + \boldsymbol{E}\times\boldsymbol{B}\Big) = 0,$$

and Eq. (2.38) which is simply Faraday's law

$$\partial_t\boldsymbol{B} - \boldsymbol{\nabla}\times\boldsymbol{E} = 0.$$

In addition to these, we have two constraint equations: Eq. (2.37), the divergence-free constraint of $\boldsymbol{B}$

$$\boldsymbol{\nabla} \cdot \boldsymbol{B} = 0,$$

and Eq. (2.42), the perfect conductivity condition

$$\boldsymbol{E} = -\boldsymbol{v} \times \boldsymbol{B},$$

which allows us to eliminate the electric field $\boldsymbol{E}$ from the other equations.

First, we split the magnetic and electric fields into

$$\boldsymbol{B} = \boldsymbol{B}_0 + \boldsymbol{B}_1, \quad \boldsymbol{E} = \boldsymbol{E}_0 + \boldsymbol{E}_1, \tag{3.82}$$

where $\boldsymbol{B}_0, \boldsymbol{E}_0 \sim \mathcal{O}(1)$ and $\boldsymbol{B}_1, \boldsymbol{E}_1 \sim \mathcal{O}(\sigma^{-1})$, and we also assume the inertial components $\boldsymbol{u}, p_g, \rho, w \sim \mathcal{O}(\sigma^{-1})$ — so we have split the magnetic and electric fields into components of order 1 and components of the same order as the inertial components.

With this splitting, with $\sigma \ll 1$ we have $B_0^2 \ll B_1^2$ and $E_0^2 \ll E_1^2$ so the 0-components are small. With $\sigma \gg 1$, we have $B_0^2 \gg B_1^2$ and $E_0^2 \gg E_1^2$ so we have the reverse with the 1-components small instead.

Substituting these definitions into the equations of RMHD above, we can then separate the equations into two components: $\mathcal{O}(1)$ parts consisting of $\boldsymbol{B}_0$ and $\boldsymbol{E}_0$, and the remaining components which will all be $\mathcal{O}(\sigma^{-1})$.

3.2.1 Force-Free Operator

For the $\mathcal{O}(1)$ components, mass conservation does not appear, and for the remainder we have momentum conservation

$$\partial_t(\boldsymbol{E}_0 \times \boldsymbol{B}_0) + \boldsymbol{\nabla} \cdot \left(-\boldsymbol{E}_0\boldsymbol{E}_0 - \boldsymbol{B}_0\boldsymbol{B}_0 + \frac{1}{2}\left(E_0^2 + B_0^2\right)\delta^{ij}\right) = 0, \tag{3.83}$$

energy conservation

$$\partial_t\left(\frac{1}{2}\left(E_0^2 + B_0^2\right)\right) + \boldsymbol{\nabla} \cdot (\boldsymbol{E}_0 \times \boldsymbol{B}_0) = 0, \tag{3.84}$$

and Faraday's law again

$$\partial_t \boldsymbol{B}_0 - \boldsymbol{\nabla} \times \boldsymbol{E}_0 = 0. \tag{3.85}$$

Meanwhile the constraints are

$$\boldsymbol{\nabla} \cdot \boldsymbol{B}_0 = 0, \tag{3.86}$$

and

$$\boldsymbol{E}_0 = -\boldsymbol{v} \times \boldsymbol{B}_0. \tag{3.87}$$

Given that this is derived in an identical manner, there should be little surprise that the equations are the same as that of FFDE. The second constraint of Eq. (3.87) is special since $\boldsymbol{v}$ does not appear elsewhere in these equations; in order to close this system we can use the same adjustments as with FFDE and instead impose

$$\boldsymbol{B}_0 \cdot \boldsymbol{E}_0 = 0, \tag{3.88}$$

and

$$B_0^2 - E_0^2 > 0. \tag{3.89}$$

Since this system is just FFDE, we can treat these equations in exactly the same manner as we would any other FFDE method. We therefore choose to refer to this part of the split operator as the force-free operator.

The fact that this system is simply FFDE also allows us to use integration schemes created by other authors for this system. For example, in section 2.2 we derived an alternate system of equations for FFDE which act directly on the $\boldsymbol{B}_0$ and $\boldsymbol{E}_0$. However, for this thesis we simply used the system as above, Eqs. (3.83) to (3.86), (3.88) and (3.89).

The force-free system corresponds to the $\boldsymbol{\mathcal{L}}_0$ operator from Eq. (3.80). As noted above, our splitting has eliminated the $\boldsymbol{Q}_1$ terms from this operator.

Conservation

In section 2.2.1, we noted that the conservation equations of FFDE are not independent of each other, so we have an overdetermined system with seven conservation equations with just four independent equations.

Analytically there is no issue here. We simply have several equations we can choose from that are all satisfied, and we can drop any equations we like. Numerically, however, the situation is more problematic.

We have previously described our integration scheme, a conservation scheme, meaning that it maintains conservation of the conserved variables to machine precision. This is useful for the accurate modelling of discontinuous solutions. For RMHD, this means maintaining conservation of mass, energy, momentum and Faraday's law. Our splitting scheme should ideally maintain this property as well.

Unfortunately, the loss of independence makes this difficult. Our integration scheme will update all seven of the conserved variables with fluxes consistent with neighbouring cells to keep the variables conserved. However, generally speaking they will not be consistent with each other. Truncation error in the integration scheme means that the values no longer agree with each other.

For instance, in the force-free operator we have the conserved quantity $\boldsymbol{B}_0$ and the conserved quantity $\boldsymbol{S}_0 = \boldsymbol{E}_0 \times \boldsymbol{B}_0$. Given their definitions, these variables must obviously satisfy $\boldsymbol{B}_0 \cdot \boldsymbol{S}_0 = 0$, since one is the cross product of the other with another vector.

But after stepping forward the integration scheme by a time step, we get new states for the variables $\hat{\boldsymbol{B}}_0$ and $\hat{\boldsymbol{S}}_0$. While these variables will all be conserved independently due to the integration scheme, they will not generally satisfy the condition $\hat{\boldsymbol{B}}_0 \cdot \hat{\boldsymbol{S}}_0 = 0$, due to the truncation error in the integration scheme. It would therefore be impossible to find an $\boldsymbol{E}_0$ for which $\boldsymbol{S}_0 = \boldsymbol{E}_0 \times \boldsymbol{B}_0$, and the same applies to the conserved force-free energy $\frac{1}{2}\left(B_0^2 + E_0^2\right)$ (McKinney, 2006).

This leaves us with a significant problem, since it means we cannot maintain conservation for all seven variables *and* keep the variables consistent with each other. Outside of some unknown, clever integration scheme/correction we have no choice but to either allow conservation for (at least) some of the conserved variables to be only maintained to truncation error, or we allow the conditions to be violated.

We therefore concluded that allowing conservation to be relaxed a little was the better option. The result is that despite the integration scheme being a conservative method, the conservation is not maintained to machine precision but to truncation error. Thus the scheme is now highly dependent on the accuracy of the integration scheme, and so it is highly desirable to reduce truncation error as much as possible, via the higher order spatial and time integration schemes discussed previously. Unfortunately, the spatial interpolation must reduce in order near discontinuities, and will generally also reduce in order near strong gradients as well, since the algorithm cannot tell the difference. As such, cases with large gradients or discontinuities will see more error in the conservation of energy and momentum over time.

3.2.2 Interaction Operator

We can now collect the remaining terms in the total RMHD operator into another operator. These terms include terms of order $\sim \mathcal{O}\left(\sigma^{-1}\right)$ as well as those of order $\sim \mathcal{O}\left(\sigma^{-2}\right)$. We keep these terms so that the overall system of the force-free operator $\boldsymbol{\mathcal{L}}_0$ together with this operator $\boldsymbol{\mathcal{L}}_1$ does not drop any terms of RMHD, so these operators together match RMHD exactly.

Since these terms describe the interaction between the inertial terms and the electromagnetic fields, we will call this operator the Interaction operator.

For these equations we retain the entirety of mass conservation

$$\partial_t\left(\rho u^0\right) + \boldsymbol{\nabla} \cdot (\rho \boldsymbol{u}) = 0, \tag{3.90}$$

since it does not appear at all in the force-free operator. For momentum conservation, the remainder of this equation is

$$\partial_t\Big(wu^0\boldsymbol{u}+\boldsymbol{E}_0\times\boldsymbol{B}_1+\boldsymbol{E}_1\times\boldsymbol{B}_0+\boldsymbol{E}_1\times\boldsymbol{B}_1\Big)+\boldsymbol{\nabla}\cdot\Big(w\boldsymbol{u}\boldsymbol{u}-\boldsymbol{E}_0\boldsymbol{E}_1-\boldsymbol{E}_1\boldsymbol{E}_0-\boldsymbol{E}_1\boldsymbol{E}_1$$
$$-\boldsymbol{B}_0\boldsymbol{B}_1-\boldsymbol{B}_1\boldsymbol{B}_0-\boldsymbol{B}_1\boldsymbol{B}_1+\Big(p_g+\boldsymbol{E}_0\cdot\boldsymbol{E}_1+\boldsymbol{B}_0\cdot\boldsymbol{B}_1+\frac{1}{2}\Big(E_1^2+B_1^2\Big)\Big)\,\delta^{ij}\Big)=0, \quad (3.91)$$

while for energy conservation what remains is

$$\partial_t\Big(wu^0u^0-p_g+\boldsymbol{E}_0\cdot\boldsymbol{E}_1+\boldsymbol{B}_0\cdot\boldsymbol{B}_1+\frac{1}{2}\Big(E_1^2+B_1^2\Big)\Big)$$
$$+\boldsymbol{\nabla}\cdot\Big(wu^0\boldsymbol{u}+\boldsymbol{E}_0\times\boldsymbol{B}_1+\boldsymbol{E}_1\times\boldsymbol{B}_0+\boldsymbol{E}_1\times\boldsymbol{B}_1\Big)=0, \quad (3.92)$$

and finally Faraday's law takes on the simple form

$$\partial_t\boldsymbol{B}_1-\boldsymbol{\nabla}\times\boldsymbol{E}_1=0. \quad (3.93)$$

For the constraints, the divergence-free constraint is simply

$$\boldsymbol{\nabla}\cdot\boldsymbol{B}_1=0, \quad (3.94)$$

but we need to be more careful with the perfect conductivity condition.

In the force-free operator we had to alter the PC equation to deal with $\boldsymbol{E}_0$ instead of $\boldsymbol{v}$. Ideally, we would have split the PC condition with $\boldsymbol{v}=\boldsymbol{v}_0+\boldsymbol{v}_1$ so that

$$\boldsymbol{E}_0=-\boldsymbol{v}_0\times\boldsymbol{B}_0 \quad \text{and} \quad \boldsymbol{E}_1=-\boldsymbol{v}_0\times\boldsymbol{B}_1-\boldsymbol{v}_1\times\boldsymbol{B}_0-\boldsymbol{v}_1\times\boldsymbol{B}_1. \quad (3.95)$$

However, we had to alter the PC condition into $\boldsymbol{B}_0\cdot\boldsymbol{E}_0=0$ for the force-free operator since $\boldsymbol{v}$ does not appear. While this altered constraint guarantees that a $\boldsymbol{v}$ that satisfies $\boldsymbol{E}_0=-\boldsymbol{v}\times\boldsymbol{B}_0$ does exist, this $\boldsymbol{v}$ is not unique as adding an arbitrary component parallel to $\boldsymbol{B}_0$ also satisfies condition.

Generally speaking $\boldsymbol{B}_1$ will not be parallel to $\boldsymbol{B}_0$, so this lack of knowledge about $\boldsymbol{v}_0$ makes Eq. (3.95) unsuitable. We could technically split $\boldsymbol{v}$ further into

$$\boldsymbol{v}=\boldsymbol{v}_0+s\boldsymbol{B}_0+\boldsymbol{v}_1,$$

where $\boldsymbol{v}_0=\left(\boldsymbol{E}_0\times\boldsymbol{B}_0\right)/B^2$, i.e. the drift velocity, $s\boldsymbol{B}_0\sim\mathcal{O}(1)$ and $\boldsymbol{v}_1\sim\mathcal{O}(\sigma^{-1})$. But this is becoming excessively complicated and would make calculating primitives from conservatives even more cumbersome.

Instead of splitting, we can simply keep the PC condition complete as is, which allows us to rearrange as

$$\boldsymbol{E}_1=-\left(\boldsymbol{E}_0+\boldsymbol{v}\times\boldsymbol{B}_0\right)-\boldsymbol{v}\times\boldsymbol{B}_1. \quad (3.96)$$

Note how the bracket $(\boldsymbol{E}_0+\boldsymbol{v}\times\boldsymbol{B}_0)$ should be $\sim\mathcal{O}(\sigma^{-1})$ to match the order of the remaining components, but both components are actually $\sim\mathcal{O}(1)$. This is a reflection of the fact that for large σ we expect $\boldsymbol{v}$ to be close to the drift velocity that makes this bracket equal to 0, besides a component parallel to $\boldsymbol{B}_0$ which leaves it unchanged. If σ is large this could cause a problem, since $\boldsymbol{E}_1$ depends on the small difference between two relatively large values. In practice this has not caused a noticeable issue however, since σ would need to be very large to cause an appreciable numerical error.

3.2.3 Overall Method

In the course of a single time step of this method, we first step forward the force-free system of Eq. (3.80)

$$\frac{\partial \boldsymbol{Q}_0}{\partial t} + \boldsymbol{\mathcal{L}}_0(\boldsymbol{Q}_0) = 0,$$

where we have dropped the $\boldsymbol{Q}_1$-dependence from the operator $\boldsymbol{\mathcal{L}}_0$.

We start with the force-free system because it is not dependent on $\boldsymbol{Q}_1$. We can therefore calculate fluxes and primitive variables $\boldsymbol{P}_0$ without needing these variables, and we can step forward this system completely independently.

After stepping forward the force-free operator, we then step the interaction system of Eq. (3.81)

$$\frac{\partial \boldsymbol{Q}_1}{\partial t} + \boldsymbol{\mathcal{L}}_1(\boldsymbol{Q}_0, \boldsymbol{Q}_1) = 0,$$

using the $\boldsymbol{Q}_0$ at the start of the time step to calculate the fluxes, and then the $\boldsymbol{Q}_0$ at the end of the time step to calculate the $\boldsymbol{P}_1$ at this time, using a variable conversion algorithm.

To be precise: The operator $\boldsymbol{\mathcal{L}}_1(\boldsymbol{Q}_0, \boldsymbol{Q}_1)$ is used to calculate the flux gradients of the interaction fluxes. These fluxes are calculated from the $\boldsymbol{Q}_0^n$ and $\boldsymbol{Q}_1^n$, i.e. the state at the initial point of the time step.

This is used to update the $\boldsymbol{Q}_1^n$ by a time step. At this time we first calculate the force-free primitives $\boldsymbol{P}_0^{n+1}$ from the $\boldsymbol{Q}_0^{n+1}$. Then we calculate the interaction primitives $\boldsymbol{P}_1^{n+1}$ from the $\boldsymbol{Q}_1^{n+1}$ and the $\boldsymbol{P}_0^{n+1}$.

So far, the force-free system is completely unaffected by the interaction system. We know that the force-free system has issues with cases like current sheets, so we must do something about this. Moreover, if we leave them alone then $\boldsymbol{B}_1$ and $\boldsymbol{E}_1$ could potentially grow until they break the $\mathcal{O}(\sigma^{-1})$ condition, making the operator splitting method a meaningless alteration.

The solution to this is quite simple: at the end of each time step, we recombine the $\boldsymbol{B}_0$ and $\boldsymbol{B}_1$ as well as the $\boldsymbol{E}_0$ and $\boldsymbol{E}_1$, and set $\boldsymbol{B}_0$ and $\boldsymbol{E}_0$ to their totals. That is, at the end of each time step, we set

$$\boldsymbol{B}_0 = \boldsymbol{B}_0 + \boldsymbol{B}_1 \quad \text{and} \quad \boldsymbol{B}_1 = 0, \tag{3.97}$$

$$\boldsymbol{E}_0 = \boldsymbol{E}_0 + \boldsymbol{E}_1 \quad \text{and} \quad \boldsymbol{E}_1 = 0, \tag{3.98}$$

so we set the force-free magnetic field equal to the total magnetic field, and the same with the electric field. Since $\boldsymbol{B}_1$ and $\boldsymbol{E}_1$ start the time step at 0 and end it at order $\mathcal{O}(\sigma^{-1})$, this automatically enforces $\boldsymbol{B}_1, \boldsymbol{E}_1 \sim \mathcal{O}(\sigma^{-1})$, and this also allows the interaction system to affect the force-free system.

For first order in time this is a complete time step. But at higher order in time, things are more complicated. We are using an RK method to increase the time accuracy, and this requires that we calculate the value of the $\boldsymbol{Q}_0$ and $\boldsymbol{Q}_1$ at several intermediate points in time; in particular, the choices of RK methods for second and third order time stepping both require a mid step of half the time step.

The force-free operator is independent of the interaction system, thus we can fully integrate this system by a full time step without any interference from the interaction system.

However, since the interaction operator $\boldsymbol{\mathcal{L}}_1$ depends on both $\boldsymbol{Q}_1$ *and* $\boldsymbol{Q}_0$, we also need the value of force-free system $\boldsymbol{Q}_0$ for the mid steps as well. We need the force-free system to calculate the interaction primitives $\boldsymbol{P}_1$ as well.

This requires that we also calculate the force-free system at the same time. This can be done in three different ways:

1. Use the same Runge-Kutta method for both operators, and step forward both systems together for every sub-step.

2. Use different Runge-Kutta methods for either operator, which have the same sub-step times. For instance, the second and third order time stepping schemes we described in section 3.1.5 both use the same sub-step time points.

3. For each sub-step, perform a full time step of the force-free system to this sub-step. For instance, the Runge-Kutta scheme we use is Kutta's classic third order method, which requires two sub-steps, one at the midpoint time $t_{n+1/2} = (t_{n+1} + t_n)/2$, and one at the end point of the time step t_{n+1}. So we can perform two full steps of the force-free system, once to $t_{n+1/2}$ and once again to t_{n+1}, and use these values for calculating the fluxes and primitives of the interaction system.

First of all, the second method is not likely a good choice, as it is not even clear that this method would retain the higher order time stepping for the scheme. Since the interaction operator does not affect the force-free operator, the force-free operator at least would retain higher order convergence, but it is not clear at all that the interaction operator would retain this. We therefore decided against this scheme — especially since using the third order operator for both is only a single extra time step for the interaction system anyway.

Since the third method means we are running the force-free system with half the time step (i.e. half the Courant number C_u), the third method clearly requires more calculation per time step. A different Runge-Kutta method could mean even more time steps for the force-free system. With that said, the force-free system is much simpler and cheaper to calculate computationally speaking. Furthermore, at high σ the accuracy of the force-free system becomes much more important, so by doing twice as many time steps we can increase the accuracy of the method — although decreasing the time step without increasing the resolution is known to increase dissipation. We could even do multiple full steps of the force-free system for each of these sub-steps.

The other advantage of decoupling the systems in this manner is that we could independently increase the resolution of the force-free system as well. Doing so would be beneficial as the accuracy of the force-free system is significantly more important, both due to the system being dominant at $\sigma \gg 1$ and because this would reduce truncation error and thus reduce loss of conservation.

The recombination step is one of the main reasons we have not tried increasing the resolution of the force-free system independently of the interaction system. Since we would only have the values of the interaction variables at some of the equivalent force-free grid points, we would need to create another interpolation scheme to find these values off the interaction grid. Moreover, in higher dimensions this would need to be a fully multidimensional interpolation scheme as well, as mentioned above. Given its complexity and limited advantage, we will use the first time stepping method for the remainder of this thesis.

3.2.4 Integration Scheme

Since we are integrating the two operators (semi-)independently, we are free to choose different integration schemes for the two operators. Thus we can choose the method and the specifics of the method for both operators.

Interaction Operator

Although different integration schemes could have been applied to the interaction operator, the complexity of the equations lead us to simply use an HLL method as described previously. This is an especially simple method to use, and we can practically use it "out of the box" so to speak, without needing to do any complex tasks such as determining all the eigenvectors.

The only task we need to do is calculate the maximal signal velocities S_L and S_R for the system. We have two clear choices: Use the speed of light, or use the fast speeds.

Using the speed of light is of course guaranteed to be fast enough, as no signal can go faster than light to begin with. Moreover, in the high-σ regime the fast speeds are very close to the speed of light most of the time. This choice also avoids any difficulty calculating phase speeds. However, this choice will cause fast waves and fast shocks to be more diffusive like all the other waves with HLL solver, because we are not accurately resolving these features. This will also be the case at low σ, where the fast speeds are no longer close to the speed of light.

This is *especially* the case when the fluid velocity is high enough to cause the true fast speeds to both be positive or negative; as we have described before, in the HLL solver in such cases the output is simply the flux of one of the initial constant regions outside the Riemann fan, since the Riemann fan is wholly on one side of the origin $x = 0$. However, with the use of the speed of light this would never happen, and the result of this solver is thus significantly different than otherwise.

We can therefore use the fast phase speeds instead. These fast speeds should match the fast speeds of the overall total RMHD system, so we can just use the same expressions for the phase speeds given in Eq. (2.64), for the most general case. Unfortunately, this does mean that generally we will need to solve a quartic polynomial for every Riemann problem, although since this can be done analytically this is not exceptionally slow. For our code, we use these fast speeds for the interaction operator, as this was found to make the results in high Lorentz factor flows (where the Fast speeds can be significantly different from the speed of light) less diffusive, while having little effect when the fast speeds are both close to the speed of light. Thus there is little reason not to use this choice.

Force-Free Operator

As the simpler of the two operators, the force-free operator affords us the most flexibility in choosing the integration method, since this makes it easier to apply different methods. As discussed previously, when using our Finite difference scheme we have the choice of which solver to use — although we have still chosen to use an HLL solver, like with the interaction operator.

As with the interaction operator, this gives us some choice over what signal velocities to use. We know that the overall system is RMHD, so it may be appropriate to use the fast speeds, like with the interaction operator. This gives some small complication, since now the force-free operator does depend on the interaction system, unlike our discussion in section 3.2.1. This would cause a problem if we were to use the split-time stepping method described above, where the interaction operator is integrated with a shorter time step than the interaction operator, since we would not know the value of interaction system at the mid-steps that we would need to calculate the fast phase speeds.

Alternatively, we could use the speed of light as our signal velocity. Keeping the force-free operator independent of the interaction system as discussed previously, this should in fact be the “correct” choice, since the fast phase speeds in the force-free system are always the speed of light in all directions.

In practice, testing the code against both choices of velocity has shown that the code can be numerically unstable when using the fast phase speeds for the force-free system. We therefore have chosen to always use the speed of light as the maximal signal velocities, and thus the force-free system remains fully independent of the interaction system (at least until the recombination step).

As a result, the two HLL operators are using two different phase speeds — the interaction operator is using the full RMHD fast phase speeds, while the force-free operator is using the force-free fast phase speeds. In high-σ states with relatively low fluid velocity, these values are quite close together, but as σ decreases or the velocity increases they can become quite significantly different — this is most notable when the fluid is supersonic, i.e. faster than the fast phase speed, as in this case the HLL signal velocities are all on one side of $x = 0$, and the output is the left or right state flux, instead of the central HLL flux.

We can still use a different Riemann solver for the force-free instead, however. Unlike full RMHD, for which an exact Riemann solver is a fairly intractable problem and excessively complex with little gain, Riemann problems in FFDE are much simpler to solve exactly since the general equations for non-linear waves given in section 2.4 is much simpler.

In particular, only fast waves can change the magnetic pressure $p_m = (B^2 - E^2)/2$, and only Alfvén waves can change E_x, the component of the electric field parallel to the wave directions. This means that solving the system exactly reduces to determining the values of p_m and E_x in the central region of the Riemann fan bounded by Alfvén waves (Komissarov, 2002). This is even easier in the degenerate case, as the degenerate waves are even simpler.

However, an exact solver no matter how simple it can be calculated is still often excessive for maintaining accuracy; for sufficiently small jumps simpler solvers work without issue, and although quite simple this method still requires an iterative solver.

As an alternative we could instead use a Linear Riemann solver, as described above in section 3.1.2. As such a solver resolves all the waves (albeit approximately) it reduces the diffusivity of the Alfvén waves compared to the HLL solver, which drops these waves.

This of course comes at the cost of increased computational complexity, as we need to solve a system of Linear equations to find the amplitudes of each wave, and we need to identify and treat degenerate cases independently.

These previous methods are all based on the conservative method described in section 3.1. The advantage of a conservative method is of course the fact that conservation is maintained up to the numerical error, which is very useful for properly modelling discontinuous solutions such as shocks.

However, we have previously noted in section 3.2.1 that conservation cannot be maintained for the force-free operator to machine precision. Thus the advantage of a conservative method is not achievable to begin with, at least not for all the variables. Thus there may be some value in using a different scheme entirely.

In section 2.2 we derived a different set of evolution equations, acting directly on the $\boldsymbol{B}$ and $\boldsymbol{E}$ for FFDE. Some authors, such as Komissarov (2004a); Mahlmann *et al.* (2021) have used these equations for modelling FFDE, instead of the conservation laws. We could therefore apply these same methods to the force-free operator, giving us a completely different method for integrating the force-free operator.

Low Magnetisation Regime

The integration scheme detailed above is of course tailored towards the high σ regime. In this regime, the force-free system dominates the dynamics, and the scheme appears similar to a perturbation scheme.

However, as we will see in chapters 4 and 5, testing has indicated that the code behaves well even outside of this regime in low magnetisation as well. In this regime, at the start of the time step we still have $\boldsymbol{B}_0 = \boldsymbol{E}_0 = 0$, so that we essentially have all the electromagnetic terms collected in the force-free system, and all the inertial terms in the interaction system.

The following discussion is more easily understood in the context of a first-order scheme, hence we will assume such from here on.

During each time step, the force-free operator will update the electromagnetic terms as if the system is force-free; at the end of the time step, $\boldsymbol{B}_0$ and $\boldsymbol{E}_0$ are the electromagnetic fields of a purely force-free evolution, even though overall the system is not force-free and can have a non-negligible Lorentz force.

The interaction operator meanwhile starts without any electromagnetic fields. Thus the initial flux calculated is ignorant of the electromagnetic fields, and is equivalent to the flux for a purely hydrodynamic case, and the conservatives are updated accordingly. However, at the end of each iteration we must calculate the primitives from these conservatives, and it is here that the force-free fields become important, as the expressions for the interaction conservatives Eqs. (3.90) to (3.93) involve the force-free fields. In effect, the hydrodynamic flow has induced electric and magnetic fields (assuming the flow was not parallel to the magnetic field).

The final step recombines the force-free and interaction electric and magnetic fields. It is at this point that the force-free system becomes “aware” of the plasma inertia. Thus in this step, the electromagnetic evolution is no longer force-free.

In effect, we have split the system into two components: A force-free evolution of the magnetic fields, and a hydrodynamic evolution of the plasma inertia. At the end of the time step, the effect of this hydrodynamic flow on the electric and magnetic fields is determined, and this is used to correct the force-free evolution.

In higher order time integration, the picture becomes more complex because the sub-steps will have non-zero $\boldsymbol{B}_1$ and $\boldsymbol{E}_1$, and so the interaction system will be affected by the force-free fields. However, the reverse is not true, so the force-free system will only become affected by the plasma inertia at the end of each time step.

Since our splitting has retained all the terms of RMHD, the evolution of the system will be consistent with a normal RMHD code. The only exception is the lack of conservation for the force-free fields, which is negligible at low σ since the electromagnetic fields are small.

3.2.5 Extending to Higher Dimensions

As we will show in the next chapter, the integration scheme described above is fully capable of handling the 1D code besides a few relatively minor issues, many of which we will manage to correct. Thanks to the fact that the code is a finite difference scheme instead of a finite volume scheme, the extension to multidimensional problems is relatively simple.

If we recall from section 3.1.1, we discretised the 1D spatial terms into the semi-discrete equation of Eq. (3.16)

$$\frac{d\boldsymbol{Q}_i}{dt} + \sum_i \frac{1}{\Delta x}\left(\hat{\boldsymbol{F}}_i^+ - \hat{\boldsymbol{F}}_i^-\right) = \boldsymbol{S}.$$

So from the x-boundary fluxes $\hat{\boldsymbol{F}}_i^\pm$ and source terms $\boldsymbol{S}$ we can calculate the first derivative $d\boldsymbol{Q}_i/dt$ of each of the i cells.

This extends quite simply into two dimensions as

$$\frac{d\boldsymbol{Q}_{i,j}}{dt} + \frac{1}{\Delta x}\left(\hat{\boldsymbol{F}}_{i,j}^+ - \hat{\boldsymbol{F}}_{i,j}^-\right) + \frac{1}{\Delta y}\left(\hat{\boldsymbol{G}}_{i,j}^+ - \hat{\boldsymbol{G}}_{i,j}^-\right) = \boldsymbol{S}, \tag{3.99}$$

for the i, j cell, where $\hat{\boldsymbol{G}}_{i,j}^\pm$ are the y-boundary fluxes, naturally equivalent to the x-boundary fluxes. They must also satisfy the same conditions as the x-boundary fluxes of

Eqs. (3.17) and (3.18), which ensure that boundary fluxes are shared between neighbouring cells and that they produce high-order estimates for the flux at the cell centres.

As we mentioned previously in section 3.1.1, thanks to using a finite difference scheme the reconstructions for the Riemann problems described in section 3.1.3 can be done one dimensionally. That is, to construct the x-boundary Riemann problems, we only need to interpolate in the x-direction, and the same for the y-boundaries. The same is also true of the DER step. We thus have no need of a fully multidimensional reconstruction scheme, which would otherwise be necessary in a typical finite volume scheme based on cell averages.

Thus the calculations of the $\hat{\boldsymbol{F}}^{\pm}_{i,j}$ and the $\hat{\boldsymbol{G}}^{\pm}_{i,j}$ can be done with the same method described in section 3.1, applied to the x-boundaries and y-boundaries individually. Hence the method can be extended to two dimensions with ease, and the extension to three dimensions follows in much the same way.

However, there is one major caveat to our assertion that the system can be extended to higher dimensions easily: That of the divergence-free conditions on $\boldsymbol{B}_0$ and $\boldsymbol{B}_1$, Eqs. (3.86) and (3.94). In 1D, these conditions combine with the two components of Faraday's law in Eqs. (3.85) and (3.93) to give the simple condition that both B^x_0 and B^x_1 are constant in both space and time over the entire domain, effectively reducing the number of evolution equations by two.

However, in higher dimensions this reduction is no longer possible. All three components of $\boldsymbol{B}$ are now able to vary in all cells in both space and time. This gives us a significant problem: truncation error and numerical error are now capable of violating these divergence-free conditions. Numerically, the conditions act as initial conditions for the initial state of the system, and the basic equations have no intrinsic effect of removing these violations (Falle *et al.*, 1998). The result is naturally that the violations will grow over the course of the simulation, and will frequently grow large enough to alter the results or even crash the code entirely (Brackbill and Barnes, 1980). This is an effect that we have also observed in two dimensional tests as well.

This particular problem is not unique to our method, and indeed all models of even non-relativistic MHD must contend with this issue (Falle *et al.*, 1998; Komissarov, 1999a). Of course, this means we have a multitude of different possible corrections to this flaw that have been proposed over the years.

Some of these methods include:

1. Solve the Poisson equation $\nabla^2\phi + \boldsymbol{\nabla} \cdot \boldsymbol{B} = 0$ for the pseudo-potential ϕ, and then use the result to correct the magnetic field by setting the magnetic field to the solenoidal component $\boldsymbol{B}^* = \boldsymbol{B} - \nabla\phi$ (e.g. Zachary *et al.* (1994)). Although this

is highly effective, it is also quite expensive computationally to solve the Poisson equation.

2. Use the integral form of the induction equation Eq. (2.48) to enforce the condition exactly (e.g. Evans and Hawley (1988)), a method known as “constrained transport”. This method requires using a staggered grid, so that we have the value of the magnetic field at the cell interface centres, and the cell edge centres as well.

3. Alter the equations to include the extra terms that $\boldsymbol{\nabla}\cdot\boldsymbol{B} \neq 0$ would imply, effectively suppressing the effect of non-zero divergence on the results (e.g. Zachary *et al.* (1994)). Unfortunately, these equations are no longer conservation laws (Brackbill and Barnes, 1980; Komissarov, 1999a).

4. Use a vector potential $\boldsymbol{A}$ such that $\boldsymbol{B} = \boldsymbol{\nabla}\times\boldsymbol{A}$ to describe the magnetic field instead of $\boldsymbol{B}$ (e.g. Bell and Lucek (1995)). Since the divergence of a curl is always zero, this would necessarily enforce $\boldsymbol{\nabla}\cdot\boldsymbol{B} = 0$. This method naturally requires different equations on $\boldsymbol{A}$ compared to $\boldsymbol{B}$. More importantly, like the previous method these equations are not conservation laws (Komissarov, 1999a).

5. Use the generalised Lagrange multiplier (GLM) method to diffuse and attenuate non-zero divergence (e.g. Komissarov (2007)). Although this method does not enforce the condition exactly, it is the simplest to implement and the equations remain conservation laws.

As one of the simplest to implement in addition to retaining the conservation laws, we opted to use the last method, the GLM method. Proposed in Munz *et al.* (2000) and explored further in Dedner *et al.* (2002), the idea behind this method is to convert the constraint $\boldsymbol{\nabla}\cdot\boldsymbol{B} = 0$ into an evolution equation that we can evolve with the rest of the system, that has the effect of dispersing the $\boldsymbol{\nabla}\cdot\boldsymbol{B}$ across the domain as well as causing the magnitude to decay as well.

With this method, we need only convert the divergence constraint into one more conservation equation and add an extra term to Faraday’s law. Specifically, we modify Eqs. (2.37) and (2.38) into (Komissarov, 2007)

$$\frac{\partial \boldsymbol{B}}{\partial t} + \boldsymbol{\nabla}\times\boldsymbol{E} + \boldsymbol{\nabla}\phi = 0, \tag{3.100}$$

$$\frac{\partial \phi}{\partial t} + \boldsymbol{\nabla}\cdot\boldsymbol{B} = -\kappa\phi, \tag{3.101}$$

where ϕ is a new dynamical variable (a pseudo-potential) and κ is a constant parameter. Eq. (3.101) naturally implies that the new variable ϕ is a conserved variable, which we can evolve along with the rest of the system without issue. We also now have a source term in Eq. (3.101), but this particular form of source term is very simple to deal with.

In order to understand the effect of these alterations, we can take the partial derivative of Eq. (3.101) with respect to time to get

$$\frac{\partial^2 \phi}{\partial t^2} + \kappa \frac{\partial \phi}{\partial t} + \frac{\partial}{\partial t}(\boldsymbol{\nabla} \cdot \boldsymbol{B}) = 0. \tag{3.102}$$

Now we take the divergence of Eq. (3.100) to obtain

$$\frac{\partial}{\partial t}(\boldsymbol{\nabla} \cdot \boldsymbol{B}) + \nabla^2 \phi = 0, \tag{3.103}$$

since the divergence of curl is 0. We can then use this equation to substitute into Eq. (3.102) for $\partial_t(\boldsymbol{\nabla} \cdot \boldsymbol{B})$ and therefore we find (Komissarov, 2007)

$$\frac{\partial^2 \phi}{\partial t^2} + \kappa \frac{\partial \phi}{\partial t} - \nabla^2 \phi = 0, \tag{3.104}$$

so ϕ satisfies the telegraph equation. It thus follows that ϕ is transported at the speed of light by hyperbolic waves, and decays provided $\kappa > 0$.

If we further take the time derivative of Eq. (3.103) then we will get

$$\frac{\partial^2}{\partial t^2}(\boldsymbol{\nabla} \cdot \boldsymbol{B}) + \nabla^2 \left(\frac{\partial \phi}{\partial t} \right) = 0. \tag{3.105}$$

We can then take the Laplacian of Eq. (3.101), and thus substitute for $\nabla^2(\partial_t \phi)$ to give

$$\frac{\partial^2}{\partial t^2}(\boldsymbol{\nabla} \cdot \boldsymbol{B}) - \nabla^2 \left(\boldsymbol{\nabla} \cdot \boldsymbol{B}\right) - \kappa \nabla^2 \phi = 0, \tag{3.106}$$

and finally we use Eq. (3.103) again to eliminate the $\nabla^2 \phi$ and obtain (Komissarov, 2007)

$$\frac{\partial^2}{\partial t^2}(\boldsymbol{\nabla} \cdot \boldsymbol{B}) + \kappa \frac{\partial}{\partial t}(\boldsymbol{\nabla} \cdot \boldsymbol{B}) - \nabla^2 \left(\boldsymbol{\nabla} \cdot \boldsymbol{B}\right) = 0. \tag{3.107}$$

Thus $\boldsymbol{\nabla} \cdot \boldsymbol{B}$ satisfies the same telegraph equation, and therefore is also transported at the speed of light, and decays with $\kappa > 0$. Thus it is clear that with these adjustments, the natural evolution of $\boldsymbol{\nabla} \cdot \boldsymbol{B}$ and ϕ forwards in time is towards $\boldsymbol{\nabla} \cdot \boldsymbol{B}(\boldsymbol{x}, t) = 0$ and $\phi(\boldsymbol{x}, t) = 0$, unless prevented by the boundary conditions.

To use this method for our split-operator method, we need to make the same alterations as in Eqs. (3.100) and (3.101) to both the force-free operator and the interaction operator. In other words, we alter Eqs. (3.85) and (3.86) into

$$\frac{\partial \boldsymbol{B}_0}{\partial t} + \boldsymbol{\nabla} \times \boldsymbol{E}_0 + \boldsymbol{\nabla} \phi_0 = 0, \tag{3.108}$$

$$\frac{\partial \phi_0}{\partial t} + \boldsymbol{\nabla} \cdot \boldsymbol{B}_0 = -\kappa \phi_0, \tag{3.109}$$

and we also alter Eqs. (3.93) and (3.94) into

$$\frac{\partial \boldsymbol{B}_1}{\partial t} + \boldsymbol{\nabla} \times \boldsymbol{E}_1 + \boldsymbol{\nabla} \phi_1 = 0, \tag{3.110}$$

$$\frac{\partial \phi_1}{\partial t} + \boldsymbol{\nabla} \cdot \boldsymbol{B}_1 = -\kappa \phi_1. \tag{3.111}$$

Thus we must introduce *two* new variables ϕ_0 and ϕ_1 instead of just one — although at high σ we should find that $|\phi_1| \ll |\phi_0|$, so the ϕ_1 will likely be much less important at high σ.

Source Terms

The source term in Eq. (3.101) needs special consideration. In the integration scheme described in chapter 3 we did include the possibility of source terms, but we did not describe how to deal with them. For 1D ideal RMHD source terms do not appear, but they can appear for multidimensional systems, in particular with non-Cartesian coordinates.

If we start with the general conservation law Eq. (2.119) we have

$$\frac{\partial \boldsymbol{Q}}{\partial t} + \frac{\partial \boldsymbol{F}}{\partial x} + \frac{\partial \boldsymbol{G}}{\partial y} + \frac{\partial \boldsymbol{H}}{\partial z} = \boldsymbol{S}.$$

We already know how to solve the homogeneous equations

$$\frac{\partial \boldsymbol{Q}}{\partial t} + \frac{\partial \boldsymbol{F}}{\partial x} + \frac{\partial \boldsymbol{G}}{\partial y} + \frac{\partial \boldsymbol{H}}{\partial z} = 0, \tag{3.112}$$

without any source terms, so the obvious method to solve the full system is to use another operator splitting method (Komissarov, 2007). That is, we first solve Eq. (3.112) then solve the pure source term operator

$$\frac{\partial \boldsymbol{Q}}{\partial t} = \boldsymbol{S}, \tag{3.113}$$

and alternate between these two operators each time step.

In our case, the source term $\boldsymbol{S}$ only has one non-zero component; that is, we only need to solve

$$\frac{\partial \phi}{\partial t} = -\kappa \phi, \tag{3.114}$$

which we can easily solve analytically as

$$\phi(\boldsymbol{r}, t) = \phi(\boldsymbol{r}, t_0)\, e^{-\kappa(t-t_0)}. \tag{3.115}$$

Therefore all we need to do to apply this source term is to decay the value of ϕ in each cell exponentially every time step. More complex source terms usually require using numerical methods to solve Eq. (3.113), so the fact that we can solve this analytically is very convenient.

The Value of κ

We clearly have some choice as to the value of κ; as we have noted above we need $\kappa > 0$, but this still leaves us with a large amount of freedom. The value of κ serves to alter to rate at which both ϕ and $\boldsymbol{\nabla} \cdot \boldsymbol{B}$ decay. Clearly, too small a value for κ would mean that it does not decay meaningfully. Although as we described above the GLM method also advects the $\boldsymbol{\nabla} \cdot \boldsymbol{B}$ errors away from their source, effectively diluting the issue across the domain, if the source generates $\boldsymbol{\nabla} \cdot \boldsymbol{B}$ to quickly or if the domain is finite, e.g. a periodic domain, then $\boldsymbol{\nabla} \cdot \boldsymbol{B}$ may be able to grow sufficiently to cause problems.

Although this would seem to imply that it should be made as large as possible in order to eliminate $\boldsymbol{\nabla} \cdot \boldsymbol{B}$, numerically we find Eq. (3.101) implies that making κ very large causes ϕ to decay in a very small number of time steps, thus preventing it from having an effect on $\boldsymbol{B}$ via Eq. (3.100).

In other words, let us consider the operator splitting method described above, that performs a step of the homogeneous system Eq. (3.112) followed by a source step Eq. (3.113). In our case the source step is Eq. (3.115), the exponential decay of ϕ. Thus with sufficiently large κ, the value of ϕ decays so much that it can have no effect during the next step of Eq. (3.112).

Thus the optimal value of κ — i.e. that which minimises $\boldsymbol{\nabla} \cdot \boldsymbol{B}$ — is somewhere between a κ so small that little to no decay occurs and a κ so large that ϕ decays too quickly. From numerical tests, a value of $\kappa = 100$ works well at the resolutions we tested, from 100×100 up to resolution 400×400. However, other values for κ are likely more optimal. Indeed, the optimal value even depends on the particular case being modelled. Various authors (Dedner *et al.*, 2002; Tricco and Price, 2012) have suggested different values for κ.

However, from testing there appears to be little to gain from a more optimal choice of κ. So long as κ is sufficient to clear $\boldsymbol{\nabla} \cdot \boldsymbol{B}$ errors from the system such that it is not causing no apparent problems, and a more optimal value for κ gives little to no benefit.

Thus for all our 2D tests, we simply set $\kappa = 100$ *regardless of the resolution,* C_u*, or the nature of the test case itself.*

Another point we may note is that the fact that we apply the system twice implies we could use two different values of κ for Eqs. (3.109) and (3.111). However, we believe this is unlikely to be particularly useful. This is because if ϕ_0 and ϕ_1 have similar magnitudes, like what would happen with $\sigma \approx 1$, it is unlikely that two different values of κ would be useful. On the other hand, at high σ we will have that ϕ_1 is much smaller than ϕ_0 and so a change in κ will have little overall effect.

One problem that may be worth bearing in mind is that this divergence cleaning method does not enforce an *exact* divergence-free condition on $\boldsymbol{B}$, i.e. generally we will have $\boldsymbol{\nabla} \cdot \boldsymbol{B} \neq 0$. If we let $\delta\boldsymbol{B}$ be the minimum adjustment needed (in a least-squares sense) so that $\boldsymbol{\nabla} \cdot (\boldsymbol{B} + \delta\boldsymbol{B}) = 0$, then the magnitude of the error $\delta\boldsymbol{B}$ only depends on the form of the $\boldsymbol{B}$-field and its magnitude. Since this is independent of the σ^{-1} scaling, it is possible that at high σ the magnitude of this error is of a similar order or greater than the scale of the interaction system. It is then possible that this may cause problems such as large errors in the interaction system.

It may be then that a divergence cleaning scheme that enforces an exact divergence-free condition on at least $\boldsymbol{B}_0$ is preferable to the GLM method we have opted for here. However, testing has shown that at least for the cases we have considered this does not seem necessary, and so we have not attempted this scheme due to it being far more complicated to implement than the current GLM method.

3.2.6 Primitive Variable Conversion

As noted previously, it is necessary to write the system in terms of simpler quantities called primitive variables such as mass density ρ or gas pressure p_g, in order to be able to calculate the fluxes and apply boundary conditions — as well as simply to understand the current state of the system.

There is a lot of freedom in choosing what quantities to use for these primitives. For use in conservative numerical models, we desire a set of variables that have the following properties:

1. $\boldsymbol{Q}(\boldsymbol{P})$ is an invertible function over the domain of physically possible states.
2. $\boldsymbol{Q}, \boldsymbol{F}_x, \boldsymbol{F}_y, \boldsymbol{F}_z$ can be calculated as easily as possible from $\boldsymbol{P}$.
3. $\boldsymbol{P}$ can be calculated easily from $\boldsymbol{Q}$.

Of course, there are many other desirable properties we could ask for, but these are the most important. While the first two properties are relatively simple — in fact the way we have written the equations themselves naturally suggest a set we could use — the third property is much harder to satisfy.

For the force-free system the natural choice is of course $\boldsymbol{B}_0$ and $\boldsymbol{E}_0$. We do need to be careful though, since these variables need to satisfy the PC conditions $\boldsymbol{B}_0 \cdot \boldsymbol{E}_0 = 0$ and $B_0^2 > E_0^2$, so an arbitrary pair $\boldsymbol{B}_0$ and $\boldsymbol{E}_0$ will not generally satisfy these conditions. In other words, we are choosing six variables for a system with only five degrees of freedom (or four degrees in 1D). Unfortunately, there is no obvious choice of just five variables that would always work. Dropping one of the elements of $\boldsymbol{B}_0$ or $\boldsymbol{E}_0$ cannot always work, as if the corresponding element of $\boldsymbol{E}_0$ or $\boldsymbol{B}_0$ is 0 (for instance, if we have dropped E_0^x and $B_0^x = 0$) then the remaining elements of $\boldsymbol{B}_0$ and $\boldsymbol{E}_0$ only have three degrees of freedom left. As such, we keep all six of $\boldsymbol{B}_0$ and $\boldsymbol{E}_0$, and simply enforce $\boldsymbol{B}_0 \cdot \boldsymbol{E}_0$ on them.

For the interaction system, we can use the magnetic field $\boldsymbol{B}_1$ as primitive variables since they are conservative variables, and the other conservative variables have simple descriptions in terms of these variables.

The next natural choice is to use mass density ρ and gas pressure p_g as primitives, since they both appear almost on their own, and the entropy density w is related to these variables via the Equation of State.

For the remaining variables, we still need to describe the fluid velocity. This gives us two possible natural choices; we can choose to use either the 3-velocity $\boldsymbol{v}$ or we can use the spatial components of the 4-velocity $\boldsymbol{u}$. Either choice allows us to calculate the Lorentz factor γ, and thereby completes the set of primitive variables, since we can fully calculate all the conservative variables and fluxes in terms of these variables after implementing the PC condition to calculate $\boldsymbol{E}_1$.

Both of these choices to describe the velocity are quite similar. At low velocity they are in fact almost identical in value; the differences between them become significant only at high Lorentz factors, since at high Lorentz factor the magnitude of $\boldsymbol{v}$ tends to 1, the speed of light, while $\boldsymbol{u}$ is unbounded. This fact makes $\boldsymbol{v}$ insensitive at high Lorentz factors, and small changes in $\boldsymbol{v}$ then correspond to large changes in γ, and therefore large changes in the conservative variables. We therefore chose $\boldsymbol{u}$ as the velocity description, since it does not have this problem.

In conclusion then, we have for our choices of primitive variables

$$\boldsymbol{P}_0 = \begin{pmatrix} \boldsymbol{B}_0 \\ \boldsymbol{E}_0 \end{pmatrix}, \quad \boldsymbol{P}_1 = \begin{pmatrix} \rho \\ \boldsymbol{u} \\ p_g \\ \boldsymbol{B}_1 \end{pmatrix}, \tag{3.116}$$

for the force-free primitives $\boldsymbol{P}_0$ and interaction primitives $\boldsymbol{P}_1$.

Although these choices of primitive variables $\boldsymbol{P}_0$ and $\boldsymbol{P}_1$ in Eq. (3.116) allow for us to calculate the corresponding conservative variables $\boldsymbol{Q}_0$ and $\boldsymbol{Q}_1$ easily, since the numerical method updates the conservative variables each time step (and during each time step) we also need to calculate the primitive variables from these conservative variables, in order to calculate the corresponding fluxes. This calculation needs to be as fast as possible, since it will be performed several times each time step for every cell in the domain, so the speed of this calculation is one of the chief bottlenecks in the speed of the method.

Force-Free

For the force-free variables, this calculation is quite simple. Following Komissarov (2002), we have

$$\boldsymbol{P}_0 = \begin{pmatrix} \boldsymbol{B}_0 \\ \boldsymbol{E}_0 \end{pmatrix} \quad \text{and} \quad \boldsymbol{Q}_0 = \begin{pmatrix} \boldsymbol{B}_0 \\ \boldsymbol{S}_0 \\ U_0 \end{pmatrix} = \begin{pmatrix} \boldsymbol{B}_0 \\ \boldsymbol{E}_0 \times \boldsymbol{B}_0 \\ \frac{1}{2}(B_0^2 + E_0^2) \end{pmatrix}, \tag{3.117}$$

for our primitive and conservative variables. We have the magnetic field $\boldsymbol{B}_0$ directly, and only need to calculate the electric field $\boldsymbol{E}_0$. This can be done simply using the Poynting flux $\boldsymbol{S}_0 = \boldsymbol{E}_0 \times \boldsymbol{B}_0$, as this implies

$$\boldsymbol{E}_0 = \frac{1}{B^2}\left(\boldsymbol{B}_0 \times \boldsymbol{S}_0\right), \tag{3.118}$$

and so we do not need to use energy conservation at all.

Unfortunately, things are not quite as simple as they seem. We can clearly see that the system is overdetermined, with seven conservative variables and six primitive variables; moreover, the PC condition $\boldsymbol{B}_0 \cdot \boldsymbol{E}_0 = 0$ reduces the number of free primitive variables down to just five.

Although analytically the conservative variables will satisfy these conditions, we noted in section 3.2.1 that for our numerical method there will be a small error in at least some of the variables on the order of the truncation error, as noted by McKinney (2006). The result is that the conservatives will generally by slightly inconsistent with each other and will not correspond to any $\boldsymbol{B}_0$ and $\boldsymbol{E}_0$ exactly.

We could make alterations to this conversion method to try to suppress any issues that this causes, since this can cause the momentum and/or energy to not be conserved properly. But since this problem is perhaps the most significant issue with this method, we will leave it as it stands for now and discuss this problem further in chapter 4. For now, we will simply use Eq. (3.118).

Interaction

In comparison to the force-free system, calculating the interaction primitives is much more complicated — although we at least do not have any problems with an overdetermined system.

There are multiple methods that have been developed for this task for normal RMHD (Del Zanna *et al.*, 2007; Newman and Hamlin, 2014), but for our new code we will need to develop our own new version. With that said, we will be able to borrow some of these methods, as the equations are of course closely related.

In this case, our variables are

$$\boldsymbol{P}_1 = \begin{pmatrix} \rho \\ \boldsymbol{u} \\ p_g \\ \boldsymbol{B}_1 \end{pmatrix}, \quad \boldsymbol{Q}_1 = \begin{pmatrix} D \\ \boldsymbol{S}_1 \\ U_1 \\ \boldsymbol{B}_1 \end{pmatrix} = \begin{pmatrix} \rho\gamma \\ w\gamma^2\boldsymbol{v} + \boldsymbol{E}_1 \times \boldsymbol{B}_0 + \boldsymbol{E}_0 \times \boldsymbol{B}_1 + \boldsymbol{E}_1 \times \boldsymbol{B}_1 \\ w\gamma^2 - p + \boldsymbol{E}_0 \cdot \boldsymbol{E}_1 + \boldsymbol{B}_0 \cdot \boldsymbol{B}_1 + \frac{1}{2}(E_1^2 + B_1^2) \\ \boldsymbol{B}_1 \end{pmatrix}. \tag{3.119}$$

Note how the conservative variables are dependent on the force-free variables $\boldsymbol{B}_0$ and $\boldsymbol{E}_0$; we therefore need these variables before we can calculate the $\boldsymbol{P}_1$.

Once again, we can just use the magnetic field $\boldsymbol{B}_1$ directly, since it is already a primitive variable. If we insert the expression for $\boldsymbol{E}_1 = -\left(\boldsymbol{E}_0 + \boldsymbol{v} \times \boldsymbol{B}_0\right) - \boldsymbol{v} \times \boldsymbol{B}_1$, then this leaves us with calculating the reduced five primitive variables $\boldsymbol{R}$ from the reduced five conservative variables $\boldsymbol{T}$

$$\boldsymbol{R} = \begin{pmatrix} \rho \\ \boldsymbol{u} \\ p_g \end{pmatrix}, \quad \boldsymbol{T} = \begin{pmatrix} D \\ \boldsymbol{S}_1 \\ U_1 \end{pmatrix}. \tag{3.120}$$

An obvious method to use is a multivariate Newton method. However, while this has proved reasonably successful for our code, this method does require inverting a 5×5 matrix every iteration, and while it may be possible to do this symbolically and thus skip the matrix inversion this itself can be quite difficult to find.

As such, we decided to find an improved method instead, preferably with as few free dimensions as possible.

1D Secant Method

In order to speed up the variable conversion as much as possible we want to find a method with as few dimensions as possible, hopefully without sacrificing the stability of the method.

Starting with the conservative variables, we have

$$\boldsymbol{T} = \begin{pmatrix} D \\ \boldsymbol{S}_1 \\ U_1 \end{pmatrix} = \begin{pmatrix} \rho\gamma \\ w\gamma^2\boldsymbol{v} + \boldsymbol{E}_1 \times \boldsymbol{B}_0 + \boldsymbol{E}_0 \times \boldsymbol{B}_1 + \boldsymbol{E}_1 \times \boldsymbol{B}_1 \\ w\gamma^2 - p + \boldsymbol{E}_0 \cdot \boldsymbol{E}_1 + \boldsymbol{B}_0 \cdot \boldsymbol{B}_1 + \frac{1}{2}(E_1^2 + B_1^2) \end{pmatrix}. \tag{3.121}$$

We can eliminate $\boldsymbol{E}_1$ by substituting with the expression from the PC condition $\boldsymbol{E}_1 = -\left(\boldsymbol{E}_0 + \boldsymbol{v} \times \boldsymbol{B}\right)$, where we have $\boldsymbol{B} = \boldsymbol{B}_0 + \boldsymbol{B}_1$ as the total magnetic field.

With this substitution, we can manipulate the expressions to obtain

$$\boldsymbol{E}_1 \times \boldsymbol{B} = B^2\boldsymbol{v} - \left(\boldsymbol{B} \cdot \boldsymbol{v}\right)\boldsymbol{B} - \boldsymbol{E}_0 \times \boldsymbol{B}, \tag{3.122}$$

as well as

$$\boldsymbol{E}_0 \cdot \boldsymbol{E}_1 = \boldsymbol{v} \cdot \left(\boldsymbol{E}_0 \times \boldsymbol{B}\right) - E_0^2, \tag{3.123}$$

and finally

$$\frac{1}{2}E_1^2 = \frac{1}{2}\Big(B^2v^2 - (\boldsymbol{B}\cdot\boldsymbol{v})^2\Big) - \boldsymbol{v}\cdot(\boldsymbol{E}_0\times\boldsymbol{B}) + \frac{1}{2}E_0^2. \tag{3.124}$$

Using these, we can insert into the expression for $\boldsymbol{S}_1$ to obtain

$$\boldsymbol{S}_1 = w\gamma^2\boldsymbol{v} + B^2\boldsymbol{v} - (\boldsymbol{B}\cdot\boldsymbol{v})\,\boldsymbol{B} - \boldsymbol{E}_0\times\boldsymbol{B}_0, \tag{3.125}$$

meanwhile for U_1 we get

$$U_1 = w\gamma^2 - p + \boldsymbol{B}_0\cdot\boldsymbol{B}_1 + \frac{1}{2}B_1^2 - \frac{1}{2}E_0^2 + \frac{1}{2}\Big(B^2v^2 - (\boldsymbol{B}\cdot\boldsymbol{v})^2\Big)\,. \tag{3.126}$$

For the sake of convenience, we can collect all the known values on the left hand side and define new variables

$$\boldsymbol{S} = \boldsymbol{S}_1 + \boldsymbol{E}_0\times\boldsymbol{B}_0, \tag{3.127}$$

and

$$U = U_1 - \boldsymbol{B}_0\cdot\boldsymbol{B}_1 - \frac{1}{2}B_1^2 + \frac{1}{2}E_0^2, \tag{3.128}$$

so overall the new system we are solving is

$$D = \rho\gamma, \tag{3.129}$$

$$\boldsymbol{S} = \Big(W + B^2\Big)\,\boldsymbol{v} - (\boldsymbol{B}\cdot\boldsymbol{v})\,\boldsymbol{B} \tag{3.130}$$

$$U = W - p + \frac{1}{2}\Big(B^2v^2 - (\boldsymbol{B}\cdot\boldsymbol{v})^2\Big)\,, \tag{3.131}$$

where $W = w\gamma^2$.

Note that given the definition of $\boldsymbol{S}_1$ in Eq. (3.121) and the definition of $\boldsymbol{S}$ in Eq. (3.127), we have for $\boldsymbol{S}$

$$\boldsymbol{S} = W\boldsymbol{v} + \boldsymbol{E}\times\boldsymbol{B}, \tag{3.132}$$

where $\boldsymbol{E} = \boldsymbol{E}_0 + \boldsymbol{E}_1$. This $\boldsymbol{S}$ is therefore equivalent to the total momentum in the system, force-free and interaction combined. Similarly, for U we find

$$U = w\gamma^2 - p + \frac{1}{2}E^2. \tag{3.133}$$

This is not quite identical to the total energy of the system because we have subtracted the known magnetic terms from U; in other words, the total energy in the system is actually $U_{tot} = U + \frac{1}{2}B^2$.

Together, this has two consequences. First, it means that both $\boldsymbol{S}$ and U are $\mathcal{O}(1)$ expressions, and not $\mathcal{O}(\sigma^{-1})$. This may cause problems at high σ, as these quantities become insensitive to changes in the interaction terms making this variable conversion less accurate. However, we will see later that such problems can be avoided.

Second, this also means that the system we are solving in Eqs. (3.129) to (3.131) is actually identical to the system we would be solving for in a normal RMHD scheme, without splitting. Thus it should be possible to use conversion routines intended for normal RMHD schemes for our scheme as well, such as Del Zanna *et al.* (2003, 2007); Mignone and McKinney (2007); Newman and Hamlin (2014); Kalinani *et al.* (2022).

Selecting one of these schemes that has proven successful then, we follow the work of Del Zanna *et al.* (2003, 2007). Hence we can use Eq. (3.130) to take the square of $\boldsymbol{S}$ to give

$$S^2 = \left(W + B^2\right)^2 v^2 - \left(2W + B^2\right) (\boldsymbol{B} \cdot \boldsymbol{v})^2 , \tag{3.134}$$

as well as the dot product of $\boldsymbol{S}$ with $\boldsymbol{B}$ to get

$$\boldsymbol{B} \cdot \boldsymbol{v} = \frac{\boldsymbol{S} \cdot \boldsymbol{B}}{W}; \tag{3.135}$$

the latter of which allows us to eliminate $\boldsymbol{B} \cdot \boldsymbol{v}$ from all the equations, so we have

$$S^2 = \left(W + B^2\right)^2 v^2 - \left(2W + B^2\right) \frac{(\boldsymbol{S} \cdot \boldsymbol{B})^2}{W^2}, \tag{3.136}$$

and

$$U = W - p_g + \frac{1}{2} B^2 v^2 - \frac{1}{2} \frac{(\boldsymbol{S} \cdot \boldsymbol{B})^2}{W^2}. \tag{3.137}$$

So we have successfully reduced the system to just three unknowns, W, p_g and v^2. The relation between ρ, p_g and w is given in our case by the polytropic EOS $w = \rho + \kappa p_g$ with $\kappa = \Gamma/(\Gamma - 1)$, so we can use the definition of W and Eq. (3.129) to find that

$$p_g = \frac{1}{\kappa} \left(W \left(1 - v^2\right) - D\sqrt{1 - v^2} \right), \tag{3.138}$$

which we can use to eliminate p_g from Eq. (3.137) to obtain a cubic expression for W

$$a_3\left(v^2\right) W^3 + a_2\left(v^2\right) W^2 + a_0 = 0, \tag{3.139}$$

where

$$a_3\left(v^2\right) = 1 - \frac{1 - v^2}{\kappa}, \tag{3.140}$$

$$a_2\left(v^2\right) = \frac{1}{2} B^2 v^2 - U + D \frac{\sqrt{1 - v^2}}{\kappa}, \tag{3.141}$$

$$a_0 = -\frac{1}{2} (\boldsymbol{S} \cdot \boldsymbol{B})^2 , \tag{3.142}$$

so now we have just two equations and two unknowns, v^2 and W.

We thus have a choice of three methods to solve these two remaining equations. These are:

1. Solve both together as a 2D system using (for instance) a multivariate Newton Method.

2. Given W we can use Eq. (3.136) to solve exactly for v^2. Inserting this into Eq. (3.139) we obtain a function $\boldsymbol{F}_1(W, v^2(W))$ which we can solve using any 1D root finding method.

3. Given v^2 we can solve the cubic Eq. (3.139) exactly for W. Inserting this into Eq. (3.136) we obtain a function $\boldsymbol{F}_2(v^2, W(v^2))$, which we can again solve using any 1D root finding method.

Del Zanna *et al.* (2007) give a compelling reason to choose the third option here; first of all, we would expect that reducing the dimension of the system would be faster, and so the choice is between option 2 and option 3. Between these two, the value of v^2 is restricted to $0 \leq v^2 < 1$ while W is restricted to $W \geq 0$. Between these two variables it is more important to maintain the bounds on v^2, since the expression for a_2 includes $\sqrt{1 - v^2}$, and so we cannot allow $v^2 > 1$. It is thus more reasonable to use option 3 with v^2 as our iteration variable, since this allows us to control v^2, and keep it within the valid region.

The cubic equation in Eq. (3.139) can of course have three roots, so we must determine which is correct. By studying the behaviour of the roots, it is possible to show that the desired root must be the lone, positive root. During iterations, we may find that the current value of v^2 does not allow for a positive solution to the cubic, however we find that there appears to be little problem allowing it to be negative during iterations, as the routine is still able to output the correct solution in the end.

Although it may work well in some cases, at high velocities as v^2 approaches the limit of 1 it becomes increasingly insensitive to changes, which may lead to a loss of accuracy in this case. We could instead use the Lorentz factor γ as the iteration variable, but this time since $1 \leq \gamma$ this variable is instead insensitive to changes at low velocities, leading to inaccuracies in this case instead. Thus we can choose $u^2 = \gamma^2 - 1$ instead, which has no upper limit as with γ, but also approaches 0 at low velocities. Since we have

$$v^2 = \frac{u^2}{1 + u^2}, \tag{3.143}$$

the change to the equations is minimal.

Once we have converged to a solution for u^2 and W, we can compute the remaining primitives as

$$w = \frac{W}{\gamma^2}, \tag{3.144}$$

$$\rho = \frac{D}{\gamma}, \tag{3.145}$$

$$p_g = \frac{w - \rho}{\kappa}, \tag{3.146}$$

$$\boldsymbol{B} \cdot \boldsymbol{v} = \frac{\boldsymbol{S} \cdot \boldsymbol{B}}{W}, \tag{3.147}$$

$$\boldsymbol{v} = \frac{\boldsymbol{S} + (\boldsymbol{B} \cdot \boldsymbol{v})\,\boldsymbol{B}}{B^2 + W}, \tag{3.148}$$

$$\boldsymbol{E}_1 = -\left(\boldsymbol{E}_0 + \boldsymbol{v} \times \boldsymbol{B}\right), \tag{3.149}$$

and this completes the variable conversion scheme. From here on, this method shall be referred to as Method 1.

In comparison to the previous multivariate Newton scheme, this method is significantly improved by the reduction in the degrees of freedom. Instead of inverting a 5×5 matrix every iteration, we instead need to solve a cubic equation and then compute a single step of a Secant method (or univariate Newton method, or otherwise), which requires far fewer computations per iteration.

This method is not without its own potential issues, however. We have already noted previously that when σ is large, $\boldsymbol{S}$ and U are insensitive to changes in the interaction terms and the method is therefore likely to be less accurate in this regime. This error will scale with the numerical error, since the fundamental cause is the loss of accuracy that comes from truncating the approximations of these values in floating point expressions. We therefore would expect this error to become significant when σ^{-1} is of the order of the numerical error.

However, the fact that we have conservation error as discussed in section 3.2.4 that is of the order of the truncation error, this error will be comparatively inconsequential until σ is quite large, so this issue is likely not particularly important at low σ. Moreover, in order to calculate the Jacobian in the previous multivariate Newton method it is necessary to substitute for $\boldsymbol{E}_1$ using the PC condition Eq. (3.96), which itself has a problem with cancellation of $\mathcal{O}(1)$ values anyway, so this method has the same problem.

Testing

In order to test the two methods, we will measure four different properties:

1. Total Time
2. Relative Error
3. Failure Rate

The first of these is quite simple, as the total real time taken to converge.

Relative error is a measure of how close the solution reached is to the true solution. We calculate this by taking the absolute difference between the calculated primitives and the correct primitives for a given problem, and then dividing by the correct primitives to get a relative error instead of absolute error. We use a relative error because absolute error would bias higher values of σ, since the values of the interaction primitives become smaller at higher σ, thus the absolute error falls with them. However, since the correct velocity and $\boldsymbol{E}_1$ can potentially be 0 or close to it, this relative error is only particularly suitable for testing density and pressure. Thus we are only testing the error in these two quantities, and disregarding the error in velocity and $\boldsymbol{E}_1$. Although this may ignore error specific to these two quantities, in most cases we believe it unlikely that the error in these would differ significantly.

Finally, failure rate measures the number of failed convergences to total tests. That is, if for some reason the method fails to find a result — perhaps it was not converging to a solution, or maybe the system exited the range of physical values and caused the Lorentz factor to become imaginary — then we count this case as a failure, and compare the number of failures to the total number of tests.

In terms of the relative significance of these three measures, it is clear that in order of importance they are failure rate, relative error, and total time.

In order to test these schemes thoroughly, we require a large bank of varied test cases to test them against. However, with so many different possible input variables, including density, pressure, velocity, $\boldsymbol{B}_0$, $\boldsymbol{B}_1$, $\boldsymbol{E}_0$ in addition to the various possibilities for the initial guess, testing them systematically is quite difficult. We therefore instead test them using a random initial state, choosing a random set of variables to test them against each time.

Due to the known relationships between the variables including conditions like $\boldsymbol{B}_0 \cdot \boldsymbol{E}_0 = 0$, as well as the relative sizes of the variables with $\boldsymbol{B}_0, \boldsymbol{E}_0, \boldsymbol{v} \sim \mathcal{O}(1)$ and $\rho, p_g, \boldsymbol{B}_1, \boldsymbol{E}_1 \sim \mathcal{O}(\sigma^{-1})$, any random set of initial variables will not be appropriate for testing.

We thus carefully construct the random state to attempt to reproduce a state that may reasonably occur. This is done as follows:

1. First, a parameter σ' is chosen randomly from the log-uniform distribution, so that σ' ranges from 10^a and 10^b, for some values a and b we can choose later. The parameter σ' encodes the relative scales of the large and small variables, making it closely related to the σ of the final state. Note however that this parameter is *not* the value of σ for the final random state itself.

2. Pressure p_g and Density ρ are chosen from a uniform distribution on $[0, 1]$.

3. Vectors $\boldsymbol{u}_0, \boldsymbol{u}_1, \boldsymbol{B}_0$ and $\boldsymbol{B}_1$ are chosen with a uniformly distributed direction in 3D. The magnitude of $\boldsymbol{u}_1$ and $\boldsymbol{B}_1$ is uniformly distributed on $[0, 1]$, while the magnitude of $\boldsymbol{B}_0$ is uniformly distributed on $[0.5, 1]$ respectively. For $\boldsymbol{u}_0$, the magnitude is first uniformly distributed on $[0, 1]$ before being multiplied by another variable with

a log-uniform distribution, ranging from 1 to 10^c (Note that $\boldsymbol{u}_0$ and $\boldsymbol{u}_1$ represent 4-velocities).

4. A "temperature" parameter θ is chosen randomly from the log-uniform distribution, from 0.1 to 10. This parameter is intended to encode the temperature of the plasma, as the ratio of pressure to density, to model hot or cold plasmas. If $\theta > 1$ then the plasma is "hot", and we further divide the density ρ by θ. If $\theta \leq 1$ then the plasma is "cold", and we instead multiply the pressure p_g by θ. It is done in this manner to ensure that neither the density nor the pressure is increased, so that the magnitude of σ is not reduced by this step.

5. Given these random variables, first all the small variables $\rho, p_g, \boldsymbol{B}_1, \boldsymbol{u}_1$ are divided by the parameter σ' to make them small.

6. $\boldsymbol{u}_0$ is converted to a 3-velocity $\boldsymbol{v}_0$, which is then used to set $\boldsymbol{E}_0 = -\boldsymbol{v}_0 \times \boldsymbol{B}_0$.

7. We set $\boldsymbol{u} = \boldsymbol{u}_0 + \boldsymbol{u}_1$ as the full velocity of the state. This step is why we use 4-velocities, not 3-velocities, as in that case we could end up with $v^2 \geq 1$.

8. Finally, we calculate the 3-velocity $\boldsymbol{v}$ and set $\boldsymbol{E}_1 = -\left(\boldsymbol{E}_0 + \boldsymbol{v} \times \boldsymbol{B}\right)$.

In this manner we can construct a random state, for which we can roughly select the range of σ by choosing the limits a and b for the range of σ', and the maximum Lorentz factor by choosing c.

We are not finished however, as we also need an initial guess. For Method 1, we need only u^2. Any arbitrary random values would not be suitable. During the run of the actual code, the initial guess used is simply the previous state for the given grid point. This is obviously not available here, but we do know that the change between consecutive iterations in the state of any given grid point is not going to be particularly large; even with fast shocks moving near the speed of light, the difference between consecutive iterations can still be fairly small. Thus in order to test the conversion scheme on a relevant test, we need an initial guess which is fairly close to the true solution.

For that reason, we construct an initial guess by obtaining three different random variables distributed uniformly on $[0.9, 1.1]$. We then multiply each of the three components of $\boldsymbol{u}$ in the solution by a different one of these random variables, to represent a variance of around 10% in each of the three components of $\boldsymbol{u}$, after which we use u^2 of this altered $\boldsymbol{u}^*$ as the initial guess.

Now that we have constructed our test bed, we can finally present some of the results. Figs. 3.11a and 3.11c give the results of time taken and relative error, with $a = 1$ and

$b = 8$ so that σ' ranges from 10^1 to 10^8, and with $c = 10$ so that the Lorentz factor is capped at around 10.

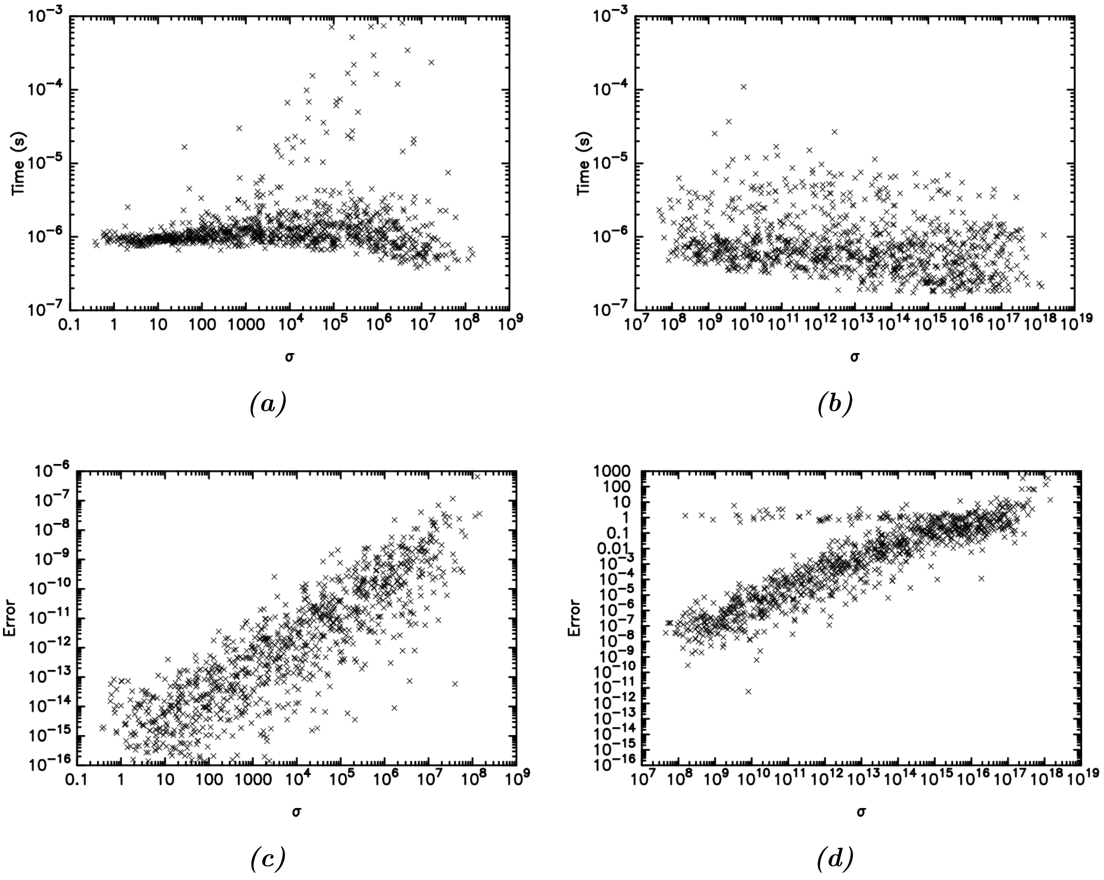

(a) *(b)*

(c) *(d)*

Figure 3.11: *Log-log plots of Time taken (top row) and relative error (bottom row) against σ for* 1,000 *randomly distributed tests of Method 1. Lorentz factor is capped at around* 10. *Each cross represents an individual test. (a) Time vs. σ, $10 \leq \sigma' \leq 10^8$. (b) Time vs. σ, $10^9 \leq \sigma' \leq 10^{18}$. (c) Error vs. σ, $10 \leq \sigma' \leq 10^8$. (d) Error vs. σ, $10^9 \leq \sigma' \leq 10^{18}$. Cases of the* 1,000 *where the algorithm failed to converge have been excluded.*

We can see clearly that Method 1 is quite fast, taking typically around 10^{-6} seconds to calculate a solution. On the other hand, we can clearly see an increase in error with σ, with the error increasing approximately proportional to σ.

We may also note a few sporadic cases in Fig. 3.11a which appear to have taken far longer to converge. While these cases are more common at higher σ, the trend is weak. In addition, a separate test against of 100,000 cases led to 488 outright failures to converge, a failure rate of around 0.5%.

These poor convergence cases correspond to cases where the secant method appears to straddle the root; instead of converging, the iterations steps just oscillate around the correct solution until it happens to put the iteration closer to the solution than previous.

Once the iteration is close enough to the solution, the algorithm can finally converge. This is also the cause of many of the convergence failures, as these occur when the procedure hits the iteration limit of 1,000 iterations.

If we change the range of σ' to 10^9 to 10^{18} (Figs. 3.11b and 3.11d) then the failure rate of Method 1 actually decreases to 257 out of 100,000, and curiously the convergence appears to become a little faster — although as we can see from Fig. 3.11d, the relative error of the solution is much too poor here to be useful.

Reducing Error

We can see from Fig. 3.11 that Method 1 suffers from a significant flaw, in that the error increases proportional to σ until it is simply too large to be useful. Reducing this error is therefore a very important objective.

The first source of error to consider lies in the algorithm for solving the cubic. The method used in Fig. 3.11 was a fairly basic cubic solving algorithm, which uses Cardano's method for cases with one real root, and trigonometric formulae for the case of three real roots. But we can have some problematic cases, since while a_3 cannot be small as it is bounded by $1 - 1/\kappa \leq a_3 \leq 1$, both a_2 and a_0 can be small quantities, and independently of each other. In order to remedy these to some extent, we used a Newton method to improve imperfect solutions.

By improving the accuracy of the cubic solver using a collection of different methods including asymptotic expansions as well as methods from Blinn (2006) and Press (2007), we were able to successfully eliminate errors arising from solving the cubic. These methods were also a little faster than the original scheme, as they are entirely analytic.

Cancelling Large Quantities The second problem with the variable conversion Method 1 is that several of the quantities themselves contain cancellation of large quantities. For instance, $\boldsymbol{S} \cdot \boldsymbol{B}$ will be close to 0 at large σ since the force-free component of $\boldsymbol{S}$ is orthogonal to $\boldsymbol{B}_0$, which is itself almost equal to $\boldsymbol{B}$. However, both $\boldsymbol{S}$ and $\boldsymbol{B}$ are not close to 0, and so most of this must cancel out in the dot product leading to significant numerical error.

If we expand $\boldsymbol{S} = \boldsymbol{S}_0 + \boldsymbol{S}_1$ and $\boldsymbol{B} = \boldsymbol{B}_0 + \boldsymbol{B}_1$ then the solution to this is quite simple

$$\begin{aligned} \boldsymbol{S} \cdot \boldsymbol{B} &= \boldsymbol{S}_0 \cdot \boldsymbol{B}_0 + \boldsymbol{S}_0 \cdot \boldsymbol{B}_1 + \boldsymbol{S}_1 \cdot \boldsymbol{B} \\ &= \boldsymbol{S}_0 \cdot \boldsymbol{B}_1 + \boldsymbol{S}_1 \cdot \boldsymbol{B}, \end{aligned} \tag{3.150}$$

which no longer has any issues with cancellation.

We can attempt to apply a similar method to other problematic components of Method 1, to see if we can cancel out the large quantities. Beginning with Eq. (3.141), we can substitute for U using Eq. (3.128) to give

$$a_2 = \frac{1}{2}\left(B^2 v^2 - E_0^2\right) - U_1 + \boldsymbol{B}_0 \cdot \boldsymbol{B}_1 + \frac{1}{2}B_1^2 + D\frac{\sqrt{1-v^2}}{\kappa}. \tag{3.151}$$

The only terms left which are $\mathcal{O}(1)$ are B^2v^2 and E_0^2, so their difference can be a source of significant error.

If we introduce the force-free drift velocity

$$\boldsymbol{v}_0 = \frac{1}{B_0^2}\boldsymbol{E}_0 \times \boldsymbol{B}_0, \tag{3.152}$$

then clearly $v_0^2 = E_0^2/B_0^2$, so we can write $B^2v^2 - E_0^2$ as

$$B^2v^2 - E_0^2 = B^2v^2 - B_0^2 v_0^2 = B_0^2\left(v^2 - v_0^2\right) + \left(2\left(\boldsymbol{B}_0 \cdot \boldsymbol{B}_1\right) + B_1^2\right)v^2, \tag{3.153}$$

and hence

$$a_2 = \frac{1}{2}\left(B_0^2\left(v^2 - v_0^2\right) + \left(2\left(\boldsymbol{B}_0 \cdot \boldsymbol{B}_1\right) + B_1^2\right)v^2\right) - U_1 + \boldsymbol{B}_0 \cdot \boldsymbol{B}_1 + \frac{1}{2}B_1^2 + D\frac{\sqrt{1-v^2}}{\kappa}, \tag{3.154}$$

thus the error has been mostly eliminated. The term $B_0^2\left(v^2 - v_0^2\right)$ is now the only term which is $\mathcal{O}(1)$ so there may be issues if $v^2 \approx v_0^2$.

One method of remedying this would be to use 4-velocity instead. If we let

$$u^2 = \frac{v^2}{1-v^2}, \quad \text{and} \quad u_0^2 = \frac{v_0^2}{1-v_0^2}, \tag{3.155}$$

then $v^2 - v_0^2$ becomes

$$v^2 - v_0^2 = \frac{u^2 - u_0^2}{\left(1+u^2\right)\left(1+u_0^2\right)}. \tag{3.156}$$

Thus the problem has shifted from when $v^2 - v_0^2$ is small to when $u^2 - u_0^2$ is small. This makes the error u^2 times smaller than before, and so when u^2 is large, this error is reduced. Of course, we could still have problems when u^2 is also small.

The only other part which may have problems is Eq. (3.136), which also features a mix of large and small quantities. It is not immediately clear how to deal with this case. Even if we expand $\boldsymbol{B}$ and others, large quantities still do not all cancel. However, if we divide the cubic Eq. (3.139) by W^2, then we obtain the expression

$$\frac{\boldsymbol{S} \cdot \boldsymbol{B}}{W^2} = 2\left(a_3 W + a_2\right), \tag{3.157}$$

which we can substitute into Eq. (3.136). If we let

$$\bar{U} = U_1 - \boldsymbol{B}_0 \cdot \boldsymbol{B}_1 - \frac{1}{2}B_1^2 = U - \frac{1}{2}E_0^2, \tag{3.158}$$

then after substituting Eq. (3.157) into Eq. (3.136) and cancelling out terms in B^4, we arrive at

$$W^2 v^2 + 4UW + 4\left(p_g - W\right)\left(W + \frac{1}{2}B^2\right) = \\ S_1^2 + 2\left(\boldsymbol{S}_0 \cdot \boldsymbol{S}_1\right) - 2\bar{U}B^2 - B_0^2 v_0^2 \left(B_1^2 + 2\left(\boldsymbol{B}_0 \cdot \boldsymbol{B}_1\right)\right), \quad (3.159)$$

where we note that now all terms are at most $\mathcal{O}(\sigma^{-1})$.

Secant Method Although the method described above is usually very effective, it can sometimes have some difficulties with specific cases. Most commonly, the initial guess may not be good enough to be inside the region of fast convergence for the Secant method, and the result is that the iteration parameter jumps around, often to either side of the solution.

This is a well known issue with the Secant method; while more stable than Newton's method, it still does not have the guaranteed convergence of the bisection method. Naturally, this being well known means that there are several methods to remedy it.

We chose to follow (Martínez, 1994) and add a relaxation parameter $0 < \omega \leq 1$ to the method. If we denote the normal update to x_n by the secant method by $x_{n+1} = x_n + F$, then the relaxation parameter is used to change the update to $x_{n+1} = x_n + \omega F$. This reduces the change in x_{n+1} and prevents the iterates from jumping over the true solution.

However, this comes at the cost of reduced order of convergence. Thus the best choice may be to start with $\omega = 1$ to allow unproblematic cases to converge quickly, before reducing ω until the method converges for the more troublesome cases.

In our case, reducing ω at specific iteration counts was found to do the trick; we reduce ω via the scheme: $\omega = 0.9$ at iteration 16, $\omega = 0.8$ at iteration 32, $\omega = 0.7$ at iteration 64, $\omega = 0.6$ at iteration 128, and $\omega = 0.5$ at iteration 256. This scheme was found to be able to allow even the most difficult cases to converge eventually.

An alternative (that we have not implemented thus far) is to apply the Brent-Dekker method instead (Dekker, 1969; Brent, 1971) The basic idea behind this algorithm is to combine the secant method with the bisection method, in order to take advantage of the secant method's rate of convergence and the bisection method's guaranteed convergence.

Testing Method 2

With these adjustments to Method 1, we shall call the resulting new method as "Method 2". We can now try retesting it again, to see if we have successfully reduced the error. Fig. 3.12 shows the results of testing this altered method. We can see that thanks to our adjustments, nearly all the error at high σ has been eliminated. Where once the error increased with σ, it is now flat, and does not appear to increase with σ at all, even all the way up to $\sigma = 10^{18}$, which is well beyond the level of σ at which we needed it to work. Thus Method 2 is now superior to Method 1 in all properties — including number of failures, for which there were no convergence failure cases in 100,000 tests, even for the high-σ range $10^9 \leq \sigma' \leq 10^{18}$ — making it all around the best option.

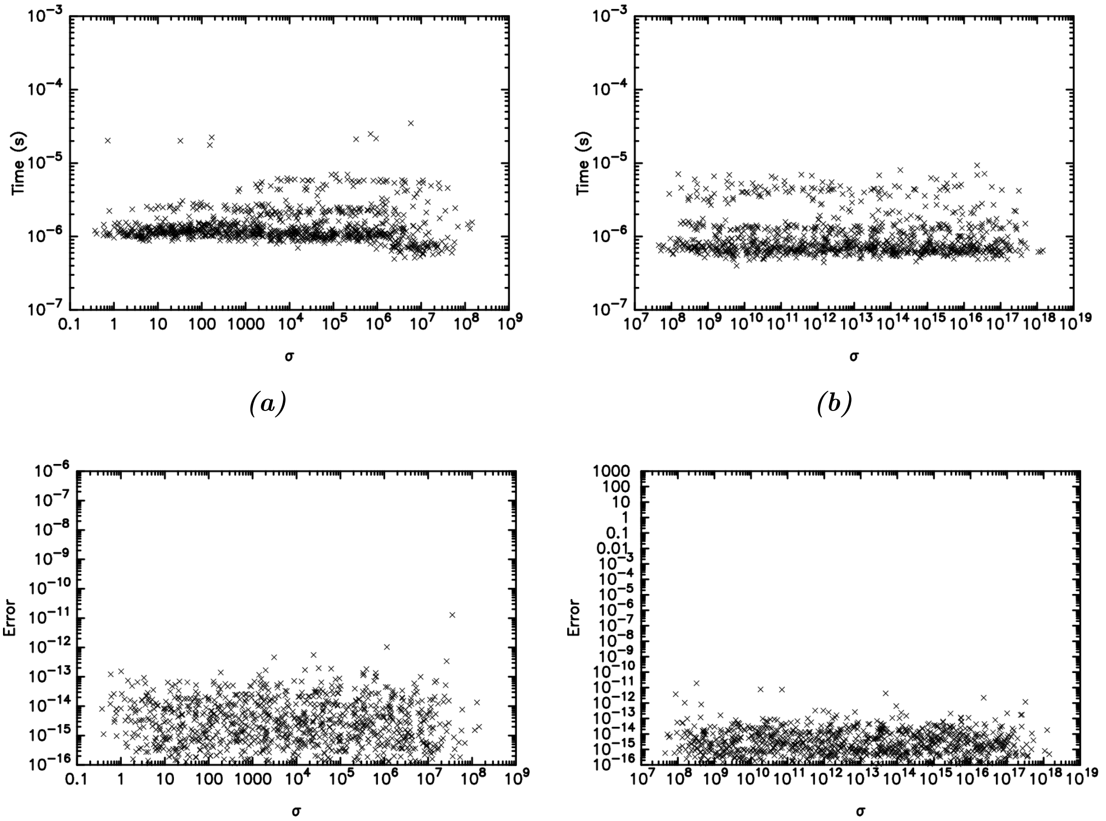

(a) *(b)*

(c) *(d)*

Figure 3.12: *Time taken and relative error against* σ *for* 1,000 *randomly distributed tests of Method 2. Lorentz factor is capped at around* 10. *Each cross represents an individual test. (a) Time vs.* σ*,* $10 \leq \sigma' \leq 10^8$*. (b) Time vs.* σ*,* $10^9 \leq \sigma' \leq 10^{18}$*. (c) Error vs.* σ*,* $10 \leq \sigma' \leq 10^8$*. (d) Error vs.* σ*,* $10^9 \leq \sigma' \leq 10^{18}$*.*

Previously we tried to eliminate the error arising from $v^2 \approx v_0^2$, but were only able to eliminate some of the error. Fig. 3.13a shows the relative error in Method 2 against $v^2 - v_0^2$. We can see a small spike at $v^2 = v_0^2$ indicating that there is still some error here, but at least for this test bed the problem is rather insignificant.

Another issue we have neglected is the effects of large γ. Fig. 3.13b shows the results of error for tests with $1 \leq \gamma \leq 10^3$, plotted against γ. Like σ before, there is a clear increase in error as σ increases, approximately proportional to γ^2. This would appear to be a significant problem like with σ, but while the error is large at high Lorentz factors, in practice we do not expect to have exceptionally high Lorentz factors with $\gamma > 10^3$.

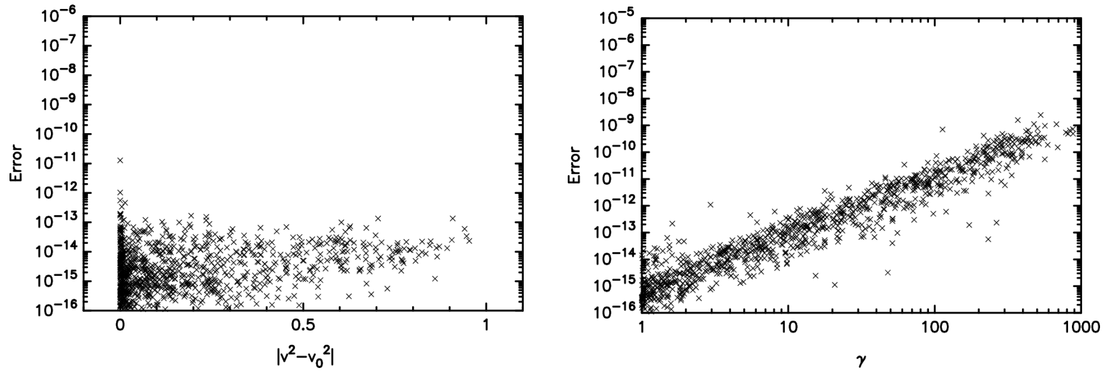

(a) *(b)*

Figure 3.13: *Relative error against* $v^2 - v_0^2$ *and* γ *for* 1,000 *randomly distributed tests with* $10 \leq \sigma' \leq 10^8$*. Each cross represents an individual test. (a) Error vs.* $v^2 - v_0^2$*,* $1 \leq \gamma \leq 10$*. (b) Error vs.* γ*,* $1 \leq \gamma \leq 10^3$*.*

In conclusion, we have successfully developed a primitive conversion scheme that maintains low error even into extreme values of σ of $\sigma > 10^{18}$ or more (assuming our test bed was a fully representative sample of possible states of the system, of course). Thanks to this reduction in error, we can be quite confident that any failures of the overall scheme are not caused by this primitive conversion algorithm. This method is also quite fast as well as each iteration only needs to solve a cubic equation and perform a single 1D Secant method step, as opposed to the basic 5D Newton method we developed initially.

Thus for all the tests in chapters 4 and 5 we use Method 2 to convert the conservatives into primitives.

One thing to note is that when developing this scheme, we pointed out that we could adapt an already existing conversion algorithm for RMHD for our interaction terms. Thus we followed the method proposed by Del Zanna *et al.* (2007) for RMHD since we asserted that our scheme should be able to use an adaptation of an RMHD solver. However, there are of course multiple different solvers in the literature we could use, and it is possible that we could have used any of them.

However, it is not clear if any other schemes will allow for the cancellations that we used in our scheme to avoid the errors. All schemes for inverting RMHD naturally work with relatively large quantities like the total momentum and energy, and it may be that depending on the scheme, cancellation is difficult, if at all possible.

3.2.7 Primitive Interpolation

Previously in section 3.1.3, we discussed the interpolation scheme that reconstructs the variables at the cell boundaries to set up the Riemann problems. At that time we were considering interpolation in terms of the primitives $\boldsymbol{P}$, but in practice we can choose any set of variables satisfying the conditions set above for primitives, including either the primitives we have chosen or the conservatives.

Different choices of interpolating variables will naturally give different results for the interpolation. For instance, a contact discontinuity only features a jump in ρ, out of all the primitives discussed above. But of the conservatives, there is a jump in conserved mass, momentum and energy.

However, although interpolating on the conservatives could be a good choice, doing so requires that we convert them back into primitives in order to calculate the fluxes, adding extra variable conversion steps that could significantly slow the code. In practice, we have generally chosen to interpolate on the primitives.

Since interpolation does not consider any bounds on the variables themselves, such as the bound $\rho, p_g > 0$ on the density and gas pressure, it is plausible that interpolation may occasionally break such conditions, which is not desirable. This is one of the reasons we have chosen to use the 4-velocity $\boldsymbol{u}$ instead of the 3-velocity $\boldsymbol{v}$, since $\boldsymbol{v}$ is bound by $0 \leq v^2 < 1$ while $\boldsymbol{u}$ is only bounded from below by $u^2 \geq 0$. In practice, we have found that the bounds on ρ and p_g are not typically broken and can easily be dealt with via a minimum lower bound on each variables, such as 10^{-6}.

Other bounds prove more challenging however, especially bounds or restrictions that involve multiple variables. Particularly notable are the PC conditions on the force-free system and the interaction system. For the force-free system, we must satisfy $\boldsymbol{B}_0 \cdot \boldsymbol{E}_0 = 0$. Generally speaking an arbitrary polynomial interpolation will not satisfy this condition at the boundaries. There are not many obvious remedies to this issue; the only method that immediately springs to mind is that we could select one of the components of $\boldsymbol{B}_0$ or $\boldsymbol{E}_0$ and change that variable alone to satisfy the condition.

$\boldsymbol{B}_0$ is a known conserved quantity, so it seems reasonable to choose to alter $\boldsymbol{E}_0$ only. This gives us three choices, but these choices are not all equivalent. If the corresponding component of $\boldsymbol{B}_0$ or $\boldsymbol{E}_0$ is 0, then changing this variable will have no effect on the condition. For the remainder, the amount by which they change could be significant, and minimising this change is desirable since the interpolated value should be close to the “true” value.

One possibility is to simply choose the component that will change the least if we impose the condition. This can easily be identified as the variable whose corresponding component is the largest, since small changes in this variable will have the largest effects on $\boldsymbol{B}_0 \cdot \boldsymbol{E}_0$ and thereby minimise the amount by which the variable would need to change. However, this could still potentially be a relatively large change in the component.

An alternative would be to change more than one component, and eliminate the component of $\boldsymbol{E}_0$ parallel to $\boldsymbol{B}_0$ by setting

$$\boldsymbol{E}_0 = \boldsymbol{E}_0 - \boldsymbol{B}_0 \frac{(\boldsymbol{B}_0 \cdot \boldsymbol{E}_0)}{B_0^2}. \tag{3.160}$$

This is equivalent to be the value of $\boldsymbol{E}_0$ that satisfies the $\boldsymbol{B}_0 \cdot \boldsymbol{E}_0 = 0$ that is closest in a least-squares sense to the original $\boldsymbol{E}_0$.

For the interaction system, this condition-breaking only occurs if we interpolate $\boldsymbol{E}_1$ as well as the remaining primitives ρ, $\boldsymbol{u}$, p_g and $\boldsymbol{B}_1$, which would generally not satisfy the full PC condition Eq. (3.96). With that said, we also need the force-free variables available and so we still need to contend with the same problem as before.

This gives a new method of satisfying $\boldsymbol{B}_0 \cdot \boldsymbol{E}_0 = 0$ that was not available previously — since we have access to the 4-velocity $\boldsymbol{u}$ now, we could set $\boldsymbol{E}_0 = -\boldsymbol{v} \times \boldsymbol{B}_0$ to automatically satisfy $\boldsymbol{B}_0 \cdot \boldsymbol{E}_0 = 0$. Then we could similarly set $\boldsymbol{E}_1 = -\boldsymbol{v} \times \boldsymbol{B}_1$ to satisfy Eq. (3.96) as well. Unfortunately, this breaks third-order convergence for the scheme, and is thus not suitable as a method for remedying this problem unless we can find a condition for when to turn this part of the code on or off. This condition would need to be chosen such that the PC condition is enforced for the interpolation, when necessary, but dropped when unnecessary to allow the code to be third-order.

Alternatively, we could use the same method as with the force-free system to alter one variable of $\boldsymbol{B}_0$ and $\boldsymbol{E}_0$, and then enforce Eq. (3.96) to set

$$\boldsymbol{E}_1 = -\left(\boldsymbol{E}_0 + \boldsymbol{v} \times \boldsymbol{B}_0\right) - \boldsymbol{v} \times \boldsymbol{B}_1. \tag{3.161}$$

This is problematic because at high σ the quantity $\boldsymbol{E}_0 + \boldsymbol{v} \times \boldsymbol{B}_0$ should be $\mathcal{O}(\sigma^{-1})$. But these quantities are both $\mathcal{O}(1)$, so this quantity is the difference of two large quantities. As we were discussing previously in section 3.2.6 this is a major source of error in numerical schemes, so this calculation of $\boldsymbol{E}_1$ is highly susceptible to error at high σ. Unfortunately, finding an $\boldsymbol{E}_0$ which eliminates this problem in some way is difficult, besides the method given previously which as we noted does not allow for third-order convergence.

There is in fact one more somewhat surprising alternative: simply leave these conditions unsatisfied. In the solution of the HLL solver, none of these conditions need to be satisfied exactly in order to get a valid result. We still need to calculate phase speeds, but for this we are using full RMHD phase speeds, so we do not need $\boldsymbol{E}$, it will automatically be assumed to be $\boldsymbol{E} = -\boldsymbol{v} \times \boldsymbol{B}$ during the calculation of phase speeds. For the force-free system, these phase speeds need not be calculated at all as we use the speed of light. Note that this choice only works for the HLL solver; the other solvers need to calculate the Alfvén phase speeds, and we can see from section 2.2.2 that these phase speeds are only physical if $B^2 - E^2 > 0$.

In practice, we have found that enforcing the PC condition via Eqs. (3.160) and (3.161) can occasionally be helpful — specifically for stationary fast shocks — but there are alternative methods that also help in those cases as well anyway. Furthermore, for some tests such as magnetic island collapse in section 5.2.4, this alteration actually causes problems with the code, and causes it to fail when running with the third order code. As such, we decided to leave $\boldsymbol{E}_0$ and $\boldsymbol{E}_1$ alone, i.e. we do not enforce the PC condition for any of the tests presented in chapters 4 and 5.

3.2.8 Summary of the Scheme

To finish this chapter, we will summarise the equations being solved, and the steps of the optimal version of the code. This includes some corrective adjustments we have not yet described — specifically, E_0-capping (see section 4.3.5) and conditional energy transfer (see section 4.3.4).

Force-Free System

The force-free sub-system consists of seven evolution equations Eqs. (3.83) to (3.85) and three constraints Eqs. (3.86), (3.88) and (3.89). The evolution equations are momentum conservation

$$\partial_t(\boldsymbol{E}_0 \times \boldsymbol{B}_0) + \boldsymbol{\nabla} \cdot \left(-\boldsymbol{E}_0\boldsymbol{E}_0 - \boldsymbol{B}_0\boldsymbol{B}_0 + \frac{1}{2}\left(E_0^2 + B_0^2\right)\delta^{ij}\right) = 0, \tag{3.162}$$

energy conservation

$$\partial_t\left(\frac{1}{2}\left(E_0^2 + B_0^2\right)\right) + \boldsymbol{\nabla} \cdot (\boldsymbol{E}_0 \times \boldsymbol{B}_0) = 0, \tag{3.163}$$

and Faraday's law

$$\partial_t \boldsymbol{B}_0 - \boldsymbol{\nabla} \times \boldsymbol{E}_0 = 0. \tag{3.164}$$

Meanwhile the constraints are

$$\boldsymbol{\nabla} \cdot \boldsymbol{B}_0 = 0, \quad \boldsymbol{B}_0 \cdot \boldsymbol{E}_0 = 0, \quad B_0^2 - E_0^2 > 0. \tag{3.165}$$

As we have discussed at length above, these equations are degenerate, and it is thus not necessary to evolve all of them. In particular, the easiest to drop is energy conservation. However, we do in fact evolve all seven equations for use in the corrective step of conditional energy transfer, step 13 of the summary below in section 3.2.8. The details of this step are discussed in more detail in section 4.3.4.

For a multidimensional scheme, we alter these equations slightly for the GLM scheme. In particular, an extra term is added to Faraday's Law to give Eq. (3.108)

$$\frac{\partial \boldsymbol{B}_0}{\partial t} + \boldsymbol{\nabla} \times \boldsymbol{E}_0 + \boldsymbol{\nabla}\phi_0 = 0, \tag{3.166}$$

and the constraint $\boldsymbol{\nabla}\cdot\boldsymbol{B}_0 = 0$ is converted to Eq. (3.109)

$$\frac{\partial \phi_0}{\partial t} + \boldsymbol{\nabla}\cdot\boldsymbol{B}_0 = -\kappa\phi_0. \tag{3.167}$$

Interaction System

The interaction sub-system consists of a further eight evolution equations Eqs. (3.90) to (3.93), and two constraints Eqs. (3.94) and (3.96). The evolution equations are mass conservation

$$\partial_t\left(\rho u^0\right) + \boldsymbol{\nabla}\cdot(\rho\boldsymbol{u}) = 0, \tag{3.168}$$

momentum conservation

$$\begin{aligned}\partial_t\Big(w u^0\boldsymbol{u} + \boldsymbol{E}_0\times\boldsymbol{B}_1 + \boldsymbol{E}_1\times\boldsymbol{B}_0 + \boldsymbol{E}_1\times\boldsymbol{B}_1\Big) + \boldsymbol{\nabla}\cdot\big(w\boldsymbol{u}\boldsymbol{u} - \boldsymbol{E}_0\boldsymbol{E}_1 - \boldsymbol{E}_1\boldsymbol{E}_0 - \boldsymbol{E}_1\boldsymbol{E}_1 \\ -\boldsymbol{B}_0\boldsymbol{B}_1 - \boldsymbol{B}_1\boldsymbol{B}_0 - \boldsymbol{B}_1\boldsymbol{B}_1 + \Big(p_g + \boldsymbol{E}_0\cdot\boldsymbol{E}_1 + \boldsymbol{B}_0\cdot\boldsymbol{B}_1 + \frac{1}{2}\Big(E_1^2 + B_1^2\Big)\Big)\,\delta^{ij}\Big) = 0,\end{aligned} \tag{3.169}$$

energy conservation,

$$\begin{aligned}\partial_t\Big(w u^0 u^0 - p_g + \boldsymbol{E}_0\cdot\boldsymbol{E}_1 + \boldsymbol{B}_0\cdot\boldsymbol{B}_1 + \frac{1}{2}\Big(E_1^2 + B_1^2\Big)\Big) \\ + \boldsymbol{\nabla}\cdot\Big(w u^0\boldsymbol{u} + \boldsymbol{E}_0\times\boldsymbol{B}_1 + \boldsymbol{E}_1\times\boldsymbol{B}_0 + \boldsymbol{E}_1\times\boldsymbol{B}_1\Big) = 0,\end{aligned} \tag{3.170}$$

and finally Faraday's law

$$\partial_t\boldsymbol{B}_1 - \boldsymbol{\nabla}\times\boldsymbol{E}_1 = 0, \tag{3.171}$$

while the constraints are

$$\boldsymbol{\nabla}\cdot\boldsymbol{B}_1 = 0, \quad \boldsymbol{E}_1 = -\left(\boldsymbol{E}_0 + \boldsymbol{v}\times\boldsymbol{B}_0\right) - \boldsymbol{v}\times\boldsymbol{B}_1. \tag{3.172}$$

Once again, in a multidimensional scheme these equations are modified for the GLM method so that Faraday's Law becomes Eq. (3.110)

$$\frac{\partial \boldsymbol{B}_1}{\partial t} + \boldsymbol{\nabla}\times\boldsymbol{E}_1 + \boldsymbol{\nabla}\phi_1 = 0, \tag{3.173}$$

and the constraint $\boldsymbol{\nabla}\cdot\boldsymbol{B}_1 = 0$ is converted to Eq. (3.111)

$$\frac{\partial \phi_1}{\partial t} + \boldsymbol{\nabla}\cdot\boldsymbol{B}_1 = -\kappa\phi_1. \tag{3.174}$$

The Integration Scheme Steps

At the start of each time step, we keep only the known cell values at the centre of each cell. These values are then updated via:

1. Interpolate both the force-free and interaction primitive cell values $\boldsymbol{P}_0$ and $\boldsymbol{P}_1$ to the cell boundaries using Eqs. (3.44) and (3.47). We also use the novel smoothness indicators Eq. (3.56), with $n_s = 5$.

2. If the test is multidimensional, for the x-boundary interpolations set the interpolated B_x^0 and B_x^1 for the left and right states to the average of the two sides of the Riemann problem at that location, in order to ensure the 1D condition of constant B_x^0 and B_x^1 is true at the Riemann problems. Do the same for y-boundaries but for B_y^0 and B_y^1, and the same for z.

3. Solve the Riemann problems at each cell boundary for both the force-free and interaction variables using an HLL solver as described in section 3.1.2, Eqs. (3.38) and (3.39). The force-free Riemann solver uses signal velocities of ± 1 for the HLL scheme, while the interaction solver calculates all phase speeds for all waves in both states and uses the most extreme in either direction (since the most extreme will always be fast waves, only the magnetosonic wave speeds are actually calculated). This gives the fluxes at the boundaries $\boldsymbol{F}_{i+1/2}$ (and $\boldsymbol{G}_{i+1/2}$ etc. for higher dimensions).

4. Implement the DER step as described in section 3.1.4, Eq. (3.68). A central stencil is used for the estimates of the second derivatives.

5. Using Eq. (3.16) (or Eq. (3.99) etc. for higher dimensions), calculate the Runge-Kutta sub step total gradient $\boldsymbol{K}_i$ from Eq. (3.77) for both the force-free and interaction systems.

6. Update the conservatives $\boldsymbol{Q}_0$ and $\boldsymbol{Q}_1$ using the appropriate Runge-Kutta sub-step equation from Eq. (3.77), and calculate the force-free primitives $\boldsymbol{P}_0$ of this state using Eq. (3.118).

7. Perform the E_0-capping step discussed in section 4.3.5: If $E_0^2 > B_0^2$ in any cell, cap E_0^2 by setting its magnitude to either $E_0^2 = 2U_0 - B_0^2$ (where U_0 is the conserved force-free energy determined via integration of Eq. (3.84), force-free energy conservation) or to $0.99B_0^2$, whichever is smaller.

8. Use the primitive conversion scheme Method 2 from section 3.2.6 to calculate the interaction primitives $\boldsymbol{P}_1$.

9. Apply boundary conditions to the primitives $\boldsymbol{P}_0$ and $\boldsymbol{P}_1$, and recalculate force-free and interaction conservatives $\boldsymbol{Q}_0$ and $\boldsymbol{Q}_1$ from the updated $\boldsymbol{P}_0$ and $\boldsymbol{P}_1$.

10. Perform steps 1 to 9 for the remaining two Runge-Kutta sub-steps and obtain the total gradients $\boldsymbol{K}_2$ and $\boldsymbol{K}_3$ using Eq. (3.77), changing the equation in step 5 as appropriate.

11. Use the three sub-step total gradients $\boldsymbol{K}_1$ to $\boldsymbol{K}_3$ to calculate the conservatives for the next time step, $\boldsymbol{Q}_{n+1}$.

12. Calculate the force-free primitives $\boldsymbol{P}_0$ of this state using Eq. (3.118), and apply E_0-capping again like step 7.

13. Perform the condition energy transfer step discussed in section 4.3.4: If the force-free energy calculated from $\boldsymbol{P}_0$, i.e. $U_0^* = \frac{1}{2}\left(B_0^2 + E_0^2\right)$, is less than the energy as updated via the integration scheme U_0, then transfer the difference $U_0 - U_0^*$ to the interaction energy, $U_1 = U_1 + U_0 - U_0^*$, and remove it from the force-free energy $U_0 = U_0^*$. Since this is the energy of $\boldsymbol{P}_0$ already there is no need to recalculate $\boldsymbol{P}_0$.

14. For a multidimensional scheme, solve the GLM source term equation Eq. (3.113) analytically using Eq. (3.115), with $\kappa = 100$.

This sequence of steps performs a single time step of the integration scheme.

Chapter 4

1D results

In this section we will start to test the code described in section 3.2 with various tests in 1D to find its strengths and limitations. We will also introduce various alterations to the code, in order to remedy these flaws. At the end of this chapter, we will test the convergence of the third order code for smooth solutions.

4.1 Test Configuration

Note that in all figures given below, the black crosses indicate the cell values and the red line is the exact solution, unless stated otherwise. If present, the green line is the initial state. The resolution (i.e. number of cells in the computational domain, not counting boundary cells) varies between each case, and is given in the descriptions of the plots. Since we have not used an adaptive mesh refinement scheme, which would increase resolution in specific regions to capture fine details, this resolution stays constant and the cell spacing Δx remains constant throughout as well.

For the boundary conditions, we want a simple option. One property we may desire is the so-called radiation condition, which stipulates that most (if not all) energy of a wave passing the boundary is not reflected, so that the wave passes freely thorough the boundary. Unfortunately, while a radiation boundary condition of this type is possible for individual wave modes, with seven separate wave modes it is not possible to allow all wave modes through cleanly at once.

We therefore chose to use a simple Neumann boundary condition with the gradient equal to 0 at both ends of the domain. This allows most waves to pass relatively freely, with — for the most part — little reflected back into the domain. This is easily implemented by setting the values in the boundary cells equal to the outermost cell of the integration region proper.

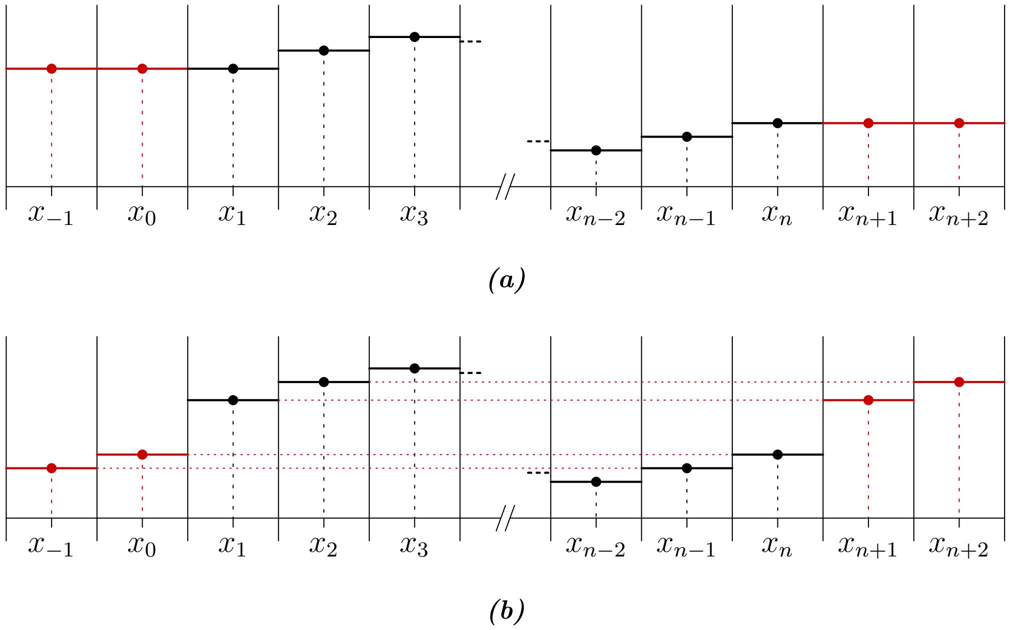

Figure 4.1: *1D Neumann (a) and periodic boundary conditions (b) applied to the same data. The computational domains have n cells from $x = x_1$ to $x = x_n$. The boundary cells at either end are drawn in red, located at $x = x_{-1}, x_0$ on the left and $x = x_{n+1}, x_{n+2}$ on the right.*

Besides a Neumann boundary condition, some tests instead use Periodic boundary conditions. There are implemented by setting the boundary cell values equal to the cells at the other end of the integration domain. Fig. 4.1 contains diagrams of these two boundary conditions, for a system with two boundary cells at each end.

4.2 Continuous Tests

We begin with continuous test cases, since these are likely to be easier to handle, due to the smaller gradients.

4.2.1 Small Amplitude Waves

For our initial test, we start with one of the simplest tests possible, that of small amplitude waves as discussed in section 2.3.2. This test is done with a constant background state, along with a superposition of left and right fast waves, left and right Alfvén waves, and left and right slow waves (i.e. all wave types, besides entropy waves), each with their own (very small) amplitudes and waveforms.

Figs. 4.2a and 4.2c show the results of this test for p_g and B_z. The background state for this test is $\rho = 10^{-5}, p_g = 5.1220 \times 10^{-6}, \boldsymbol{u} = (-1, 0.22321, -0.013397)$ and

$\boldsymbol{B} = (1, 2.2321, -0.13397)$, and so therefore we have $\sigma = 100{,}000$ and $\sigma^* = 48{,}780$. As we can see from these results, the code can handle this without significant issue, besides some small variation due to numerical diffusion. This error is less significant than it appears due to the low amplitude of the original wave.

This error can be counteracted simply by either increasing the resolution or the order of the code, as we can see on the right of Fig. 4.2 where we have run the same test with twice the resolution. We can see that the error in gas pressure and magnetic field is significantly reduced.

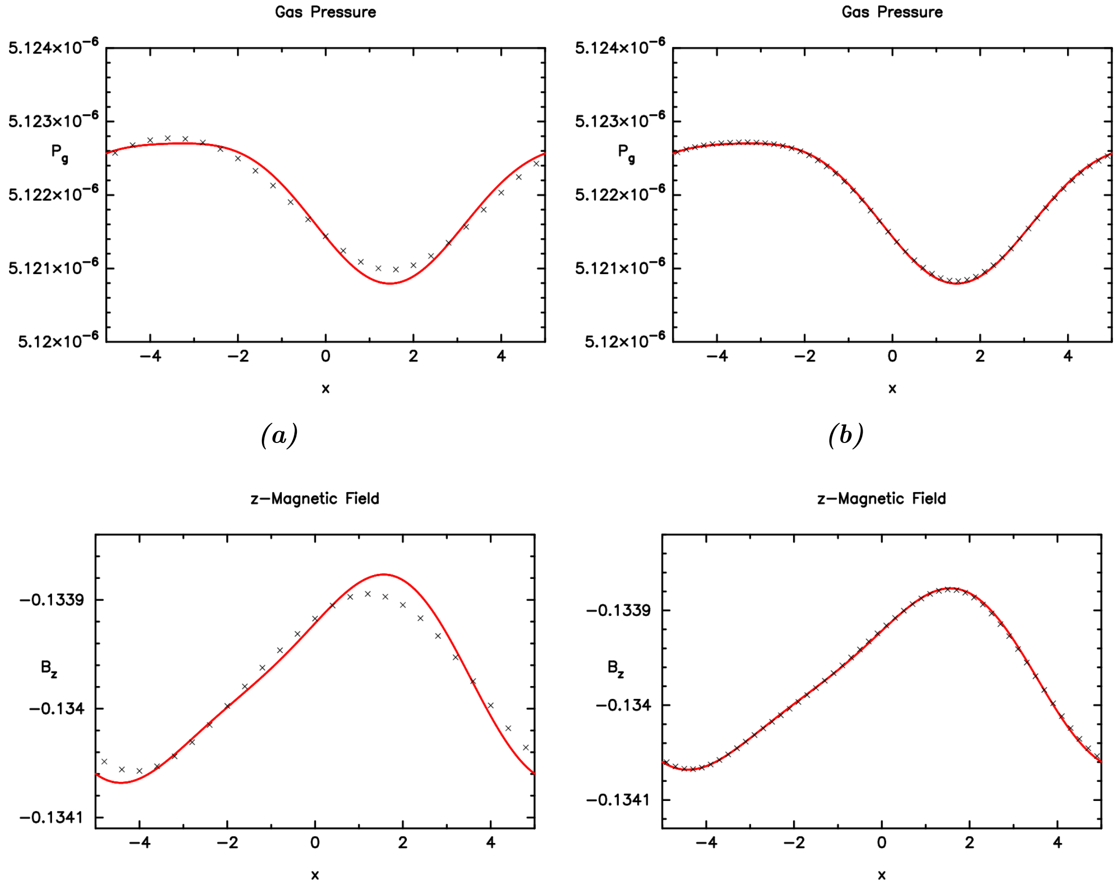

(a) *(b)*

(c) *(d)*

Figure 4.2: *p_g (top row) and B_z (bottom row) for a small-amplitude Wave test up to $t = 100$, using a third order code and Periodic BCs. The tests were run at resolution 50 (left column) and 100 (right column). In this state, the background value of $\sigma = 10^5$.*

This test demonstrates that the base code works correctly at least. The numerical solution is shown to converge to the correct solution with at least order 1 for continuous solutions. Given that the code still solves the equations of full RMHD, albeit split into separate pieces, this is not particularly unexpected.

We could now try other small amplitude tests, such as changing the background state so that one or more of the waves are degenerate. But while a Linear Riemann solver must treat these cases separately, and thus could fail independently, we are actually using an HLL solver which does not perform differently under other circumstances. Therefore further tests of this type are not likely to be particularly enlightening, and it is better to move on to more challenging, non-linear tests of our code.

4.2.2 Simple Waves

Increasing the difficulty now, we move out of the linear regime to simple waves, as discussed in section 2.3.2. These come in four different types, corresponding to the three different types of waves in RMHD, and an entropy wave. The entropy wave only has a variation in density, and is merely advected with the flow, behaving exactly the same as it did in the small amplitude case. We therefore skip this solution and move on to the other three cases.

Alfvén Waves

We start off some simple wave tests with an Alfvén wave, which we discussed in section 2.3.2. These waves are unique in that the density ρ and pressure p_g are unaffected.

Let us compare the RMHD solution with the FFDE solution, in order to determine what effects we expect the interaction system to have. In the fluid frame, the Alfvén phase speeds of RMHD are

$$\mu_a^R = \pm\frac{B_x}{\sqrt{w+B^2}} = \pm\frac{B_x}{|\boldsymbol{B}|\sqrt{1+\sigma^{-1}}} = \pm\frac{\cos\theta}{\sqrt{1+\sigma^{-1}}}, \tag{4.1}$$

meanwhile the phase speeds in FFDE are

$$\mu_a^F = \pm\frac{B_x}{|\boldsymbol{B}|} = \pm\cos\theta, \tag{4.2}$$

where θ is the angle between $\boldsymbol{B}$ and the x-axis. Comparing these we can clearly see that the introduction of the interaction terms should slow the Alfvén waves by a factor of $\sqrt{1+\sigma^{-1}}$. This effect will be more pronounced near the RMHD Alfvén wave frame instead of the fluid frame. This is especially the case for $\theta = 0$, i.e. the magnetic field parallel to the x-axis, since in this frame the FFDE Alfvén speed is in fact the speed of light, so no matter what frame we are in these waves will always move at this speed.

We can also compare the eigenvectors; in RMHD and in the fluid frame, we have from Eq. (4.1) that $\mu_a = \pm B_x/\sqrt{\mathcal{E}}$, so from Eq. (2.75) the variations in u^α, $\boldsymbol{B}$ and $\boldsymbol{E}$ are

$$d\boldsymbol{B} = (0, -B_z, B_y), \quad du^\alpha = \pm\frac{1}{\sqrt{w+B^2}}(0,0,B_z,-B_y),$$

$$d\boldsymbol{E} = \pm\frac{1}{\sqrt{w+B^2}}\left(-\left(B_y^2+B_z^2\right), B_xB_y, B_xB_z\right),$$

where the sign indicates the direction of the wave in the x-axis. Meanwhile, for FFDE, Eq. (2.113) in the fluid frame ($\boldsymbol{E} = 0$) gives $\mu_a^\pm = \pm B_x/B$, and so with inserting this into Eq. (2.115), the eigenvectors are then

$$d\boldsymbol{B} = (0, -B_z, B_y)\,, \quad d\boldsymbol{E} = \frac{1}{B}\left(-\left(B_y^2 + B_z^2\right), B_x B_y, B_x B_z\right).$$

Hence these are identical besides a factor of $\sqrt{1+\sigma^{-1}}$ just like with the phase speed, which serves to reduce the relative variation of $\boldsymbol{E}$ in RMHD compared to FFDE, with the difference approaching 0 as $\sigma \to \infty$.

Problem	Figure	State at $\phi = 0$	State at $\phi = \pi/2$
Low-σ Alfvén Wave, $\mu = -0.3$	4.3	$\boldsymbol{u} = (-0.78878, -0.73030, 0)$, $\boldsymbol{B} = (2, 4.1931, 0)$, $\rho = 10$, $p_g = 5$, $\sigma = 0.66667$, $\sigma^* = 0.30929$	$\boldsymbol{u} = (-0.78878, -0.71554, -0.14606)$, $\boldsymbol{B} = (2, 4.1084, 0.83863)$, $\rho = 10$, $p_g = 5$, $\sigma = 0.66667$, $\sigma^* = 0.30929$
High-σ Alfvén Wave, $\mu = 0.94$	4.4	$\boldsymbol{u} = (-0.21587, -4.0249, 0)$, $\boldsymbol{B} = (2.7, 2.6379, 0)$, $\rho = 0.01$, $p_g = 0.01$, $\sigma = 162$, $\sigma^* = 9.3932$	$\boldsymbol{u} = (-0.21587, -3.8395, -1.2075)$, $\boldsymbol{B} = (2.7, 2.5164, 0.79138)$, $\rho = 0.01$, $p_g = 0.01$, $\sigma = 162$, $\sigma^* = 9.3932$

Table 4.1: *Initial test case data for both 1D Alfvén wave tests. "μ" is the phase velocity of the wave. Given here is the state at phase $\phi = 0$ and $\phi = \pi/2$. Since the domain is $[-5, 5]$ for both tests, this is the initial states at the locations $x = -5$ and $x = -2.5$, respectively.*

Thus the effects of the interaction system on the results should be fairly subtle in the fluid frame, only serving to slow the waves down and decrease $d\boldsymbol{E}$. Naturally, these effects should be more pronounced at lower σ, as the system diverges from the pure force-free system.

As with the small amplitude waves, the phase speed of Alfvén waves is invariant across them, and therefore the whole wave moves together at constant speed without changing over time. We can choose the waveform of our tests to our liking as well.

For our tests here, we construct the Alfvén wave starting in the de Hoffmann-Teller frame. In this frame, the Alfvén wave reduces to a rotation in magnetic field and velocity, keeping them parallel. So, starting with the magnetic field without a z-component, $\boldsymbol{B} = (B_x, B_\perp, 0)$, the magnetic field is rotated in a sine wave fashion.

That is, if we let $\psi(x)$ be the rotation of the magnetic field at position x, then

$$\boldsymbol{B}(x) = (B_x, B_\perp \cos(\psi(x)), B_\perp \sin(\psi(x)))\,, \tag{4.3}$$

where $\psi(x)$ is given by

$$\psi(x) = \sin^{-1}\left(A \sin(\phi(x))\right), \quad \phi(x) = \frac{2\pi x}{L}, \tag{4.4}$$

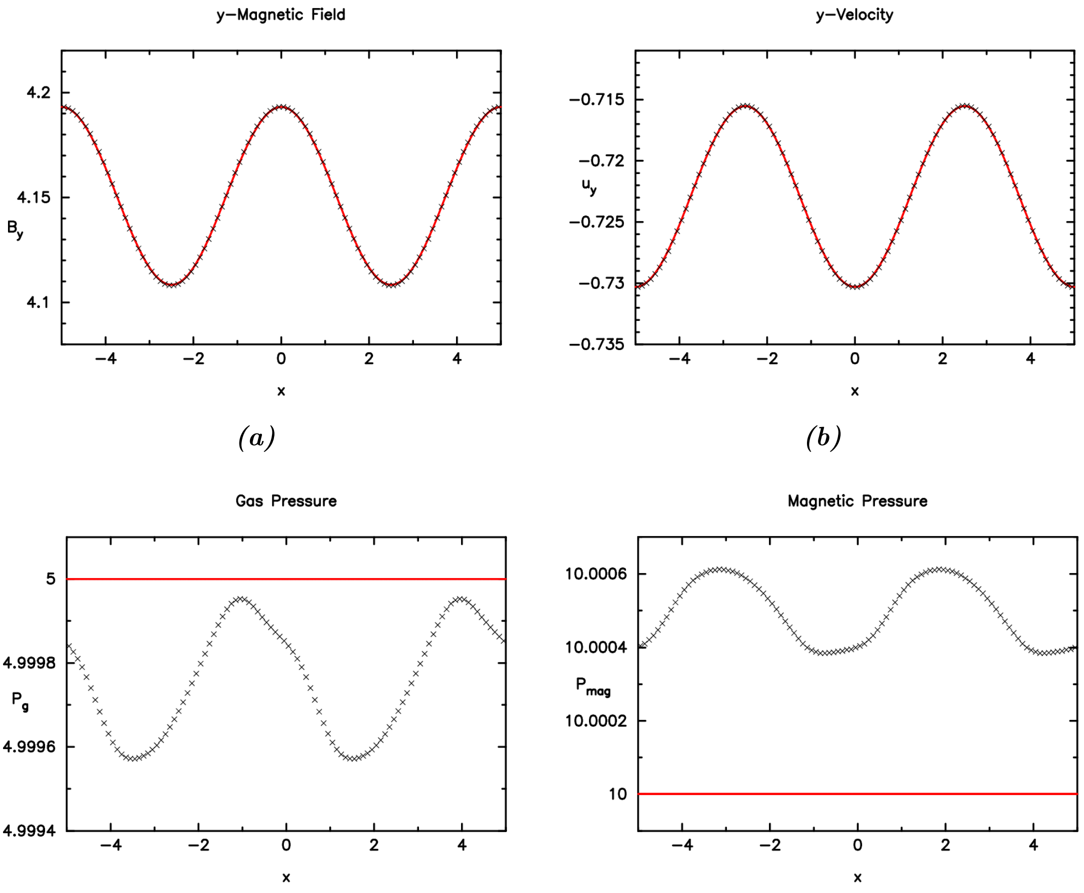

(a) *(b)*

(c) *(d)*

Figure 4.3: *B_y (a), u_y (b), p_g (c) and p_m (d) for a low-σ Alfvén wave test up to $t = 100$, at resolution 100, using a third order code and periodic BCs. In this case, $\sigma = 0.66667$.*

where where L is the width of the domain, and A is the amplitude of the rotation wave. In both tests we performed, $A = 0.3$.

Table 4.1 contains the data for both Alfvén wave tests performed. In this table, the state at $\phi = 0$ and $\phi = \pi/2$ is given, and the remaining states are given by Eqs. (4.3) and (4.4).

Fig. 4.3 shows the results of testing our code on a relatively low σ Alfvén wave outside the fluid frame, with periodic boundary conditions. As we can see, the method is clearly capable of handling this case with relatively few issues. The system has generated some variation in the gas pressure and magnetic pressure that should not be there, but even for other RMHD solvers this tends to happen anyway, due to truncation error and other sources of error. This error is concentrated around specific regions of the wave, and is particularly pronounced at the extrema of the magnetic field. As this test is at a low value of σ, the correction coming from the interaction terms is quite significant.

Fig. 4.4 shows the results of an Alfvén wave at high σ. This σ is high enough that typical RMHD schemes would not be able to handle this case, but here we can see that

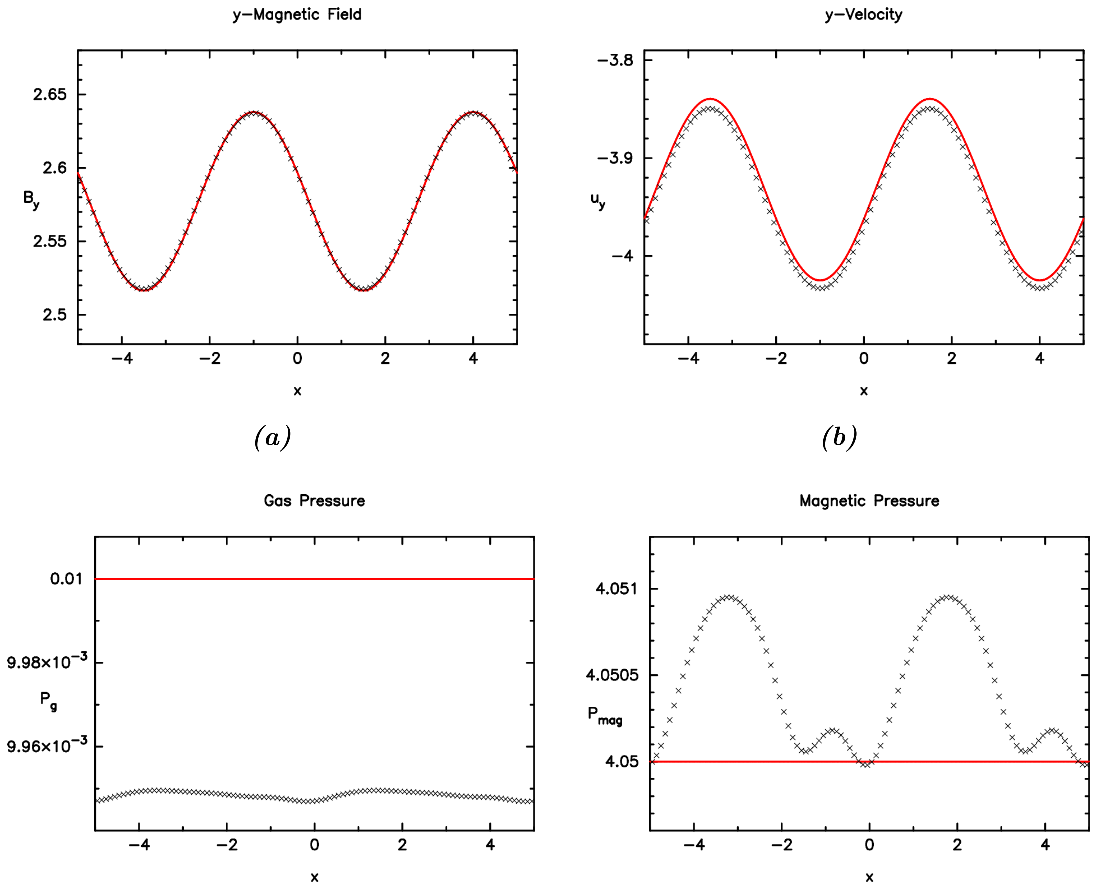

(a) *(b)*

(c) *(d)*

Figure 4.4: *B_y (a), u_y (b), p_g (c) and p_m (d) for a high-σ Alfvén wave test up to $t = 100$, at resolution 100, using a third order code and Periodic BCs. In this case, $\sigma = 196.20$.*

the wave is handled reasonably well. The magnetic field is very close to the exact solution. However, we do see some problems with p_g, p_m and $\boldsymbol{u}$. The same problem as before with induced variation in p_g and p_m is present and more pronounced than before. The density and gas pressure overall slowly drifts over time, in conjunction with a drift in the velocity as well. This drift is much more pronounced at lower integration order, so this error is clearly associated with the truncation error of the scheme.

We can see from these two tests that our code is quite comfortable with Alfvén waves, at both high and low σ. In both cases there was some error in the gas and magnetic pressure — specifically there is systematic error that is converting gas pressure into magnetic pressure — but this was not particularly significant.

Moreover, the error in p_m is only notable because it is constant in the exact solution, so the error immediately jumps out on observation. The error in $\boldsymbol{B}$ and $\boldsymbol{E}$ is in fact of comparable size to the error in p_m, but is much less obvious since these variables are not constant across the wave.

The only exception to this is the error in $\boldsymbol{u}$ which is able to vary more significantly in the direction parallel to $\boldsymbol{B}_0$, since this is not constrained by the relatively large values in the force-free system. In the remaining components of $\boldsymbol{u}$ orthogonal to $\boldsymbol{B}_0$, the variation is once again relatively small.

Rarefactions

We now move onto rarefaction waves. These solutions come in two kinds, slow and fast rarefactions, dependent on which type the eigenvector used for their construction belongs to. These solutions are discussed in section 2.3.2. Table 4.2 contains the test case data for all the rarefaction tests considered. Given in the table is the data for the left state (the constant state beyond the left end of the rarefaction), and the data for the right state as well. The rest of the rarefaction is connected continuously between these two states by integrating Eq. (2.162) numerically.

Problem	Figure	Left State	Right State
Low-σ Slow Rarefaction, $\mu_l = 0.23703$, $\mu_r = 0.25581$	4.5	$\boldsymbol{u} = (-0.01, 0.22321, -0.013397)$, $\boldsymbol{B} = (1, 0.85622, 0.083013)$, $\rho = 1$, $p_g = 2.1$, $\sigma = 0.17956$, $\sigma^* = 0.17099$	$\boldsymbol{u} = (0.018733, 0.32185, -0.0053551)$, $\boldsymbol{B} = (1, 0.57325, 0.058210)$, $\rho = 1.0928$, $p_g = 2.3637$, $\sigma = 0.11793$, $\sigma^* = 0.10682$
High-σ Slow Rarefaction, $\mu_l = 0.13880$, $\mu_r = 0.17220$	4.6	$\boldsymbol{u} = (-0.01, 0.22321, -0.013397)$, $\boldsymbol{B} = (1, 0.73205, -2.7321)$, $\rho = 0.01$, $p_g = 0.005$, $\sigma = 286.83$, $\sigma^* = 273.15$	$\boldsymbol{u} = (0.037388, 0.26236, -0.14375)$, $\boldsymbol{B} = (1, 0.73183, -2.7312)$, $\rho = 0.013499$, $p_g = 0.0074591$, $\sigma = 198.46$, $\sigma^* = 181.93$
Low-σ Fast Rarefaction, $\mu_l = 0.51214$, $\mu_r = 0.65213$	4.7	$\boldsymbol{u} = (-0.5, 0.27321, 0.073205)$, $\boldsymbol{B} = (1, 2.2321, -0.13397)$, $\rho = 0.501$, $p_g = 1.2$, $\sigma = 0.85244$, $\sigma^* = 0.64093$	$\boldsymbol{u} = (-0.31981, 0.21866, 0.064735)$, $\boldsymbol{B} = (1, 2.6121, -0.15090)$, $\rho = 0.62027$, $p_g = 1.59530$, $\sigma = 0.97807$, $\sigma^* = 0.84734$
High-σ Fast Rarefaction, $\mu_l = 0.97709$, $\mu_r = 0.98788$	4.8	$\boldsymbol{u} = (-1, 0.22321, -0.013397)$, $\boldsymbol{B} = (1, 2.2321, -0.13397)$, $\rho = 0.01$, $p_g = 0.005$, $\sigma = 101.63$, $\sigma^* = 49.574$	$\boldsymbol{u} = (-0.70023, 0.11581, -0.0069516)$, $\boldsymbol{B} = (1, 2.4545, -0.14733)$, $\rho = 0.012633$, $p_g = 0.0068281$, $\sigma = 120.17$, $\sigma^* = 79.914$

Table 4.2: *Initial test case data for all 1D rarefaction tests. The left and right states correspond to the constant states at either end of the rarefaction.* μ_l *and* μ_r *are the phase velocities of the given rarefaction in those states respectively.*

Slow Rarefaction Waves

We start with slow rarefactions. Slow rarefactions are somewhat unique compared to fast and Alfvén modes in that the variation in the electromagnetic components $\boldsymbol{B}$ and $\boldsymbol{E}$ is of the same order as the inertial components ρ, p_g and $\boldsymbol{u}$. Thus this case could potentially be handled fully by the interaction system alone, with the force-free system merely providing a background $\boldsymbol{B}_0$ and $\boldsymbol{E}_0$ without needing to be evolved.

Slow waves do not appear in the force-free system, so there is no force-free counterpart to compare these rarefactions to. If we tried to test the same $\boldsymbol{B}$ and $\boldsymbol{E}$ of a slow rarefaction on pure FFDE, we would expect to find that they simply split into four separate waves like any other initial condition in FFDE that is not purely a fast or Alfvén wave. Thus the action of the interaction operator in this case should be to suppress this action, and keep the wave held together.

One special case of slow rarefactions is a so-called switch-off slow rarefaction. In this case, the state of the system in the upstream state has $\boldsymbol{B}_\perp \neq 0$ while the downstream state has $\boldsymbol{B}_\perp = 0$, so the rarefaction has the effect of "switching off" the perpendicular component of the magnetic field. For some integration schemes this test is more difficult than an arbitrary slow rarefaction. In particular, Linear Riemann solvers must treat the degenerate $\boldsymbol{B}_\perp = 0$ state differently, and so this test challenges the scheme in a particularly special way. The HLL solver we are using does not treat these states differently however, and so our scheme does not have any particular difficulty with this type of solution.

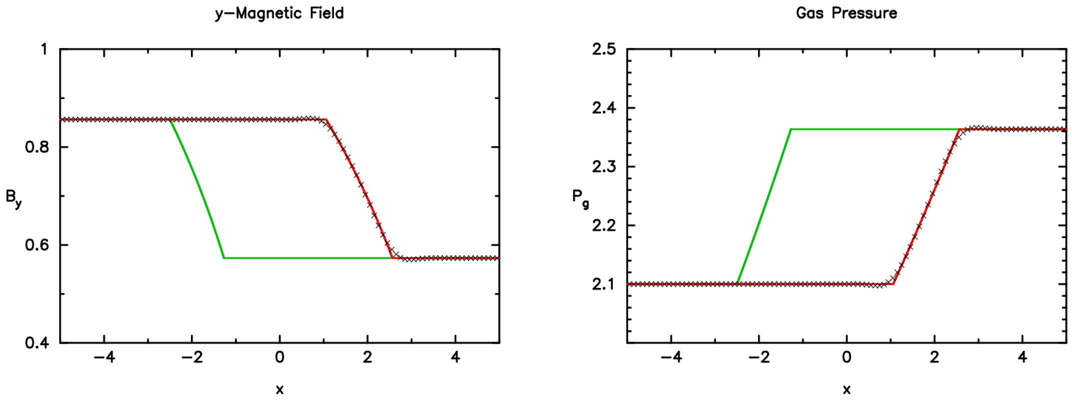

(a) *(b)*

Figure 4.5: *B_y (a) and p_g (b) for a low-σ slow rarefaction wave test up to $t = 15$, at resolution 100, using a third order code and Neumann BCs. In this case, $\sigma = 0.17956$ at the left end of the rarefaction, and $\sigma = 0.11793$ at the right.*

Figs. 4.5 and 4.6 show the results of two slow rarefaction tests. In both cases the rarefaction here moves slowly to the right and slowly expands as it does so.

We can see that the low-σ test in Fig. 4.5 agrees closely to the exact solutions in both gas pressure and magnetic field, with the exception of the weak discontinuities at either end of the waves where the numerical solution is slightly smoothed compared to the exact solution. This artefact is common to most methods of modelling RMHD, and also will tend to 0 as the resolution is increased. This is therefore not significant enough to be

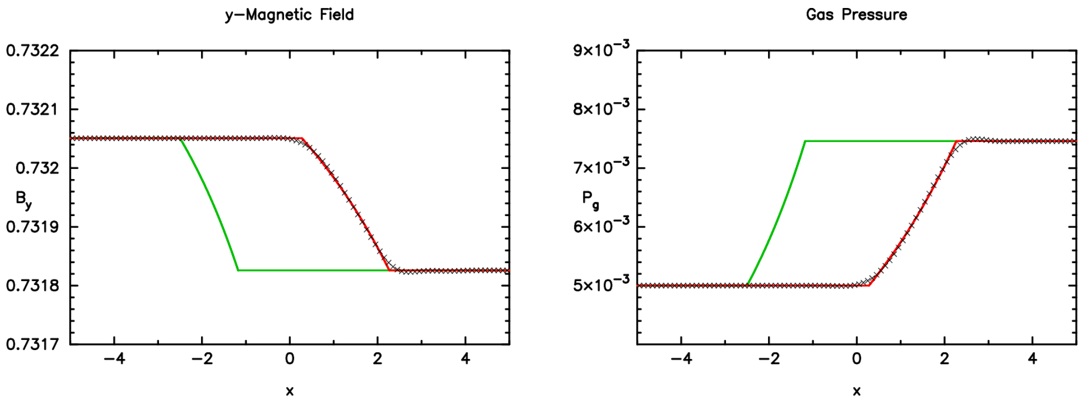

(a)

(b)

Figure 4.6: *B_y (a) and p_g (b) for a high-σ slow rarefaction wave test up to $t = 20$, at resolution 100, using a third order code and Neumann BCs. In this case, $\sigma = 286.83$ at the left end of the rarefaction, and $\sigma = 198.46$ at the right.*

called a problem.

For the high-σ test in Fig. 4.6 we get much the same results, the code is able to handle the case without any difficulty. Like before there is some smoothing around the weak discontinuities, but this is still not unexpected.

Fast Rarefaction Waves

The final continuous test for which we have an exact solution is fast rarefactions. As above, these solutions are discussed in section 2.3.2. Unlike their slow counterparts, the variation of $\boldsymbol{B}$ and $\boldsymbol{E}$ is now large, and of comparable scale to the magnitude of $\boldsymbol{B}$ and $\boldsymbol{E}$. This test should therefore be a more comprehensive and difficult test for the code than slow rarefactions, since now both operators are significant.

Unlike slow waves, fast waves do exist in pure FFDE, and we can therefore compare the wave modes like we did with Alfvén waves. Even in the fluid frame, the fast phase speed is still a fairly complex expression. However, for the variation in the variables we can see from Eq. (2.76) that these are

$$d\boldsymbol{u} = \begin{pmatrix} \mu_f^2 - \mu_a^2 \\ \frac{B_x B_y}{\mathcal{E}}\left(a_s^2 - 1\right) \\ \frac{B_x B_z}{\mathcal{E}}\left(a_s^2 - 1\right) \end{pmatrix}, \quad d\boldsymbol{B} = \frac{\mu_f^2 - a_s^2\mu_a^2}{\mu_f}\begin{pmatrix} 0 \\ B_y \\ B_z \end{pmatrix},$$

$$d\boldsymbol{E} = \left(\left(\mu_f^2 - \mu_a^2\right) - \frac{B_x^2}{\mathcal{E}}\left(a_s^2 - 1\right)\right)\begin{pmatrix} 0 \\ B_z \\ -B_y \end{pmatrix},$$

$$dp_g = \frac{w a_s^2}{\mu_f}\left(\mu_f^2 - \mu_a^2\right), \quad d\rho = \frac{\rho\, dp_g}{w a_s^2} = \frac{\rho}{\mu_f}\left(\mu_f^2 - \mu_a^2\right),$$

where μ_f is the fast Wave speed. Meanwhile, for FFDE we have from Eq. (2.114) that

$$d\boldsymbol{B} = \mu_f \left(0, B_y, B_z\right), \quad d\boldsymbol{E} = \mu_f^2 \left(0, B_z, -B_y\right),$$

in FFDE $\mu_f = \pm 1$ of course, so the factor on $d\boldsymbol{E}$ vanishes, and the choice of direction of the fast wave only flips the $d\boldsymbol{B}$ vector.

Comparing these, we can see that fast waves in RMHD have more of a difference from the FFDE solution than for the case of Alfvén waves. The magnetic and electric field variations in RMHD are once again parallel to their FFDE counterparts, but the exact difference between them is a dependant on the magnetisation σ, the direction of $\boldsymbol{B}$, the fast speed μ_f and the local sound speed a_s, which itself depends on the plasma temperature and thus gas pressure p_g and density ρ.

One particular property of fast Waves at high σ is that the fact that the fast wave speed approaches the speed of light means that in the fluid frame the rarefaction barely spreads, and mostly just moves through the fluid at almost the speed of light, with the interaction system having little effect. By contrast, in a frame near that of the rarefaction the difference between the speeds at either end is much more significant, and may even change sign. So in this frame the interaction system must be having a far larger impact despite being otherwise the same wave, at the same σ.

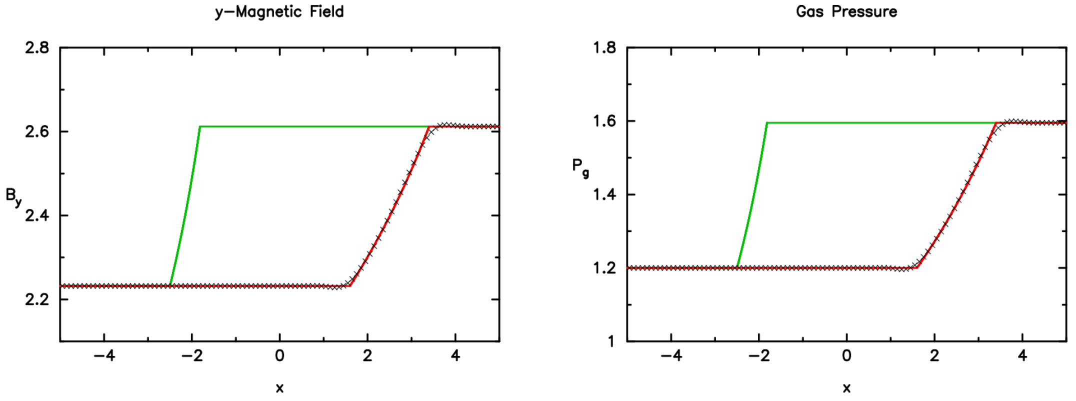

(a) *(b)*

Figure 4.7: *B_y (a) and p_g (b) for a low-σ fast rarefaction wave test up to $t = 8$, at resolution 100, using a third order code and Neumann BCs. In this case, $\sigma = 0.85244$ at the left end of the rarefaction, and $\sigma = 0.97807$ at the right.*

This is easily explained with the observation that while σ is large, near the wave frame we have $\sigma^* = \sigma/\gamma^2 \sim \mathcal{O}(1)$. As discussed in section 2.4, this means that the magnitude of some of the values in the interaction system are in fact relatively large. Thus the same test from different frames is treated very differently by the integration scheme, as the interaction variables will be larger in a frame where σ^* is not small.

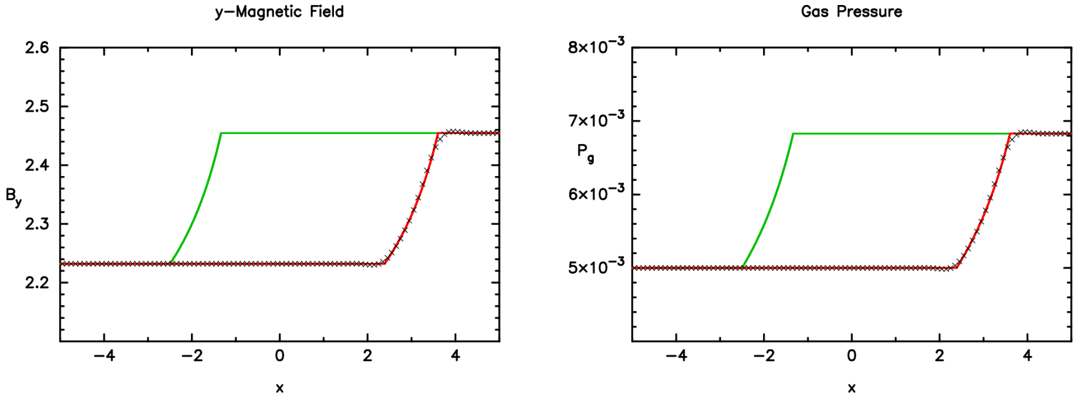

(a) *(b)*

Figure 4.8: B_y *(a) and* p_g *(b) for a high-*σ *fast rarefaction wave test up to* $t = 5$*, at resolution* 100*, using a third order code and Neumann BCs. In this case,* $\sigma = 101.63$ *at the left end of the rarefaction, and* $\sigma = 120.17$ *at the right.*

Figs. 4.7 and 4.8 show the results of fast rarefaction tests at high and low σ. We can see that the code again has little difficulty handling these tests. We still have the artefacts at the weak discontinuities at either end like the slow rarefaction tests, but the results are otherwise very good.

In summary, the method appears perfectly capable of handling most kinds of continuous solutions with few difficulties or problems, at least for the range of σ we have tested. The method does appear to have some difficulty with Alfvén waves, but this error is generally not large. Therefore, for at least 1D cases without any discontinuities, this method is able to run without major problems provided that the gradients do not become too large. Of course, continuous solutions are generally easier to handle by integration schemes, so the real tests for the method are discontinuous tests.

4.3 Discontinuous Tests

We have seen that the code is already quite capable at handling all kinds of continuous solutions in 1D. But this is only half the story, as we also need to check the code against discontinuous solutions, such as shocks and contact discontinuities. The initial data for all test cases considered is contained in tables 4.3 and 4.4.

These test cases are all initially constructed with a smooth “tanh” profile instead of a sharp discontinuity. Numerical diffusion causes each discontinuity to be spread over several cells during the run of the test, while factors such as non-linear steepening cause this to tend to a finite limit, and thus the discontinuities tend to a settled profile (besides contact discontinuities, for which there are no steepening effects, and only the reduction

Problem	Figure(s)	Left State	Right State
Hot Contact Discontinuity, $\mu = 0.37139$	4.9	$\boldsymbol{u} = (0.6, -0.066987, -1.1160)$, $\boldsymbol{B} = (1, -0.36603, 1.3660)$, $\rho = 0.00006$, $p_g = 0.01$, $\sigma = 36.440$, $\sigma^* = 13.962$	$\boldsymbol{u} = (0.6, -0.066987, -1.1160)$, $\boldsymbol{B} = (1, -0.36603, 1.3660)$, $\rho = 0.0003$, $p_g = 0.01$, $\sigma = 36.223$, $\sigma^* = 13.878$
Cold Contact Discontinuity, $\mu = 0.37139$	4.10	$\boldsymbol{u} = (0.6, -0.066987, -1.1160)$, $\boldsymbol{B} = (1, -0.36603, 1.3660)$, $\rho = 0.01$, $p_g = 0.0002$, $\sigma = 135.16$, $\sigma^* = 51.787$	$\boldsymbol{u} = (0.6, -0.066987, -1.1160)$, $\boldsymbol{B} = (1, -0.36603, 1.3660)$, $\rho = 0.001$, $p_g = 0.0002$, $\sigma = 810.98$, $\sigma^* = 310.72$
Low-σ Slow Shock, $\mu = -0.28735$	4.11	$\boldsymbol{u} = (-0.51129, -0.10170, 0.058719)$, $\boldsymbol{B} = (1, -0.46051, 0.26588)$, $\rho = 6.9577$, $p_g = 3.7851$, $\sigma = 0.052669$, $\sigma^* = 0.041303$	$\boldsymbol{u} = (-0.53134, 0.086603, -0.005)$, $\boldsymbol{B} = (1, -0.95623, 0.55208)$, $\rho = 6.3113$, $p_g = 3.3218$, $\sigma = 0.1$, $\sigma^* = 0.077978$
High-σ Slow Shock, $\mu = 0.24254$	4.12	$\boldsymbol{u} = (0.18266, -0.84803, 0.48961)$, $\boldsymbol{B} = (1, -0.69461, 0.40104)$, $\rho = 0.026338$, $p_g = 0.036496$, $\sigma = 7.5165$, $\sigma^* = 3.7729$	$\boldsymbol{u} = (-0.67524, -0.12990, 0.075)$, $\boldsymbol{B} = (1, -0.71760, 0.41431)$, $\rho = 0.0043349$, $p_g = 0.0022815$, $\sigma = 100$, $\sigma^* = 67.638$
Low-σ Fast Shock, $\mu = 0$	4.13 and 4.19	$\boldsymbol{u} = (-0.35067, 0.072168, -0.041666)$, $\boldsymbol{B} = (1, -2.4342, 1.4054)$, $\rho = 23.499$, $p_g = 31.508$, $\sigma = 0.054702$, $\sigma^* = 0.048413$	$\boldsymbol{u} = (-2, 0.086603, -0.05)$, $\boldsymbol{B} = (1, -0.86603, 0.5)$, $\rho = 4.1202$, $p_g = 2.1685$, $\sigma = 0.1$, $\sigma^* = 0.019960$
Low-σ Fast Shock, $\mu = 0.90286$	4.14	$\boldsymbol{u} = (1.4166, 0.072168, -0.041666)$, $\boldsymbol{B} = (1, -4.1180, 2.37752)$, $\rho = 23.499$, $p_g = 31.508$, $\sigma = 0.054702$, $\sigma^* = 0.018151$	$\boldsymbol{u} = (0.048555, 0.086603, -0.05)$, $\boldsymbol{B} = (1, -0.47055, 0.27167)$, $\rho = 4.1202$, $p_g = 2.1685$, $\sigma = 0.1$, $\sigma^* = 0.098779$
Weak High-σ Fast Shock, $\mu = 0$	4.15 and 4.20	$\boldsymbol{u} = (21.762, 0, 0)$, $\boldsymbol{B} = (15.811, 172.22, 298.30)$, $\rho = 1$, $p_g = 1$, $\sigma = 100.00$, $\sigma^* = 0.21072$	$\boldsymbol{u} = (8.3126, 0.13033, 0.22573)$, $\boldsymbol{B} = (15.811, 173.61, 300.71)$, $\rho = 2.6179$, $p_g = 4.4198$, $\sigma = 119.42$, $\sigma^* = 1.7019$
Weak High-σ Fast Shock, $\mu = -0.99504$	4.16	$\boldsymbol{u} = (0.85573, 0, 0)$, $\boldsymbol{B} = (15.811, 10.405, 18.022)$, $\rho = 1$, $p_g = 1$, $\sigma = 100.00$, $\sigma^* = 57.728$	$\boldsymbol{u} = (-0.22530, 0.13033, 0.22573)$, $\boldsymbol{B} = (15.811, 24.381, 42.230)$, $\rho = 2.6179$, $p_g = 4.4198$, $\sigma = 119.42$, $\sigma^* = 106.75$

Table 4.3: *Initial test case data for all 1D discontinuity tests, part 1. "μ" is the phase velocity of the discontinuity for the given data. The discontinuities were initially located at $x = 0$ (thus "left" refers to $x < 0$ and "right" to $x > 0$), with a smooth "tanh" profile over a handful of cells.*

of numerical diffusion as the gradient drops).

The results of these tests are best when the initial profile is close to this settled profile. When the initial discontinuity is too sharp (or too wide) the system will emit the difference between the settled profile and the initial profile as extra waves which can affect the results.

In many cases this can even cause the code to fail, as these waves can have very high

Problem	Figure(s)	Left State	Right State
Strong High-σ Fast Shock, $\mu = 0$	4.17 and 4.21 to 4.23	$\boldsymbol{u} = (-0.84070, 0.40157, -0.23184)$, $\boldsymbol{B} = (1, -1.8622, 1.0751)$, $\rho = 0.011895$, $p_g = 0.83089$, $\sigma = 1.4042$, $\sigma^* = 0.73066$	$\boldsymbol{u} = (-100, 2.5981, -1.5)$, $\boldsymbol{B} = (1, -0.8660, 0.5)$, $\rho = 0.0001$, $p_g = 0.0001$, $\sigma = 2120.1$, $\sigma^* = 0.21180$
Strong High-σ Fast Shock, $\mu = 0.99995$	4.18 and 4.25	$\boldsymbol{u} = (52.372, 0.40157, -0.23184)$, $\boldsymbol{B} = (1, -98.174, 56.681)$, $\rho = 0.011895$, $p_g = 0.83089$, $\sigma = 1.4042$, $\sigma^* = 0.00051173$	$\boldsymbol{u} = (4.2780, 2.5981, -1.5)$, $\boldsymbol{B} = (1, -2.5390, 1.4659)$, $\rho = 0.0001$, $p_g = 0.0001$, $\sigma = 2120.1$, $\sigma^* = 74.912$
Low-σ Current sheet, $\mu = 0$	4.26	$\boldsymbol{u} = (0, -0.71962, -0.046410)$, $\boldsymbol{B} = (0, 0.13397, 2.2321)$, $\rho = 10$, $p_g = 20$, $\sigma = 0.036842$, $\sigma^* = 0.024238$	$\boldsymbol{u} = (0, -0.71962, -0.046410)$, $\boldsymbol{B} = (0, -0.13397, -2.2321)$, $\rho = 10$, $p_g = 20$, $\sigma = 0.036842$, $\sigma^* = 0.024238$
Low-σ Current sheet, $\mu = -0.5$	4.27	$\boldsymbol{u} = (-0.71181, -0.71962, -0.046410)$, $\boldsymbol{B} = (0, 0.15470, 2.5774)$, $\rho = 10$, $p_g = 20$, $\sigma = 0.036842$, $\sigma^* = 0.018179$	$\boldsymbol{u} = (-0.71181, -0.71962, -0.046410)$, $\boldsymbol{B} = (0, -0.15470, -2.5774)$, $\rho = 10$, $p_g = 20$, $\sigma = 0.036842$, $\sigma^* = 0.018179$
High-σ Current sheet, $\mu = 0$	4.28, 4.30 and 4.32	$\boldsymbol{u} = (0, -0.0098076, 0.58301)$, $\boldsymbol{B} = (0, -1.2321, 1.8660)$, $\rho = 0.001$, $p_g = 0.001$, $\sigma = 926.87$, $\sigma^* = 691.69$	$\boldsymbol{u} = (0, -0.0098076, 0.58301)$, $\boldsymbol{B} = (0, 1.2321, -1.8660)$, $\rho = 0.001$, $p_g = 0.001$, $\sigma = 926.87$, $\sigma^* = 691.69$
High-σ Current sheet, $\mu = 0.5$	4.29, 4.31 and 4.33	$\boldsymbol{u} = (0.66833, -0.0098076, 0.58301)$, $\boldsymbol{B} = (0, -1.4226, 2.1547)$, $\rho = 0.001$, $p_g = 0.001$, $\sigma = 926.87$, $\sigma^* = 518.77$	$\boldsymbol{u} = (0.66833, -0.0098076, 0.58301)$, $\boldsymbol{B} = (0, 1.4226, -2.1547)$, $\rho = 0.001$, $p_g = 0.001$, $\sigma = 926.87$, $\sigma^* = 518.77$

Table 4.4: *Initial test case data for all 1D discontinuity tests, part 2. "μ" is the phase velocity of the discontinuity for the given data. The discontinuities were initially located at $x = 0$ (thus "left" refers to $x < 0$ and "right" to $x > 0$), with a smooth "tanh" profile over a handful of cells.*

amplitudes, pushing the conservatives outside the bounds of physically meaningful states. Thus we must be careful in the exact initial profile.

The exact shape of this settled profile is difficult to determine ahead of time, thus the initial profiles of these tests are simply "tanh" profiles. Given some variable q with left and right states q_L and q_R, we set the initial profile to

$$q(x) = \frac{1}{2}\left(\tanh\left(\frac{x-c}{a}\right)+1\right)(q_R - q_L) + q_L, \tag{4.5}$$

where c gives the initial centre of the discontinuity (for all 1D tests, we have $c = 0$) and a is a parameter determining the width of the discontinuity. Clearly the function $q(x)$ satisfies $q(x) \to q_L$ as $x \to -\infty$ and $q(x) \to q_R$ as $x \to \infty$, as desired.

While we use the same a for each individual variable in each test, the value of a is chosen independently for each test to match the settled profile to some extent, which can be much wider in some cases. All tests were done with $\Delta x = 0.1$, and since all tests had $0.1 \le a \le 0.4$, the initial discontinuity was spread over anywhere from 6 or so cells to 24 or more.

4.3.1 Contact Discontinuities

To start off with, we will begin with contact discontinuities that are stationary with respect to the fluid and hence are simply advected with the flow, as discussed in section 2.3.1. As we derived there, if we have $B_x \neq 0$ then the only primitive variable that can change in a stationary discontinuity is the density ρ, implying the contact plane between two plasmas of different density — hence the term "contact" discontinuity.

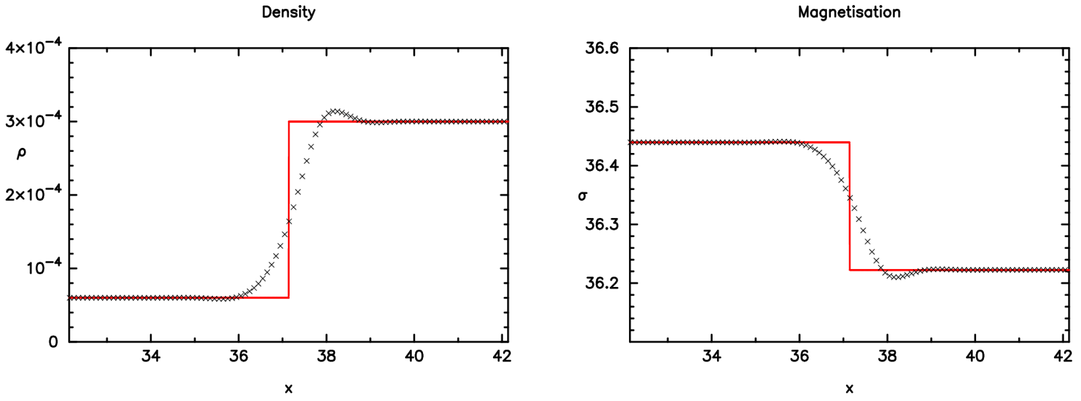

(a) *(b)*

Figure 4.9: *ρ (a) and σ (b) for a high-σ Contact Discontinuity in a hot plasma, with $\sigma = 36.440$ and $p_g/\rho = 166.67$ for $x < 0$, and $\sigma = 36.223$ and $p_g/\rho = 33.333$ for $x > 0$ at time $t = 0$. The test was run until $t = 100$ at resolution 100, using a third order code, Neumann BCs, width parameter $a = 0.1$, and an initial domain of $[-5, 5]$ which we have shifted during the test to follow the discontinuity.*

These are by far the simplest case we can try, as without changing $\boldsymbol{B}$ or $\boldsymbol{E}$, this is entirely within the interaction system. Moreover $\boldsymbol{u}$ is also unchanged, and so the changes are constrained to the small $\mathcal{O}(\sigma^{-1})$ variables. That is, since density ρ is the only variable that changes and this variable is $\sim \mathcal{O}(\sigma^{-1})$, any truncation or numerical errors in the integration can only effect $\sim \mathcal{O}(\sigma^{-1})$ changes to the other variables.

We can see from the equations of RMHD that a cold plasma with $\rho \gg p_g$ might be more difficult to handle than a hot plasma with $\rho \ll p_g$. This is because for a hot plasma we have $w \approx 4p_g$, and so a change in just ρ only significantly affects the conserved mass $\rho\gamma$, while for a cold plasma the changes in the conserved energy and momentum would also be significant. A cold plasma thus also features a more significant change in σ across the discontinuity.

With all that said, the code will still likely have no real issues with a cold plasma anyway for the reasons mentioned above.

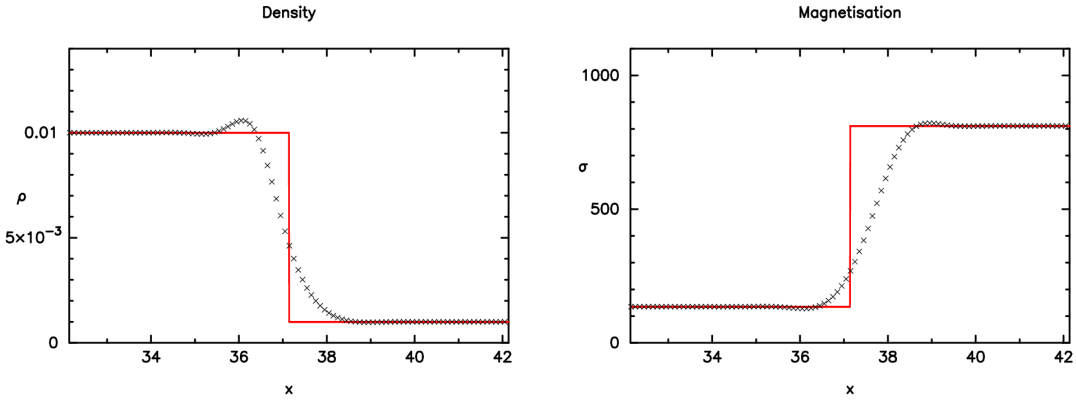

(a) *(b)*

Figure 4.10: *ρ (a) and σ (b) for a high-σ Contact Discontinuity in a cold plasma, with $\sigma = 135.16$ and $p_g/\rho = 0.02$ for $x < 0$, and $\sigma = 810.98$ and $p_g/\rho = 0.2$ for $x > 0$ at time $t = 0$. The test was run until $t = 100$ at resolution 100, using a third order code, Neumann BCs, width parameter $a = 0.1$, and an initial domain of $[-5, 5]$ which we have shifted during the test to follow the discontinuity.*

Figs. 4.9 and 4.10 give the results of a test for a contact discontinuity in a hot and cold plasma respectively at high σ. These tests are both of moving discontinuities (with respect to the cell grid), and with the phase velocity of these two cases ($\mu =$ in both cases) it would only take until $t = 20$ or so to leave the initial domain of $[-5, 5]$. In order to run these tests for longer then, we have made the domain "follow" the shock.

This is done by shifting all cells over by one every few iterations, to keep up with the exact solution. For most cells, this fully defines the new shifted value. But at the edge of the domain that we are moving towards, the cell at the end has no known value as it was previously outside the domain. For these cells, their value is set at the boundary values — since we are using Neumann Boundary Conditions, this means its value is simply set equal to the cell to its side.

As we expected, the code is perfectly capable of handling these tests without much issue. The only real issue is that the discontinuities are fairly diffuse and spread over several cells. This is a combination of two issues: first, the HLL method we are using is known to cause any waves that are not explicitly resolved in the Riemann Solver to be more diffuse. Since the HLL method we are using only resolves the fast waves, Alfvén, slow and Contact waves will be more diffuse. Second, the phase speed of the wave is constant across the discontinuity and so there is a lack of non-linear wave steepening to force the discontinuity to be sharp.

4.3.2 Alfvén Discontinuities

As discussed in section 2.3.1, Alfvén discontinuities are effectively equivalent to the continuous case, but collapsed into a single, discontinuous jump instead of a smooth transition. This is due to the fact that the Alfvén phase speed is an invariant of the Alfvén wave.

Although such a case is certainly *analytically* different from the continuous counterpart, numerically speaking any discontinuity will always be spread over at least a couple of cells. Moreover, we always start the discontinuous tests with a smooth tanh profile since the scheme has difficulty with exceptionally sharp discontinuities. Thus the discontinuous case is practically indistinguishable from the continuous case. The discontinuity will have a finite width, and so it is equivalent to the continuous case.

We therefore find that there is little reason to specifically test an Alfvén discontinuity as a separate case from the continuous Alfvén waves already tested in section 4.2.2, so we will not consider this case here.

4.3.3 Slow Shocks

We now move on to slow shocks. Like their continuous counterparts of slow rarefactions, these shocks feature a small variation in $\boldsymbol{B}$ and $\boldsymbol{E}$ and so are likely to be easier for the code to handle since the shock is on the scale of the interaction system.

Figs. 4.11 and 4.12 show the results of a slow shock test at low and high σ respectively. We can clearly see that the code has little to no difficulty with either the low- or high-σ cases. The only problem is that the shock is fairly wide, which is likely a consequence of using HLL, which like contact discontinuities does not resolve slow shocks, leading to increased numerical dissipation.

The small discontinuity in $\boldsymbol{B}$ and $\boldsymbol{E}$ at high σ means that the force-free system derivatives is at a similar or smaller scale to that of the interaction system. Since the force-free system is where we expect more problems due to the lack of conservation as noted in section 3.2.4, the fact that the code can handle slow shocks without problems is not unexpected.

4.3.4 Fast Shocks

Now that we have successfully tested the code against slow shocks, we will move on to testing fast shocks. Along with current sheets, these tests are likely to be the most difficult to handle at high σ for two main reasons: First, these shocks move at almost the speed of light in the upstream fluid frame, so small errors could push them into superluminal

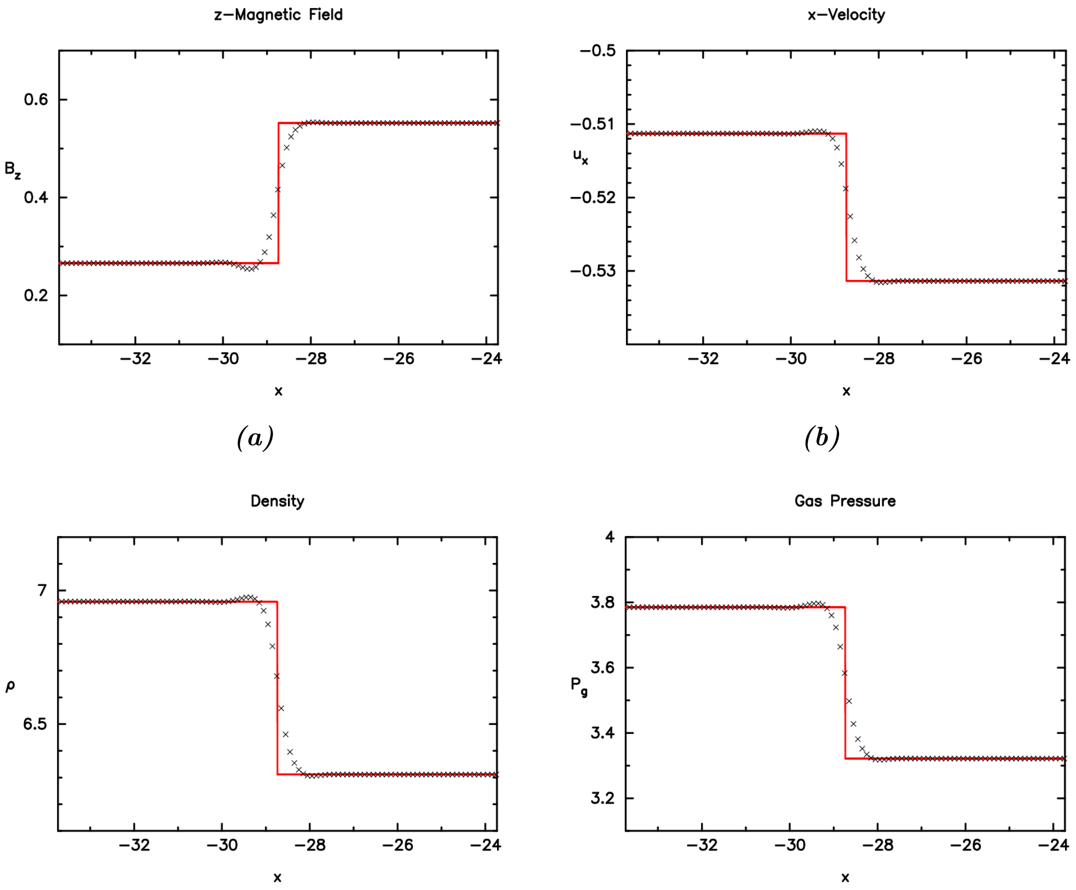

(a) *(b)*

(c) *(d)*

Figure 4.11: *B_z (a), u_x (b), ρ (c) and p_g (d) for a test of a low-σ slow shock up to $t = 100$, at resolution 100, using a third order code, Neumann BCs, width parameter $a = 0.1$, and an initial domain of $[-5, 5]$ which we have shifted during the test to follow the shock. In this case, $\sigma = 0.1$ on the left and $\sigma = 0.052669$ on the right.*

speeds. Second, they can feature large changes in both the electromagnetic and inertial terms, making them the ultimate test of the code's ability to handle high σ cases.

As with the continuous case, there is a stark difference between this solution in the upstream fluid frame compared to the shock frame, since in FFDE there is no shock frame and thus this frame must feature large corrections from the inertial operator. Once again, this is because even with $\sigma \gg 1$ we would still have $\sigma^* \approx 1$, thus the inertial terms in the shock frame are of comparable size to the electromagnetic terms.

Meanwhile, the Lorentz factor downstream can be far smaller than upstream for a strong shock, so that in the shock frame the downstream value of σ^* will be relatively close to σ. However, such strong shocks will also lead to a large decrease in σ downstream, as the density and gas pressure increase by several orders of magnitude.

Hence both upstream and downstream, the value of σ^* will be relatively small in the shock frame both for strong shocks, and for weak shocks where the downstream velocity

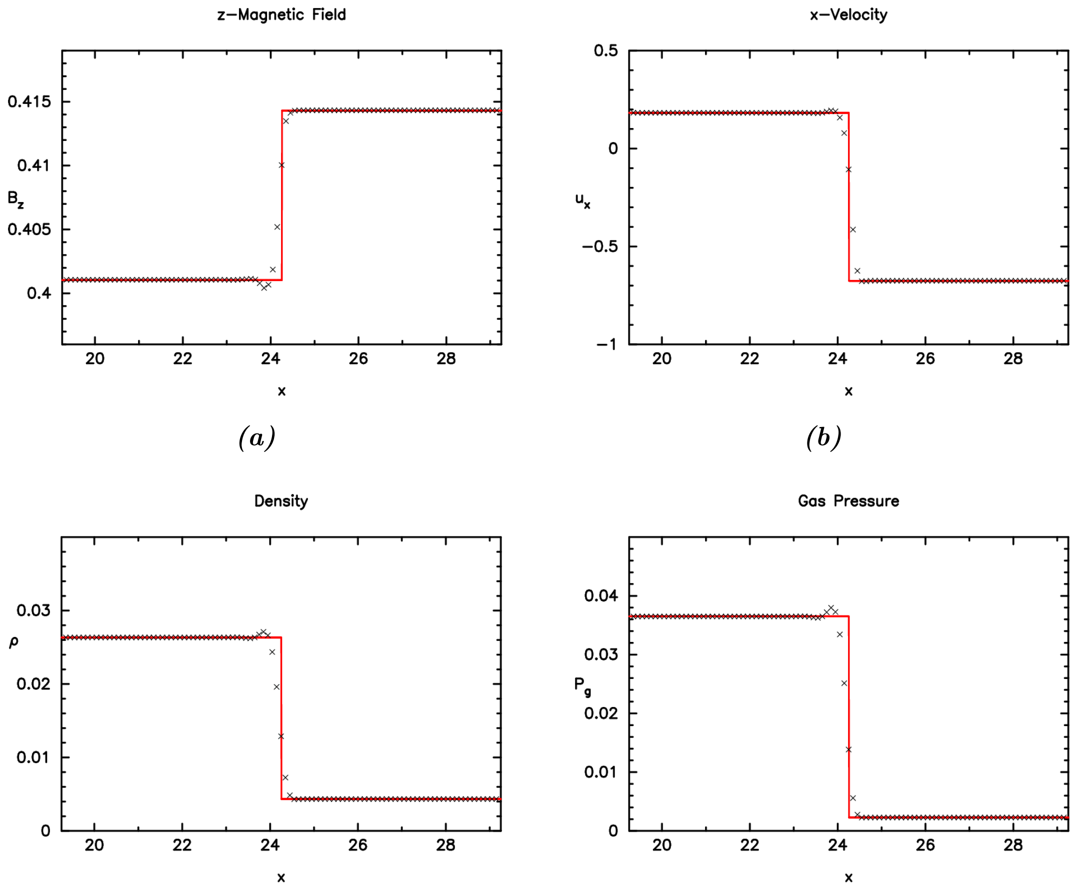

(a) *(b)* *(c)* *(d)*

Figure 4.12: *B_z (a), u_x (b), ρ (c) and p_g (d) for a test of a high-σ slow shock up to $t = 100$, at resolution 100, using a third order code and Neumann BCs, width parameter $a = 0.1$, and an initial domain of $[-5, 5]$ which we have shifted during the test to follow the shock. In this case, $\sigma = 100$ on the left and $\sigma = 7.5165$ on the right.*

will be almost as fast — as can be seen in tables 4.3 and 4.4 for the high-σ fast shocks.

On the other hand, in (or near) the fluid frame, σ^* will be close to σ. So if we are near the upstream fluid frame, the upstream inertial components will be much smaller than the electromagnetic components. If we are near the downstream frame however it depends on the strength of the shock.

For weak shocks, the downstream state will be similar to the upstream state, and thus have high σ and comparable σ^*. For strong shocks, σ downstream will already be smaller than the upstream state, and the value of γ will be quite large as well, as (in the shock frame) the shock slows the downstream fluid significantly. Thus in the upstream frame, the downstream fluid is moving quite quickly as well. Therefore the downstream σ and σ^* will be relatively small for a strong shock.

Thus between the upstream fluid frame and the shock frame, the interaction components change from $\mathcal{O}(\sigma^{-1})$ in the upstream frame all the way up to match or exceed the force-free components at $\mathcal{O}(1)$ in the shock frame. Given how different these conditions are, we may expect the code to behave differently in these two cases, so it is worth testing both.

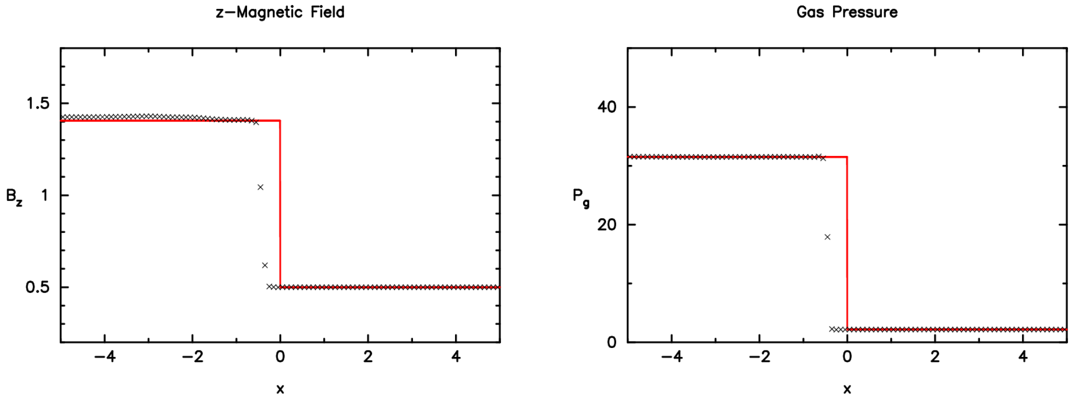

(a) *(b)*

Figure 4.13: *B_z (a) and p_g (b) for a test of a stationary, low-σ fast shock up to $t = 100$, at resolution 100, using a third order code, Neumann BCs, width parameter $a = 0.1$, and a domain of $[-5, 5]$. In this case, $\sigma = 0.054702$ on the left and $\sigma = 0.1$ on the right, while $\sigma^* = 0.048413$ on the left and $\sigma^* = 0.019960$ on the right.*

Fig. 4.13 shows a test of a fast shock at low σ in the shock frame. In this case the code seems able to handle the shock without great difficulty. Besides the fact that the shock appears to be drifting slowly to the left with phase speed $\mu \approx -0.0025$, there are no other obvious problems. This drift is a result of the system coming to stabilise in a slightly different shock configuration to the initial conditions. In contrast to the previous slow shock tests, this shock is quite sharp — both because in this case the HLL solver does resolve this wave, and also because there is appreciable non-linear steepening keeping the shock sharp.

Fig. 4.14 features the same shock but now in a different frame, close to that of the upstream fluid frame. Since σ is low, the difference between these frames is not exceptionally different, and the code handles the shock with relative ease. As before, the shock is kept sharp and it moves with respect to the grid at the expected velocity. The shock is spread over a few more cells than that of the shock frame test, but an increase in dissipation for a moving shock is common among shock-capturing schemes. There does, however, appear to be a small change in the magnetic field downstream compared to the exact solution. This could be explained by the shock settling to a different solution compared to the initial conditions, but we will see later that this may not be the case.

Clearly the code has little difficulty at low σ, so now we move on to high σ. High-σ fast shocks are among the hardest cases for the code to deal with. In the upstream fluid frame,

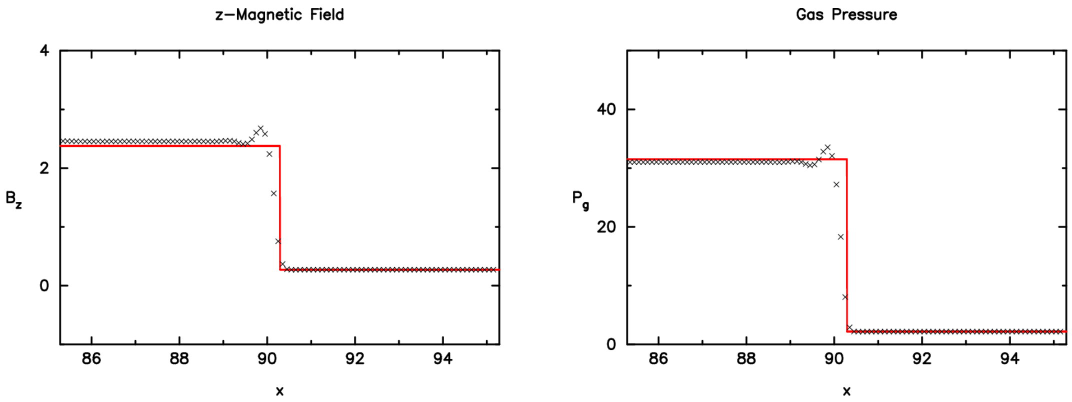

(a) *(b)*

Figure 4.14: *B_z (a) and p_g (b) for a test of a moving, low-σ fast shock up to $t = 100$, at resolution 100, using a third order code, Neumann BCs, width parameter $a = 0.2$, and an initial domain of $[-5, 5]$ which we have shifted during the test to follow the shock. This shock is the same as in Fig. 4.13 but in a different frame, where the shock moves with shock velocity $\mu = 0.90286$. As a Lorentz invariant σ is the same, with $\sigma = 0.054702$ on the left and $\sigma = 0.1$ on the right. However, the value of σ^* is now $\sigma^* = 0.018151$ on the left and $\sigma^* = 0.098779$ on the right.*

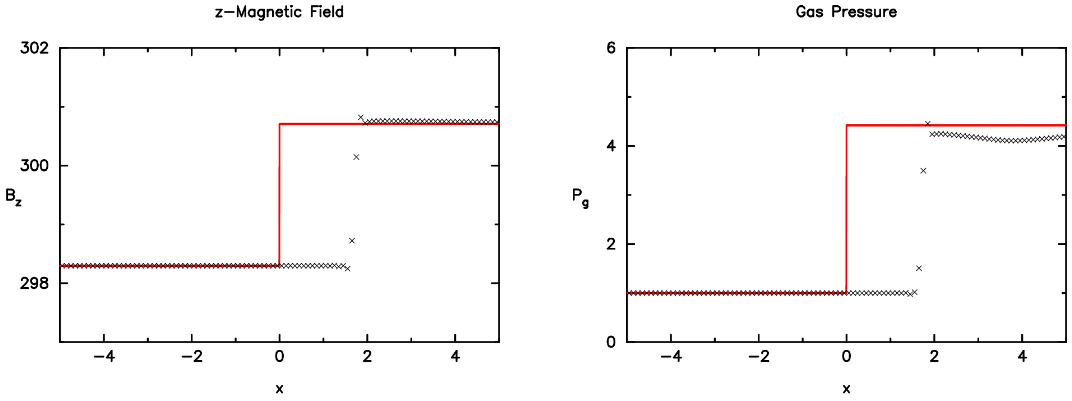

(a) *(b)*

Figure 4.15: *B_z (a) and p_g (b) for a test of a weak, stationary, high-σ fast shock up to $t = 100$, at resolution 100, using a third order code, Neumann BCs, width parameter $a = 0.1$, and an initial domain of $[-5, 5]$. In this case, $\sigma = 1.4042$ on the left and $\sigma = 2120.1$ on the right, while $\sigma^* = 0.73066$ on the left and $\sigma^* = 0.21180$ on the right.*

these shocks are moving faster than the fast phase speed which is itself very close to the speed of light. Since this is the case the phase speed of similar states is not significantly different, and so the non-linear steepening that would otherwise help to keep them sharp is very weak, allowing the shocks to spread out due to diffusion. In addition to this, fast shocks can feature large gradients in the magnetic field and very large changes in gas pressure, and thus also large changes in σ.

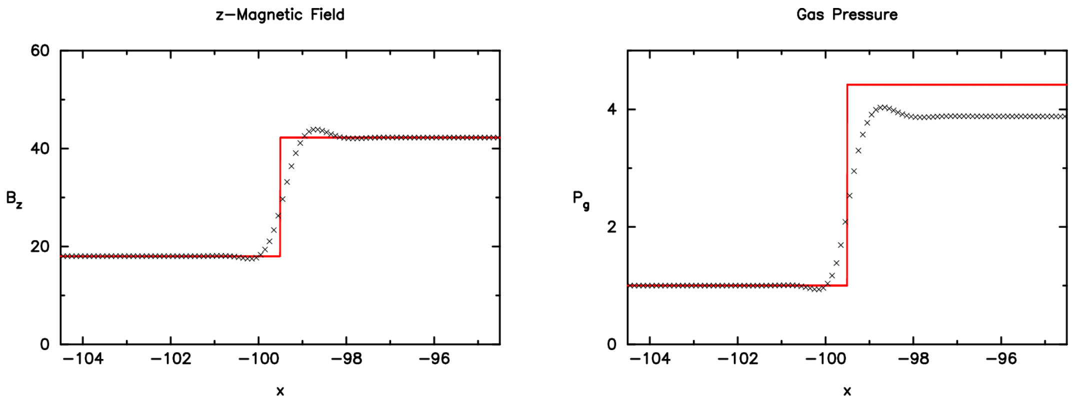

(a) *(b)*

Figure 4.16: *B_z (a) and p_g (b) for a test of a weak, moving, high-σ fast shock up to $t = 100$, at resolution 100, using a third order code, Neumann BCs, width parameter $a = 0.2$, and an initial domain of $[-5, 5]$ which we have shifted during the test to follow the shock. Once again, this shock is Fig. 4.15 in a different frame, with the shock now moving with velocity $\mu = 0.9999458$. σ is thus the same with $\sigma = 1.4042$ on the left and $\sigma = 2120.1$ on the right. However, we now have $\sigma^* = 0.00051173$ on the left and $\sigma^* = 74.912$ on the right.*

In order to properly identify how well the code deals with this difficult case, we will include two different shock cases, with one shock much weaker than the other in terms of the change in gas pressure and σ. Fig. 4.15 shows the results for the first, weaker shock in the shock frame.

Like with the low-σ case, the code handles this test quite well, with little difficulty. The shock is spread over only a few cells, and the results are more or less correct — although the drift of the shock is much more significant here, with a shock velocity of around $\mu \approx 0.018$.

Fig. 4.16 shows the results for the same shock in the fluid frame. This time the shock is spread over quite a few cells, unlike the low-σ moving shock in Fig. 4.14. This is due to the weak non-linear steepening we described above. The jump in magnetic field appears to be quite accurate, but we can see a clear drop in the gas pressure downstream compared to the expected value, similar to the change in magnetic field in the low-σ moving shock.

Fig. 4.17 shows a test of a much stronger fast shock at high σ in the shock frame; in this case, the gas pressure increases by around four orders of magnitude — although thanks to the high σ the change in magnetic field strength is comparatively smaller.

Once again, the shock is drifting to the left, this time with velocity $\mu \approx -0.022$. More notably however, like the moving shocks before the magnetic field downstream appears to be slightly different compared to the exact solution. Again, this could be explained by the

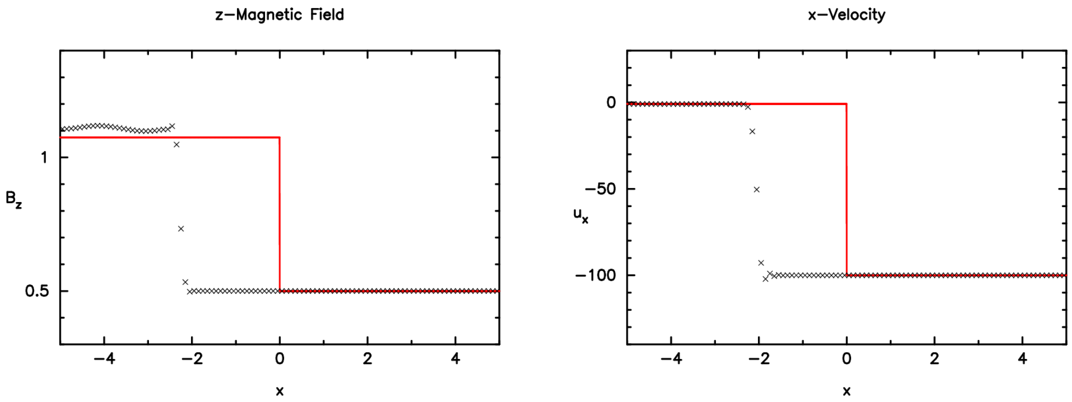

(a) *z-component of magnetic field.* ***(c)***

(b)

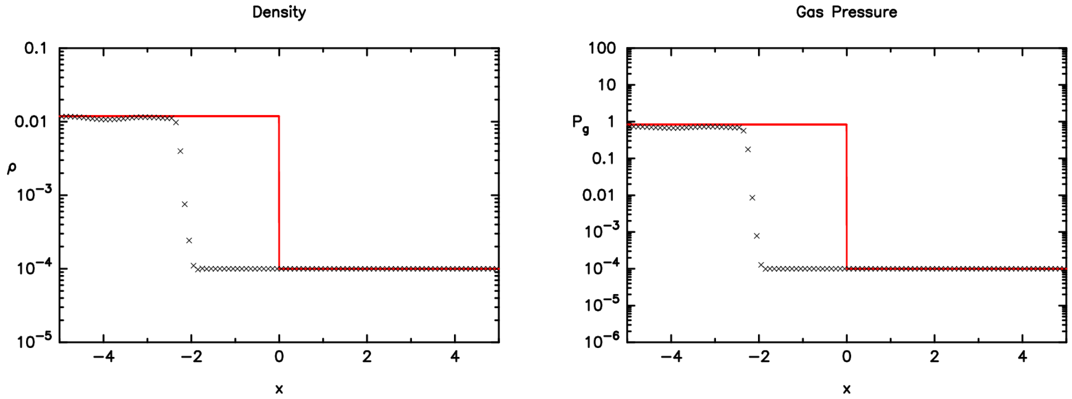

(d) ***(e)***

Figure 4.17: *B_z (a), u_x (b), ρ (c) and p_g (d) for a test of a stationary, high-σ fast shock up to $t = 100$, at resolution 100, using a third order code, Neumann BCs, width parameter $a = 0.1$, and an initial domain of $[-5, 5]$. In this case, $\sigma = 1.4042$ on the left and $\sigma = 2120.1$ on the right, while $\sigma^* = 0.73066$ on the left and $\sigma^* = 0.21180$ on the right.*

shock settling to a different solution.

There is another significant issue (not visible in the plots themselves): in order to avoid the model crashing due to various problems — such as the variable conversion failing to converge as u^2 exceeds infinity, or gas pressure dropping below 0 — it is often necessary to run the test at a small value for the Courant number, perhaps as low as $C_u = 0.05$ (although it was not necessary in this particular instance). This is highly undesirable, since the smaller this value is the more iterations we need to run the model for the same time. In addition, low C_u is known to be associated with increased diffusivity of the numerical model, and thus raising C_u as high as possible is usually considered to be very important.

The low value of C_u is needed sometimes because the total energy and total momentum are very close together, due to the large Lorentz factor of the plasma upstream of the shock. One condition for a physically meaningful state is that the total momentum $\boldsymbol{M}$ and total

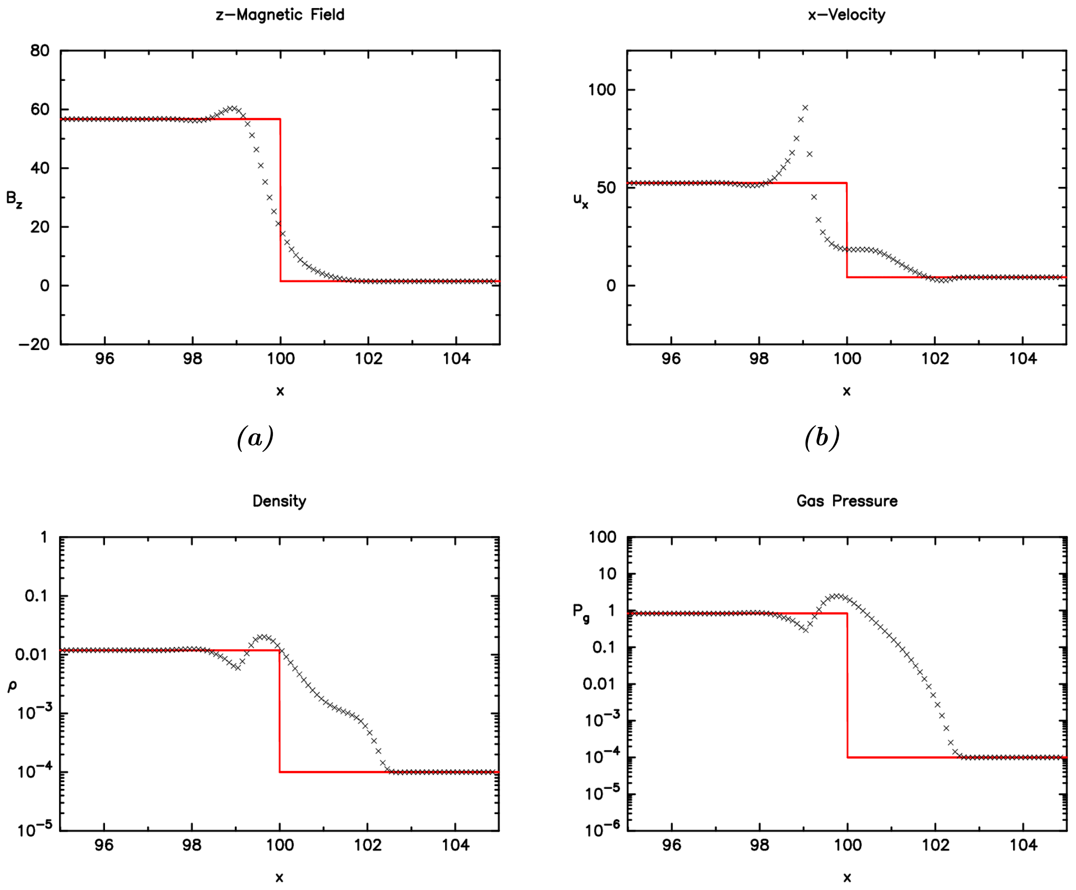

(a) *(b)*

(c) *(d)*

Figure 4.18: *B_z (a), u_x (b), ρ (c) and p_g (d) for a test of a moving, high-σ fast shock up to $t = 100$, at resolution 100, using a third order code, Neumann BCs, width parameter $a = 0.4$, and an initial domain of $[-5, 5]$ which we have shifted during the test to follow the shock. Once again, this shock is Fig. 4.17 in a different frame, with the shock now moving with velocity $\mu = 0.9999458$. σ is thus the same with $\sigma = 1.4042$ on the left and $\sigma = 2120.1$ on the right. However, we now have $\sigma^* = 0.00051173$ on the left and $\sigma^* = 74.912$ on the right.*

energy E must satisfy

$$E^2 - M^2 > 0. \tag{4.6}$$

If we are in a state where we have $M^2/E^2 \approx 1$ (such as a high-σ, strong fast shock), then small errors in the fluxes can cause the state to be unphysical, causing the code to fail.

The stationary fast shock naturally satisfies this condition. Thus in order for the code to handle this state, the Courant number C_u has to be reduced, unless we can find a way to reduce the errors in the flux.

Increasing the value of C_u is a somewhat problematic affair. The main problem at the heart of this is that this fast shock we are considering is perhaps too extreme for our code to reliably handle, with an increase in pressure of over 8,000 times, and a significant change in magnetic field. In these conditions, the total momentum $\boldsymbol{M}$ is close to the limit of $E^2 > M^2$, where E is the total Energy. If it goes beyond this at any point then there will be no solution to the variable conversion, and the code will fail (although the last resort cap on u^2 described in section 3.2.6 can often catch this failure mode, so long as it is just a single, sporadic case).

With momentum so close to the limit, relatively small errors can push it over the limit, and the extreme gradients in the shock can often be enough to do so. Thus this case is quite difficult to handle, as we need to keep a tight lid on the magnitude of the errors.

This also means that seemingly unimportant (or even detrimental) alterations can be the difference between the code working at high C_u and not. For instance, one alteration that sometimes works, is to enforce the PC conditions after interpolation, as discussed by section 3.2.7. This can allow the code to handle this strong fast shock at high C_u for a second or third order code. However, if we are using this PC enforcement scheme, then we have found that the code actually fails if we do not also implement the DER correction to the third order interpolation discussed in section 3.1.4. This is quite surprising, as one might imagine that a higher order correction like this would be more likely to cause problems near discontinuities than solve them. This is indicative of the volatile nature of this test case.

We will move on from this issue for now, since as we will see later the method to correct some of the other issues with these high-σ fast shocks can also help with the volatility problem as well, and negate the necessity of a low C_u value.

Fig. 4.18 shows the same shock in the fluid frame, and the issues are even more apparent here. The shock appears to have constructed a complicated structure — although this could be the shock actually being several waves together; since in this frame, the high fluid velocities mean that several wave modes have phase velocities near the speed of light, at least in the downstream state with $u_x = 52.372$. With that said, this test at least does not require a small value for C_u unlike the stationary case, and works fine at $C_u = 0.4$.

Another problem we can see in Fig. 4.18 is that the shock is very wide. This is most likely attributable to the near-total lack of non-linear steepening, and thus there is little keeping the shock sharp. It is for this reason that we decided to upgrade the code to third order, although there is still significant widening of the shock here even with this.

Conservation Error

Besides the instability of the code, the noticeable differences between the downstream values of ρ, p_g and B_z compared to the initial values in several of the previous tests is concerning. In the stationary case, there also appears to be a small oscillation (most clearly visible in the plot of B_z, Fig. 4.17b) and the shock itself is drifting the left. As mentioned, this could be explained by the system merely settling to a different solution, but this may not be the actual cause.

While the moving fast shock in Fig. 4.18 appears to *ultimately* reach a similar state downstream of the shock to the initial conditions, the shock itself is very wide and has developed a complex structure. This time, the complex structure is not an aspect shared by the previous fast shock tests.

We can see that the new shock in Fig. 4.17 features a smaller jump in density in gas pressure, and a larger jump in B_z. Only the downstream variables are affected; this is to be expected, since the upstream fluid is currently moving faster than the fast phase speed and so no changes can propagate into this region. This shock is also moving to the left, albeit quite slowly at $v = -0.05$.

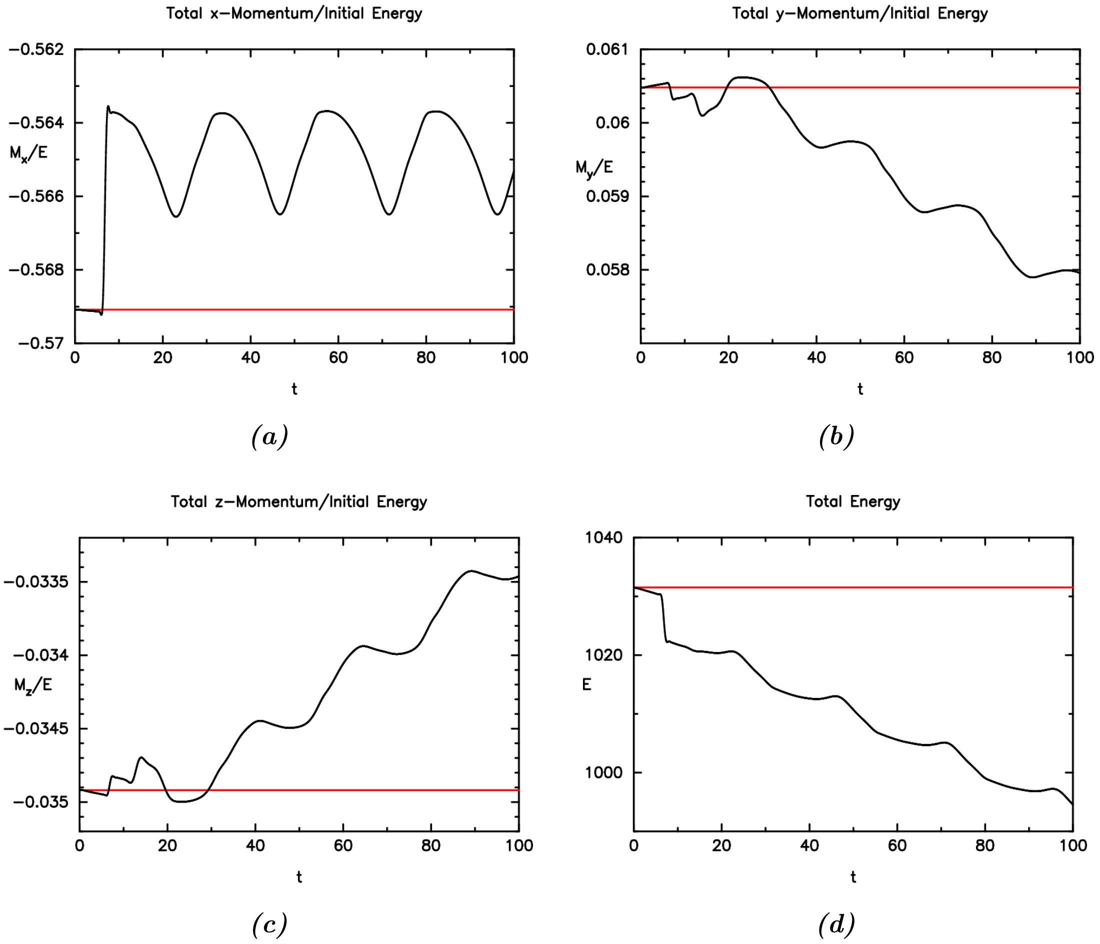

(a) *(b)*

(c) *(d)*

Figure 4.19: *x-component (a), y-component (b), and z-component (c) of the total momentum divided by initial total energy, as well as total energy (d) in the system over time for the stationary shock test Fig. 4.13. The red line indicates the initial value of each.*

In section 3.2.6 we noted that the force-free system is unable to fully conserve all the energy and momentum. It may be that the problem here is related. Indeed, Figs. 4.19

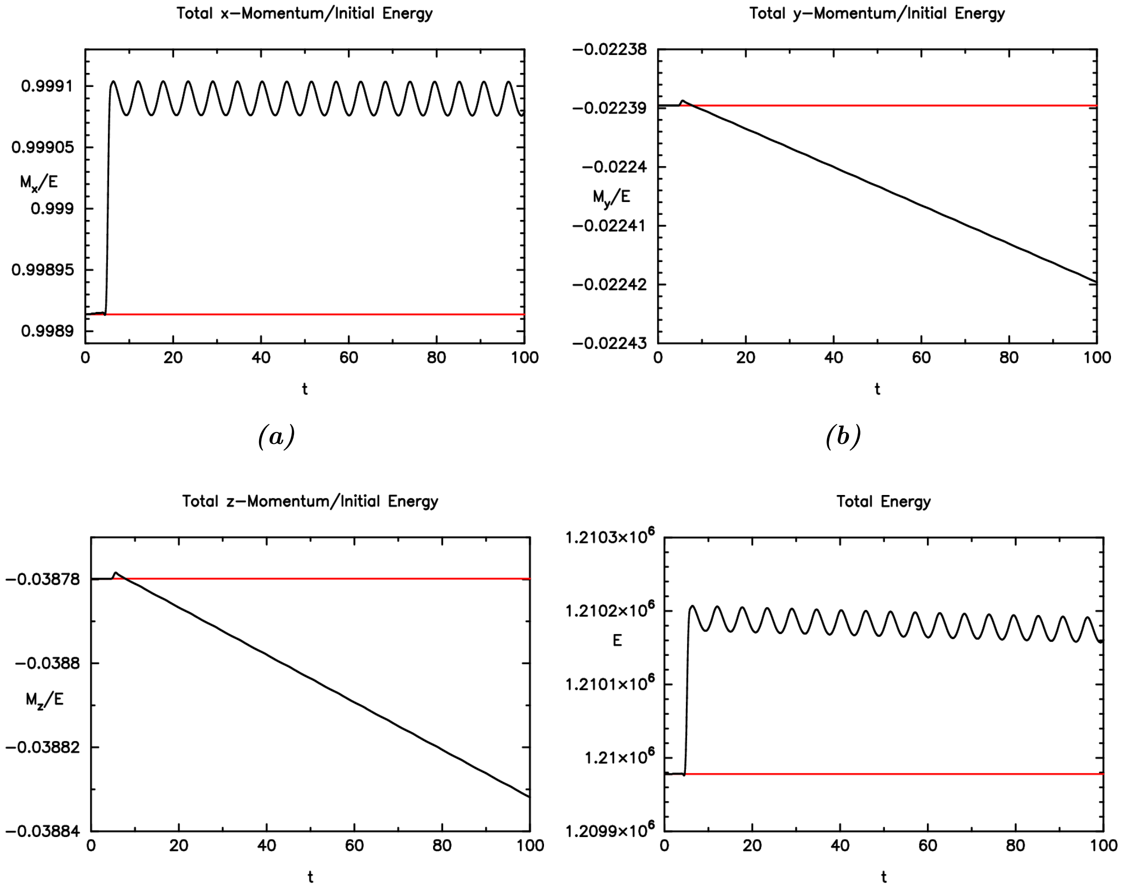

(a) *(b)*

(c) *(d)*

Figure 4.20: *x-component (a), y-component (b), and z-component (c) of the total momentum divided by initial total energy, as well as total energy (d) in the system over time for the stationary shock test Fig. 4.15. The red line indicates the initial value of each.*

to 4.21 show the total conserved RMHD variables in the system over time for the stationary shocks in Figs. 4.13, 4.15 and 4.17. We can clearly see that these conserved variables are not conserved, although the error is relatively small each time step.

This problem is not quite as bad as these plots make this appear, however. Some of this drift in the total energy and momentum over time is not due to loss of conservation. If we refer back to the results these came from then we can see that in all three cases the shock itself has ended up moving against the grid, in contrast to the initial solution which was stationary. This movement across the grid is responsible for some of the drift in the variables, since as the shock moves across the grid the proportion of the grid that is in the upstream and downstream states changes, thereby changing the totals of the conserved variables.

This motion across the grid is also responsible for something else: These plots of the total conserved variables also show an oscillation in many of the conserved variables, in all three fast shock cases in Figs. 4.19 to 4.21. We can associate these oscillations with the

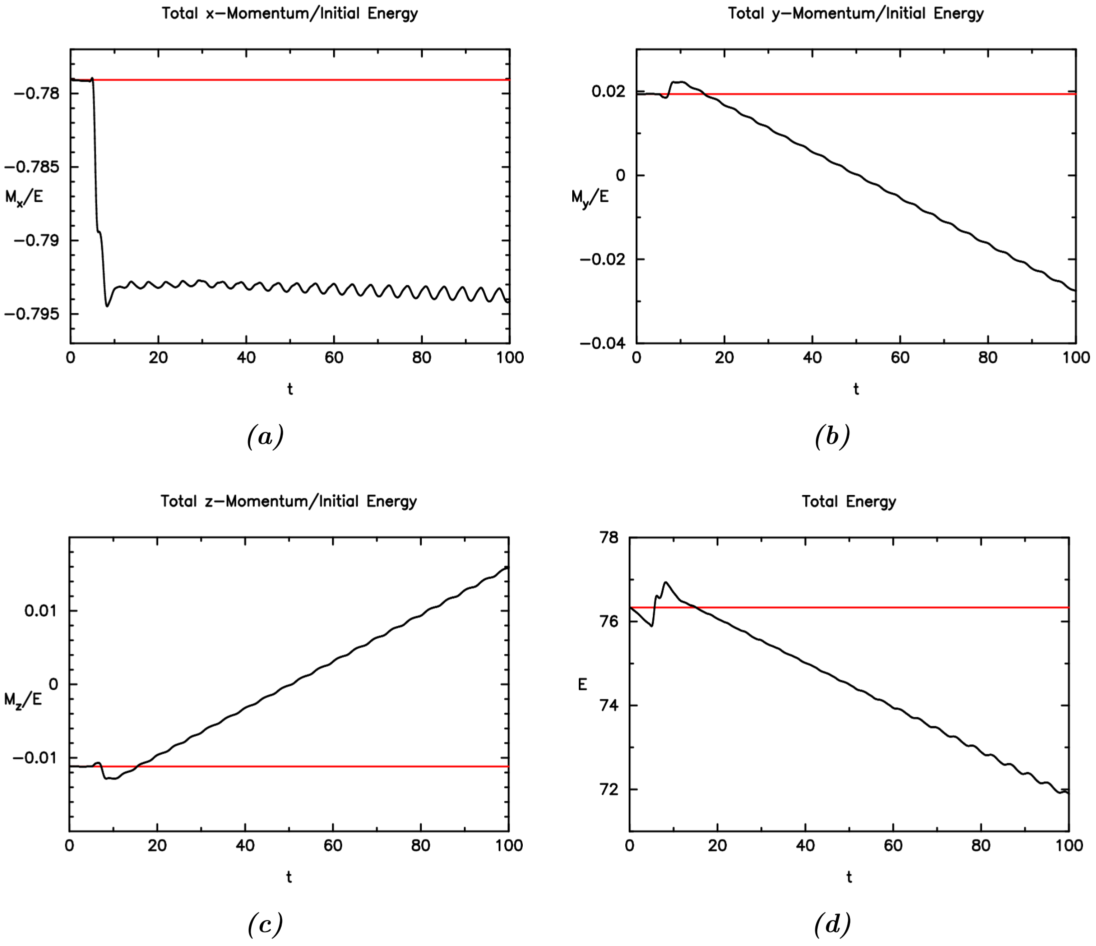

(a) *(b)*

(c) *(d)*

Figure 4.21: *x-component (a), y-component (b), and z-component (c) of the total momentum divided by initial total energy, as well as total energy (d) in the system over time for the stationary shock test Fig. 4.17. The red line indicates the initial value of each.*

movement of the shock across the grid because the period of the oscillations matches the movement across the grid. That is, there is exactly one complete oscillation for each grid point travelled. The fact that the high-σ shocks are moving faster than the low-σ shock is clearly visible.

Besides the movement of the shock across the grid, there is still the overall failure of accurate conservation to consider. The cause of this error is something that has been identified previously; in section 3.2.6 we discussed the method of converting variables from conserved to primitive in the force-free and interaction operators. In the force-free operator, we noted that due to the system being overdetermined, it was not possible (by this method) to maintain conservation of all the conserved variables down to numerical error. We can only maintain to conservation down to truncation error for at least three of the conserved variables.

After converting the conserved variables to primitives, at the end of the time step we perform the recombination step, where $\boldsymbol{B}_0$ and $\boldsymbol{B}_1$ are added back together and $\boldsymbol{B}_0$ is set to their total, and the same for $\boldsymbol{E}$. This then necessitates recalculating the conserved variables, but since the $\boldsymbol{B}_0$ and $\boldsymbol{E}_0$ did not completely match their conserved counterparts, after recalculating the conservatives this mismatch error is then lost.

This error should be present in all the previous tests, but it is only really noticeable here for a couple of reasons:

1. The error is in the force-free operator, so tests that only rely on the interaction operator or tests at small σ where the interaction operator is relatively large will not see significant issues from this.

2. The error will be more pronounced near large gradients or discontinuities, since the truncation error will be larger.

Correcting Conservation error

Correcting this error has no obvious solution. The first idea would be to reduce the truncation error, but since we are having issues near discontinuities increasing the order of the code will have limited effect, since we need to reduce the order near discontinuities anyway. Furthermore, increasing resolution may improve the situation for continuous solutions, but discontinuities become sharper in response, which could paradoxically increase the error instead.

One method that comes to mind is that while the force-free system cannot deal with this error the interaction system is not overdetermined, so if we moved the error into the interaction system then it may be able to handle it.

At the end of the time step, prior to calculating primitives, we have the conserved variables $\boldsymbol{B}_0, \boldsymbol{M}_0$ and U_0 for the magnetic field, momentum and energy from the force-free system respectively. We also have the conserved variables $D, \boldsymbol{B}_1, \boldsymbol{M}_1$ and U_1 for the conserved mass, magnetic field, momentum and energy for the interaction system respectively.

In section 3.2.6 we described the method used to convert these to primitives. Starting with the force-free system, we seek a $\boldsymbol{B}_0$ and $\boldsymbol{E}_0$ to match the $\boldsymbol{B}_0, \boldsymbol{M}_0$ and U_0, i.e. so that we have

$$\boldsymbol{Q}\begin{pmatrix}\boldsymbol{B}_0\\ \boldsymbol{E}_0\end{pmatrix} = \begin{pmatrix}\boldsymbol{B}_0\\ \boldsymbol{M}_0\\ U_0\end{pmatrix}. \tag{4.7}$$

As noted previously, this is generally impossible, due to truncation error making the conserved variables inconsistent. All we can do is find a “good enough” $\boldsymbol{B}_0$ and $\boldsymbol{E}_0$ that is as close as we can get it. Our dilemma is that no matter how close we try, there will generally always be a non-zero difference

$$\begin{pmatrix} \boldsymbol{B}_0 \\ \boldsymbol{M}_0 \\ U_0 \end{pmatrix} - \boldsymbol{Q}\begin{pmatrix} \boldsymbol{B}_0 \\ \boldsymbol{E}_0 \end{pmatrix} = \delta\boldsymbol{Q} = \begin{pmatrix} \delta\boldsymbol{B}_0 \\ \delta\boldsymbol{M}_0 \\ \delta U_0 \end{pmatrix}, \tag{4.8}$$

with $\delta\boldsymbol{Q}$ on the order of the truncation error.

The proposed solution is very simple — we take this error $\delta\boldsymbol{Q}$ and add it to the interaction system instead. That is, after calculating the force-free primitives we then move the error over by setting

$$\begin{pmatrix} \boldsymbol{B}_0 \\ \boldsymbol{M}_0 \\ U_0 \end{pmatrix} \to \begin{pmatrix} \boldsymbol{B}_0 - \delta\boldsymbol{B}_0 \\ \boldsymbol{M}_0 - \delta\boldsymbol{M}_0 \\ U_0 - \delta U_0 \end{pmatrix}, \tag{4.9}$$

for the force-free conservatives and

$$\begin{pmatrix} D \\ \boldsymbol{B}_1 \\ \boldsymbol{M}_1 \\ U_1 \end{pmatrix} \to \begin{pmatrix} D \\ \boldsymbol{B}_1 + \delta\boldsymbol{B}_0 \\ \boldsymbol{M}_1 + \delta\boldsymbol{M}_0 \\ U_1 + \delta U_0 \end{pmatrix}, \tag{4.10}$$

for the interaction conservatives. We can then calculate the interaction primitives from these new conservative variables, which for this system has a unique solution since the system is not overdetermined.

Unfortunately, there is a glaring flaw in this method, in that if the error is too large (and it is not necessarily smaller than the interaction system) then the primitive conversion may fail to find a solution. For instance, if the error in energy reduces the amount of energy in the interaction system, then it may be reduced too low for there to be a corresponding set of primitives.

Moreover, the code with this correction would appear to be more-or-less identical to a normal RMHD code, with only minor differences between them. Thus if this method somehow worked it would seem that a normal RMHD code would work anyway.

Even so, applying this method does help prove that this is indeed the cause of the problems in Figs. 4.13, 4.15 and 4.17. Running the same test of Fig. 4.17 again with this correction in Fig. 4.22 shows that the results are now working perfectly, and so this conservation error is definitely the problem at hand.

However, as noted above a normal RMHD code is also able to handle this problem, so this is not very useful at all — moreover, if we change Lorentz frame to one in which the shock is even moving at a very low shock velocity of $|v| = 0.1$ or even less then this causes the code to fail, both for a normal RMHD code and our code with this method applied.

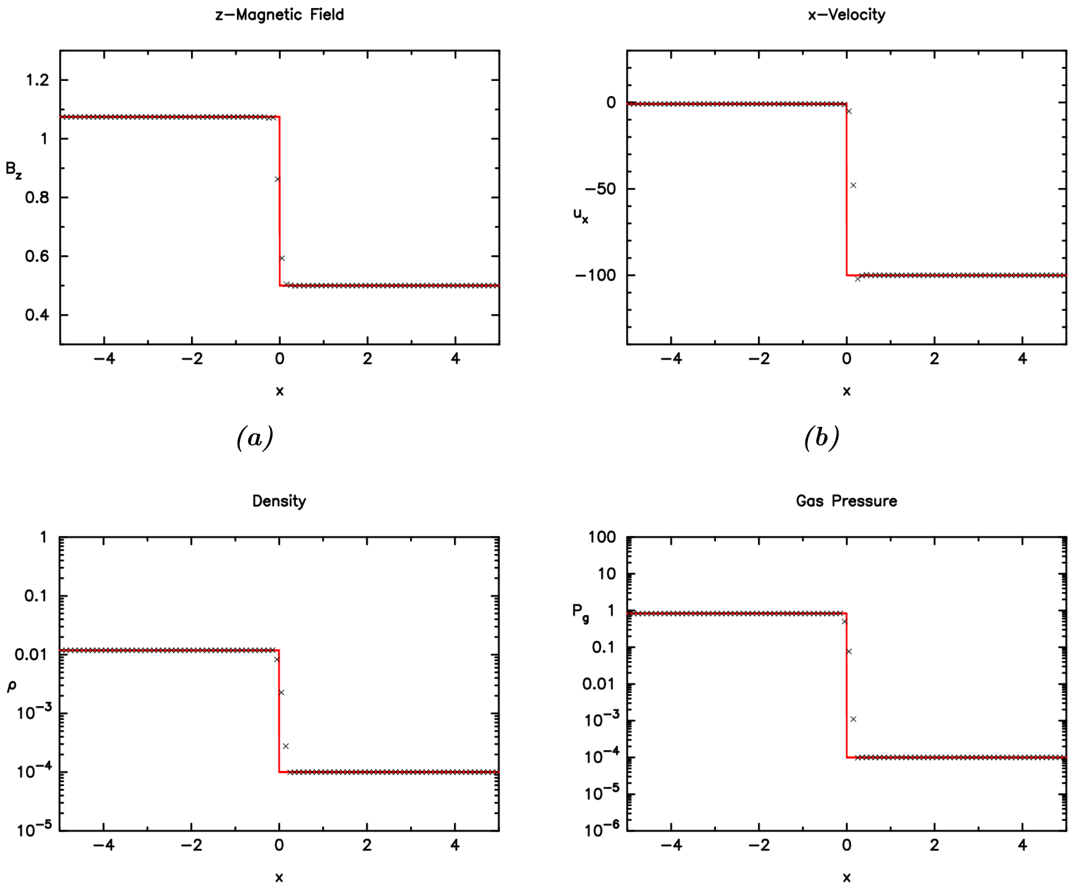

(a) *(b)*

(c) *(d)*

Figure 4.22: *B_z (a), u_x (b), ρ (c) and p_g (d) for a test of the same conditions as Fig. 4.17. This time, conservation is enforced using the conservation error shifting method detailed in section 4.3.4.*

With that said, the main reason that this correction crashes the code is that the total energy becomes too low. As noted previously, the total energy $E = U_0 + U_1$ and total momentum $\boldsymbol{M} = \boldsymbol{M}_0 + \boldsymbol{M}_1$ must satisfy $E^2 > M^2$, and these strong fast shocks tests are very close to violating this condition, with E^2/M^2 close to 1. It is generally the violation of this particular condition that causes the code to crash when running the transfer scheme.

If we write the conservation loss in energy as ΔU_0, and that of momentum as $\Delta \boldsymbol{M}_0$, then the shifting method adds ΔU_0 to the interaction energy U_1 and $\Delta \boldsymbol{M}_0$ to the interaction momentum $\boldsymbol{M}_0$, and subtracts them from the force-free counterparts. Since the condition we want to keep satisfied is

$$(U_0 + U_1)^2 > (\boldsymbol{M}_0 + \boldsymbol{M}_1)^2 \,, \tag{4.11}$$

instead of transferring all of ΔU_0 and $\Delta \boldsymbol{M}_0$, we could instead restrict the transferral to only those cases where the total energy would not drop as a result of the transfer — i.e. those cases where $\Delta U_0 > 0$. This should theoretically avoid most cases where $E^2 > M^2$

is violated due to the transferral.

If however the momentum error $\Delta \boldsymbol{M}_0$ is even more significant than ΔU_0 this transferral could still violate the condition. In practice this seems rare, but we could avoid this by simply transferring only the energy and leaving the momentum alone. Moreover, testing shows that the results for fast shocks with this conditional transfer scheme are in fact either slightly better if we do not transfer momentum, or they are not noticeably affected at all.

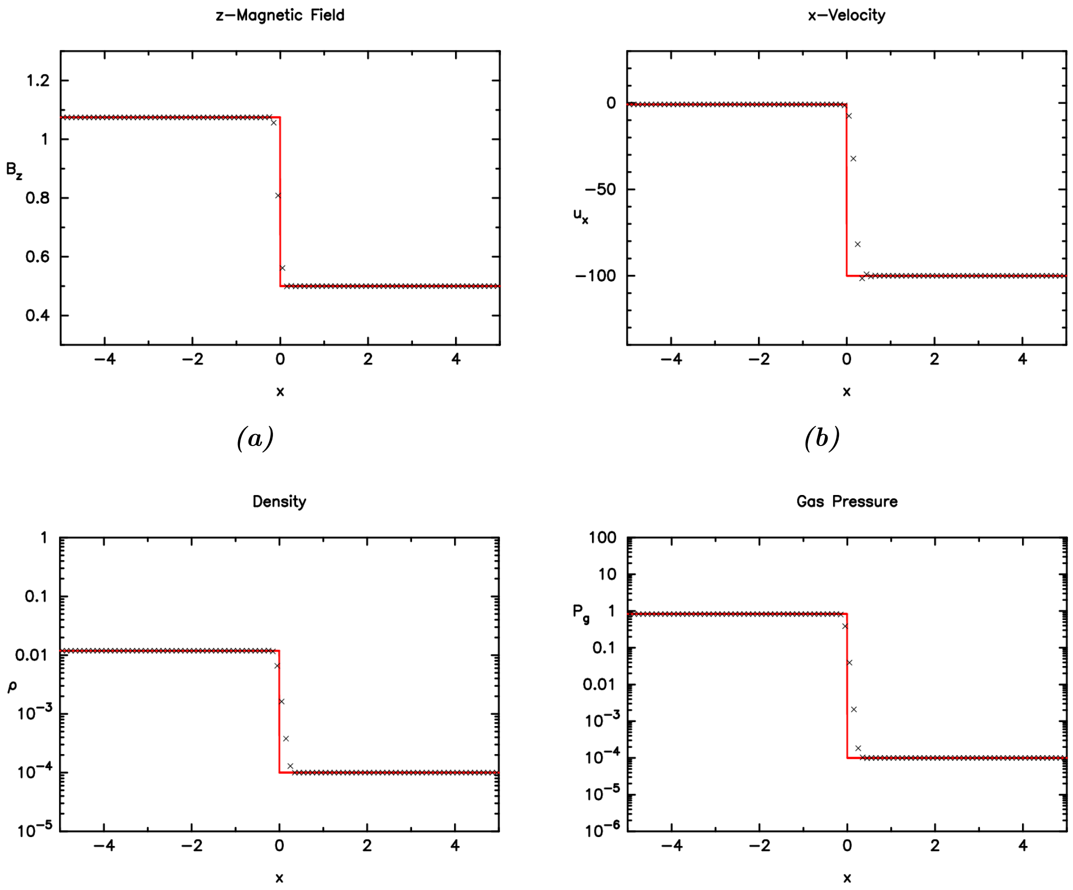

(a) *(b)*

(c) *(d)*

Figure 4.23: *B_z (a), u_x (b), ρ (c) and p_g (d) for a test of the same conditions as Fig. 4.17. This time, the energy lost from the force-free system after each time step is transferred to the interaction system using the energy error shifting method detailed in section 4.3.4.*

Performing this conditional transfer of just the energy does successfully allow the code to work, even for the moving shock. Fig. 4.23 gives the results with this conditional transfer scheme for the strong, high-σ stationary fast shock in Fig. 4.17.

As we can see, there is no longer a notable difference in the downstream variables, and in fact if we compare these results to the stationary shock with the full transfer scheme in Fig. 4.22, we can see that there is in fact little difference at all, despite the lack of momentum conservation, or the lack of energy conservation when the condition for transfer is not satisfied.

For the moving shock case, Figs. 4.24 and 4.25 show the same cases as Figs. 4.16 and 4.18 respectively, this time using the conditional energy transfer scheme. While the scheme appears to have little to no effect on the strong fast shock in Fig. 4.18, this adjustment does partially correct the issue with the loss of downstream gas pressure in the weak shock in Fig. 4.16.

Although it has no apparent effect on the strong shock, the fact that it does not make anything worse indicates that this correction is worth keeping. In addition, besides the complex shock structure for the strong fast shock, the downstream variables were already quite accurate before any corrections.

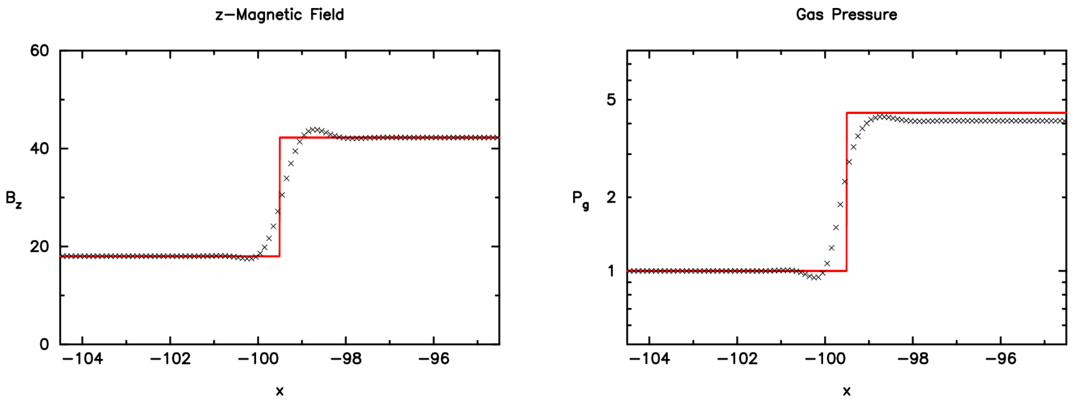

(a) *(b)*

Figure 4.24: *B_z (a) and p_g (b) for a test of the same conditions as Fig. 4.16. This time, conservation is corrected using the conditional energy error shifting method detailed in section 4.3.4.*

Other than this correction, the only alternative we have come up with is to alter the variable conversion in section 3.2.6 to try to maintain conservation of particular variables. As discussed there, we can alter the variable conversion to enforce energy conservation automatically, by setting $\boldsymbol{B}_0$ and $\boldsymbol{E}_0$ to match the conserved FF energy.

Unfortunately, altering the method in this way does not appear to have significant effects on the results of the tests — in spite of the fact that keeping energy conserved (or at least not decreasing) allows stationary fast shocks to work well.

Since it proved to be useful here, all tests in this chapter as well as most of the next chapter here have been performed with the condition energy transfer scheme, besides the previous fast shock tests. This includes the previous 1D tests performed above, like the Alfvén waves and slow shocks.

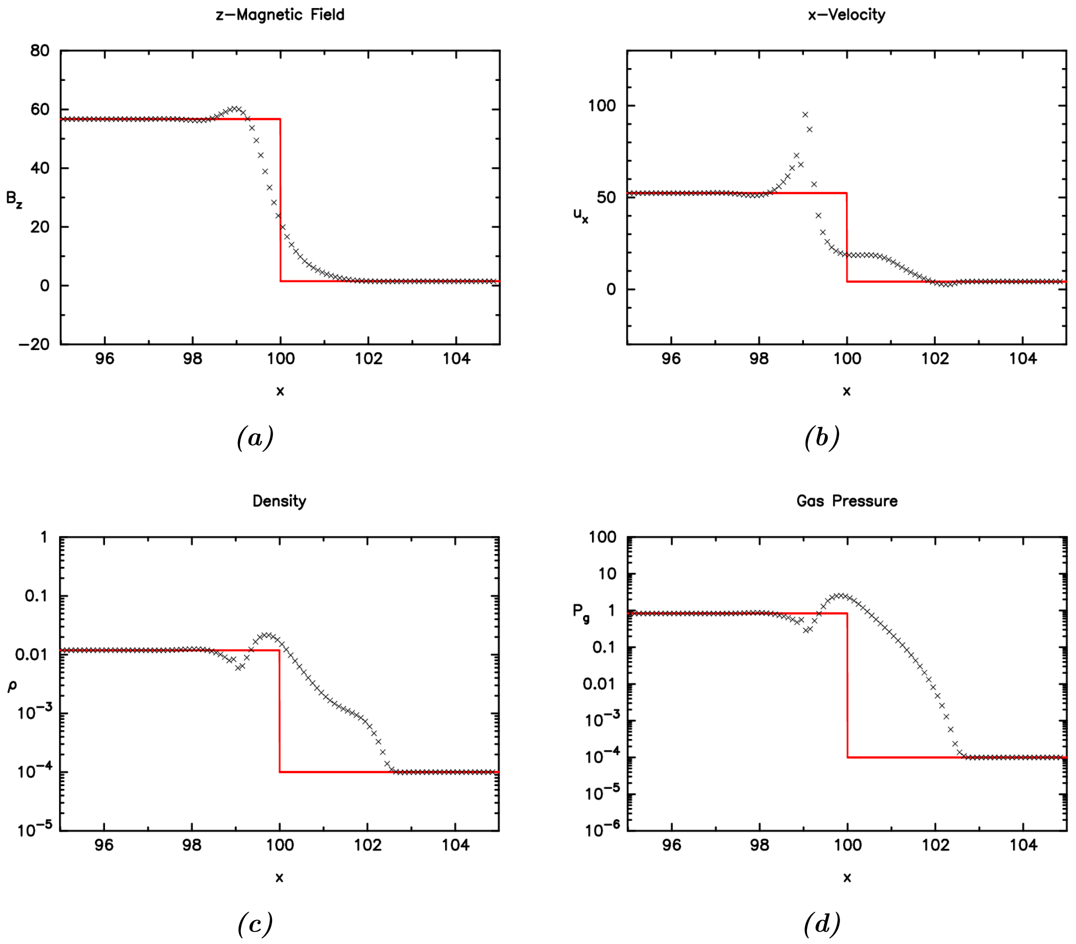

Figure 4.25: *B_z (a), u_x (b), ρ (c) and p_g (d) for a test of the same conditions as Fig. 4.18. This time, conservation is corrected using the conditional energy error shifting method detailed in section 4.3.4.*

4.3.5 Current Sheets

As features that are not properly handled by FFDE simulations, ensuring that current sheets can be handled is of paramount importance. As current sheets are discontinuities featuring large gradients in the electromagnetic fields, we may be concerned that the conservation error we have just identified may be problematic here as well, but since the magnetic field strength drops in the sheet, σ also drops so we may not need to be so concerned.

Current sheets were discussed in section 2.3.1, where we also considered all such discontinuities that are stationary with respect to the fluid. There we identified that if $B_x = 0$ then the condition that the total pressure is constant (i.e. the sum of the gas and pressures $p_t = p_m + p_g$) is sufficient for all such stationary cases.

This gives us a lot of freedom with regards to how to set up a current sheet, as we can include a change in density ρ, a change in the ratio of the pressures p_g/p_m, and a change in the direction of the magnetic field $\boldsymbol{B}$. It is this third option of changing $\boldsymbol{B}$ that is most interesting to us, as the other two variables ρ and p_g are both of order $\sim \mathcal{O}(\sigma^{-1})$. Thus if we want to keep $\sigma \gg 1$, we are limited in how much we can change these values.

Thus we are most interested in a rotation of $\boldsymbol{B}$ (in the fluid frame). Such a solution is known as a current sheet, since Ampère's law

$$\boldsymbol{\nabla} \times \boldsymbol{B} = \boldsymbol{J} + \frac{\partial \boldsymbol{E}}{\partial t}, \tag{4.12}$$

implies the existence of a charge current $\boldsymbol{J}$ in the region where the magnetic field changes direction. This is because the rotation of the magnetic field would mean $\boldsymbol{B}$ has non-zero curl, and the fact that we are in the fluid frame implies $\boldsymbol{E} = 0$ and therefore $\partial_t \boldsymbol{E} = 0$, so we must have non-zero $\boldsymbol{J}$.

The rotation of the magnetic field can be by any amount; if we let $\boldsymbol{B}_l = (0, B, 0)$ be the magnetic field to the left of the current sheet then the right is given by

$$\boldsymbol{B}_r = \begin{pmatrix} 0 \\ B\cos\theta \\ B\sin\theta \end{pmatrix}, \tag{4.13}$$

with θ the rotation of the field.

Although these solutions imply that the current sheet could be resolved in the numerical model as a rotation of the magnetic field over a small but non-zero number of cells, in practice the numerical solution tends to connect the two states directly. That is, the structure of the numerical solution to the current sheet does not rotate the magnetic field, but instead the magnetic field strength drops in the structure of the sheet. Thus the condition above of constant total pressure implies that the gas pressure must rise to compensate, heating the plasma.

In the most extreme case with $\theta = \pi$ the field rotates a half turn and so the magnetic field completely flips direction, $\boldsymbol{B}_r = -\boldsymbol{B}_l = (0, -B, 0)$. Thus in the numerical structure of the current sheet, the magnetic field magnitude drops to 0 in the centre very briefly, before flipping sign and increasing in magnitude again. In such conditions the value of σ will of course increase, reaching infinity at the point where $\boldsymbol{B} = 0$.

From this it is immediately clear why FFDE has difficulties with these conditions; since it has no gas pressure to increase there is nothing to counterbalance the current sheet. The magnetic field drops, and the fundamental condition of FFDE — that the inertial terms are negligible — is violated, as the magnitude of B^2 approaches 0 and the PC condition $B^2 - E^2 > 0$ is broken. The FFDE Riemann problem in this case has no solution.

Fig. 4.26 shows the results of a stationary current sheet at low σ, while Fig. 4.27 shows the same current sheet moving at $v = 0.5$ to the left. For the stationary case, the code appears to be able to handle the problem without difficulty. However, for the moving case

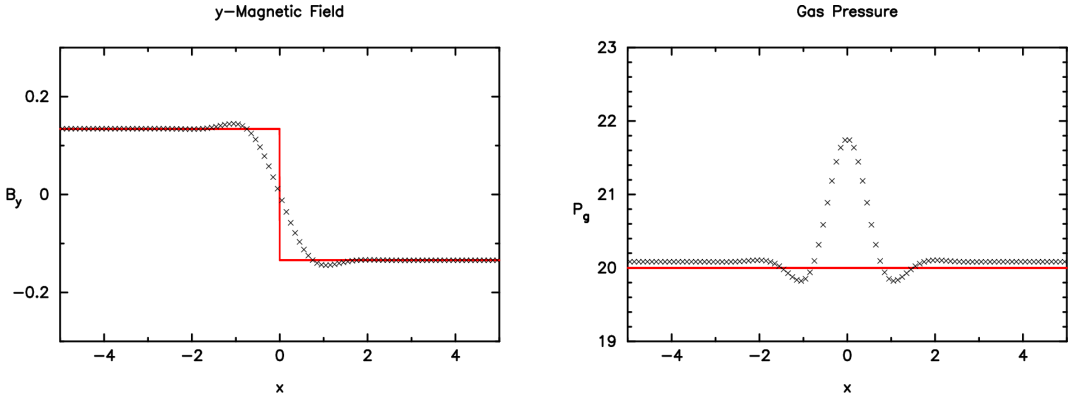

(a) *(b)*

Figure 4.26: *B_y (a) and p_g (b) for a stationary current sheet test, run until $t = 100$ at resolution 100, using a third order code, Neumann BCs, width parameter $a = 0.1$, and a domain of $[-5, 5]$. In this case, $\sigma = 0.036842$ in the left and right states, but drops to 0 at the centre of the current sheet.*

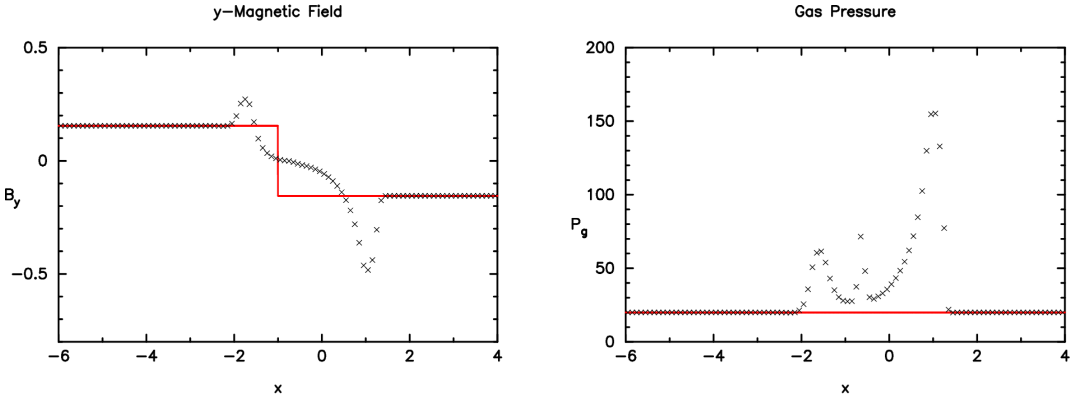

(a) *(b)*

Figure 4.27: *B_y (a) and p_g (b) for a moving current sheet test, run until $t = 3$ at resolution 100, using a third order code, Neumann BCs, width parameter $a = 0.1$, and an initial domain of $[-5, 5]$ which we have shifted during the test to follow the current sheet. This test is the same case as Fig. 4.26, but in a different frame with the current sheet now moving with phase velocity $\mu = -0.5$, so σ is the same as before with $\sigma = 0.036842$ in the left and right states.*

there are clearly very significant errors in which the system immediately emits waves in both directions, that reduce the magnitude of B_y to near-zero and significantly heat the plasma.

Fig. 4.28 shows the results of a stationary current sheet at high σ. Once again, the code can handle the stationary case without much issue, although the sheet has become relatively wide (note that this width is a little exaggerated by the logarithmic plot of gas pressure, it would not look so wide in a non-logarithmic plot).

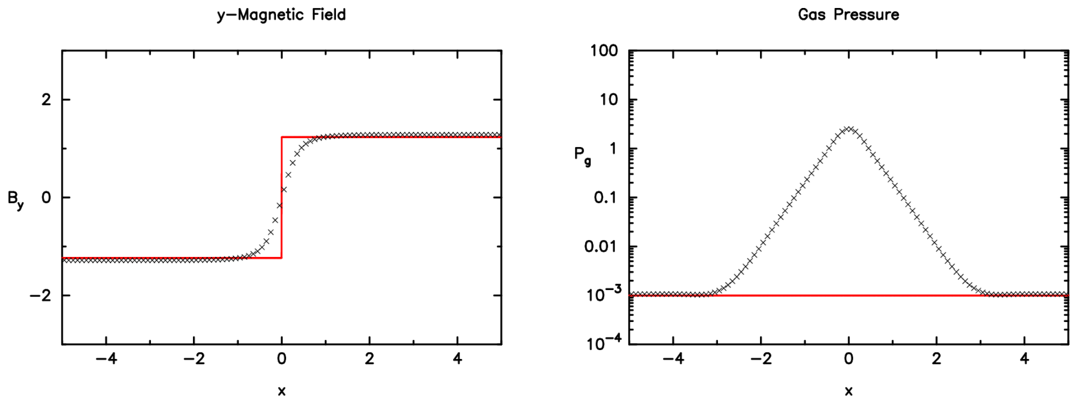

(a) *(b)*

Figure 4.28: *B_y (a) and p_g (b) for a stationary current sheet test, run until $t = 100$ at resolution 100, using a third order code, Neumann BCs, width parameter $a = 0.1$, and a domain of $[-5, 5]$. In this case, $\sigma = 926.87$ in the left and right states, but drops to 0 at the centre of the current sheet.*

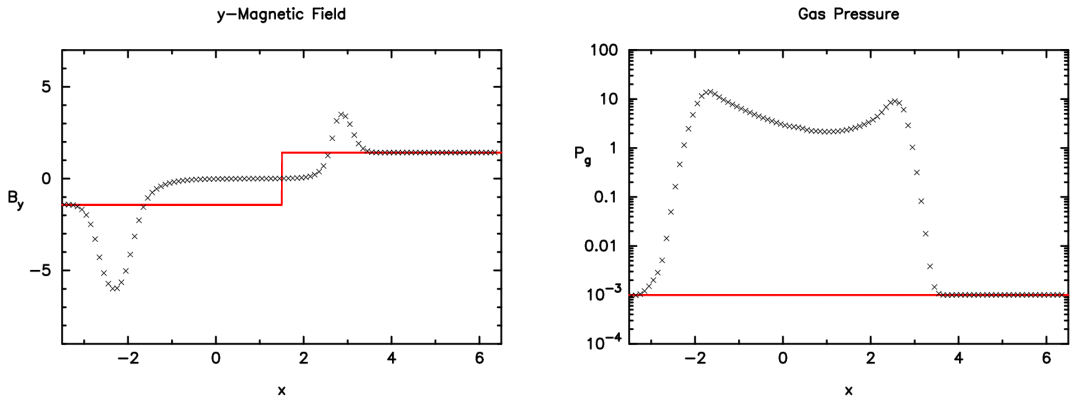

(a) *(b)*

Figure 4.29: *B_y (a) and p_g (b) for a moving current sheet test, run until $t = 3$ at resolution 100, using a third order code, Neumann BCs, width parameter $a = 0.3$, and an initial domain of $[-5, 5]$ which we have shifted during the test to follow the current sheet. Again this test is the same as Fig. 4.28 but in a different frame with the current sheet now moving at $\mu = 0.5$, so σ is the same as before with $\sigma = 926.87$ in the left and right states.*

Fig. 4.29 shows the results for the same current sheet in a different frame, with the sheet moving at $v = 0.5$ now. Much like the low-σ case, the system has immediately collapsed and sent out waves to the left and right which carry away B_y, and this time giving a noticeable increase in the gas pressure.

While the example cases here will immediately fail, previous tests were able to last at least a few iterations before giving incorrect results. In these cases, after a few iterations the test would suddenly jump, producing a large spike in pressure at the current sheet and sending out waves in either direction. Sometimes these waves would have no apparent effect on the current sheet, but eventually one would carry away most of the B_y away.

After analysing the tests carefully, we eventually determined the cause of this error. Consider the case of $\boldsymbol{B}_l = (0, B, 0), \boldsymbol{B}_r = (0, -B, 0)$. Since the magnetic field in the numerical solution changes directly between the left and right states, we always have $B_x = B_z = 0$. Near the centre of the current sheet, the magnetic field drops in magnitude very sharply and eventually flips sign.

In the force-free system, $\boldsymbol{B}_0$ frequently drops so sharply that we have $E_0^2 > B_0^2$ in violation of Eq. (3.89); surprisingly, for our code this generally does not cause obvious problems in itself. This is because the equations themselves do not have much problem with violating this constraint, and the only real problem is that the Alfvén phase speeds are non-physical in this case. Since we are using an HLL solver, these phase speeds are never needed and so this issue does not often cause any problems, and the code can continue running unabated.

Since the integration method steps forward by finite time steps each iteration, the magnitude of $\boldsymbol{B}_0$ never actually reaches 0, as it will instead jump over this point from $B > 0$ to $B < 0$. However, how close the system comes to 0 differs each time a cell passes through the transition. The system is chaotic enough that this distance is effectively random.

Occasionally then, the magnitude of $\boldsymbol{B}_0$ drops exceptionally low and becomes very nearly 0, as the time step update happens to place it closer to 0 than usual as it flips sign. In the variable conversion described in section 3.2.6, we set $\boldsymbol{E}_0$ via Eq. (3.118)

$$\boldsymbol{E}_0 = \frac{1}{B^2} \left(\boldsymbol{S}_0 \times \boldsymbol{B}_0 \right).$$

Since $\boldsymbol{S}_0$ remained at a similar magnitude as before, the result is that the magnitude of $\boldsymbol{E}_0$ increases to compensate. In one particular test case of a current sheet we examined, the value of $\boldsymbol{B}_0$ dropped to approximately $\boldsymbol{B}_0 \sim 10^{-5}$ while we had $\boldsymbol{S}_0 \sim 10^{-4}$, thus the magnitude of $\boldsymbol{E}_0$ became $\boldsymbol{E}_0 \sim 10$, *far* larger than it should be. Thus $\boldsymbol{B}_0$ is near 0 while $\boldsymbol{E}_0$ is very large, an enormous violation of the condition $B^2 - E^2 > 0$.

When these highly inconsistent values of $\boldsymbol{B}_0$ and $\boldsymbol{E}_0$ are passed to the interaction system to calculate primitives, the numerical method is faced with a dilemma: if we recall the PC condition on the interaction system Eq. (3.96)

$$\boldsymbol{E}_1 = -\left(\boldsymbol{E}_0 + \boldsymbol{v} \times \boldsymbol{B}_0 \right) - \boldsymbol{v} \times \boldsymbol{B}_1,$$

then in attempting to satisfy this condition — which is enforced in the variable conversion — the code finds that the magnitude of $\boldsymbol{B}_0$ is much too small and $\boldsymbol{E}_0$ is much too large. Since $\boldsymbol{v}$ is capped at $v^2 < 1$ and $\boldsymbol{B}_1$ has not become large, in order to satisfy the condition the code must cancel out the $\boldsymbol{E}_0$ with an equally large and opposite $\boldsymbol{E}_1$.

This large $\boldsymbol{E}_1$ then causes more problems, most notably with the conserved interaction energy U_1 from Eq. (3.92)

$$U_1 = wu^0u^0 - p_g + \boldsymbol{E}_0 \cdot \boldsymbol{E}_1 + \boldsymbol{B}_0 \cdot \boldsymbol{B}_1 + \frac{1}{2}\left(E_1^2 + B_1^2\right).$$

The variable conversion subroutine has U_1 as a known quantity, and now has a very large $\boldsymbol{E}_1$ to deal with. Two terms specifically stand out, $\boldsymbol{E}_0 \cdot \boldsymbol{E}_1$ and $E_1^2/2$. Since $\boldsymbol{E}_1 \approx -\boldsymbol{E}_0$, these two terms cancel to $\approx -E_0^2/2$.

In order to match this to U_1, the subroutine has no choice but to either increase the gas pressure p_g so that the enthalpy density w increases, or increase the Lorentz factor γ (or both). Thus the end result after this chain of propagating errors is a single-cell jump in gas pressure and/or velocity, of at least one order of magnitude. This is the true origin of the sudden jump, as this spike in pressure then emits fast waves to the left and right, which carry some of the magnetic energy away from the current sheet, the scale of this emission dependent on how close $\boldsymbol{B}_0$ came to 0.

This error only appears in the moving case because the stationary current sheet is not moving across the grid, and so there is no chance for the sign change to occur. However, even a very slowly moving current sheet should encounter this issue, as the current sheet passes over the cells and the sign changes occur.

Although in both the moving tests above this problem occurred immediately, in other tests that have been performed previously this error instead occurred after a short time, and somewhat randomly. This is because B_y can "jump" over the sign change, and not reach the small value necessary to trigger this problem. However, given enough time we expect this problem to be triggered eventually.

Correcting Small $\boldsymbol{B}_0$ Error

Now that we have positively identified the cause of the error, we can now begin to correct it. Clearly, there are multiple different alterations we could make in order to attempt to correct this error. These different alterations may be mutually exclusive, and of course may not work at all.

Transition scheme

One fact that comes to mind is that the cause of the error is the force-free system. Since in the centre of the current sheet we should have $\sigma \ll 1$, as indeed we have seen in the tests, a full RMHD code instead of splitting should be able to handle it. Thus in order to correct this error we could include a condition that switches the code from splitting to full RMHD. Lehner *et al.* (2012); Paschalidis and Shapiro (2013) have already developed method for matching FFDE to RMHD, so it is not unreasonable to attempt to do something similar for our code as well.

In our case, we note that with $\boldsymbol{B}_0 = \boldsymbol{E}_0 = 0$ the equations of the interaction system reduce to the original equations of RMHD, so we do not need to include an entirely different RMHD integration scheme and could simply set $\boldsymbol{B}_0 = \boldsymbol{E}_0 = 0$ to switch the system. Aside from a few small differences, such a scheme should be more or less identical to a normal RMHD scheme.

The main such difference is that in our scheme, interpolation for the interaction system interpolates all of: $\rho, p_g, \boldsymbol{u}, \boldsymbol{B}_0, \boldsymbol{E}_0, \boldsymbol{B}_1, \boldsymbol{E}_1$. In this case with $\boldsymbol{B}_0 = \boldsymbol{E}_0 = 0$ these interpolations are irrelevant, but for the remainder, a typical ideal RMHD scheme would use the PC condition of Eq. (2.42), $\boldsymbol{E} = -\boldsymbol{v} \times \boldsymbol{B}$ to interpolate $\boldsymbol{E}$ implicitly. But in our case, we are interpolating $\boldsymbol{E}_1$ itself individually, and thus the results are a little different.

The means to correct this is clear; we can simply use the methods described in section 3.2.7 to set $\boldsymbol{E}_1$, which in this case exactly corresponds to $\boldsymbol{E}_1 = -\boldsymbol{v} \times \boldsymbol{B}_1$, thereby making this system identical to a normal ideal RMHD scheme. Of course, making our scheme identical to RMHD may not be necessary anyway.

Now that we have established a simple method of switching the scheme to normal RMHD, we propose the following correction: At the end of the time step, identify how small σ is. If it is below a specified value, instead of doing the normal recombination step Eq. (3.97)

$$\begin{aligned} \boldsymbol{B}_0 &= \boldsymbol{B}_0 + \boldsymbol{B}_1, \quad \boldsymbol{B}_1 = 0, \\ \boldsymbol{E}_0 &= \boldsymbol{E}_0 + \boldsymbol{E}_1, \quad \boldsymbol{E}_1 = 0, \end{aligned}$$

we instead do the reverse

$$\begin{aligned} \boldsymbol{B}_1 &= \boldsymbol{B}_0 + \boldsymbol{B}_1, \quad \boldsymbol{B}_0 = 0, \\ \boldsymbol{E}_1 &= \boldsymbol{E}_0 + \boldsymbol{E}_1, \quad \boldsymbol{E}_0 = 0, \end{aligned}$$

thus switching the system to full RMHD.

In order to make the transition smoother, we could also specify a transition region for σ between a pair of upper and lower limits σ_{min} and σ_{max}, so that for $\sigma \geq \sigma_{max}$ we use our normal recombination step, and for $\sigma \leq \sigma_{min}$ we use the reverse step. For the region in-between, we would use some transition function, i.e.

$$\begin{aligned} \boldsymbol{B}_0 = \alpha\left(\boldsymbol{B}_0 + \boldsymbol{B}_1\right), \quad \boldsymbol{B}_1 = (1-\alpha)\left(\boldsymbol{B}_0 + \boldsymbol{B}_1\right), \\ \boldsymbol{E}_0 = \alpha\left(\boldsymbol{E}_0 + \boldsymbol{E}_1\right), \quad \boldsymbol{E}_1 = (1-\alpha)\left(\boldsymbol{E}_0 + \boldsymbol{E}_1\right), \end{aligned}, \tag{4.14}$$

where $\alpha(\sigma)$ is a function of σ that determines how much of the total $\boldsymbol{B}$ and $\boldsymbol{E}$ goes into the force-free and interaction systems. If we use a simple linear transition, then

$$\alpha(\sigma) = \begin{cases} 0 & \text{if } \sigma \leq \sigma_{min} \\ \frac{\sigma - \sigma_{min}}{\sigma_{max} - \sigma_{min}} & \text{if } \sigma_{min} < \sigma < \sigma_{max} \\ 1 & \text{if } \sigma \geq \sigma_{max} \end{cases} \tag{4.15}$$

so that $\alpha(\sigma) \leq 0$ for $\sigma \leq \sigma_{min}$ and $\alpha(\sigma) \geq 1$ for $\sigma \geq \sigma_{max}$, with a linear transition between.

The end result of this is that as σ decreases the code transitions from the splitting scheme to a more typical RMHD scheme. Thus in the centre of the current sheet the errors of the force-free system should be avoided.

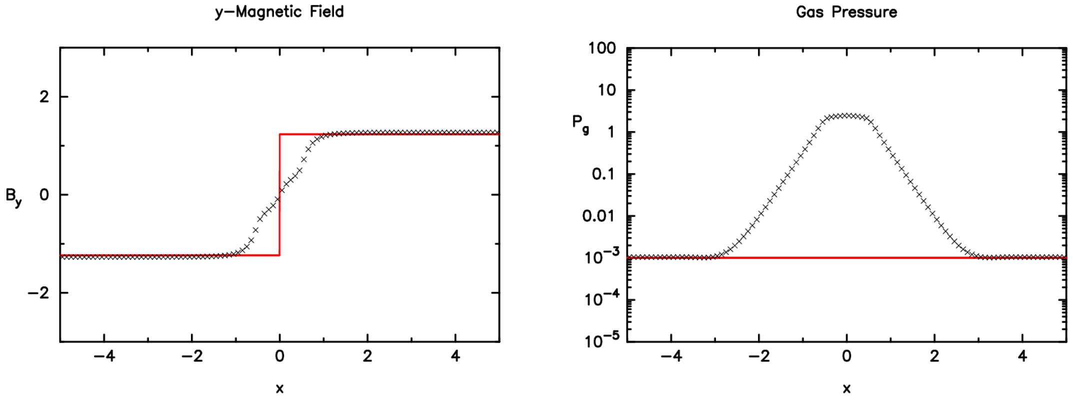

(a) *(b)*

Figure 4.30: *B_y (a) and p_g (b) for the case of Fig. 4.28 with the transition scheme detailed in section 4.3.5.*

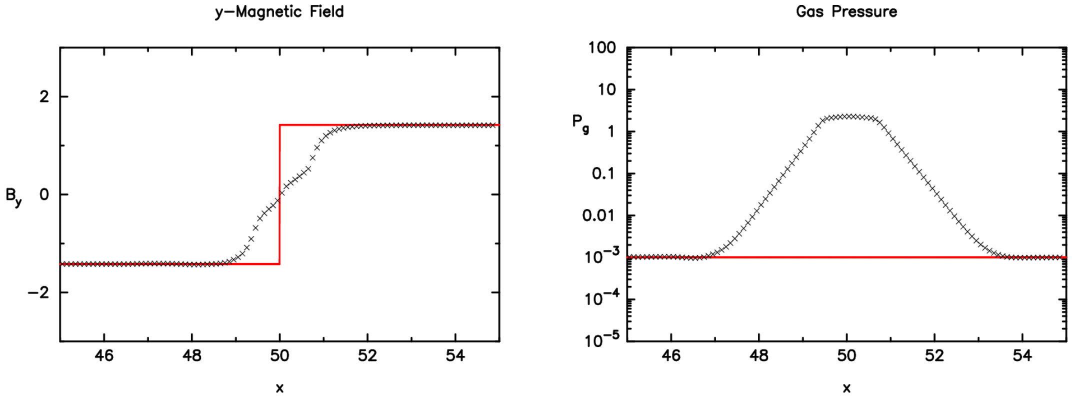

(a) *(b)*

Figure 4.31: *B_y (a) and p_g (b) for the case of Fig. 4.29, run until $t = 100$ with the DER step from section 3.1.4 turned off, and with the transition scheme detailed in section 4.3.5, and this time with a thinner initial discontinuity with width parameter $a = 0.2$.*

Figs. 4.30 and 4.31 show the results of the previous tests in Figs. 4.28 and 4.29 with this new correction. We can see that the problems have been eliminated entirely. The current sheet is able to run exactly as expected.

This method is not without its flaws, however. First, it was necessary to turn off the DER step described in section 3.1.4 from the third order interpolation scheme, in order to allow the moving current sheet in Fig. 4.31 to work — although some sort of limiting scheme that turns off the DER step near high gradients could potentially work as well.

You can also see from the plots that the transition has created a kind of structure in the results. In the gas pressure, there is a fairly wide region in the centre with a near-constant high pressure, and in the magnetic field the gradient is larger on the outside of the current sheet, but then becomes smaller towards the centre as the scheme transitions to RMHD. As a result, the stationary current sheet is now a few cells wider than it was before.

There are also problems with this scheme when expanded to 2D, at least for the GLM scheme that we are using to clean the divergence of $\boldsymbol{B}_0$ and $\boldsymbol{B}_1$ (see section 3.2.5 for the description of this scheme).

From Eqs. (3.109) to (3.110), we apply the GLM method to both the force-free system in Eqs. (3.108) and (3.109) and to the interaction system in Eqs. (3.110) and (3.111). At each time step (and sub-step), Eqs. (3.109) and (3.111) generate ϕ_0 and ϕ_1 proportional to the magnitude of $\boldsymbol{B}_0$ and $\boldsymbol{B}_1$ respectively. However, at the end of the time step we apply the transition scheme above, and so the ϕ_0 and ϕ_1 are no longer matched to the $\boldsymbol{B}_0$ and $\boldsymbol{B}_1$ that generated them.

For instance, we can consider a simple case where $\boldsymbol{B}_0 \neq 0$ at the start of the time step. At the end of the time step, $\phi_0 \neq 0$ has been induced by this $\boldsymbol{B}_0$. But now let us suppose that σ has also dropped by the end of the time step, so that $\alpha = 0$. As a result, $\boldsymbol{B}_0$ is now set to 0, and yet ϕ_0 is still non-zero. Thus the $\boldsymbol{B}_0$ and ϕ_0 have become mismatched.

Of course, this could be remedied by simply transitioning ϕ_0 and ϕ_1 just like $\boldsymbol{B}_0$ and $\boldsymbol{B}_1$ etc. This would then allow the ϕ and $\boldsymbol{B}$ to become properly matched again. However, while this could be effective, the fact that non-zero ϕ also affects neighbouring cells via Eqs. (3.108) and (3.110) means that we could have large ϕ_0 next to a cell with small $\boldsymbol{B}_0$, which again may cause problems.

Capping E0

Besides the previous method, a far simpler alternative also presents itself. In the analysis of the cause of the error given previously, we noted that the fundamental cause of this is that $\boldsymbol{E}_0$ is large while $\boldsymbol{B}_0$ is small. To remedy this then, a simple idea would be to cap the value of $\boldsymbol{E}_0$ to maintain the condition $B_0^2 - E_0^2 > 0$, which should have an effect on this problem.

We have some freedom in choosing the exact point in the code at which we apply the cap to the value of $\boldsymbol{E}_0$, and how. One method we could consider is altering the force-free primitive calculation, by selecting one of the other methods proposed in section 3.2.6 to prioritise the conservation of other variables, which may avoid the problem with $\boldsymbol{E}_0$. For instance, enforcing energy conservation with the conversion scheme may mean that $\boldsymbol{E}_0$ no longer causes the problem. However, there may be no way of doing so without violating the condition anyway.

Alternatively, we may note that the HLL method we are using for the FFDE system has no issues with violations of the $B_0^2 - E_0^2 > 0$ condition, and is able to obtain a sane estimate for the flux even if it is violated in a major way. After all, without correction the condition is in fact violated repeatedly during the tests in Fig. 4.30, and only occasionally causes major problems.

Thus we may be able to get away with a violation of the condition, provided that it is small enough to avoid the error we are trying to correct here. In particular we can keep the direction the same and simply restrict it to $E_0^2 = B_0^2$, a very minor violation of the condition that is simple to calculate.

However, for other methods such as a linear Riemann solver or even an exact solver, violations of this condition cause irreconcilable issues. For instance, the Alfvén phase speeds (required for a linear Riemann solver, unlike the HLL solver) comes out to an imaginary value if the condition is violated, as we can see from Eq. (2.113). In this instance we thus clearly need to require that the condition be satisfied. If we still keep the direction of $\boldsymbol{E}_0$ the same, then we need to choose a cap E_{max} such that $E_0^2 \leq E_{max} B_0^2$, with $E_{max} < 1$. This choice will necessarily be arbitrary of course.

Of course, this method clearly disregards conservation of all of the momentum and energy, retaining only the conservation of $\boldsymbol{B}_0$. It may be possible in some instances then that this correction will cause very significant loss of energy or momentum (since $\boldsymbol{E}_0$ is reduced this can only be a loss, not a gain). This may not be a significant issue however, since we expect σ to be small in the situations where this adjustment is relevant and therefore the increased conservation error should be relatively minor.

Figs. 4.32 and 4.33 once again shows the results of the previous tests of Figs. 4.28 and 4.29 using this correction instead, using a cap for $\boldsymbol{E}_0$ of $E_{max} = 0.99$. We can contrast these with the results from the previous correction, Figs. 4.30 and 4.31. We can clearly see that both correction methods appear to be as successful as each other — except this time we could keep the DER step in place, so the code can remain third order. In addition, unlike the transition scheme this scheme does not cause the current sheet to become wider.

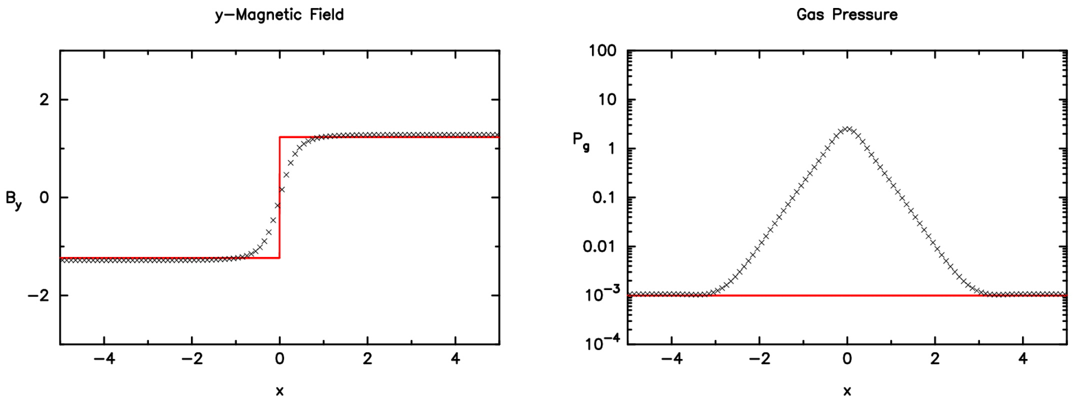

(a) *(b)*

Figure 4.32: *B_y (a) and p_g (b) for the case of Fig. 4.28 with the $\boldsymbol{E}_0$-capping scheme detailed in section 4.3.5.*

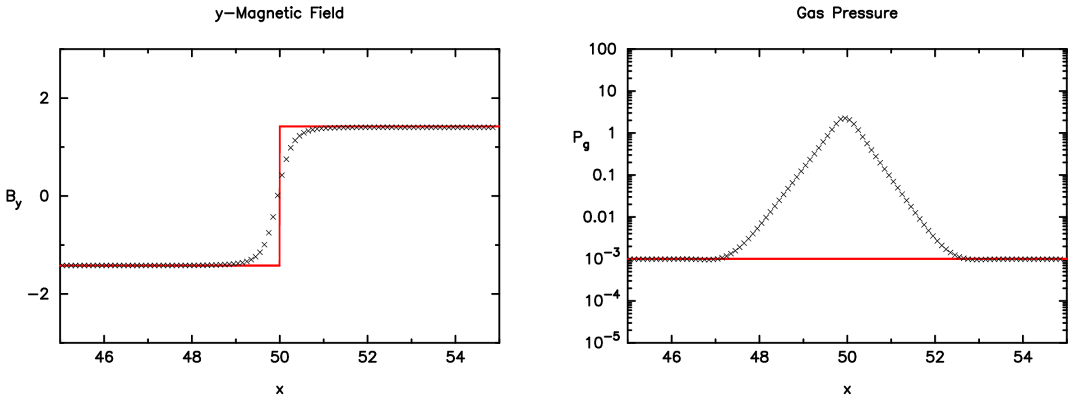

(a) *(b)*

Figure 4.33: *B_y (a) and p_g (b) for the case of Fig. 4.29, run until $t = 100$ with the $\boldsymbol{E}_0$-capping scheme detailed in section 4.3.5, and this time with an even thinner initial discontinuity with width parameter $a = 0.1$.*

We have therefore managed to create two alternative methods for correcting the error with small B_0. We can either transition the system to a standard RMHD scheme at low σ, or we can simply cap the magnitude of $\boldsymbol{E}_0$. Both methods have proven their effectiveness at dealing with the problem, although with different side effects on the structure of the current sheet.

In 1D we appear to be free to choose either correction method for this problem, with few downsides to either choice. The methods are not mutually exclusive either, so we could even use both simultaneously — in fact, maintaining the condition $B_0^2 - E_0^2 > 0$ may be a sensible choice to implement all the time, especially if we are using a method other than HLL to calculate force-free fluxes, thus it may be prudent to cap $\boldsymbol{E}_0$ no matter what.

As such, besides the previous current sheet tests we used this capping scheme for all *previous and subsequent tests.*

4.4 Convergence Testing

Besides verifying the ability of the code to handle different tests accurately, we also want to ensure that the higher order schemes we are using are in fact properly increasing the order of convergence.

First, we need to select the kind of test we want to check against. The test needs to be continuous of course, since the spatial order is reduced near discontinuities, so from among the continuous solutions we can choose from

1. Small amplitude waves,
2. Rarefactions,
3. Alfvén waves.

Small amplitude waves are unsuitable, because their small amplitude means testing convergence quickly runs into the limit of numerical precision. Unlike small amplitude waves, rarefactions and Alfvén waves have significant variation in several variables, well above numerical precision.

With rarefactions we need to be careful since even if the interior of the wave is continuous, there are weak discontinuities at either end that will break convergence, since the Taylor expansion is not valid in this region. We therefore need to restrict the convergence testing only to regions of the wave between the weak discontinuities at either end.

We also need to be careful because we cannot use periodic boundary conditions, since the upstream state of the rarefaction wave is necessarily different from the downstream state, since we know these two states must have different phase speeds for the corresponding MS wave. If the wave reaches these non-periodic boundaries, then the numerical solution will again diverge from the exact solution, since the Neumann boundary conditions will enforce zero gradient, which does not match the rarefaction solution. While we could use more complex boundary conditions, it is simpler to just restrict the convergence testing within the boundaries as well as the within the weak discontinuities.

Meanwhile, Alfvén waves are a good choice for testing convergence of the code, since they are continuous solutions and can be constructed without any weak discontinuities. They can also be constructed in a manner that returns the system to the same state on either side of the wave, allowing us to use a periodic boundary condition and run the system for as long as we desire, unlike with rarefaction tests. One factor we do need to keep in mind here though is that returning to the same state with a continuous solution necessarily means that there must be at least one critical point (i.e. derivative equal to 0) in every variable, by Rolle's theorem. Therefore the flaw in some WENO schemes near critical points detailed in section 3.1.3 will cause problems if left unaddressed.

Another factor to keep in mind is that several variables are constant in an Alfvén wave, in particular density ρ and gas pressure p_g. As two of the directly interpolated variables, flaws in the interpolation of these specific variables are not properly tested via Alfvén waves. With that said, as we have noted in the Alfvén wave test in section 4.2.2, numerical models of these waves have a tendency to induce a variation in ρ and p_g anyway due to numerical errors, and therefore these tests may in actuality test these variables interpolation as well — although we note that such variations should be small, and therefore susceptible to the same issues as with small amplitude wave tests.

4.4.1 Testing Results

Weighing these difference benefits and drawbacks, we decided to test the convergence using a circularly polarised, large-amplitude Alfvén wave, with periodic boundary conditions. This is a standard test of convergence in the literature; see for example Del Zanna *et al.* (2007); Nakamura *et al.* (2023)

Like the Alfvén wave tests of section 4.2.2, we generate this wave in the de Hoffmann-Teller frame, and then Lorentz boost by velocity v_B in the x-direction so that the wave is not stationary. However, unlike those tests the magnetic field performs a full rotation; that is, for the 1D test the magnetic field at time t in the laboratory frame is given by

$$\boldsymbol{B}(x) = \left(B_x, \gamma_B B_\perp \cos\left(\frac{2\pi\,(x - v_B t)}{2L}\right), \gamma_B B_\perp \sin\left(\psi\left(\frac{2\pi\,(x - v_B t)}{2L}\right)\right)\right), \tag{4.16}$$

where γ_B is the Lorentz factor corresponding to the Lorentz boost ($\gamma_B^{-1} = \sqrt{1 - v_B^2}$), and the period $2L$ is the domain width, so that there is exactly one wave in the domain.

For the 1D test we used the domain $[-L, L]$ with $L = 5$. We used $B_x = 2.7$ and $B_\perp = 0.9$ for the magnetic field parameters, and the Lorentz boost velocity was $v_B = 0.94$, so the wave is travelling close to the speed of light in the positive x direction. This corresponds to a Lorentz factor of $\gamma_B \approx 2.931$, thus the magnitude of the transverse magnetic field in the laboratory frame is $\gamma_B B_\perp \approx 2.638$. This is the same base state as with Fig. 4.4, so like in that case we have $\sigma = 162$. This test is therefore a relatively high σ test.

We can also do convergence tests for a 2D code. Testing of the 2D code proper is in the next chapter, but here we will include the results for convergence testing. For the 2D test, the setup is the same except the wave is rotated so that the wave is travelling with

Res.	$\lvert E(\rho)\rvert$	$\lvert E(p_g)\rvert$	$\lvert E(u_x)\rvert$	$\lvert E(u_z)\rvert$	$\lvert E(B_z)\rvert$
10	2.47×10^{-2}	7.17×10^{-1}	5.66×10^{-1}	2.20×10^{0}	3.58×10^{-1}
20	1.35×10^{-2}	7.98×10^{-2}	3.66×10^{-1}	1.63×10^{0}	4.34×10^{-2}
40	7.03×10^{-4}	1.76×10^{-3}	2.94×10^{-2}	1.80×10^{-1}	2.26×10^{-3}
80	1.18×10^{-5}	2.45×10^{-5}	4.00×10^{-4}	3.17×10^{-3}	8.76×10^{-4}
160	7.98×10^{-6}	1.82×10^{-5}	2.81×10^{-4}	2.10×10^{-3}	1.40×10^{-4}
320	1.48×10^{-6}	3.39×10^{-6}	5.36×10^{-5}	4.02×10^{-4}	1.93×10^{-5}
640	2.17×10^{-7}	5.00×10^{-7}	7.96×10^{-6}	6.03×10^{-5}	2.52×10^{-6}
1,280	2.93×10^{-8}	6.75×10^{-8}	1.08×10^{-6}	8.21×10^{-6}	3.19×10^{-7}
2,560	3.80×10^{-9}	8.76×10^{-9}	1.40×10^{-7}	1.07×10^{-6}	4.03×10^{-8}
5,120	4.84×10^{-10}	1.12×10^{-9}	1.78×10^{-8}	1.36×10^{-7}	5.10×10^{-9}
10,240	6.09×10^{-11}	1.40×10^{-10}	2.24×10^{-9}	1.72×10^{-8}	6.49×10^{-10}

Table 4.5: *L1 Norms for 1D Alfvén wave convergence tests. "Res." refers to resolution (i.e. the number of cells) and is inversely proportional to Δx and thus Δt also.*

Res.	$\lvert E(\rho)\rvert$	$\lvert E(p_g)\rvert$	$\lvert E(u_x)\rvert$	$\lvert E(u_z)\rvert$	$\lvert E(B_x)\rvert$	$\lvert E(B_z)\rvert$
10	2.16×10^{-2}	3.09×10^{-1}	1.47×10^{0}	2.07×10^{0}	1.15×10^{-1}	1.58×10^{-1}
20	8.35×10^{-3}	3.40×10^{-2}	9.19×10^{-1}	1.24×10^{0}	1.54×10^{-2}	1.92×10^{-2}
40	8.35×10^{-4}	2.15×10^{-3}	1.74×10^{-1}	1.65×10^{-1}	2.82×10^{-3}	5.16×10^{-4}
80	8.68×10^{-5}	2.04×10^{-4}	2.07×10^{-2}	1.64×10^{-2}	5.85×10^{-4}	2.44×10^{-4}
160	7.70×10^{-6}	1.72×10^{-5}	1.65×10^{-3}	1.68×10^{-3}	7.80×10^{-5}	4.90×10^{-5}
320	6.38×10^{-7}	1.40×10^{-6}	1.11×10^{-4}	1.75×10^{-4}	9.32×10^{-6}	8.07×10^{-6}
640	8.08×10^{-8}	1.84×10^{-7}	1.41×10^{-5}	2.33×10^{-5}	1.17×10^{-6}	1.17×10^{-6}
1,280	1.15×10^{-8}	2.67×10^{-8}	2.16×10^{-6}	3.33×10^{-6}	1.48×10^{-7}	1.64×10^{-7}

Table 4.6: *L1 Norms for 2D Alfvén wave convergence tests. "Res." refers to resolution (i.e. the number of cells) and is inversely proportional to Δx and Δy, and thus Δt also.*

wave vector $\boldsymbol{k} = (1, 1)$, i.e. the wave is travelling at velocity $\mu_a = 0.94$ towards the upper right. The domain in this case is $[-5, 5] \times [-5, 5]$, thus it is square, with periodic boundary conditions for both the x- and y-boundaries.

Since the wave is now travelling along the diagonal, we need to stretch the wave by $\sqrt{2}$ so that there is still exactly one wave in the domain. However, in order for the wave to match the periodic boundary conditions we actually need to fit two wave periods along the diagonal. We therefore have for the 2D test, $L = 5/\sqrt{2} \approx 7.07$.

The method we are using to test the convergence is to run the code at a given resolution n from some time $t = t_0$ until some later time $t = t_1$, with $t_1 - t_0 \gg \Delta t$ so that we have several time steps. We thus have the numerical solution a_i for a given variable $p(x)$ at time

t_1 at a set of n points in the domain, where a_i is the value in the i^{th} cell (so $1 \leq i \leq n$).

Next, we calculate the exact solution A_i at t_1 for these n points in the domain, and calculate the L1 norm of the difference between them and the numerical solution

$$|E_n(p)| = \sum_{i=1}^{n} |a_i - A_i| , \tag{4.17}$$

where $|E_n(a)|$ is then the L1-norm error for the variable a at resolution n.

If the code is order r, then we have the $a_i - A_i = \mathcal{O}(\Delta x^r) + \mathcal{O}(\Delta t^r)$, and therefore the L1 norms for each variable should satisfy $|E_n(a)| = \mathcal{O}(\Delta x^r) + \mathcal{O}(\Delta t^r)$. So if we halve the grid spacing Δx and the time step Δt, then the error should decrease by 2^r times. Since the time step is related to the grid spacing by the Courant condition $\frac{\Delta t}{\Delta x} = C_u$ and the Courant number C_u is constant, increasing the resolution/decreasing the grid spacing is matched by a corresponding decrease in time step. Therefore doubling the resolution also halves the time step.

In order to test the convergence then, we calculate the L1 norm at multiple different resolutions, doubling the resolution each time. If our code is third order as expected, then the L1 norms should decrease by $2^3 = 8$ times each time we double the resolution.

Tables 4.5 and 4.6 give the 1D and 2D results respectively of the L1 norms for each variable. The resolution is doubled successively, starting at resolution 10 and ending at resolution 10,240 in 1D, and 640 in 2D. The test in 1D was run each time until $t = 5$; at resolution 10 this is just 7 iterations, but at resolution 10,240 this is 6,400 iterations. In 2D, the test was instead run until only $t = 1$.

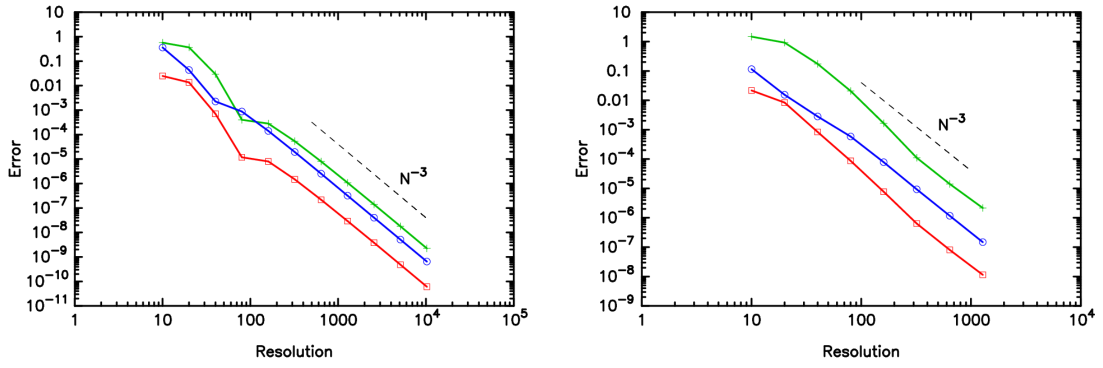

(a) *(b)*

Figure 4.34: *Log-log plots of error for ρ (red, squares), u_x (green, pluses) and B_y (blue, circles) against resolution for the circularly polarised Alfvén wave. The tests were run in 1D (a) up to $t = 5$ and in 2D (b) up to $t = 1$. A plot of an exact N^{-3} trend is included for reference.*

Fig. 4.34 gives log-log plot of the error against resolution for the 1D and 2D Alfvén wave tests. In 1D, the convergence is quite clear, although there is some variability at low resolution. In 2D, the convergence is less clear, although this can be attributed to the same variability as in 1D; in 2D, the code was not fast enough to get results at higher resolutions in reasonable time.

Chapter 5

2D results

This chapter will first introduce the 2D version of the method, in particular describing how the divergence-free constraint is overcome. It will then move on to again show simulations and tests of the method, and describe any potential issues unique to 2D.

5.1 Oblique 1D Tests

Now that we have modified our code to handle 2D problems, we can move on to test the code. Finding 1D exact solutions like in section 2.3 was already complex enough, and this unfortunately makes finding exact solutions in 2D even harder. We can however perform simple rotations of the 1D cases into oblique cases, where (for instance) the shock front of a planar fast shock is not parallel to the x- or y-axes. This allows us to turn our 1D test cases into tests of our 2D solver. We define ϕ as the rotation of the oblique test from being parallel to the y-z plane — so in other words, ϕ is the angle of the plane of the oblique test to the y-z plane.

These tests are still 1D in a sense of course, and it is conceivable that the code may not exhibit problems that it otherwise would, such as some sort of numerical artefact that only appears for truly 2D problems. Unfortunately, the only 1D test case that can be easily made fully 2D in this sense is the small amplitude wave test, since we can simply superpose multiple different wave modes of various obliquities and thereby generate a truly 2D solution. However, as we noted previously small amplitude tests are the easiest test for any model to pass and are thus not particularly useful for finding flaws beyond bugs in the code itself.

However, although they may not be fully 2D problems, it is still worth testing the code against these oblique 1D exact solutions even if we are not necessarily detecting all possible flaws of the code.

We need to be careful about the boundary conditions here for non-periodic cases. In the 1D case we opted for a simple Neumann boundary condition, with gradient set to 0. That was fine in those cases, but in 2D we have some choice over which direction the gradient is 0 at the boundary. The simplest choice to implement would be perpendicular to the boundary, so that we set the boundary cells to the value closest to them. Unfortunately, for oblique tests this can cause problems because the boundary values do not match the oblique wave in the integration region. For instance, if we have an oblique shock test the shock front will have a sudden change in direction at the boundary with this simple boundary condition.

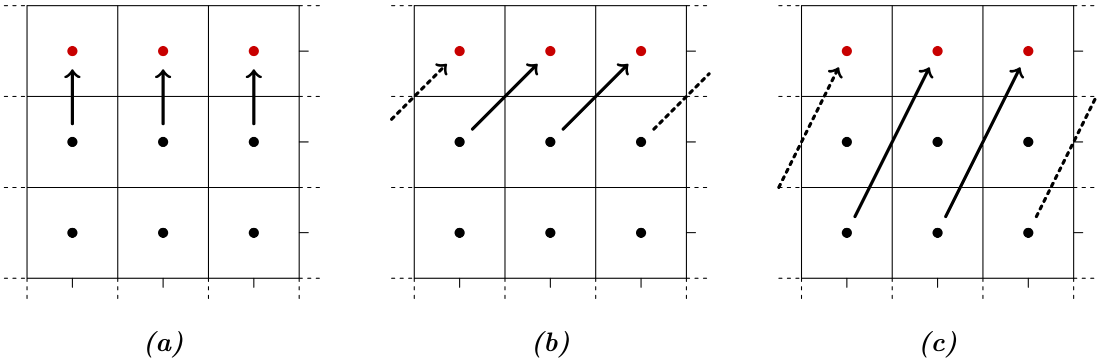

Figure 5.1: *Diagrams of 2D Neumann conditions, with* $\tan\phi = 0$ *(a),* $\tan\phi = -1$ *(b) and* $\tan\phi = -1/2$ *(c). Red cell centres indicate boundary cells, and the arrows indicate which cells these cells take their value from.*

A natural choice then is to choose that the gradient is 0 parallel to the wave front at angle ϕ — a condition that the wave itself also satisfies. Fig. 5.1 provides a diagram of Neumann BCs at the upper y-boundary for three angles of $\phi = 0$, $\phi = -\pi/4$, and $\phi \approx -0.46365$.

More generally, if $\tan\phi = n/m$ for two coprime integers n and $m > 0$, then if $C_{i,j}$ is a boundary cell on the upper y-boundary then it takes the value of cell $C_{i-n,j-m}$,

$$\boldsymbol{Q}_{i,j} = \boldsymbol{Q}_{i+n,j-m}. \tag{5.1}$$

In other words, it takes the value of the cell n cells to the right and m cells below itself, i.e. along the line with gradient $\tan\phi$. The value at other boundaries is defined similarly.

In other words, the cell takes the value of the nearest cell along the line of gradient $dy/dx = \tan\phi$ that is inside the computational domain. Of course, sometimes there is no cell along this line inside the computational domain; for instance, with $\phi = -\pi/4$ the gradient of the line means that the cells in the upper left and lower right boundary corners have no cells inside the domain to match to. For these cells we simply use the usual Neumann condition with the nearest cell.

Clearly, if n or m are large integers, these boundary conditions will be matching to cell values which are quite far away, and the corner regions with no matching cells will be quite large. In fact if n or m is larger than the x- or y-resolution respectively then there will be no matching cells at all for any of the boundary cells, as the next matching cell will beyond the other side of the domain. For this reason, when using these boundary conditions we stuck to $\phi = \pi/4$.

The test data for both continuous and discontinuous oblique tests is contained in table 5.1. Like before, we shall once again begin with the continuous cases, since as we discovered previously the code is more comfortable with these, at least in 1D. Testing the small amplitude case again is likely not worth it, so we will skip that test and move on to Alfvén waves.

Alfvén Waves

We begin testing our 2D code using the same test for high-σ Alfvén waves as in Fig. 4.4, at an oblique angle of $\phi = \pi/6$. This Alfvén wave is constructed in the same way as the version of Fig. 4.4, except it has been rotated to be oblique and the wavelength has been carefully chosen so that the wave matches at the boundaries for the periodic BCs and has exactly two waves in the domain. In addition, a constant phase shift of $\pi/2$ has been added to the rotation $\psi(x)$. That is, the magnetic field (prior to rotation of $\pi/6$ about the z-axis) is given by

$$\boldsymbol{B}(x) = \left(B_x, B_\perp \cos(\psi(x)), B_\perp \sin(\psi(x))\right).$$

In this case, unlike section 4.2.2, $\psi(x)$ is now given by

$$\psi(x) = \sin^{-1}\left(A \sin(\phi(x))\right) + \frac{\pi}{2}, \quad \phi(x) = \frac{2\pi x}{L},$$

where L is the wavelength of the Alfvén wave; since the wave is at an oblique angle to the x-axis, this length is a little longer than the domain width in the x-dimension, of 2 units. Specifically, this length is $L = 2\sec(\pi/6) \approx 2.3094$, so the wave is stretched by a factor $s \approx 1.1547$

So effectively, we first have stretched the Alfvén wave of section 4.2.2 by s, then rotated about the x-axis by $\pi/2$, then rotated about the z-axis by $\pi/6$. As a result, the phase speed μ as well as ρ, p_g, σ and σ^* are all the same, but the magnetic field at $\phi = 0$ is now $\boldsymbol{B} = (2.4150, 1.2075, 2.6379)$, with 4-velocity $\boldsymbol{u} = (-0.19308, -0.096542, -4.0249)$. Meanwhile, at a quarter-phase $\phi = \pi/2$ these are instead $\boldsymbol{B} = (2.7689, 0.49964, 2.5164)$ and $\boldsymbol{u} = (-0.73308, 0.98346, -3.8395)$. The results are given in Fig. 5.2.

If we compare to the 1D results in Fig. 4.4, we see that for this case the 2D oblique version does not introduce any new problems unique to this case. In fact, the results

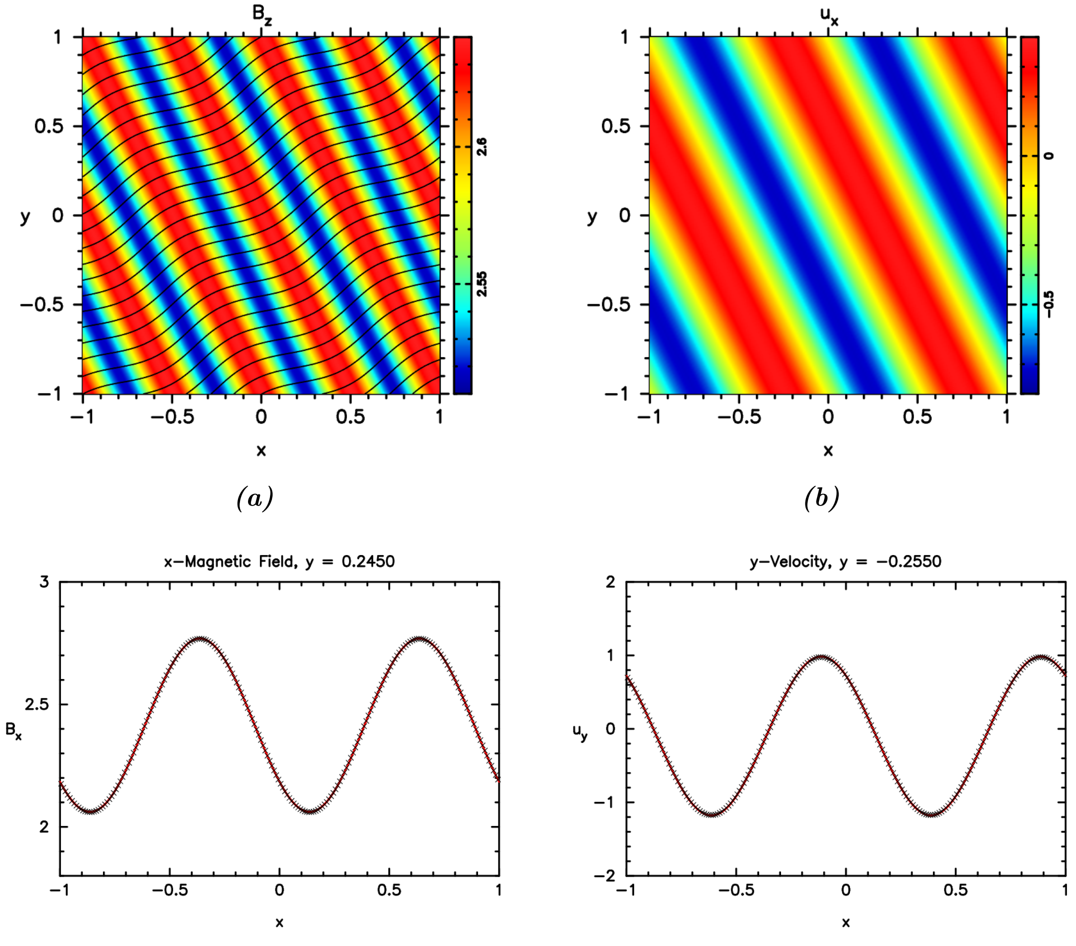

(a) (b) (c) (d)

Figure 5.2: *2D oblique Alfvén wave test results with obliquity* $\phi = \pi/6$. *This test is equivalent to Fig. 4.4, rotated anti-clockwise by* ϕ. *These plots show* B_z *with magnetic field lines (a) and* u_x *(b) over the whole domain. (c) shows a cut of* B_x *along* $y = 0.2450$ *and (c) shows a cut of* u_y *along* $y = -0.2250$, *in both cases with the exact solution given in red. This test was run until* $t = 10$, *at resolution* 200×200 *on the domain* $[-1, 1] \times [-1, 1]$, *using a third order code and Periodic BCs.*

appear better since $\boldsymbol{u}$ has drifted less from the correct values. However, this is due to the increased resolution reducing truncation error, and not because the 2D code is better.

Fast Rarefaction

The next test we will perform is that of a fast rarefaction test. This time, we use a previous test from Komissarov (1999a) of an oblique fast rarefaction. This test is of a rarefaction oriented at an angle $\phi = \frac{\pi}{4}$ to the x-axis, with the initial discontinuity through the origin at time $t = -0.5$. In this particular case, the phase speed of the rarefaction changes sign in the middle of the rarefaction, so in this frame there is a point on the rarefaction that stays stationary. The data for this test is contained in table 5.1.

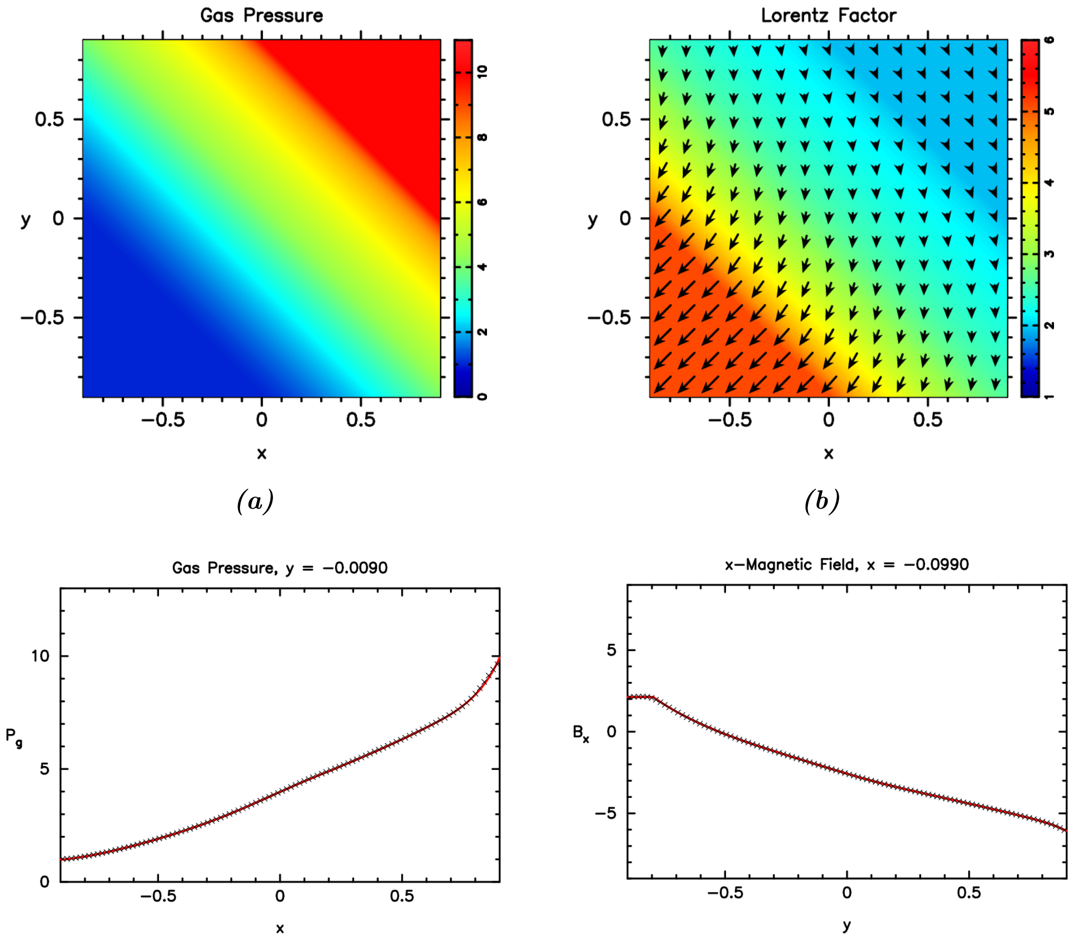

(a) *(b)*

(c) *(d)*

Figure 5.3: *2D oblique fast rarefaction test results with obliquity $\phi = \pi/4$. These plots show P_g (a) and Lorentz factor (b) over the whole domain; the arrows in (b) indicate the direction and magnitude of the 4-velocity $\mathbf{u}$. (c) shows a cut of P_g along the line $y = -0.0090$, while (d) shows a cut of B_x along the line $x = -0.0990$, in both cases with the exact solution given in red. This test was run until $t = 0.2$ at resolution 400×400 on the domain $[-1,1] \times [-1,1]$, using a third order code, oblique Neumann BCs.*

The results for this test are shown in Fig. 5.3. As we can clearly see, the code is again to handle this test easily, much like the 1D tests. The numerical results show a close match to the exact solution, even with the lowered resolution. These results are also a close match to the results of Komissarov (1999a).

Oblique Fast Shock

The final oblique 1D test we will show is of a high-σ fast shock. This test is based on the same shock as in Figs. 4.17 and 4.18, but from a different frame again. In this frame, the shock is moving towards the top right of the plot at $\mu_s = 0.99950$, having started on the line $y + x = 0.5$. This alternate frame was used because the test failed with the more

Problem	Figure	Bottom Left State ($x + y < 0$)	Top Right State ($x + y > 0$)
Fast Rarefaction, $\mu_l = -0.57952$, $\mu_r = 0.68318$, $\phi = \frac{\pi}{4}$	5.3	$\boldsymbol{u} = (-3.5355, -3.5355, 0)$, $\boldsymbol{B} = (2.1213, 4.9497, 0)$, $\rho = 0.01$, $p_g = 1$, $\sigma = 6.2728$, $\sigma^* = 0.24126$	$\boldsymbol{u} = (0.66608, -1.5308, 0)$, $\boldsymbol{B} = (-7.0523, 14.123, 0)$, $\rho = 0.056200$, $p_g = 9.9920$, $\sigma = 6.2136$, $\sigma^* = 1.6407$
High-σ Fast Shock, $\mu = 0.99950$, $\phi = \frac{\pi}{4}$	5.4	$\boldsymbol{u} = (37.360, 36.704, 0.0)$, $\boldsymbol{B} = (-79.451, 80.866, 0.0)$, $\rho = 0.011895$, $p_g = 0.83089$, $\sigma = 1.4042$, $\sigma^* = 0.00051173$	$\boldsymbol{u} = (5.1463, 0.90367, 0)$, $\boldsymbol{B} = (-1.3659, 2.7802, 0)$, $\rho = 0.0001$, $p_g = 0.0001$, $\sigma = 2120.1$, $\sigma^* = 74.912$

Table 5.1: *Initial test case data for the oblique fast rarefaction and fast shock tests.*

extreme case of $\mu_s = 0.99995$ in Fig. 4.18. The data for this test is contained in table 5.1.

This test was also set up with the tanh shape applied to the conservative variables instead of the primitives — that is, instead of setting up the initial conditions by fitting the primitive variables to a tanh shape as described in section 4.3, we instead applied this shape to the conservative variables instead. This was used because it was found to give slightly better results.

Unlike the 1D case, we also found that the method to enforce the PC condition at the boundaries described in section 3.2.7 actually causes the code to crash in this case. For this reason, all of our 2D tests (including the two previous tests above) were performed without this correction to the algorithm — although this was also true of the 1D tests in chapter 4 as well anyway.

The results for this test can be seen in Fig. 5.4. Once again, the results show a close match to the exact solution. They in fact appear to be better than the results for the other frame seen in Fig. 4.18, however running the 1D code in this frame instead gives similar results to the 2D test here, indicating that this difference is just the different reference frame. Even so, these are promising results, as this is a very strong, extreme shock that is likely beyond anything that would normally be encountered in an astrophysical setting, given that the gas pressure ratio is so large, at $p_g^r/p_g^l \approx 8300$, and similarly the ratio of magnetisation is $\sigma^r/\sigma^l \approx 1500$.

5.2 Non-Planar Tests

The previous results show that the 2D code is capable of handling much the same tests as the 1D code to similar accuracy. However, although the previous cases are decent tests of the code, the fact that they are all 1D solutions could mean that some problems may have passed undetected. On the other hand, fully 2D exact solutions of RMHD are difficult to

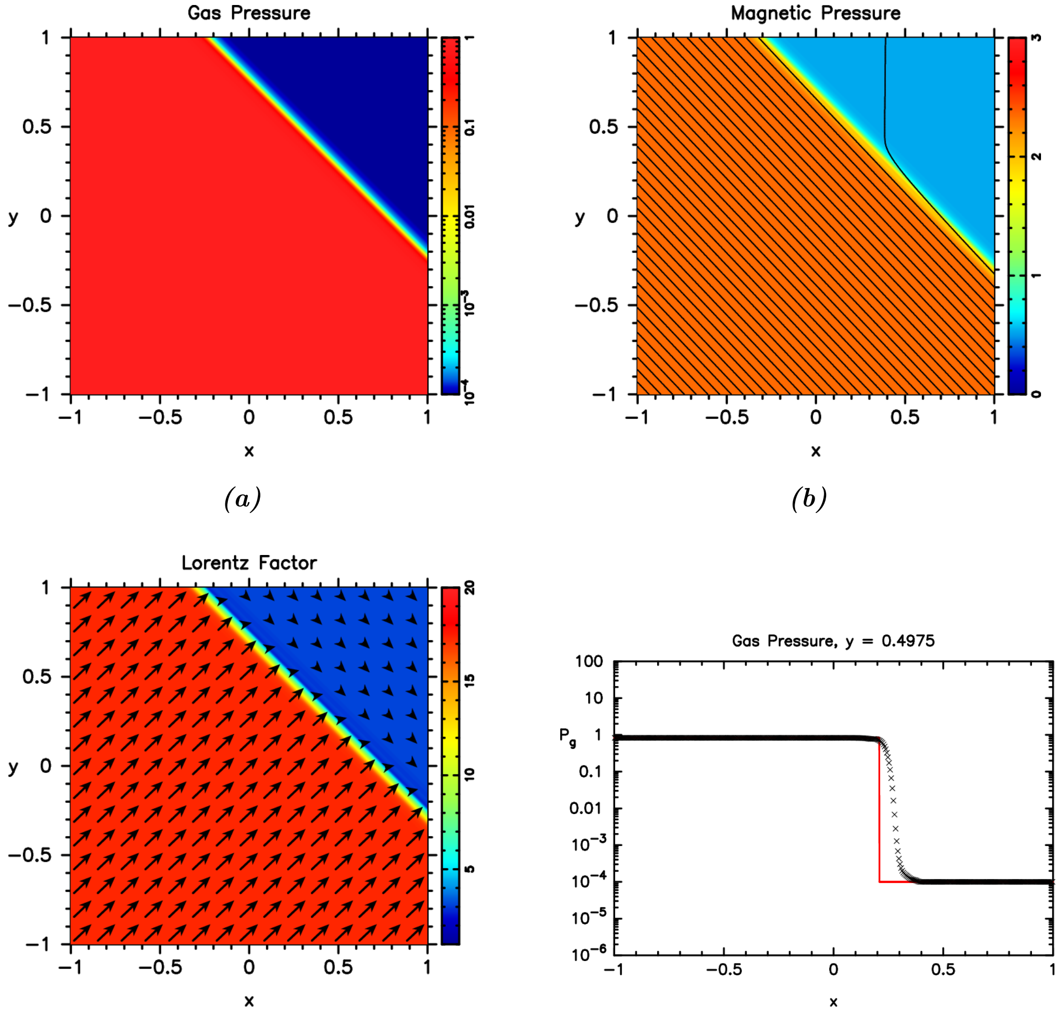

(a) *(b)* *(c)* *(d)*

Figure 5.4: *2D oblique fast Shock test results with obliquity $\phi = \pi/4$. These plots show P_g (a), P_m with magnetic field lines (b), and γ (c) over the whole domain; the arrows in (c) indicate the direction and magnitude of the 4-velocity $\boldsymbol{u}$. (d) shows a cut of p_g along the line $y = 0.4975$, with the exact solution shown in red. This test was run until $t = 1$ at resolution 200×200 on the domain $[-1, 1] \times [-1, 1]$, using a third order code and oblique Neumann BCs. This discontinuity was set up with width parameter $a = 0.3$.*

find, so we may need an alternative to test our code.

Without exact solutions, the only things we can compare against are other numerical results for the same (or similar) conditions. Although this code should be the first that can handle the high-σ regime (besides PIC codes), we can still use previous results at lower σ to test our code.

For tests at the same σ, PIC tests run at high σ also serve as useful comparisons, since these are the only tests we can compare against for high σ. We can also compare against FFDE codes, although these cases neglect the plasma inertia, so we do not expect the results to be identical.

Alternatively, while exact solutions in RMHD are hard to find, FFDE is a much simpler system, and as such there are some exact solutions we can test against, such as instabilities and known solutions. At high σ, RMHD should behave approximately the same as it approaches this limit.

5.2.1 Advection Test

One very simple test we can perform is an advection test. A variation in just density will be advected by the fluid flow without any distortion (provided the velocity is constant and uniform). Thus we can try a pure density variation and see how the code handles the case.

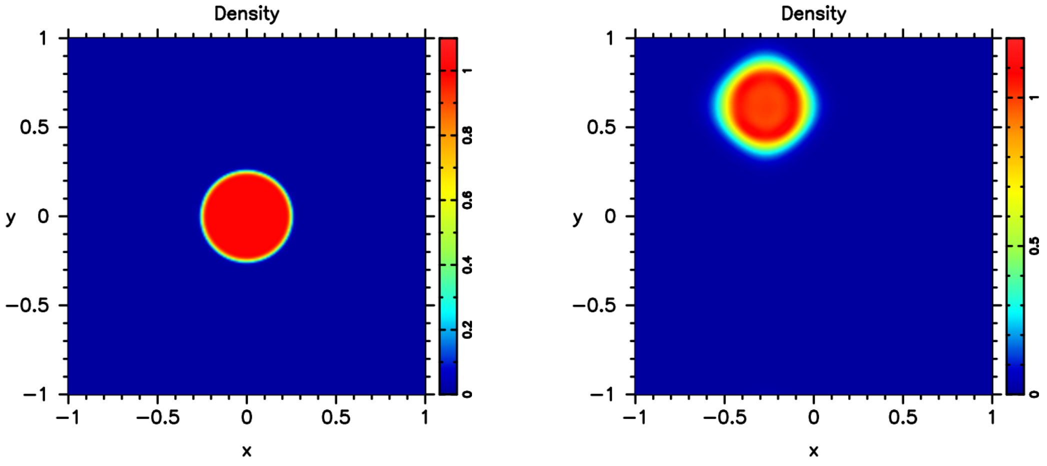

(a) *(b)*

Figure 5.5: *ρ at time $t = 0$ (a) and at time $t = 10$ (b) for a test of an advecting, high-density cylinder. This test was run at resolution 200×200 on the domain $[-1, 1] \times [-1, 1]$, using a third order code and Periodic BCs.*

For our test, the background magnetic field is $\boldsymbol{B} = (1, 0, 0)$, and the pressure is $p_g = 0.01$. In the centre of the domain, we have a cylinder of radius 1 with density $\rho = 1$, while outside of this circle the density is much lower at $\rho = 0.01$. Thus there is a large change in σ between the inside and outside of the circle, from $\sigma = 0.96$ inside to $\sigma = 20$ outside. This circle also has a smoothed radial tanh profile at the edges centred at $r = 0.25$ and with width parameter $a = \frac{2}{15} = 0.13333$, so there is no sharp discontinuity. Fig. 5.5a shows this initial density. This high-density cylinder is then advected by a constant, uniform fluid velocity $\boldsymbol{u} = (2.3, -1.6, 0)$.

Fig. 5.5b shows the results of the test at time $t = 10$. The advection velocity is the three velocity of the fluid, $\boldsymbol{v} \approx (0.77314, -0.53783, 0)$, thus the centre of the cylinder should now be at $(7.7314, -5.3783)$. However, since the boundaries are periodic, the cylinder has wrapped to the other side of the domain multiple times, so the cylinder should actually be at $(-0.2686, 0.6217)$, which matches the results. The density has diffused a little, but this is to be expected since we already know that contact discontinuities will suffer from increased diffusion with our HLL code, and without any non-linear steepening. We can also observe a small amount of distortion in the initially circular shape, indicating a small amount of anisotropy in the integration, but this is a fairly minor amount.

5.2.2 Lundquist Flux Rope

Simple variations in density are not the only feature that can be advected, however. One well known example comes from Lundquist (1950), in which they describe a "rope" of flux, a stable solution of FFDE. This case was also tested with force-free and PIC codes in Lyutikov *et al.* (2017) — although in their case they were considering colliding flux ropes, while we will merely model the advection a single flux rope, which should retain its initial shape indefinitely.

In cylindrical coordinates and in the fluid frame, the Lundquist solution takes the form

$$\boldsymbol{B}(r \leq r_j) = J_1(r\alpha)\,\boldsymbol{e}_\phi + J_0(r\alpha)\,\boldsymbol{e}_z, \tag{5.2}$$

where J_0, J_1 are the Bessel functions of zeroth and first order respectively, r_j is the radius of the rope, and $\alpha > 0$ is a parameter that can be chosen freely. Outside the flux rope, the magnetic field takes on the value at the edge,

$$\boldsymbol{B}(r > r_j) = \boldsymbol{B}(r_j)\,. \tag{5.3}$$

If we choose α such that $r_j\alpha$ is a zero of $J_1(r\alpha)$ then the field outside the cylinder will have no azimuthal component $\boldsymbol{e}_\phi$ and will be entirely into or out of the plane. It follows from the integral form of Ampère's law that in this case the total current of the flux rope in this case would be 0. This case is also convenient in that the outer field will be constant and uniform in this case as well, meaning that we can impose Periodic BCs.

We therefore chose α such that $r_j = 1$ and $r_j\alpha$ is the first zero of J_1, i.e. $\alpha \approx 3.8317$. Thus our flux rope has radius exactly $r_j = 1$. Our setup differs from the setup in Lyutikov *et al.* (2017), where the authors modify the flux rope B_z component to

$$B_z(r \leq r_j) = \sqrt{j_0(r\alpha)^2 + C},$$

where C is a constant, for which they always use $C = 0.01$. This has the effect of preventing B_z from changing sign, so without this our test does indeed have $B_z = 0$ at the first zero of J_0 inside the flux rope, at $r \approx 2.4048$. Fig. 5.6a shows the initial magnetic field z-component; note how it is negative outside the flux rope.

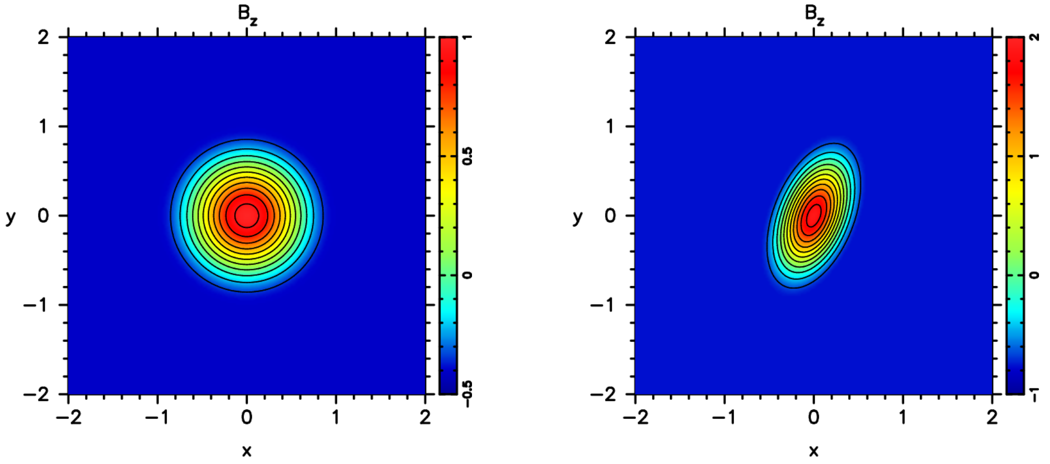

(a) *(b)*

Figure 5.6: *Initial out-of-plane magnetic field B_z for a Lundquist flux rope, in the fluid frame (a) and in a moving frame (b). The resolution is 200×200, and the domain is $[-1, 1] \times [-1, 1]$*

Besides the magnetic field, we also set $\rho = 0.000{,}01$ and $p_g = 0.000{,}05$, so the initial σ is very high, ranging from $\sigma = 772.5$ outside the flux rope to $\sigma = 4{,}758.4$ at the centre.

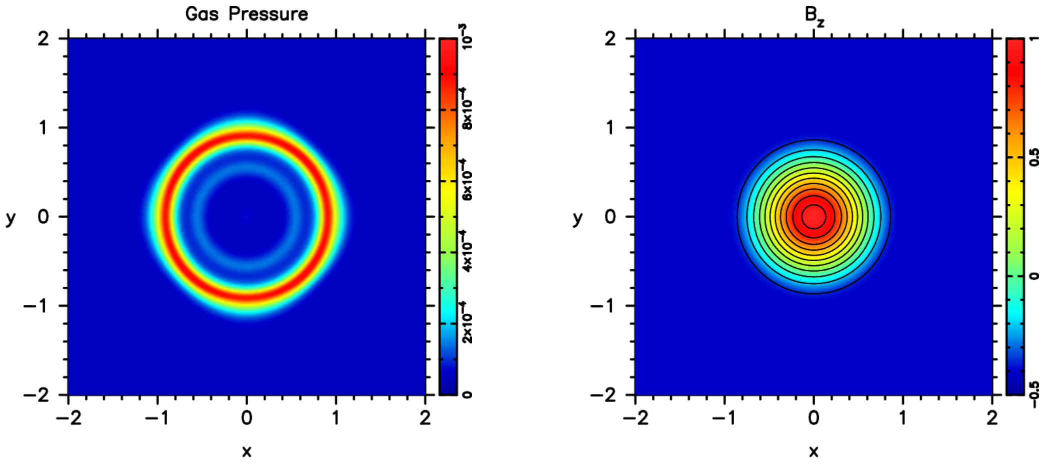

(a) *(b)*

Figure 5.7: *P_g (a) and B_z (b) for a stationary Lundquist Flux Rope. This test was run until $t = 10$ at resolution 200×200 on the domain $[-1, 1] \times [-1, 1]$, using a third order code and Periodic BCs.*

We start off with a stationary test, without any fluid velocity, $\boldsymbol{u} = (0, 0, 0)$. The results for this test can be seen in Fig. 5.7. We can see that the flux rope has generally held its shape without issue, although there is some plasma heating at the edge of the flux rope. While this plasma heating is significant compared to the background gas pressure in this case, the amount of energy the plasma has gained is small compared to the total energy of the system, including the electromagnetic parts.

Besides the stationary test, we can also perform an advected test, for which we will use fluid velocity $\boldsymbol{u} = (1.5, -0.4, 0)$. This is somewhat more involved than the density advection test, as this time we need to be careful about changing Lorentz frames. Besides performing a Lorentz transformation on the magnetic field, there is also Lorentz contraction of the Flux rope in the direction of travel. The initial magnetic field in this case can be seen in Fig. 5.6b; as a result of Lorentz contraction, the rope is no longer cylindrical.

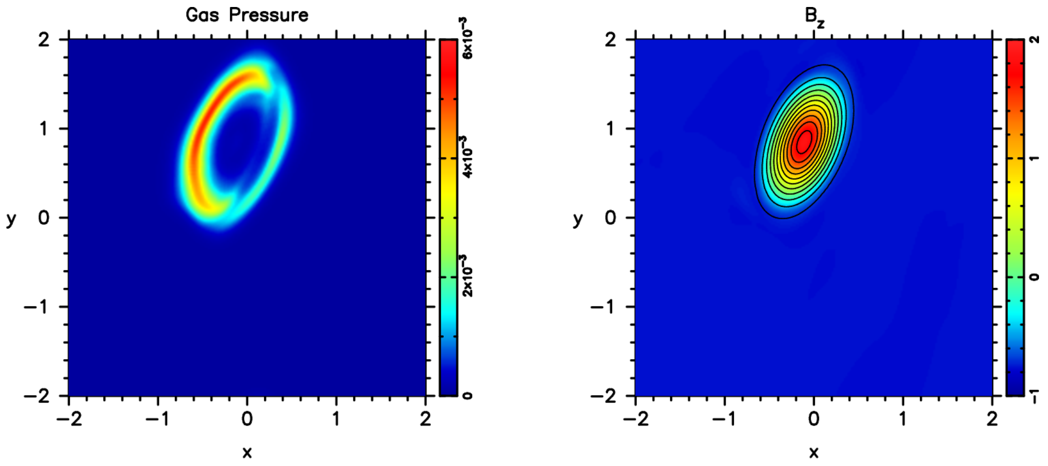

(a) *(b)*

Figure 5.8: *P_g (a) and B_z (b) for an advected Lundquist Flux Rope. This test was run until $t = 10$ at resolution 200×200 on the domain $[-1,1] \times [-1,1]$, using a third order code and Periodic BCs.*

Since 4-velocity $\boldsymbol{u} = (1.5, -0.6, 0)$ corresponds to 3-velocity $\boldsymbol{v} \approx (0.78947, -0.31579, 0)$. Thus at time $t = 10$, we would expect the centre of the flux rope to be located at $(-0.1053, 0.8421)$, where we have taken the periodic boundaries into account.

Fig. 5.8 gives the results of this advected test at $t = 10$. Clearly, the flux rope has ended up advected to the right position. Other than this, the results are much the same as the stationary version — the flux rope maintains its shape well, and there is some plasma heating at the edge of the flux rope again. However, this time the heating is non-uniform, with more heating on the side facing away from the direction of travel.

5.2.3 Cylindrical Explosion Test

The next case we shall consider is a strong cylindrical explosion test. This test was first considered by Komissarov (1999a) for a normal RMHD code, but has since become a standard test, used by several different authors including Del Zanna *et al.* (2003); Leismann *et al.* (2005); Nagataki (2009); Lora-Clavijo *et al.* (2015).

The initial background gas pressure p_g and density ρ is low, with $p_g = 3.5 \times 10^{-5}$

and $\rho = 10^{-4}$. The initial explosion is a cylinder at the centre of the domain, with radius $r = 1$. The pressure and density inside this cylinder is far higher with $p_g = 1$ and $\rho = 10^{-2}$, making this plasma much hotter. Like the advection test, the edge of the cylinder has a smoothed tanh profile centred at $r = 0.9$ with width parameter $a = \frac{2}{15} = 0.13333$. In addition, like the oblique fast shock above the tanh profile was applied to the conservative variables instead of the primitives.

The initial magnetic field in the domain is uniform, with $\boldsymbol{B} = (B, 0, 0)$ everywhere, both inside and outside the cylinder. This gives us a significant range of values for σ, since the gas pressure and density are both much higher inside the cylinder initially. Meanwhile, the initial velocity is $\boldsymbol{u} = 0$ everywhere, thus we also have $\boldsymbol{E} = 0$ everywhere. We can then perform the test for several different choices of B, giving us tests at several different values of σ.

With a cylindrical central region of hot, dense plasma situated inside a region of cold, rarefied plasma, the expected result of this test is an explosion, expanding outwards into the cold background. The exact nature of this explosion will depend on the magnitude of B.

With weak B ($\sigma \ll 1$) the expansion should be purely radial, since there is no anisotropy to break the rotational symmetry. Meanwhile, with strong B ($\sigma \gg 1$) the plasma expansion will be constrained to the magnetic field lines, although there will still be fast waves expanding in the non-parallel directions. As B increases, we should see the plasma become more and more trapped to the direction parallel to $\boldsymbol{B}$.

There are of course four special locations on the cylinder boundary. Two are at $(\pm 1, 0)$, where the magnetic field is orthogonal to the boundary. In this case, the system is degenerate, and some of the waves will travel at the same phase speed, either the Alfvén and fast waves at high B or the Alfvén and slow waves at low B — or all three for a particular choice of B.

The other two points are of course at $(0, \pm 1)$, with the magnetic field parallel to the boundary. Once again, the system is degenerate, but this time the Alfvén and slow waves are now advected along with the plasma, regardless of B. Thus in the direction parallel to the y-axis, we expect there to be only fast modes at high values of B, since the fluid is constrained at high σ to follow the magnetic field lines.

With $B \ll 1$ the test will be close to that of an unmagnetised gas. Without any major anisotropy, we would thus expect the explosion to be purely radial, with hot, dense plasma expanding uniformly in all directions. This would also serve to "push" out what magnetic field there is inside the central cylinder, creating a region of reduced magnetic pressure and bending the magnetic field lines around it.

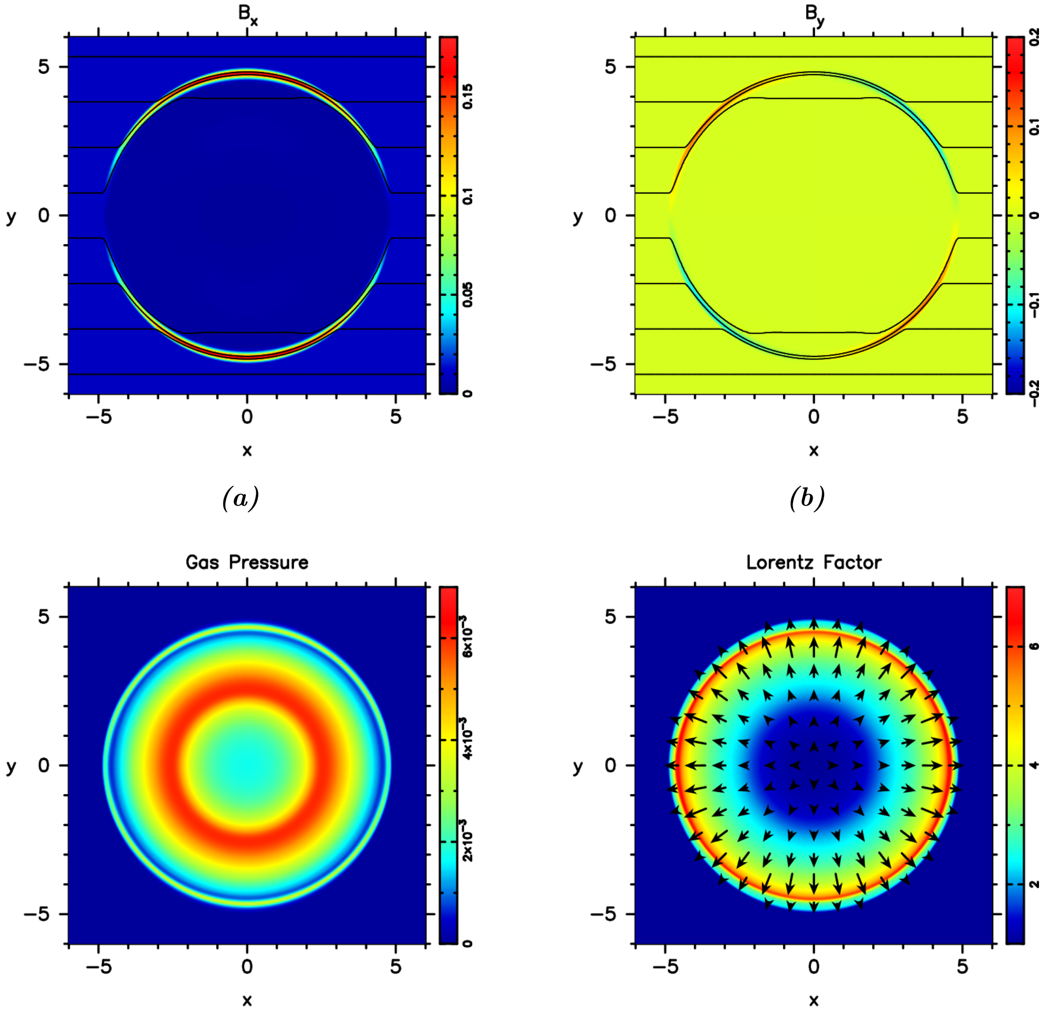

(a) *(b)*

(c) *(d)*

Figure 5.9: *B_x (a), B_y (b), p_g (c) and u_0 (d) for a cylindrical Blast wave with $\boldsymbol{B} = (0.01, 0, 0)$. Arrows in (d) indicate the direction and magnitude of $\boldsymbol{u}$. This test was run until $t = 4$ at resolution 400×400 on the domain $[-6, 6] \times [-6, 6]$, using a third order code and Neumann BCs.*

As B increases, the influence of the magnetic field begins to dominate. The magnetised plasma becomes more and more heavily constrained to the magnetic field direction, at first simply slowing the expansion orthogonal to the magnetic field before more-or-less outright eliminating any expansion other than along the magnetic field lines. The only components able to travel significantly orthogonal to the magnetic field would be the magnetic components themselves, carried by the fast waves. In addition, the degree to which the magnetic field is expelled from the central region is also reduced, until there is little to no change in the magnetic field.

Komissarov (1999a) performed this test at three different values of B, with $B_1 = 0.01$, $B_2 = 0.1$ up to $B_3 = 1$. For the initial value of σ in these cases, we find that for the first case σ ranges from $4.17 \times 10^{-1} \leq \sigma_1 \leq 2.49 \times 10^{-5}$, in the second case the range

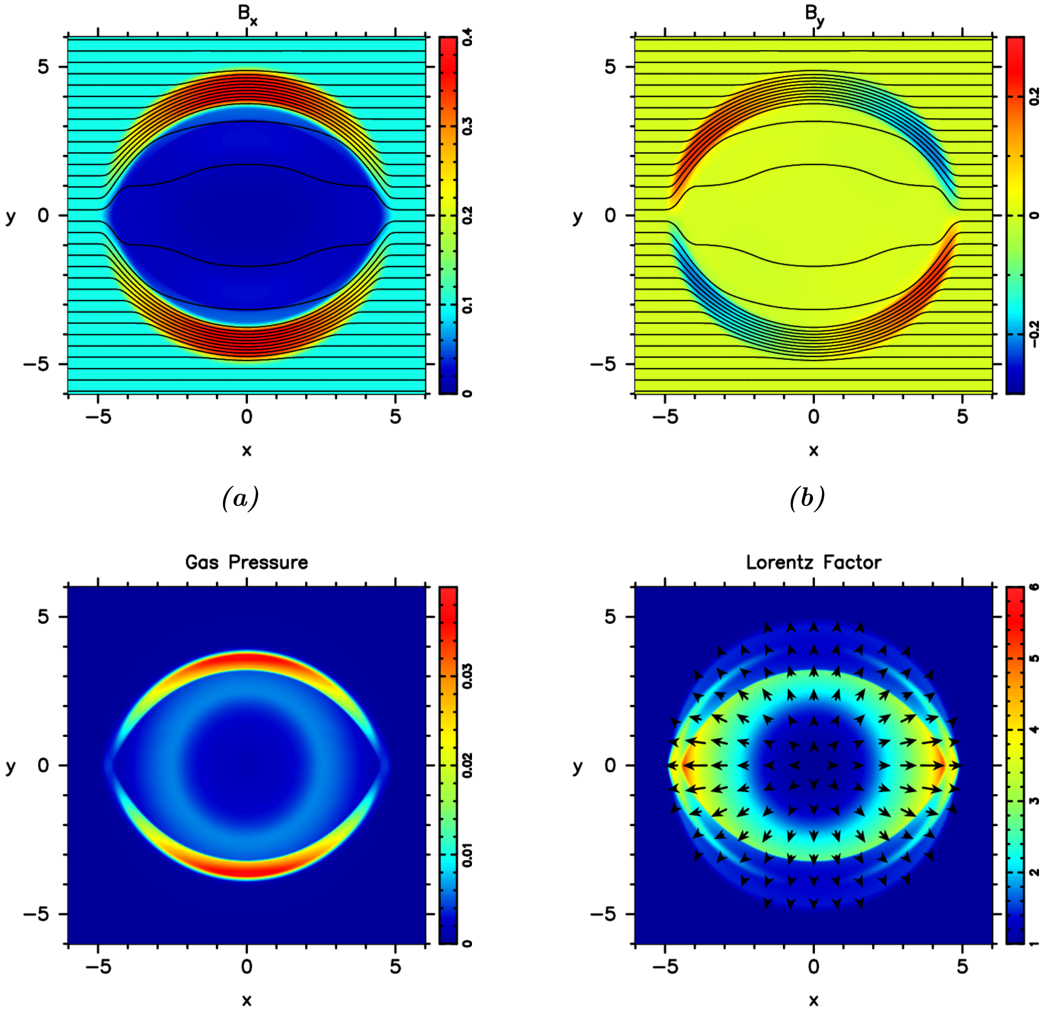

(a) *(b)*

(c) *(d)*

Figure 5.10: *B_x (a), B_y (b), p_g (c) and u_0 (d) for a cylindrical Blast wave with $\boldsymbol{B} = (0.1, 0, 0)$. Arrows in (d) indicate the direction and magnitude of $\boldsymbol{u}$. This test was run until $t = 4$ at resolution 400×400 on the domain $[-6, 6] \times [-6, 6]$, using a third order code and Neumann BCs.*

is $4.17 \times 10^1 \leq \sigma_1 \leq 2.49 \times 10^{-3}$, and in the third case the range is $4.17 \times 10^3 \leq \sigma_1 \leq 2.49 \times 10^{-1}$. The maximum σ in the third case is exceptionally high for a normal RMHD code, but as it turns out Komissarov (1999a) has been unable to replicate the results for this case, so this test may not be accurate — although as we will see later our results for the same test are a close match to those results.

We can thus perform this test for the same values for B and compare our results to these earlier results for normal RMHD, and also try probing the problem at even higher values of σ than Komissarov (1999a) was able to with an RMHD code.

Fig. 5.9 shows the results for case 1, with $B = 0.01$. This case has a fairly low σ, with the value initially of $\sigma < 1$ in both the interior and exterior regions. With this low σ, we expect a near-radial expansion of the system, and this is exactly the result we obtain. We

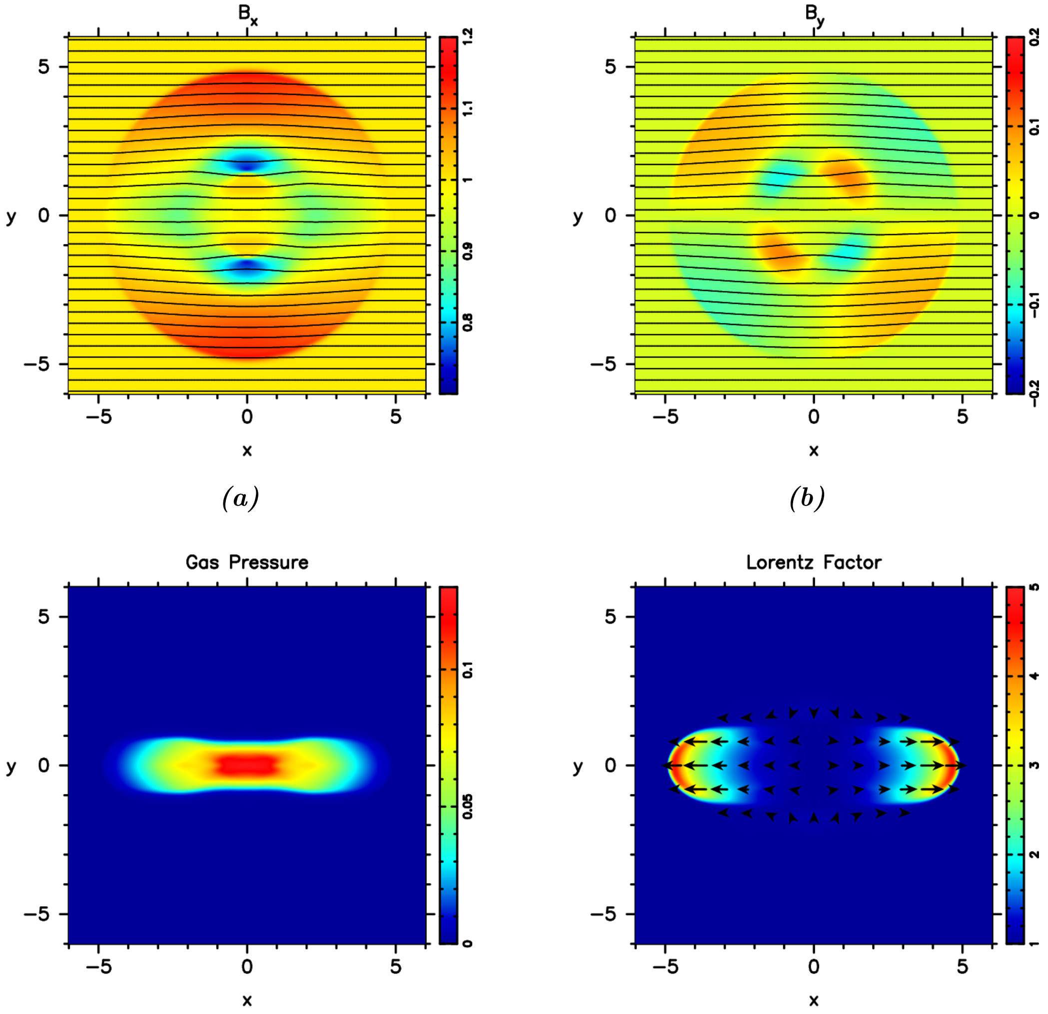

(a) *(b)*

(c) *(d)*

Figure 5.11: *B_x (a), B_y (b), p_g (c) and u_0 (d) for a cylindrical Blast wave with $\boldsymbol{B} = (1, 0, 0)$. Arrows in (d) indicate the direction and magnitude of $\boldsymbol{u}$. This test was run until $t = 4$ at resolution 400×400 on the domain $[-6, 6] \times [-6, 6]$, using a third order code and Neumann BCs.*

can clearly see also that the magnetic field has been almost entirely expelled out of the central explosion. These results are a close match to those of Komissarov (1999a).

Fig. 5.10 shows the results for case 2, $B = 0.1$. The value of σ is larger now, and there is a significant impact on the shape of the expansion. Although it is not strictly constrained to the magnetic field lines, the results are no longer approximately radial, with expansion of the plasma orthogonal to the magnetic field slowed, and with expansion of magnetic components mainly in this orthogonal direction. However, the magnetic field is still largely expelled from the interior region, just like before. Once again, these results are a close match to the results of Komissarov (1999a) for RMHD.

Fig. 5.11 shows the results for case 3, $B = 1$. σ is now quite large in the exterior region, reaching up to $\sigma = 4.17 \times 10^3$. This is the highest σ that Komissarov (1999a) considered,

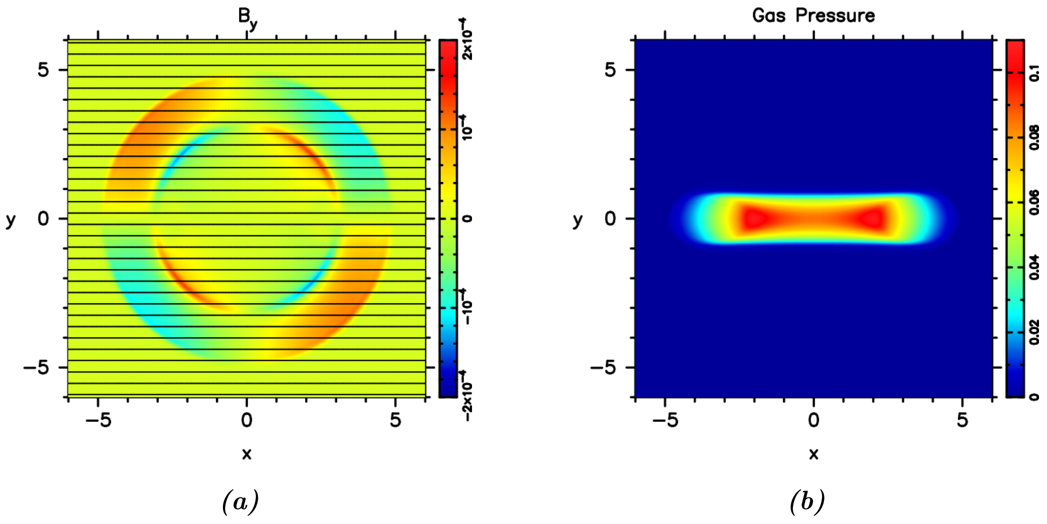

(a) *(b)*

Figure 5.12: *B_y (a) and P_g (b) for a cylindrical Blast wave with $\boldsymbol{B} = (1000, 0, 0)$. Arrows in (d) indicate the direction and magnitude of $\boldsymbol{u}$. This test was run until $t = 4$ at resolution 400×400 on the domain $[-6, 6] \times [-6, 6]$, using a third order code and Neumann BCs.*

although as mentioned above they were not able to get their code to run the test again. However, by comparison we can see that our results are a close match to the results that they did get. In this case, the strong magnetic field has almost completely constrained the expansion of the plasma to the magnetic field lines, and the magnetic field itself is barely affected by the explosion itself.

All of the results in Figs. 5.9 to 5.11 are consistent with the previous results of Komissarov (1999a), with a normal RMHD code. All three show a close match to those results, and our results also match those of others who have performed this test such as Leismann *et al.* (2005).

Finally, we decided to stress-test the code with an extreme case. Fig. 5.12 shows the results for an explosion with the magnetic field at $B = 1000$; here we have $\sigma \approx 4.5 \times 10^9$ in the outer region, a value well beyond anything a typical RMHD code could hope to model. For this case, the results are once again as expected, and besides the actual values the results are very similar to that of the less extreme case of $B = 1$ in Fig. 5.11.

This case is a very extreme case, although it should be noted that since the explosion is driven initially by a region of increased pressure and density, the induced magnetic field fluctuation is very small compared to the overall magnetic field strength. We can see from Fig. 5.12a that the fluctuation in B_y is $|\delta B_y| \leq 2 \times 10^{-4}$. Given that we have $B = 1000$, this means this fluctuation is 5×10^6 times smaller than the actual magnitude of $\boldsymbol{B}$. Thus although σ is very high in this test, the variation in $\boldsymbol{B}$ is also very small as well, which is partly why the code can handle such a high σ without issue.

5.2.4 Magnetic Island Collapse

Another test we can consider is that of the collapse of a system of magnetic islands, which has been performed previously in Lyutikov *et al.* (2017) using both FFDE and PIC codes, and Nalewajko *et al.* (2016) has performed a similar test, also using a PIC code. For the PIC tests they performed this test case at a relatively high σ; for example, in the case of Lyutikov *et al.* (2017) the mean σ ranges from $\sigma = 6$ up to $\sigma = 1360$.

Besides there being previous results we can compare our results to, the test also features the formation of current sheets, making this a very useful test of our code.

For the initial state of this system, the plasma is at rest with constant density ρ and gas pressure p_g. The only non-constant variable initially is the magnetic field $\boldsymbol{B}$. This magnetic field takes the form

$$\boldsymbol{B} = B_0 \begin{pmatrix} -\sin(2\pi\alpha y) \\ \sin(2\pi\alpha x) \\ \cos(2\pi\alpha x) + \cos(2\pi\alpha y) \end{pmatrix}, \tag{5.4}$$

where B_0 is a parameter that determines the overall magnetic field strength, and α is a parameter that determines the spatial period. For the boundary conditions we use a periodic boundary condition for both x- and y-boundaries. In order for matching boundaries to be consistent without any discontinuities α only has a finite set of possible values. These initial conditions thus create a lattice of magnetic islands or flux tubes with alternating out-of-plane magnetic field B_z, and with X-points at the corner of four adjacent islands where $\boldsymbol{B} = 0$.

This particular solution is a stationary solution of the FFDE, i.e. they are solutions of the equations of FFDE with all time derivates $\partial_t = 0$. Parker (1983) studied this configuration under the context of solar physics, and suggested that this configuration would be unstable in force-free conditions.

This magnetic field configuration actually belongs to a family of ABC structures (Arnold-Beltrami-Childress). ABC structures are divergence-free vector fields $\boldsymbol{X}$ of the form (Zhao *et al.*, 1993; Moffatt, 1986; Dombre *et al.*, 1986)

$$\boldsymbol{X} = \begin{pmatrix} A\sin z' + C\cos y' \\ B\sin x' + A\cos z' \\ C\sin y' + B\cos x' \end{pmatrix}, \tag{5.5}$$

where A, B and C are constants.

This setup has been studied both in the context of Euler flows (i.e. incompressible hydrodynamics, $\boldsymbol{\nabla} \cdot \boldsymbol{v} = 0$), where $\boldsymbol{X}$ is then the fluid velocity (Childress, 2003), as well as in the context of electromagnetics, as a magnetic field configuration (Dombre *et al.*, 1986).

ABC structures in force-free fields are known to be stable to ideal perturbations provided all three of $A, B, C \neq 0$ (Moffatt, 1986). In our case, in addition to the transformation

$$x' = 2\pi\alpha x, \quad y' = 2\pi\alpha y + \frac{\pi}{2}, \quad z' = z, \tag{5.6}$$

we have $A = 0$ and $B = C = B_0$, and therefore this setup does not satisfy this stability condition. In the case of this 2D ABC configuration, the islands can move with respect to each other and thereby reduce their interaction energy, and thus this configuration is not stable.

B^2 can be easily calculated from Eq. (5.4) to give

$$B^2 = B_0^2 \left(2 + 2\cos(2\pi\alpha x)\cos(2\pi\alpha y)\right), \tag{5.7}$$

which indicates two key points: At the centre of the magnetic islands with $x, y = n/(2\alpha)$ with $n \in \mathbb{Z}$, the magnetic field strength is at a maximum of $|\boldsymbol{B}| = 2$ (or alternatively magnetic pressure $p_m = \frac{1}{2}(B^2 - E^2) = 1$). Meanwhile, at the X-points situated at the centre of four neighbouring islands (where $x, y = (2n-1)/(4\alpha)$ with $n \in \mathbb{Z}$) the magnetic field vanishes. Thus at these X-points we have $\sigma = 0$, regardless of the overall magnetic field strength B_0.

Applying Ampère's law which we recall from Eq. (2.93)

$$\frac{\partial \boldsymbol{E}}{\partial t} = -\boldsymbol{\nabla} \times \boldsymbol{B} - \boldsymbol{J},$$

the fact that, although unstable, the system is initially in a steady state means we simply have

$$\boldsymbol{\nabla} \times \boldsymbol{B} = -\boldsymbol{J}, \tag{5.8}$$

thus we find the current $\boldsymbol{J}$ is

$$\boldsymbol{J} = B_0 \begin{pmatrix} -2\pi\alpha\sin(2\pi\alpha y) \\ 2\pi\alpha\sin(2\pi\alpha x) \\ 2\pi\alpha\cos(2\pi\alpha x) + 2\pi\alpha\cos(2\pi\alpha y) \end{pmatrix} = 2\pi\alpha\boldsymbol{B}, \tag{5.9}$$

thus the current is parallel to the magnetic field, and proportional to its magnitude.

From these results we can easily show (Lyutikov *et al.*, 2017) that each flux tube has magnetic flux $\propto B_0/\alpha^2$, energy per unit length $\propto B_0^2/\alpha^2$, helicity per unit length $\propto B_0^2/\alpha^3$ and axial current $\propto B_0/\alpha$. The helicity of both types of flux tubes has the same sign, and therefore the overall helicity in the system is non-zero.

As the islands slip past each other and towards islands with a matching sign of B_z, current sheets form at the boundary between these islands of matching B_z, as while B_z

is the same, B_x and/or B_y flips sign. Thus this particular case features the formation of current sheets, and is therefore a very useful test of our code to judge its ability to handle the formation and evolution of current sheets. As we noted in section 2.3.1, current FFDE codes cannot properly handle current sheets, and thus ensuring our code can handle this case is very important.

Since B_z is still non-zero in the current sheets while B_y and/or B_z flip sign, these current sheets may not be as extreme as the 1D case we considered in section 4.3.5. However, as with that case, the code can still have difficulty avoiding problems if we do not apply any corrections such as the $\boldsymbol{E}_0$-capping scheme described in section 4.3.5. Unfortunately, unlike the one dimensional case this alone is not enough to fix all the issues here.

Current sheets in RMHD are known to be major sources of plasma heating, due to magnetic reconnection converting electromagnetic energy into plasma energy, among other factors.

The system we are modelling ideal RMHD of course, so there should be no magnetic reconnection. However, even though our code models ideal RMHD, our code exhibits a small amount of numerical resistivity, just like many numerical models (Rembiasz *et al.*, 2017). This is due to numerical and/or truncation errors in the integration which mean that there is an effective resistance and viscosity to the fluid. These factors are one of the main drivers of numerical diffusion, seen in cases like the contact discontinuity in Figs. 4.9 and 4.10. The magnitude of this resistance depends on a number of factors, including the order of the code and the resolution. As a consequence of this, magnetic connection and the resistive Tearing instability (see the next test, section 5.2.5) can still occur in our code, thus this test can identify exactly how much resistivity there is.

However, if we test the magnetic island collapse with $\boldsymbol{E}_0$-capping alone, then we find that the amount of heating is well below what is expected. This is because capping $\boldsymbol{E}_0$ effectively removes the energy contained in the electric field from the system, and causes the total energy in the system to rapidly drop.

At heart then, this problem relates to the conservation of energy. Borrowing an idea from section 4.3.4, if we artificially force the transfer of energy to the interaction system, then the problem of energy loss may be avoided. That is, if we use the same method as in section 4.3.4 — transfer "missing" energy from the force-free system to the interaction system every time step, provided the change is positive, i.e. it increases the interaction system energy.

This scheme of transferring only when there is an energy loss in the force-free system *will* mean that the system will tend to gain energy as a whole over time of course — since whenever the system has energy loss, that loss is rectified, but an energy gain is not.

However, generally speaking this gain should be quite slow, since it is on the order of the truncation error, and this is corroborated by testing. Thus we find that this small gain in energy over time is acceptable.

Testing in the next section will show that the combination of these two correction procedures — capping $\boldsymbol{E}_0$ and conditional energy transfer — is successful in allowing our scheme to work in this case involving two dimensional current sheet formation.

Testing

With these corrections to the algorithm, we can finally begin to test this case properly. *For all the tests in this section (and in the rest of this chapter), we have performed them with both* $\boldsymbol{E}_0$*-capping and conditional energy transfer.*

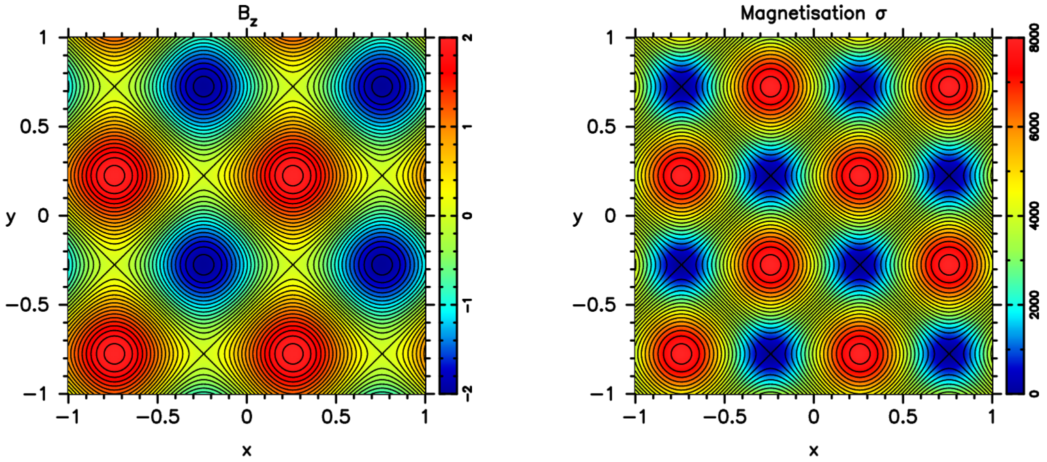

(a) ***(b)***

Figure 5.13: *B_z (a) and σ (b) for the magnetic island collapse at $t = 0$. The resolution is 200×200, and the domain is $[-1, 1] \times [-1, 1]$.*

This particular setup has a large degree of symmetry, and furthermore the instability can require a long time to grow. Since this is the case, we added some random noise and a displacement of the setup in x and y in order to break the symmetry and give the instability a kick-start. This took the form of a randomly-generated displacement of the initial conditions in Eq. (5.4) by $\delta x \approx 0.7419$ and $\delta y \approx 0.7751$, so that the actual initial conditions in the magnetic field are

$$\boldsymbol{B} = B_0 \begin{pmatrix} -\sin(2\pi\alpha(y + \delta y)) \\ \sin(2\pi\alpha(x + \delta x)) \\ \cos(2\pi\alpha(x + \delta x)) + \cos(2\pi\alpha(y + \delta y)) \end{pmatrix}. \tag{5.10}$$

In addition, some random noise is added to the initial velocity. Instead of $\boldsymbol{u} = 0$ initially, the velocity takes the form

$$200000\boldsymbol{u} = \boldsymbol{f}_{1,n}\sin((n\cos(y\pi)+220)\,\pi x) + \boldsymbol{f}_{2,n}\cos((n\sin(y\pi)+220)\,\pi x) \\ + \boldsymbol{f}_{3,n}\sin((n\cos(y\pi)+220)\,\pi x) + \boldsymbol{f}_{4,n}\cos((n\sin(y\pi)+220)\,\pi x)\,, \quad (5.11)$$

for n from 1 to 4, and where the $\boldsymbol{f}_{j,n}$ are all random vectors, with each component an independent random variable in the range $(-\sqrt{n}/2, \sqrt{n}/2)$. There is no particular reason for this exact form of the noise, this is just intended to kick start the instability to some extent and break the symmetry.

Fig. 5.13 shows these initial conditions in magnetic field with the domain $[-1,1]\times[-1,1]$ and with $\alpha = 1$. We can see that this choice of initial conditions splits the domain into a chequerboard pattern with two different types of magnetic island, one with $B_z < 0$ and the other with $B_z > 0$. With this choice of domain and α we can see that we have two periods of the initial conditions in both x and y, and therefore we have four of each type of magnetic island.

If we now run the code, we find that initially not much happens, as the instability is still in the growth stage, and is well below the magnitude of the other values. All that does occur is some settling of the solution, most notably the gas pressure exhibits some plasma heating.

However, around $t = 10$ or so, the instability finally becomes large enough to move the magnetic islands. This instability took longer to grow in our case than in Lyutikov *et al.* (2017), where the instability became notable around $t = 7$. However, the initial time of the instability is strongly dependent on the size of the initial noise we add, so this is not a particularly important factor, and does not indicate anything wrong with our results.

At this time, the islands begin to slip past each other, and we reach the state at $t = 11.5$ in Fig. 5.14. The magnetic islands of matching B_z have all split into pairs, which have slid towards each other. Where they are meeting, we can clearly see that current sheets have begun to form; this can be most clearly seen in Fig. 5.14d, where there is a clear discontinuity in B_x at $y \approx -0.3$ along the line $x = 0.0950$, matching the point where two islands of $B_z > 0$ are colliding.

These current sheets are causing very significant plasma heating, as the formerly low gas pressure has now reached levels only an order of magnitude or so below that of the magnetic pressure. This is in turn forces the plasma out the ends of the current sheets at high velocity, which is then deflected around the magnetic islands, and subsequently heats the rest of the plasma in the domain outside the magnetic islands.

After this initial collision, the current sheets begin to dissipate. The magnetic island pairs begin a slow merger process, with significantly less plasma heating than initially. However, around $t = 27$ the magnetic islands of matching B_z (of which there are now two

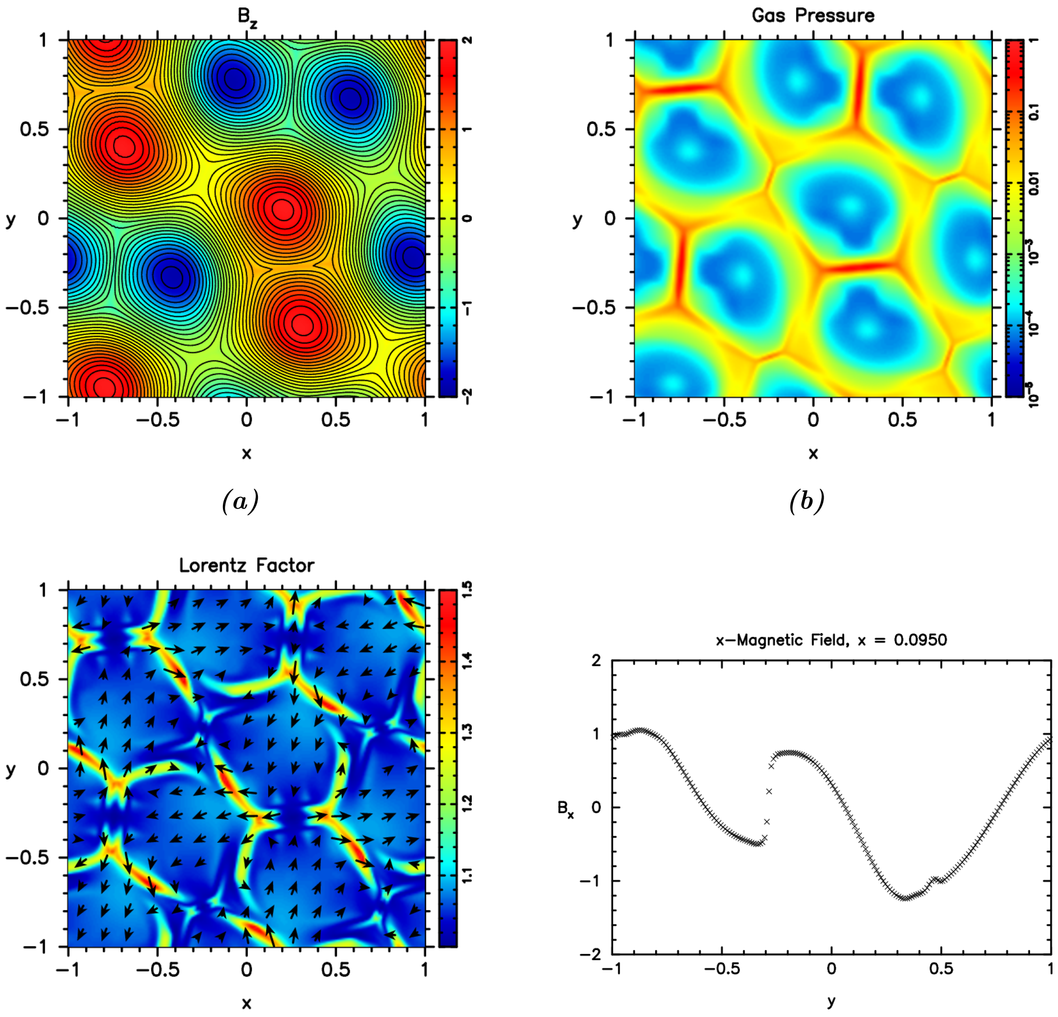

(a) *(b)*

(c) *(d)*

Figure 5.14: *B_z (a), P_g (b) and u_0 (c), as well as a slice in B_x at $x = 0.0950$ (d) for the magnetic island collapse at $t = 11.5$. For (c) the arrows show the direction and magnitude of $\boldsymbol{u}$. This test was run at resolution 200×200 on the domain $[-1, 1] \times [-1, 1]$, using a third order code and Periodic BCs.*

of each) once again begin to collide with each other, forming another set of significant current sheets.

This state at $t = 27$ can be seen in Fig. 5.15; four current sheets are forming or already have formed here, two of which are stronger than the others. These are located at $(0.75, 0.25)$, $(0.75, -0.75)$, $(-0.25, 0.75)$ and $(-0.25, -0.75)$ i.e. they are arranged in a square grid (this is a remnant of the original symmetry).

After these current sheets form, they slowly slide around until they become aligned at around $t = 31$, which can be seen in Fig. 5.16, where the two strong current sheets are now approximately aligned along $y = 0.15$. Like the initial current sheets, this current sheet now begins to dissipate, and the system enters the final stable phase, with little to no more plasma heating. This stable state agrees with the final state found by Lyutikov

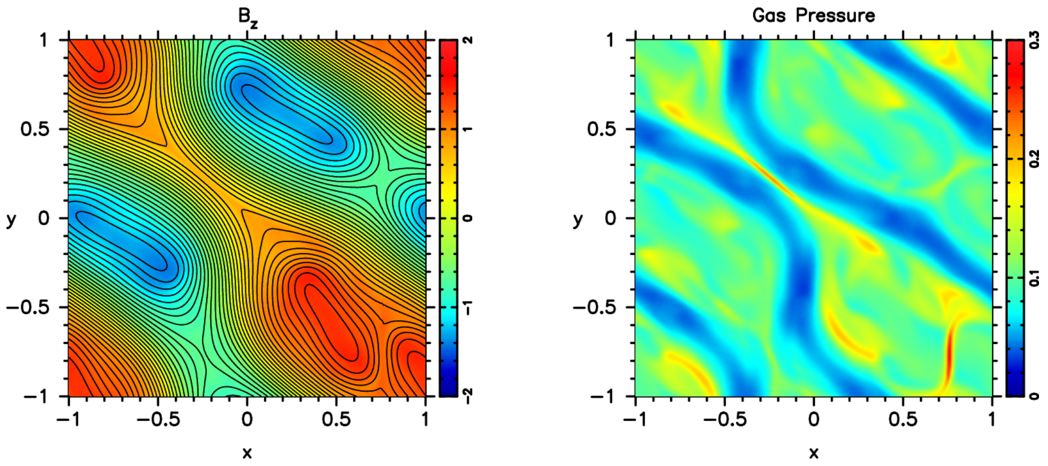

(a) *(b)*

Figure 5.15: *B_z (a) and P_g (b) for the magnetic island collapse test of Fig. 5.13 at $t = 27$.*

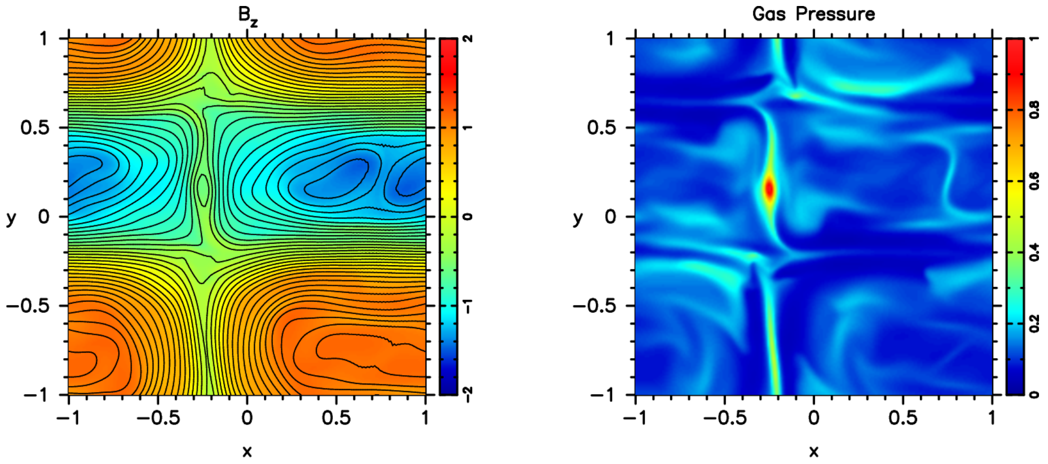

(a) *(b)*

Figure 5.16: *B_z (a) and P_g (b) for the magnetic island collapse of Fig. 5.13 at $t = 31$.*

et al. (2017) with FFDE and PIC codes as well.

Fig. 5.17 shows a comparison of the relative energy in the system, comparing the total initial energy to the relative energy in the electromagnetic terms, given by $\frac{1}{2}(E^2 + B^2)$, and the energy in the plasma, given by $w\gamma^2 - p_g$. The stages described above can be clearly seen:

In the first stage, from $t = 0$ to $t = 10$, the system is relatively constant, with a relatively small amount of energy transferring into the plasma (although relative to how much the plasma started with, this is quite a lot of energy).

At $t = 10$, the first current sheets form, and there is a large increase in plasma heating, lasting until around $t = 12$ or so. After this, there is a relatively small amount of plasma heating while the magnetic islands merge. Eventually, around $t = 29$ the second current

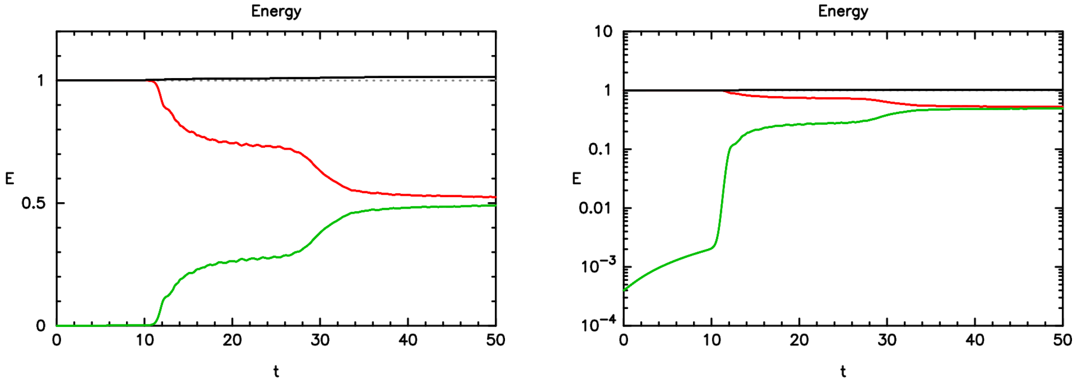

(a) Energy Comparison. *(b) log Energy Comparison.*

Figure 5.17: *A normal (a) and a Logarithmic Plot (b) of the energy in the system. The black line is the total energy, the red line is the electromagnetic energy* $\frac{1}{2}(B^2 + E^2)$*, and the green line is the plasma energy* $w\gamma^2 - p_g$*. These values are given as a relative fraction of the initial total energy, shown by the dotted line.*

sheets form, and the second burst of plasma heating occurs. Finally, around $t = 32$, the system enters a stable equilibrium, and little to no energy is transferred any more.

If we look closely at the total energy, we can see that during all this there is a slow gain in the total energy in the system. Since the BCs are periodic, this can only be a result of the conservation error we discussed in section 4.3.4. However, this level of error is quite minor compared to the overall test.

5.2.5 Tearing Instability

Another instability we can consider is the Tearing instability of Current Sheets, as has been studied previously by Komissarov *et al.* (2007b), and Komissarov and Barkov (2016).

In this instability, a current sheet "Tears" as opposing magnetic fields on either side of the sheet pinch together and annihilate in magnetic reconnection. It is unique in this case in that it is specifically a resistive instability, driven by the electrical resistance of the fluid (Komissarov *et al.*, 2007b). A perfectly conducting fluid has no way to allow the magnetic fields on either side to meet, and it is only the resistance that allows this.

As mentioned previously, even though our code aims to model ideal RMHD there is still some numerical resistivity meaning that magnetic reconnection can still occur, causing the instability to still be unstable. Although the presence of this instability is a problem for our code, it is still worth testing it, as we can get a measure of how significant the numerical resistivity is by measuring the growth rate of the instability.

For our test, we again have an initial steady state plasma with $\rho = p_g = 0.01$ constant.

We initialise the magnetic field as

$$\boldsymbol{B} = \left(B\tanh\left(\frac{x}{l}\right), 0, B\,\mathrm{sech}\left(\frac{x}{l}\right)\right), \tag{5.12}$$

where $B = 1$ is the magnetic field magnitude, and $l = 0.1$ is a characteristic length, encoding the width of the current sheet. With this setup, the magnitude of the magnetic field is constant, and thus so is the magnetic pressure and magnetisation, with $\sigma = 20$.

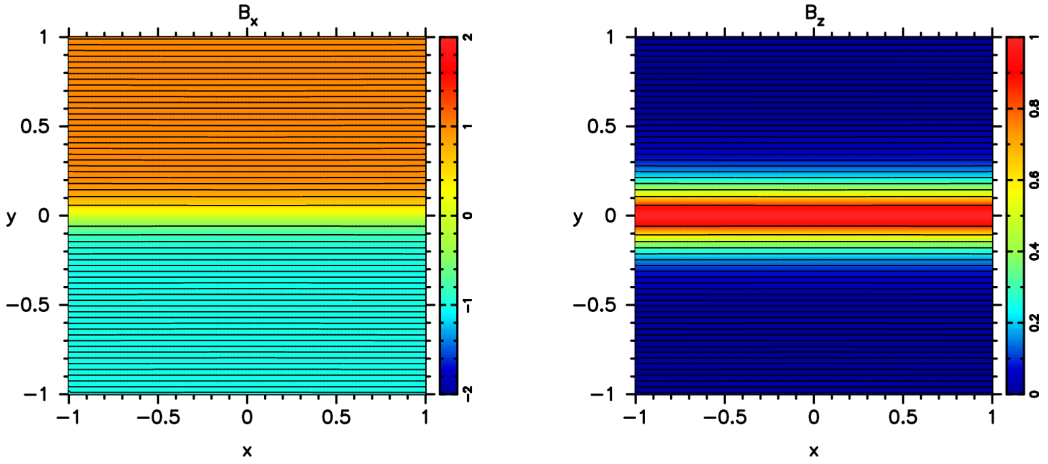

(a) *(b)*

Figure 5.18: *Initial magnetic field* B_x *(a) and* B_z *(b) for the tearing instability, with resolution* 200×200 *and domain* $[-1, 1] \times [-1, 1]$.

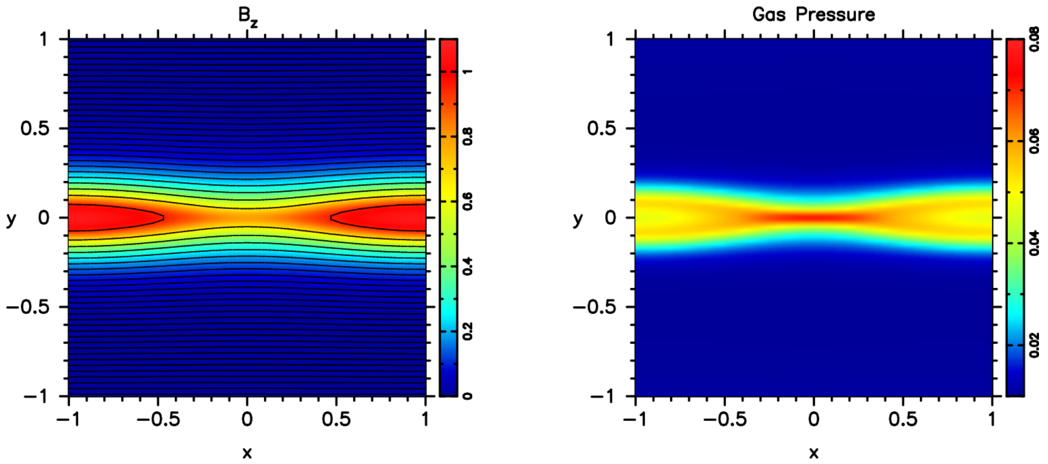

(a) *(b)*

Figure 5.19: B_z *(a) and* P_g *(b) for the tearing instability, at time* $t = 20$. *This test was run at resolution* 200×200 *on the domain* $[-1, 1] \times [-1, 1]$, *using a third order code. The left and right* x*-boundaries are periodic, while the upper and lower* y*-boundaries are Neumann BCs.*

Current sheets like this actually exhibit multiple instabilities (Komissarov and Barkov, 2016), so in order to ensure that we get a tearing instability we initialise with an extra

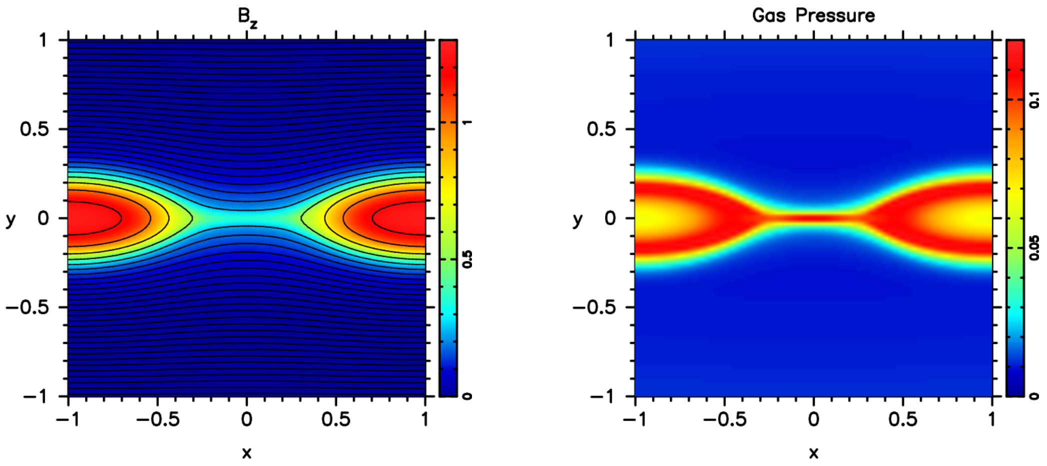

(a) *(b)*

Figure 5.20: *B_z (a) and P_g (b) for the tearing instability, at time $t = 25$. This test was run at resolution 200×200 on the domain $[-1, 1] \times [-1, 1]$, using a third order code. The left and right x-boundaries are periodic, while the upper and lower y-boundaries are Neumann BCs.*

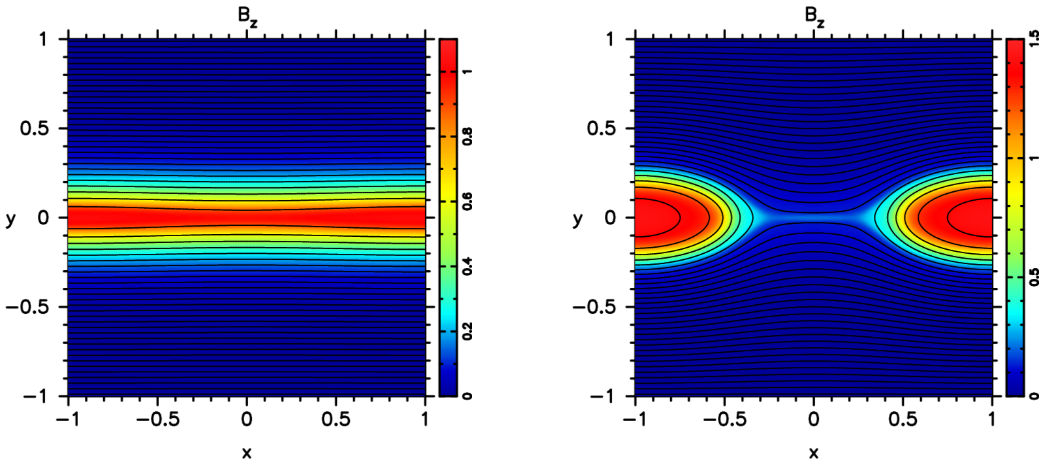

(a) *(b)*

Figure 5.21: *B_z for the tearing instability, at times $t = 50$ (a) and $t = 100$ (b). This test was run at resolution 400×400 on the domain $[-1, 1] \times [-1, 1]$, using a third order code. The left and right x-boundaries are periodic, while the upper and lower y-boundaries are Neumann BCs.*

variation in B_y given by

$$B_y = 0.001 \sin\left(\frac{2\pi x}{L}\right), \tag{5.13}$$

where L is the width of the domain along the x-axis, so that there is exactly one of these waves in the domain.

Fig. 5.18 shows the initial B_x and B_z for this setup. The flip in magnetic field direction is clearly visible.

Running this test forward in time, it takes some time for the instability to tear the current sheet, but by $t = 20$ the current sheet has begun to fully pinch, as can be seen in Fig. 5.19. Here we can see that the magnetic field lines are beginning to pinch together, and there is some significant plasma heating occurring in the pinching region. By $t = 25$, the current sheet has almost fully torn apart, and split into a magnetic island, similar to before. The plasma in this magnetic island is significantly hotter than the rest of the domain.

If we run this test again but with double the resolution in x and y, then we should find that the instability grows slower. Fig. 5.21 shows the results of this high resolution test, and as can clearly be seen, the instability grows far slower at this high resolution, showing almost no change up to $t = 50$, and by $t = 100$ it is around about the state that the test at half resolution was at $t = 25$.

Thus for this case too, the results are exactly as expected: There is some numerical resistivity, and it decreases as the grid spacing Δx decreases. In addition, previous tests at second order have shown that this resistivity is higher at lower order, as expected.

Chapter 6

Conclusion

This Chapter gives a summary of the results of this thesis. Suggestions of further progress and/or improvement are given as well.

6.1 Summary

The aim of this thesis has been to extend modelling of Relativistic MHD into the high-σ regime, for which most current models are inadequate. After discussing the fundamental equations of RMHD and its high-σ limit of FFDE in chapter 2 along with a brief discussion of some exact solutions of this complex, non-linear system, we introduced a novel approach to the high-σ regime in chapter 3.

This scheme is based on the splitting of the system into two components: A force-free system with only electromagnetic components, equivalent to the high-σ FFDE system, and an interaction system consisting of the remaining components of the full RMHD equations, which effectively characterise the interaction of the electromagnetic fields with the plasma itself.

By dividing the system in this manner, the model is able to handle the high-σ regime by relaxing strict conservation of the momentum and energy in the force-free system. This allows the model to avoid problems in normal RMHD models associated with the near-degeneracy of the equations in the high-σ limit.

In chapter 4 we tested the code against 1D exact solutions and demonstrated that the code was capable of handling smooth solutions with ease. The code gave excellent results at both low and high magnetisations for small amplitude waves, Alfvén waves and both fast and slow rarefactions. Furthermore, we showed that the code converges at third order to the exact solution for such smooth solutions.

While the code was also able of handling slow shocks without any problems, the code had more difficulty with fast shocks and current sheets. However, we showed that a simple adjustment to the code in capping E_0^2 to less than B_0^2 in the force-free system was sufficient to allow current sheets to perform as desired at high σ.

We had more difficulty with fast shocks, especially strong shocks at high σ. We were able to find a way to allow stationary shocks to work better by enforcing energy conservation to occur in cases where there would otherwise be a loss of energy, but while this saw some improvement for moving fast shocks, it did not eliminate the error, especially for strong fast shocks. However, this strong shock we tested against was so strong that it may be more extreme than anything we can expect to find in a typical astrophysical scenario, so this flaw may not be all that significant. Moreover, although the error was quite significant in inertial quantities such as the gas pressure, in the magnetic field and electric fields the relative error in their values was much less significant.

In chapter 5 we moved to test the code against two-dimensional tests. First, we needed to implement a fix for the divergence-free constraints on $\boldsymbol{B}_0$ and $\boldsymbol{B}_1$, that were previously trivial to deal with in 1D. We chose to fix this with a GLM method for each of $\boldsymbol{B}_0$ and $\boldsymbol{B}_1$, since this is one of the simplest methods to implement and proved in later tests to be sufficient.

Moving on to the tests, we began with 1D tests that had been rotated to be oblique with respect to the grid, to make the tests two-dimensional. The 2D code proved to be able to handle these tests almost as well as the 1D cases, although the 2D code was slightly worse at handling the extreme fast shock, as it was not able to handle the shock in the same frame as in 1D — although by reducing the shock velocity a little, the 2D code became able to handle it well as before.

We then tested the system against truly 2D cases. First, it handled an advection test without difficulty, besides some expected diffusion. Then we tested it against a Lundquist flux rope, for which the code also handled it well, with only a relatively small amount of plasma heating at the interface of the flux rope and the background medium.

The code was also able to handle the cylindrical explosion test at multiple different values of σ, matching previous results from Komissarov (1999a); Nagataki (2009); Lora-Clavijo *et al.* (2015) among others — including with $\sigma > 10^9$, well above the level typically expected in astrophysics, as well as beyond any previous tests — thus proving the code capable of handling extremely high σ.

The magnetic island collapse test was particularly important because it featured the formation and dynamics of several current sheets. This was particularly important as methods prior to our new method find the most difficulty with these cases. By using the same scheme of enforcing energy conservation that improved stationary fast shocks, this test was also able to give excellent results, which match previous results such as those of Lyutikov *et al.* (2017) done with FFDE and PIC schemes quite closely.

Finally, we tested the code against a resistive tearing instability like in Komissarov *et al.* (2007b) and Komissarov and Barkov (2016), showing that the code has some numerical resistivity. This numerical resistivity was reduced as the resolution of the test was increased, as we expected.

All in all, the 1D and 2D codes are capable of handling most tests without difficulty, only showing issues in the most extreme cases with high σ, high Lorentz factor γ and a strong discontinuity all at once. Otherwise, the code only has relatively minor issues, such as diffusion for fast shocks due to the weak non-linear steepening.

6.2 Future Progress

The code as it stands is already capable of being used to test real astrophysical scenarios in 2D. However, most relevant cases require additions to the code, such as an axisymmetric extension to model cases with rotational symmetry e.g. jets or accretion discs, or a fully 3D extension, or the inclusion of general relativity. In addition, it may still be possible to improve the current code. As such, there are still improvements that can be made, and further extensions to the code.

6.2.1 Extending the Code

Altering the Computational Domain

The current code is at most a Cartesian 2D code which assumes symmetry along the z-axis. That is, it assumes that all of the variables are constant in the z-direction. Unfortunately, as mentioned above, most astrophysical scenarios do not satisfy this condition. Although it can be used to study cases like current sheets in isolation, most cases like black holes and jets do not have this kind of symmetry. Thus in order to model these scenarios, we need to alter the domain.

Three Dimensions First and most obviously, we can try to extend the code to a fully 3D version. This could be done now quite easily, as extending from the 3D code to the 2D code should not introduce any new issues like the extension from 1D to 2D has with the divergence of $\boldsymbol{B}$. Thus this extension is as simple as adding another dimension to the domain and calculating the fluxes for the new cell boundaries, in the same way as before.

However, the 2D code is already somewhat slow, and so the 3D code would likely run too slowly without also implementing it in a high-performance form, e.g. using parallelisation.

Besides this problem, we do not expect there to be any other issues with extending the code to 3D. We do not know of any other problems that could arise from extending to 3D that would not have already made themselves known at 2D. It is technically plausible that there is some numerical instability that will only occur in 3D or higher, however we do not currently know of anything that could trigger this problem.

Axisymmetry Although extending the code to 3D would involve some work in implementing a high-performance version, we could instead try using an axisymmetric scheme to get a form of 3D test.

Axisymmetry is that assumption that the variables are all symmetric along some axis. For instance, our 1D and 2D codes already axisymmetric, as they assume that the variables are constant along one or more axes.

However, if we change coordinate systems then we can choose a different axis along which we assume symmetry. For instance, if we change to cylindrical coordinates and then assume the system is rotationally symmetric about the z-axis, then we can treat cells with the same r and z position as the same cell and neglect the angle θ, and in so doing reduce the number of dimensions by one.

This would allow us to study systems where we can expect some degree of rotational symmetry, such as jets and black holes. This method has been used frequently in the past, such as by Lind *et al.* (1989) for models MHD jets, and Komissarov (1999b) for models of RMHD jets. However, the assumption of symmetry can in some cases suppress instabilities that would otherwise occur in a fully 3D code.

Implementing this would be more difficult than a simple extension to 3D, as it would involve adding source terms to handle the coordinates, which are no longer the simple Cartesian coordinates we have been using. However, the code should be able to run much faster as the domain is still 2D.

General Relativity

The current code only handles Special Relativity. Given that most of the high-σ regimes this code will be useful for occur near compact objects such as Pulsars and Black Holes where general relativity is important, extending the code to include general relativity is a clear next step.

The inclusion of general relativity instead of special relativity modifies the covariant equations of RMHD in Eqs. (2.2) to (2.8) by replacing the Minkowski metric $\eta^{\alpha\beta}$ with a more general metric $g^{\alpha\beta}$. This alters the conservation equations, and means that we now have to deal with source terms.

The overall method for shock-capturing, GRMHD schemes (Del Zanna *et al.*, 2007; Komissarov, 2004b; Gammie *et al.*, 2003) are largely similar to SRMHD schemes (Komissarov, 1999a; Mignone *et al.*, 2007): We interpolate cell values to the interfaces, calculate fluxes, then use these fluxes to update conservative variables.

The actual method to do this varies. For instance, in Komissarov (2004b), for each cell interface they transform frames to the local fiducial observer (FIDO) — that is, to a frame that is stationary with respect to the cell boundary. Then they interpolate cell values to this boundary. In this situation, one can use the same Riemann solver here (such as the HLL solver we use) to evaluate the boundary fluxes in GRMHD as one does in SRMHD.

After solving the Riemann problems at all the cell interfaces, each of the resultant Riemann problem solutions are transformed back into the laboratory frame from which the full system is described. These fluxes can then be used just like before to update the conserved variables in each cell. It is then also possible to use the same primitive variable calculation algorithms as before.

On the other hand, Del Zanna *et al.* (2007) take a different approach that obviates the need to transform between different reference frames. Instead of switching back and forth, the values in the system are described in the frame of the local FIDO at all times. This modifies the equations of GRMHD, but besides the source terms the system remains a set of conservation laws; in fact, the conserved quantities are the same as in SRMHD besides a factor of $\sqrt{\gamma}$, where γ is the determinant of γ^{ij}, the spatial components of the metric tensor $g^{\alpha\beta}$ (this factor is present even with the previous method). The main differences are in the fluxes, and these differences are much easier to deal with since changes to the conservative variables would require changes to the primitive conversion algorithm.

These considerations are all we need to deal with black holes, pulsars and other similar cases, since these are relatively simple to deal with in GR as the metric is static. That is, we can neglect the self-gravity of the plasma and electromagnetic fields, due to the dominance of the central compact object, so that the metric can be effectively assumed to be static. In other words, the plasma can be treated as simply in the presence of a very strong gravitational field.

For cases like supernovae however, there is no compact object to dominate the stress-energy tensor, and so we must evolve the spacetime metric along with the plasma. This is especially challenging because the equations of General Relativity are highly non-linear and difficult to solve. However, GRMHD codes that do evolve the metric have already been developed (Duez *et al.*, 2005; Shibata and Sekiguchi, 2005; Mösta *et al.*, 2014), and since the Einstein equations are not coupled directly to the GRMHD equations — their only connection being the metric tensor itself — the same methods used to evolve the metric for these GRMHD codes should also be applicable to our code without any need to adapt them.

As such, converting to the code to a general relativistic scheme could be simpler than it may first appear. Generally, the most difficult part to deal with will most likely be the new source terms, so long as the metric is static.

6.2.2 Improving or Altering the Code

Reducing Conservation Error

As one of the clearest deficits of the method, reducing the conservation error of the code is a clear target. Since the conservation error is tied to the truncation error of the time integration and spatial interpolation, one of the first methods of doing so that comes to mind is to increase the order of the code further from third order. This would also reduce dissipation and allow discontinuous solutions to be resolved sharper.

Several higher order interpolation methods already exist. The WENO scheme introduced in Jiang and Shu (1996) is order $2r-1$, and can theoretically allow r to be arbitrarily high (although since we want a stencil that does not contain a discontinuity, increasing the size of the stencils is not always desirable). Fifth order (Henrick *et al.*, 2005) and higher (Shi *et al.*, 2003) schemes have been introduced and improved over time, so increasing at least to fifth order seems relatively doable.

However, such a method would not decrease the conservation error near discontinuities, since the order of the code is reduced here. Since these cases are where the most error occurs, increasing the order of the code has diminishing returns. In fact, increasing the order of the code should make discontinuities sharper, which could actually *increase* the amount of conservation error instead — although in practice we have found that increasing the code from second to third order did reduce the error for fast shocks to a degree, and the second order code was also a significant improvement over the initial first order code.

On the extreme end, some kind of integration scheme for the force-free system that fully conserves the force-free variables could potentially solve this problem entirely. However, it is not at all clear how to go about creating such a scheme. Moreover, it may well be that the very reason our scheme works in the first place is because it relaxes exact conservation of energy and momentum. It is entirely possible that an exactly conserving scheme would not work as a result of this.

Thus we believe that aiming for this kind of full conservation of the force-free variables is not useful, as it is not clear how to do so, and it may not work at all.

Alternate Riemann Solver

One possibility that could improve the code is to change Riemann solver, as was considered in section 3.2.4. We could even use different types of Riemann solver for the force-free and Interaction operators. We discussed a few different types of Riemann solvers in section 3.1.2.

The main advantage of switching Riemann solvers for us is that the current HLL solver is known to be quite diffusive in particular for any waves not resolved by the HLL solver itself. For us, that means that Alfvén waves, slow waves and contact discontinuities have stronger diffusion. We could instead use a Riemann solver that does resolve these waves, such as an exact solver, a linear solver, or a modification of an HLL solver that resolves further waves — such as HLLC which resolves the contact discontinuity (Toro *et al.*, 1994; Honkkila and Janhunen, 2007), or HLLD which resolves the Alfvén and contact discontinuities (Mignone *et al.*, 2009). Using any one of these alternate Riemann solvers could help to reduce diffusion for the currently-unresolved waves — although currently the wave with the worst diffusion problems is the fast wave, which is already resolved, so the benefits here will be limited.

If we tried to use a different Riemann solver for the interaction system, we would clearly need to develop a new one (although it may be simpler than it appears to convert a solver for RMHD into one for the interaction system). For the force-free system however, there are already some known solvers, since this is equivalent to just FFDE. For instance, Komissarov (2002) describes both a linear and an exact Riemann solver.

Using this would mean that we would need to enforce the PC conditions after interpolation, however. If the PC conditions are violated then a linear Riemann solver would have problems calculating phase speeds, since (for example) now we need to calculate the Alfvén phase speeds for FFDE, instead of just using ± 1 for the fast phase speeds — and this is before even attempting to calculate eigenvectors. An exact Riemann solver would have even worse problems, since we are trying find the exact solution for a problem that does not even satisfy the constraints of the system.

Unfortunately, enforcing the PC conditions after interpolation was something that was found to cause problems in the 2D code. It is currently not clear what specifically caused this issue, so it may be possible to avoid it, but at the moment it looks like trying to use a different Riemann solver may not work. With that said, in testing we have found that enforcing the force-free PC conditions has significantly less impact than enforcing the full force-free and interaction PC conditions, at least with regards to stationary 1D fast shocks. Thus it may be that we can get away with only enforcing the force-free PC condition, and so use a different Riemann solver for just this operator.

Evolving $\boldsymbol{B}_0$ and $\boldsymbol{E}_0$ Directly

In chapter 1, we discussed different methods of modelling FFDE. In particular, we noted that while some codes use an $\boldsymbol{S}$-$\boldsymbol{B}$ formulation of FFDE and integrate the momentum conservation law for $\boldsymbol{S}$ — our own code included — other codes use an $\boldsymbol{E}$-$\boldsymbol{B}$ formulation and evolve Maxwell's equations directly instead.

Thus we could try using this formulation for our force-free solver instead. Since conserving the force-free energy and momentum is not currently possible, the advantage of using a scheme to conserve them to numerical error is lost. Thus shifting the force-free operator integration scheme to one which uses these equations instead may be a good idea.

Indeed, some authors such as Komissarov (2004a); Mahlmann *et al.* (2021) have already implemented such a scheme for FFDE and General Relativistic FFDE already, achieving comparable results to the alternative scheme. Thus it is quite likely that such a scheme will also work with our code as well. This scheme can also be implemented using a conservative finite difference method like the one we already use, except the equations also includes source terms in the form of the current $\boldsymbol{J}$, as well as an extra constraint on the electric field in the form of Gauss' law, Eq. (2.94) $\boldsymbol{\nabla} \cdot \boldsymbol{E} = \rho_c$.

However, our energy transfer scheme required the inclusion of energy conservation in order to determine the lost energy due to truncation error. Thus if we used this scheme, we would need to still include energy conservation as an extra equation. In addition, as noted in chapter 1, if Gauss' law is not enforced exactly then this may also require the inclusion of an extra equation in the form of charge conservation, in order to be used as part of a divergence cleaning algorithm.

Alternative Divergence Cleaning Algorithms

In section 3.2.5 we mentioned several different alternatives for resolving the problem with $\boldsymbol{\nabla} \cdot \boldsymbol{B} = 0$ in dimensions higher than 1D. Ultimately, we chose the GLM method at least partly due to its simplicity of implementation.

However, the GLM method does have a flaw in that it does not enforce the constraint exactly. As the code runs, the system builds up some non-zero $\boldsymbol{\nabla} \cdot \boldsymbol{B}$ a little above the truncation error. We have already noted previously that at high σ this could be larger than σ^{-1}, and thus larger than the interaction system.

It is therefore possible that this could cause problems with our code, as the resultant errors in $\boldsymbol{B}_0$ become more significant than the interaction system itself.

Thus it may be advisable to change the divergence cleaning algorithm to one that enforces the constraint exactly, such as Method 2 (Constrained Transport, e.g. Evans and Hawley (1988)) described in section 3.2.5, using the integral form of Eq. (2.48) to enforce the condition. This method does however involve using a staggered grid for the magnetic field, making it significantly more complex than the GLM method.

One thing to note is that we need to clean both $\boldsymbol{B}_0$ and $\boldsymbol{B}_1$ of violations of the condition. At high σ, where we are more likely to see a benefit of enforcing the condition exactly, only the divergence of $\boldsymbol{B}_0$ is significant at truncation error scales. Thus, we may in fact only need to apply the alternative method to $\boldsymbol{B}_0$, and not $\boldsymbol{B}_1$. That is, we could use different divergence cleaning schemes for $\boldsymbol{B}_0$ and $\boldsymbol{B}_1$. However, using a staggered grid in this instance could cause a problem in the recombination step, as then we would not have the values of $\boldsymbol{B}_0$ and $\boldsymbol{B}_1$ at the same locations, forcing us to interpolate them before recombination.

In addition, at high σ, the effect on $\boldsymbol{B}_1$ is likely insignificant. However, at low σ both $\boldsymbol{B}_0$ and $\boldsymbol{B}_1$ can have relatively significant values, in which case there may be unforeseen consequences to using two different divergence cleaning algorithms for these two components of the magnetic field.

Bibliography

B. Abbott *et al.* (LIGO-Virgo Collaboration). 2016a. Observation of Gravitational Waves from a Binary Black Hole Merger. *Physical Review Letters.* **116**(6), article no: 061102.

B. Abbott *et al.* (LIGO-Virgo Collaboration). 2016b. Properties of the Binary Black Hole Merger GW150914. *Physical Review Letters.* **116**(24), article no: 241102.

B. Abbott *et al.* (LIGO-Virgo Collaboration). 2017a. GW170814: A Three-Detector Observation of Gravitational Waves from a Binary Black Hole Coalescence. *Physical Review Letters.* **119**(14), article no: 141101.

B. Abbott *et al.* (LIGO-Virgo Collaboration). 2017b. GW170817: Observation of Gravitational Waves from a Binary Neutron Star Inspiral. *Physical Review Letters.* **119**(16), article no: 161101.

B. Abbott, R. Abbott, T. D. Abbott, F. Acernese, K. Ackley, C. Adams, T. Adams, P. Addesso, R. X. Adhikari, V. B. Adya, *et al.* 2017c. Multi-messenger Observations of a Binary Neutron Star Merger. *The Astrophysical Journal Letters.* **848**(2), article no: L12.

R. Abbott *et al.* (LIGO-Virgo-KAGRA Collaboration). 2022. First joint observation by the underground gravitational-wave detector KAGRA with GEO 600. *Progress of Theoretical and Experimental Physics.* **2022**(6), article no: 063F01.

R. Abuter *et al.* (GRAVITY Collaboration). 2023. Polarimetry and astrometry of NIR flares as event horizon scale, dynamical probes for the mass of Sgr A*. *Astronomy & Astrophysics.* **677**, article no: L10.

K. Akiyama *et al.* (Event Horizon Telescope Collaboration). 2019a. First M87 Event Horizon Telescope Results. I. The Shadow of the Supermassive Black Hole. *The Astrophysical Journal Letters.* **875**(1), article no: L1.

K. Akiyama *et al.* (Event Horizon Telescope Collaboration). 2019b. First M87 Event Horizon Telescope Results. VI. The Shadow and Mass of the Central Black Hole. *The Astrophysical Journal Letters.* **875**(1), article no: L6.

K. Akiyama *et al.* (Event Horizon Telescope Collaboration). 2022. First Sagittarius A* Event Horizon Telescope Results. I. The Shadow of the Supermassive Black Hole in the Center of the Milky Way. *The Astrophysical Journal Letters.* **930**(2), article no: L12.

D. Alic, P. Moesta, L. Rezzolla, O. Zanotti, and J. L. Jaramillo. 2012. Accurate Simulations of Binary Black Hole Mergers in Force-free Electrodynamics. *The Astrophysical Journal.* **754**(1), article no: 36.

M. A. Aloy, J. M. Ibáñez, J. M. Martí, and E. Müller. 1999. GENESIS: A High-Resolution Code for Three-dimensional Relativistic Hydrodynamics. *The Astrophysical Journal Supplement Series.* **122**(1), article no: 151.

P. Amaro-Seoane, S. Aoudia, S. Babak, P. Binétruy, E. Berti, A. Bohé, C. Caprini, M. Colpi, N. J. Cornish, K. Danzmann, *et al.* 2012. Low-frequency gravitational-wave science with eLISA/NGO. *Classical and Quantum Gravity.* **29**(12), article no: 124016.

A. M. Anile and S. Pennisi. 1986. On the mathematical structure of test relativistic magnetofluiddynamics. *Annales de l'I.H.P. Physique théorique.* **46**(1), pp. 27–44.

A. M. Anile. 1989. *Relativistic fluids and magneto-fluids.* Cambridge: Cambridge University Press.

U. M. Ascher and L. R. Petzold. 1998. *Computer Methods for Ordinary Differential Equations and Differential-Algebraic Equations.* 1^{st} ed. Philadelphia: Society for Industrial and Applied Mathematics.

M. P. Bachynski. 1961. Plasma Physics-An Elementary Review. *Proceedings of the IRE.* **49**(12), pp. 1751–1766.

D. Balsara. 2001. Total Variation Diminishing Scheme for Relativistic Magnetohydrodynamics. *The Astrophysical Journal Supplement Series.* **132**(1), article no: 83.

P. Barai, D. Proga, and K. Nagamine. 2011. Smoothed particle hydrodynamics simulations of black hole accretion: A step to model black hole feedback in galaxies. *Monthly Notices of the Royal Astronomical Society.* **418**(1), pp. 591–611.

A. R. Bell and S. G. Lucek. 1995. Magnetohydrodynamic jet formation. *Monthly Notices of the Royal Astronomical Society.* **277**(4), pp. 1327–1340.

M. Ben-Artzi and J. Falcovitz. 1984. A Second-Order Godunov-Type Scheme for Compressible Fluid Dynamics. *Journal of Computational Physics.* **55**(1), pp. 1–32.

H. Bethe. 1990. Supernova mechanisms. *Reviews of Modern Physics.* **62**(4), pp. 801–866.

D. Bhattacharya and E. P. J. van den Heuvel. 1991. Formation and evolution of binary and millisecond radio pulsars. *Physics Reports.* **203**(1–2), pp. 1–124.

C. K. Birdsall and A. B. Langdon. 1985. *Plasma Physics Via Computer Simulation.* New York: McGraw-Hill.

J. A. Biretta and W. Junor. 1995. The Parsec-Scale Jet in M87. *Proceedings of the National Academy of Sciences of the United States of America.* **92**(25), pp. 11364–11367.

R. D. Blandford and R. L. Znajek. 1977. Electromagnetic extraction of energy from Kerr black holes. *Monthly Notices of the Royal Astronomical Society.* **179**(3), pp. 433–456.

R. D. Blandford. 1977. Spectrum of a radio pulse from an exploding black hole. *Monthly Notices of the Royal Astronomical Society.* **181**(3), pp. 489–498.

J. F. Blinn. 2006. How to Solve a Cubic Equation, Part 2: The 11 Case. *IEEE Computer Graphics and Applications.* **26**(4), pp. 90–100.

M. Bocher. 1906. Introduction to the Theory of Fourier's Series. *Annals of Mathematics.* **7**(3), pp. 81–152.

C. Bond, D. Brown, A. Freise, and K. A. Strain. 2017. Interferometer techniques for gravitational-wave detection. *Living Reviews in Relativity.* **19**(1), article no: 3.

M. Boyle, D. Hemberger, D. A. Iozzo, G. Lovelace, S. Ossokine, H. P. Pfeiffer, M. A. Scheel, L. C. Stein, C. J. Woodford, A. B. Zimmerman, *et al.* 2019. The SXS collaboration catalog of binary black hole simulations. *Classical and Quantum Gravity.* **36**(19), article no: 195006.

J. U. Brackbill and D. C. Barnes. 1980. The Effect of Nonzero $\nabla \cdot B$ on the numerical solution of the magnetohydrodynamic equations. *Journal of Computational Physics.* **35**(3), pp. 426–430.

R. P. Brent. 1971. An algorithm with guaranteed convergence for finding a zero of a function. *The Computer Journal.* **14**(4), pp. 422–425.

M. Brio, A. R. Zakharian, and G. M. Webb. 2001. Two-Dimensional Riemann Solver for Euler Equations of Gas Dynamics. *Journal of Computational Physics*. **167**(1), pp. 177–195.

E. Burns, D. Svinkin, E. Fenimore, D. A. Kann, J. F. A. Fernández, D. Frederiks, R. Hamburg, S. Lesage, Y. Temiraev, A. Tsvetkova, *et al.* 2023. GRB 221009A: The BOAT. *The Astrophysical Journal Letters*. **946**(1), article no: L31.

A. Burrows and D. Vartanyan. 2021. Core-collapse supernova explosion theory. *Nature*. **589**(7840), pp. 29–39.

A. Burrows, D. Vartanyan, and T. Wang. 2023. Black Hole Formation Accompanied by the Supernova Explosion of a 40 M $_\odot$ Progenitor Star. *The Astrophysical Journal*. **957**(2), article no: 68.

J. Casper, C.-W. Shu, and H. Atkins. 1994. Comparison of two formulations for high-order accurate essentially nonoscillatory schemes. *AIAA Journal*. **32**(10), pp. 1970–1977.

B. Cerutti, A. Philippov, K. Parfrey, and A. Spitkovsky. 2015. Particle acceleration in axisymmetric pulsar current sheets. *Monthly Notices of the Royal Astronomical Society*. **448**(1), pp. 606–619.

B. Cerutti and A. M. Beloborodov. 2017. Electrodynamics of Pulsar Magnetospheres. *Space Science Reviews*. **207**(1), pp. 111–136.

J. Česenek, M. Feistauer, J. Horáček, V. Kučera, and J. Prokopová. 2013. Simulation of compressible viscous flow in time-dependent domains. *Applied Mathematics and Computation*. **219**(13), pp. 7139–7150.

A. Y. Chen and A. M. Beloborodov. 2014. Electrodynamics of Axisymmetric Pulsar Magnetosphere with Electron-Positron Discharge: A Numerical Experiment. *The Astrophysical Journal Letters*. **795**(1), article no: L22.

S. Childress. 2003. New Solutions of the Kinematic Dynamo Problem. *Journal of Mathematical Physics*. **11**(10), pp. 3063–3076.

D. A. Clarke, M. Norman, and J. Burns. 1986. Numerical Simulations of a Magnetically Confined Jet. *The Astrophysical Journal Letters*. **311**, pp. 63–67.

N. Cornish and T. Robson. 2017. Galactic binary science with the new LISA design. *Journal of Physics: Conference Series*. **840**, article no: 012024.

R. Courant, K. Friedrichs, and H. Lewy. 1928. Über die partiellen Differenzengleichungen der mathematischen Physik. *Mathematische Annalen.* **100**(1), pp. 32–74.

R. Courant and D. Hilber. 1989. *Methods of Mathematical Physics.* Hoboken, New Jersey: John Wiley & Sons.

W. Dai and P. R. Woodward. 1994. An Approximate Riemann Solver for Ideal Magnetohydrodynamics. *Journal of Computational Physics.* **111**(2), pp. 354–372.

S. F. Davis. 1988. Simplified Second-Order Godunov-Type Methods. *SIAM Journal on Scientific and Statistical Computing.* **9**(3), pp. 445–473.

F. de Hoffmann and E. Teller. 1950. Magneto-Hydrodynamic Shocks. *Physical Review.* **80**(4), pp. 692–703.

J.-P. De Villiers, J. F. Hawley, and J. H. Krolik. 2003. Magnetically Driven Accretion Flows in the Kerr Metric. I. Models and Overall Structure. *The Astrophysical Journal.* **599**(2), pp. 1238–1253.

J.-P. De Villiers and J. F. Hawley. 2003. A Numerical Method for General Relativistic Magnetohydrodynamics. *The Astrophysical Journal.* **589**(1), pp. 458–480.

A. Dedner, F. Kemm, D. Kröner, C.-D. Munz, T. Schnitzer, and M. Wesenberg. 2002. Hyperbolic Divergence Cleaning for the MHD Equations. *Journal of Computational Physics.* **175**(2), pp. 645–673.

T. J. Dekker. 1969. Finding a zero by means of successive linear interpolation. In: B. Dejon and P. Henrici, eds. *Constructive Aspects of the Fundamental Theorem of Algebra.* London: Wiley-Interscience, pp. 37–48.

L. Del Zanna, N. Bucciantini, and P. Londrillo. 2003. An efficient shock-capturing central-type scheme for multidimensional relativistic flows. II. Magnetohydrodynamics. *Astronomy & Astrophysics.* **400**(2), pp. 397–413.

L. Del Zanna, O. Zanotti, N. Bucciantini, and P. Londrillo. 2007. ECHO: A Eulerian conservative high-order scheme for general relativistic magnetohydrodynamics and magnetodynamics. *Astronomy & Astrophysics.* **473**(1), pp. 11–30.

N. Deppe, F. Hébert, L. E. Kidder, and S. A. Teukolsky. 2022. A high-order shock capturing discontinuous Galerkin-finite difference hybrid method for GRMHD. *Classical and Quantum Gravity.* **39**, article no: 19.

P. Diener, S. Rosswog, and F. Torsello. 2022. Simulating neutron star mergers with the Lagrangian Numerical Relativity code SPHINCS_BSSN. *The European Physical Journal A*. **58**(4), article no: 74.

W. Dixon. 1978. *Special Relativity: The Foundation of Macroscopic Physics*. Cambridge: Cambridge University Press.

T. Dombre, U. Frisch, J. M. Greene, M. Hénon, A. Mehr, and A. M. Soward. 1986. Chaotic streamlines in the ABC flows. *Journal of Fluid Mechanics*. **167**, pp. 353–391.

W.-S. Don and R. Borges. 2013. Accuracy of the Weighted Essentially Non-Oscillatory Conservative Finite Difference Schemes. *Journal of Computational Physics*. **250**(C), pp. 347–372.

M. D. Duez, Y. T. Liu, S. L. Shapiro, and B. C. Stephens. 2005. Relativistic magnetohydrodynamics in dynamical spacetimes: Numerical methods and tests. *Physical Review D*. **72**(2), article no: 024028.

M. Dumbser, D. S. Balsara, E. F. Toro, and C.-D. Munz. 2008. A unified framework for the construction of one-step finite volume and discontinuous Galerkin schemes on unstructured meshes. *Journal of Computational Physics*. **227**(18), pp. 8209–8253.

C. Eckart. 1940. The Thermodynamics of Irreversible Processes. III. Relativistic Theory of the Simple Fluid. *Physical Review*. **58**(10), pp. 919–924.

A. Eckart, R. Genzel, T. Ott, and R. Schödel. 2002. Stellar orbits near Sagittarius A*. *Monthly Notices of the Royal Astronomical Society*. **331**(4), pp. 917–934.

B. Einfeldt. 1988. On Godunov-Type Methods for Gas Dynamics. *SIAM Journal on Numerical Analysis*. **25**(2), pp. 294–318.

A. Einstein. 1915. Die Feldgleichungen der Gravitation. *Sitzungsberichte der Königlich Preussischen Akademie der Wissenschaften*. pp. 844–847.

T. Erber. 1966. High-Energy Electromagnetic Conversion Processes in Intense Magnetic Fields. *Reviews of Modern Physics*. **38**(4), pp. 626–659.

Z. B. Etienne, V. Paschalidis, R. Haas, P. Mösta, and S. L. Shapiro. 2015. IllinoisGRMHD: an open-source, user-friendly GRMHD code for dynamical spacetimes. *Classical and Quantum Gravity*. **32**(17), article no: 175009.

C. R. Evans and J. F. Hawley. 1988. Simulation of Magnetohydrodynamic Flows: A Constrained Transport Model. *The Astrophysical Journal*. **332**, pp. 659–677.

S. A. E. G. Falle and S. S. Komissarov. 1996. An upwind numerical scheme for relativistic hydrodynamics with a general equation of state. *Monthly Notices of the Royal Astronomical Society.* **278**(2), pp. 586–602.

S. A. E. G. Falle, S. S. Komissarov, and P. Joarder. 1998. A multidimensional upwind scheme for magnetohydrodynamics. *Monthly Notices of the Royal Astronomical Society.* **297**(1), pp. 265–277.

J. Fernández-Pato, M. Morales-Hernández, and P. García-Navarro. 2018. Implicit finite volume simulation of 2D shallow water flows in flexible meshes. *Computer Methods in Applied Mechanics and Engineering.* **328**, pp. 1–25.

K. O. Friedrichs. 1954. Symmetric hyperbolic linear differential equations. *Communications on Pure and Applied Mathematics.* **7**(2), pp. 345–392.

K. O. Friedrichs. 1974. On the laws of relativistic electro-magneto-fluid dynamics. *Communications on Pure and Applied Mathematics.* **20**(6), pp. 749–808.

C. L. Fryer and K. C. B. New. 2003. Gravitational Waves from Gravitational Collapse. *Living Reviews in Relativity.* **6**(2), article no: 1.

C. F. Gammie, J. C. McKinney, and G. Tóth. 2003. HARM: A Numerical Scheme for General Relativistic Magnetohydrodynamics. *The Astrophysical Journal.* **589**(1), pp. 444–457.

X. Ge, B.-X. Zhao, W.-H. Bian, and R. F. Green. 2019. The Blueshift of the C IV Broad Emission Line in QSOs. *The Astronomical Journal.* **157**(4), article no: 148.

B. Giacomazzo and L. Rezzolla. 2006. The exact solution of the Riemann problem in relativistic magnetohydrodynamics. *Journal of Fluid Mechanics.* **562**, pp. 223–259.

S. K. Godunov. 1959. A difference method for numerical calculation of discontinuous solutions of the equations of hydrodynamics. *Matematicheskii Sbornik.* **47**(3), pp. 271–306.

J. P. H. Goedbloed and S. Poedts. 2004. *Principles of Magnetohydrodynamics: With Applications to Laboratory and Astrophysical Plasmas.* Cambridge: Cambridge University Press.

P. Goldreich and W. H. Julian. 1969. Pulsar Electrodynamics. *The Astrophysical Journal.* **157**(2), pp. 869–880.

A. V. Gruzinov. 1999. [Pre-print]. Stability in Force-Free Electrodynamics. *arXiv: Astrophysics.*

S. F. Gull and M. S. Longair. 1973. A Numerical Model of the Structure and Evolution of Young Supernova Remnants. *Monthly Notices of the Royal Astronomical Society.* **161**(1), pp. 47–69.

Y. Ha, C. H. Kim, H. Yang, and J. Yoon. 2016. Sixth-order Weighted Essentially Nonoscillatory Schemes Based on Exponential Polynomials. *SIAM Journal on Scientific Computing.* **38**(4), pp. A1987-A2017.

Y. Ha, C. H. Kim, H. Yang, and J. Yoon. 2020. Construction of an Improved Third-Order WENO Scheme with a New Smoothness Indicator. *Journal of Scientific Computing.* **82**(3), article no: 63.

A. K. Harding and D. Lai. 2006. Physics of strongly magnetized neutron stars. *Reports on Progress in Physics.* **69**(9), pp. 2631–2708.

E. G. Harris. 1957. Relativistic Magnetohydrodynamics. *Physical Review.* **108**(6), pp. 1357–1360.

A. Harten, P. D. Lax, and B. van Leer. 1983. On Upstream Differencing and Godunov-Type Schemes for Hyperbolic Conservation Laws. *SIAM Review.* **25**(1), pp. 35–61.

A. Harten, B. Engquist, S. Osher, and S. R. Chakravarthy. 1987. Uniformly high order accurate essentially non-oscillatory schemes, III. *Journal of Computational Physics.* **71**(2), pp. 231–303.

R. Hartmann and P. Houston. 2002. Adaptive Discontinuous Galerkin Finite Element Methods for the Compressible Euler Equations. *Journal of Computational Physics.* **183**(2), pp. 508–532.

J. Healy and C. O. Lousto. 2022. Fourth RIT binary black hole simulations catalog: Extension to eccentric orbits. *Physical Review D.* **105**(12), article no: 124010.

A. K. Henrick, T. D. Aslam, and J. M. Powers. 2005. Mapped weighted essentially non-oscillatory schemes: Achieving optimal order near critical points. *Journal of Computational Physics.* **207**(2), pp. 542–567.

Q. Henry, F. Larrouturou, and C. Le Poncin-Lafitte. 2023. Electromagnetic fields in compact binaries: A post-Newtonian approach. *Physical Review D.* **108**(2), article no: 024020.

A. Hewish, S. J. Bell, J. D. H. Pilkington, P. F. Scott, and R. A. Collins. 1968. Observation of a Rapidly Pulsating Radio Source. *Nature.* **217**(5130), pp. 709–713.

K. Hirotani, R. Krasnopolsky, H. Shang, K.-i. Nishikawa, and M. Watson. 2021. Two-dimensional Particle-in-cell Simulations of Axisymmetric Black Hole Magnetospheres. *The Astrophysical Journal.* **908**(1), article no: 88.

V. Honkkila and P. Janhunen. 2007. HLLC solver for ideal relativistic MHD. *Journal of Computational Physics.* **223**(2), pp. 643–656.

F. Huško and C. G. Lacey. 2023. Active galactic nuclei jets simulated with smoothed particle hydrodynamics. *Monthly Notices of the Royal Astronomical Society.* **520**(4), pp. 5090–5109.

R. L. Ingraham. 1973. Algorithm for Solving the Nonlinear Pulsar Equation. *The Astrophysical Journal.* **186**, pp. 625–630.

D. J. Jackson. 1999. *Classical Electrodynamics.* 3rd ed. New York: Wiley.

A. Jeffrey and T. Taniuti. 1984. *Non-Linear Wave Propagation With Applications to Physics and Magnetohydrodynamics.* Cambridge, Massachusetts: Academic Press.

G.-S. Jiang and C.-W. Shu. 1996. Efficient Implementation of Weighted ENO Schemes. *Journal of Computational Physics.* **126**(1), pp. 202–228.

L. Ju, D. G. Blair, and C. Zhao. 2000. Detection of gravitational waves. *Reports on Progress in Physics.* **63**(9), article no: 1317.

C. Kalapotharakos and I. Contopoulos. 2009. Three-dimensional numerical simulations of the pulsar magnetosphere: preliminary results. *Astronomy & Astrophysics.* **496**(2), pp. 495–502.

J. V. Kalinani, R. Ciolfi, W. Kastaun, B. Giacomazzo, F. Cipolletta, and L. Ennoggi. 2022. Implementing a new recovery scheme for primitive variables in the general relativistic magnetohydrodynamic code Spritz. *Physical Review D.* **105**(10), article no: 103031.

R. Keppens and Z. Meliani. 2008. Linear wave propagation in relativistic magnetohydrodynamics. *Physics of Plasmas.* **15**(10), article no: 102103.

J.-Y. Kim *et al.* (Event Horizon Telescope Collaboration). 2020. Event Horizon Telescope imaging of the archetypal blazar 3C 279 at an extreme 20 microarcsecond resolution. *Astronomy & Astrophysics.* **640**, article no: A69.

M. Kino, F. Takahara, K. Hada, K. Akiyama, H. Nagai, and B. W. Sohn. 2015. Magnetization Degree at the Jet Base of M87 Derived from the Event Horizon Telescope Data: Testing the Magnetically Driven Jet Paradigm. *The Astrophysical Journal.* **803**(1), article no: 30.

K. Kohri, R. Narayan, and T. Piran. 2005. Neutrino-dominated Accretion and Supernovae. *The Astrophysical Journal.* **629**(1), article no: 341.

A. V. Koldoba, O. A. Kuznetsov, and G. V. Ustyugova. 2002. An approximate Riemann solver for relativistic magnetohydrodynamics. *Monthly Notices of the Royal Astronomical Society.* **333**(4), pp. 932–942.

S. S. Komissarov. 1997. On the properties of Alfven waves in relativistic magnetohydrodynamics. *Physics Letters A.* **232**(6), pp. 435–442.

S. S. Komissarov. 1999a. A Godunov-type scheme for relativistic magnetohydrodynamics. *Monthly Notices of the Royal Astronomical Society.* **303**(2), pp. 343–366.

S. S. Komissarov. 1999b. Numerical simulations of relativistic magnetized jets. *Monthly Notices of the Royal Astronomical Society.* **308**(4), pp. 1069–1076.

S. S. Komissarov. 2001. Direct numerical simulations of the Blandford-Znajek effect. *Monthly Notices of the Royal Astronomical Society.* **326**(3), pp. L41-L44.

S. S. Komissarov. 2002. Time-dependent, Force-Free, degenerate electrodynamics. *Monthly Notices of the Royal Astronomical Society.* **336**(3), pp. 759–766.

S. S. Komissarov. 2004a. Electrodynamics of black hole magnetospheres. *Monthly Notices of the Royal Astronomical Society.* **350**(2), pp. 427–448.

S. S. Komissarov. 2004b. General relativistic magnetohydrodynamic simulations of monopole magnetospheres of black holes. *Monthly Notices of the Royal Astronomical Society.* **350**(4), pp. 1431–1436.

S. S. Komissarov. 2006. On Some Recent Developments in Numerical Methods for Relativistic MHD. In: *AIP Conference Proceedings, 14–17 December 2005, Ann Arbor, Michigan.* New York: AIP Publishing, pp. 129–149.

S. S. Komissarov. 2007. Multidimensional numerical scheme for resistive relativistic magnetohydrodynamics. *Monthly Notices of the Royal Astronomical Society.* **382**(3), pp. 995–1004.

S. S. Komissarov, M. V. Barkov, N. Vlahakis, and A. Königl. 2007a. Magnetic acceleration of relativistic active galactic nucleus jets. *Monthly Notices of the Royal Astronomical Society.* **380**(1), pp. 51–70.

S. S. Komissarov, M. V. Barkov, and M. Lyutikov. 2007b. Tearing instability in relativistic magnetically dominated plasmas. *Monthly Notices of the Royal Astronomical Society.* **374**(2), pp. 415–426.

S. S. Komissarov and M. V. Barkov. 2009. Activation of the Blandford-Znajek mechanism in collapsing stars. *Monthly Notices of the Royal Astronomical Society.* **397**(3), pp. 1153–1168.

S. S. Komissarov and M. Lyutikov. 2011. On the origin of variable gamma-ray emission from the Crab nebula. *Monthly Notices of the Royal Astronomical Society.* **414**(3), pp. 2017–2028.

S. S. Komissarov and M. V. Barkov. 2016. Relativistic tearing and drift-kink instabilities in two-fluid simulations. *Monthly Notices of the Royal Astronomical Society.* **458**(2), pp. 1939–1947.

C. Kouveliotou, C. A. Meegan, G. J. Fishman, N. P. Bhat, M. S. Briggs, T. M. Koshut, W. S. Paciesas, and G. N. Pendleton. 1993. Identification of Two Classes of Gamma-Ray Bursts. *The Astrophysical Journal Letters.* **413**, article no: L101.

D. Ł. Król, Ł. Stawarz, M. C. Begelman, J.-M. Martí, M. Perucho, and B. A. Petrenko. 2022. Magnetization of Relativistic Current-carrying Jets with Radial Velocity Shear. *The Astrophysical Journal.* **929**(2), article no: 181.

W. Kundt. 2016. A Uniform Description of All the Astrophysical Jets. In: F. Giovannelli and L. Sabau-Graziati, eds. *Proceedings of Frontier Research in Astrophysics — PoS(FRAPWS2014), 26–31 May 2014, Palermo.* Italy: Proceedings of Science, article no: 25.

M. W. Kunz, A. A. Schekochihin, and J. M. Stone. 2014. Firehose and Mirror Instabilities in a Collisionless Shearing Plasma. *Physical Review Letters.* **112**(20), article no: 205003.

M. W. Kunz, J. M. Stone, and E. Quataert. 2016. Magnetorotational Turbulence and Dynamo in a Collisionless Plasma. *Physical Review Letters.* **117**(23), article no: 235101.

L. D. Landau and E. M. Lifshitz. 1959. *Fluid mechanics.* Oxford: Pergamon Press.

R. J. LeVeque. 2002. *Finite Volume Methods for Hyperbolic Problems.* Cambridge: Cambridge University Press.

L. Lehner, C. Palenzuela, S. L. Liebling, C. Thompson, and C. Hanna. 2012. Intense electromagnetic outbursts from collapsing hypermassive neutron stars. *Physical Review D.* **86**(10), article no: 104035.

T. Leismann, L. Antón, M. A. Aloy, E. Müller, J. M. Martí, J. A. Miralles, and J. M. Ibáñez. 2005. Relativistic MHD simulations of extragalactic jets. *Astronomy & Astrophysics.* **436**(2), pp. 503–526.

A. Lichnerowicz. 1967. *Relativistic Hydrodynamics and Magnetohydrodynamics.* New York: W. A. Benjamin.

E. H. Lieb and H.-T. Yau. 1987. A Rigorous Examination of the Chandrasekhar Theory of Stellar Collapse. *The Astrophysical Journal.* **323**, pp. 140–144.

K. R. Lind, D. G. Payne, D. L. Meier, and R. D. Blandford. 1989. Numerical Simulations of Magnetized Jets. *The Astrophysical Journal.* **344**, pp. 89–103.

D. Liptai and D. J. Price. 2019. General relativistic smoothed particle hydrodynamics. *Monthly Notices of the Royal Astronomical Society.* **485**(1), pp. 819–842.

X.-D. Liu, S. Osher, and T. Chan. 1994. Weighted Essentially Non-oscillatory Schemes. *Journal of Computational Physics.* **115**(1), pp. 200–212.

C. S. Liu, V. K. Tripathi, and B. Eliasson. 2019. Vlasov and Particle-in-Cell Simulations. In: ???. *High-Power Laser-Plasma Interaction.* Cambridge: Cambridge University Press, pp. 263–274.

F. D. Lora-Clavijo, A. Cruz-Osorio, and F. S. Guzmán. 2015. CAFE: A New Relativistic MHD Code. *The Astrophysical Journal Supplement Series.* **218**(2), article no: 24.

S. Lundquist. 1950. Magnetohydrostatic fields. *Arkiv för Fysik.* **2**, pp. 361–365.

M. Lyutikov and D. Uzdensky. 2003. Dynamics of Relativistic Reconnection. *The Astrophysical Journal.* **589**(2), pp. 893–901.

M. Lyutikov, L. Sironi, S. S. Komissarov, and O. Porth. 2017. Particle acceleration in relativistic magnetic flux-merging events. *Journal of Plasma Physics.* **83**(6), article no: 635830602.

M. Lyutikov, S. S. Komissarov, L. Sironi, and O. Porth. 2018. Particle acceleration in explosive relativistic reconnection events and Crab Nebula gamma-ray flares. *Journal of Plasma Physics.* **84**(2), article no: 635840201.

P. Mösta, B. C. Mundim, J. A. Faber, R. Haas, S. C. Noble, T. Bode, F. Löffler, C. D. Ott, C. Reisswig, and E. Schnetter. 2014. GRHydro: a new open-source general-relativistic magnetohydrodynamics code for the Einstein toolkit. *Classical and Quantum Gravity.* **31**(1), article no: 015005.

D. MacDonald and K. S. Thorne. 1982. Black-hole electrodynamics - an absolute-space/universal-time formulation. *Monthly Notices of the Royal Astronomical Society.* **198**(2), pp. 345–382.

A. MacFadyen and S. Woosley. 1999. Collapsars: Gamma-Ray Bursts and Explosions in "Failed Supernovae". *The Astrophysical Journal.* **524**(1), pp. 262–289.

J. F. Mahlmann, M. A. Aloy, V. Mewes, and P. Cerdá-Durán. 2021. Computational general relativistic Force-Free electrodynamics - I. Multi-coordinate implementation and testing. *Astronomy & Astrophysics.* **647**, article no: A57.

J. M. Martí and E. Müller. 2003. Numerical Hydrodynamics in Special Relativity. *Living Reviews in Relativity.* **6**(1), article no: 7.

J. M. Martínez. 1994. Sor-Secant Methods. *SIAM Journal on Numerical Analysis.* **31**(1), pp. 217–226.

D. V. Martynov, E. D. Hall, B. P. Abbott, R. Abbott, T. D. Abbott, C. Adams, R. X. Adhikari, R. A. Anderson, S. B. Anderson, K. Arai, *et al.* 2016. Sensitivity of the Advanced LIGO detectors at the beginning of gravitational wave astronomy. *Physical Review D.* **93**(11), article no: 112004.

G. Mattia, L. Del Zanna, M. Bugli, A. Pavan, R. Ciolfi, G. Bodo, and A. Mignone. 2023. Resistive relativistic MHD simulations of astrophysical jets. *Astronomy & Astrophysics.* **679**, article no: A49.

J. E. McClintock and R. A. Remillard. 2006. Black hole binaries. In: W. Lewin and M. van der Klis, eds. *Compact stellar X-ray sources.* Cambridge: Cambridge University Press, pp. 157–213.

J. C. McKinney and C. F. Gammie. 2004. A Measurement of the Electromagnetic Luminosity of a Kerr Black Hole. *The Astrophysical Journal.* **611**(2), pp. 977–995.

J. C. McKinney. 2006. General relativistic Force-Free electrodynamics: a new code and applications to black hole magnetospheres. *Monthly Notices of the Royal Astronomical Society.* **367**(4), pp. 1797–1807.

L. Mestel. 1973. Force-free pulsar magnetospheres. *Astrophysics and Space Science.* **24**, pp. 289–297.

A. Mignone and J. C. McKinney. 2007. Equation of state in relativistic magnetohydrodynamics: variable versus constant adiabatic index. *Monthly Notices of the Royal Astronomical Society.* **378**(3), pp. 1118–1130.

A. Mignone, G. Bodo, S. Massaglia, T. Matsakos, O. Tesileanu, C. Zanni, and A. Ferrari. 2007. PLUTO: A Numerical Code for Computational Astrophysics. *The Astrophysical Journal Supplement Series.* **170**(1), pp. 228–242.

A. Mignone, M. Ugliano, and G. Bodo. 2009. A five-wave Harten-Lax-van Leer Riemann solver for relativistic magnetohydrodynamics. *Monthly Notices of the Royal Astronomical Society.* **393**(4), pp. 1141–1156.

A. Mignone, P. Rossi, G. Bodo, A. Ferrari, and S. Massaglia. 2010a. High-resolution 3D relativistic MHD simulations of jets. *Monthly Notices of the Royal Astronomical Society.* **402**(1), pp. 7–12.

A. Mignone, P. Tzeferacos, and G. Bodo. 2010b. High-order conservative finite difference GLM-MHD schemes for cell-centered MHD. *Journal of Computational Physics.* **229**(17), pp. 5896–5920.

T. Minoshima, T. Miyoshi, and Y. Matsumoto. 2019. A High-order Weighted Finite Difference Scheme with a Multistate Approximate Riemann Solver for Divergence-free Magnetohydrodynamic Simulations. *The Astrophysical Journal Supplement Series.* **242**, article no: 2.

C. Misner, K. Thorne, and J. Wheeler. 1973. *Gravitation.* San Francisco: W. H. Freeman.

H. K. Moffatt. 1986. Magnetostatic equilibria and analogous Euler flows of arbitrarily complex topology. Part 2. Stability considerations. *Journal of Fluid Mechanics.* **166**, pp. 359–378.

J. Monaghan. 1992. Smoothed particle hydrodynamics. *Annual Review of Astronomy and Astrophysics.* **30**, pp. 543–574.

D. J. Mortlock, S. J. Warren, B. P. Venemans, M. Patel, P. C. Hewett, R. G. McMahon, C. Simpson, T. Theuns, E. A. Gonzáles-Solares, A. Adamson, *et al.* 2011. A luminous quasar at a redshift of z = 7.085. *Nature.* **474**(7353), pp. 616–619.

C.-D. Munz, R. Schneider, E. Sonnendrücker, and U. Voss. 1999. Maxwell's equations when the charge conservation is not satisfied. *Comptes Rendus de l'Académie des Sciences - Series I - Mathematics.* **328**(5), pp. 431–436.

C.-D. Munz, P. Omnes, R. Schneider, E. Sonnendrücker, and U. Voß. 2000. Divergence Correction Techniques for Maxwell Solvers Based on a Hyperbolic Model. *Journal of Computational Physics.* **161**(2), pp. 484–511.

H. Nagakura, A. Burrows, D. Vartanyan, and D. Radice. 2020. Core-collapse supernova neutrino emission and detection informed by state-of-the-art three-dimensional numerical models. *Monthly Notices of the Royal Astronomical Society.* **500**(1), pp. 696–717.

S. Nagataki. 2009. Development of a General Relativistic Magnetohydrodynamic Code and Its Application to the Central Engine of Long Gamma-Ray Bursts. *The Astrophysical Journal.* **704**(2), pp. 937–950.

K. Nakamura, T. Miyoshi, C. Nonaka, and H. R. Takahashi. 2023. Relativistic resistive magneto-hydrodynamics code for high-energy heavy-ion collisions. *The European Physical Journal C.* **83**(3), article no: 229.

K. Nalewajko, J. Zrake, Y. Yuan, W. E. East, and R. D. Blandford. 2016. Kinetic Simulations of the Lowest-Order Unstable Mode of Relativistic Magnetostatic Equilibria. *The Astrophysical Journal.* **826**(2), article no: 115.

W. I. Newman and N. D. Hamlin. 2014. Primitive Variable Determination in Conservative Relativistic Magnetohydrodynamic Simulations. *SIAM Journal of Scientific Computing.* **36**(4), pp. 661–683.

S. C. Noble, J. H. Krolik, and J. F. Hawley. 2009. Direct Calculation of the Radiative Efficiency of an Accretion Disk Around a Black Hole. *The Astrophysical Journal.* **692**(1), pp. 411–421.

M. L. Norman, L. Smarr, M. D. Smith, and J. R. Wilson. 1981. Hydrodynamic formation of twin-exhaust jets. *The Astrophysical Journal.* **247**(1), pp. 52–58.

I. Okamoto. 1992. The evolution of a black hole's Force-Free magnetosphere. *Monthly Notices of the Royal Astronomical Society.* **254**(2), pp. 192–220.

J. P. Ostriker and J. E. Gunn. 1969. On the Nature of Pulsars. I. Theory. *The Astrophysical Journal.* **157**, pp. 1395–1417.

J. Pétri. 2016. Theory of pulsar magnetosphere and wind. *Journal of Plasma Physics.* **82**(5), article no: 635820502.

F. Pacini. 1967. Energy Emission from a Neutron Star. *Nature.* **216**(5115), pp. 567–568.

F. Pacini. 1968. Rotating Neutron Stars, Pulsars and Supernova Remnants. *Nature.* **219**(5150), pp. 145–146.

C. Palenzuela, L. Lehner, O. Reula, and L. Rezzolla. 2009. Beyond ideal MHD: towards a more realistic modelling of relativistic astrophysical plasmas. *Monthly Notices of the Royal Astronomical Society.* **394**(4), pp. 1727–1740.

C. Palenzuela, T. Garrett, L. Lehner, and S. L. Liebling. 2010. Magnetospheres of black hole systems in force-free plasma. *Physical Review D.* **82**(4), article no: 044045.

K. Parfrey, A. Spitkovsky, and A. M. Beloborodov. 2017. Simulations of the magnetospheres of accreting millisecond pulsars. *Monthly Notices of the Royal Astronomical Society.* **469**(3), pp. 3656–3669.

E. N. Parker. 1983. Magnetic neutral sheets in evolving fields. I - General theory. *The Astrophysical Journal.* **264**(1), pp. 635–647.

V. Paschalidis and S. L. Shapiro. 2013. A new scheme for matching general relativistic ideal magnetohydrodynamics to its force-free limit. *Physical Review D.* **88**(10), article no: 104031.

H. Petschek. 1958. Aerodynamic Dissipation. *Reviews of Modern Physics.* **30**(3), pp. 966–974.

A. A. Philippov and A. Spitkovsky. 2014. Ab initio pulsar magnetosphere: Three-Dimensional particle-in-cell simulations of axisymmetric pulsars. *The Astrophysical Journal Letters.* **785**(2), article no: L33.

R. Popham, S. Woosley, and C. Fryer. 1999. Hyperaccreting Black Holes and Gamma-Ray Bursts. *The Astrophysical Journal.* **518**(1), pp. 356–374.

O. Porth, S. S. Komissarov, and R. Keppens. 2013. Three-dimensional magnetohydrodynamic simulations of the Crab nebula. *Monthly Notices of the Royal Astronomical Society.* **438**(1), pp. 278–306.

K. G. Powell. 1994. An Approximate Riemann Solver for Magnetohydrodynamics (That works in more than one dimension). In: M. Y. Hussaini, B. Leer, and J. Rosendale, eds. *Upwind and High-Resolution Schemes*. Berlin: Springer Berlin, Heidelberg, pp. 570–583.

W. H. Press. 2007. *Numerical Recipes: The Art of Scientific Computing*. 3$^{\text{rd}}$ ed. Cambridge: Cambridge University Press.

D. J. Price. 2012. Smoothed particle hydrodynamics and magnetohydrodynamics. *Journal of Computational Physics*. **231**(3), pp. 759–794.

Q. Qian, C. Fendt, and C. Vourellis. 2018. Jet Launching in Resistive GR-MHD Black Hole-Accretion Disk Systems. *The Astrophysical Journal*. **859**(1), pp. 28.

F. A. Rasio, S. L. Shapiro, and S. A. Teukolsky. 1989. Solving the Vlasov Equation in General Relativity. *The Astrophysical Journal*. **344**, pp. 146–157.

D. R. Rayburn. 1977. A numerical study of the continuous beam model of extragalactic radio sources. *Monthly Notices of the Royal Astronomical Society*. **179**(4), pp. 603–617.

M. Reinecke, W. Hillebrandt, and J. C. Niemeyer. 2002. Refined numerical models for multidimensional type Ia supernova simulations. *Astronomy & Astrophysics*. **386**(3), pp. 936–943.

C. Reisswig, S. Husa, L. Rezzolla, E. N. Dorband, D. Pollney, and J. Seiler. 2009. Gravitational-wave detectability of equal-mass black-hole binaries with aligned spins. *Physical Review D*. **80**(12), article no: 124026.

T. Rembiasz, M. Obergaulinger, P. Cerdá-Durán, M.-Á. Aloy, and E. Müller. 2017. On the Measurements of Numerical Viscosity and Resistivity in Eulerian MHD Codes. *The Astrophysical Journal Supplement Series*. **230**(2), article no: 18.

L. Rezzolla, E. R. Most, and L. R. Weih. 2018. Using Gravitational-wave Observations and Quasi-universal Relations to Constrain the Maximum Mass of Neutron Stars. *The Astrophysical Journal Letters*. **852**(2), article no: L25.

B. Ripperda, F. Bacchini, O. Porth, E. R. Most, H. Olivares, A. Nathanail, L. Rezzolla, J. Teunissen, and R. Keppens. 2019. General-relativistic Resistive Magnetohydrodynamics with Robust Primitive-variable Recovery for Accretion Disk Simulations. *The Astrophysical Journal Supplement Series*. **244**(1), article no: 10.

P. L. Roe. 1981. Approximate Riemann solvers, parameter vectors, and difference schemes. *Journal of Computational Physics*. **43**(2), pp. 357–372.

S. Rosswog. 2010. Conservative, special-relativistic smoothed particle hydrodynamics. *Journal of Computational Physics.* **229**(22), pp. 8591–8612.

B. R. Ryan, S. M. Ressler, J. C. Dolence, C. Gammie, and E. Quataert. 2018. Two-temperature GRRMHD Simulations of M87. *The Astrophysical Journal.* **864**(2), article no: 126.

E. Süli and D. F. Mayers. 2003. *An Introduction to Numerical Analysis.* Cambridge: Cambridge University Press.

A. Sądowski, R. Narayan, A. Tchekhovskoy, and Y. Zhu. 2013. Semi-implicit scheme for treating radiation under M1 closure in general relativistic conservative fluid dynamics codes. *Monthly Notices of the Royal Astronomical Society.* **429**(4), pp. 3533–3550.

B. Schutz. 2009. *A First Course in General Relativity.* 2$^{\mathrm{nd}}$ ed. Cambridge: Cambridge University Press.

K. Schwarzschild. 1916. Über das Gravitationsfeld eines Massenpunktes nach der Einsteinschen Theorie. *Sitzungsberichte der Königlich Preussischen Akademie der Wissenschaften.* **3**, pp. 189–196.

O. Shemmer, H. Netzer, R. Maiolino, E. Oliva, S. Croom, E. Corbett, and L. di Fabrizio. 2004. Near Infrared Spectroscopy of High Redshift Active Galactic Nuclei. I. A Metallicity-Accretion Rate Relationship. *The Astrophysical Journal.* **614**(2), pp. 547–557.

J. Shi, Y.-T. Zhang, and C.-W. Shu. 2003. Resolution of high order WENO schemes for complicated flow structures. *Journal of Computational Physics.* **186**(2), pp. 690–696.

M. Shibata and Y.-i. Sekiguchi. 2005. Magnetohydrodynamics in full general relativity: Formulation and tests. *Physical Review D.* **72**(4), article no: 044014.

I. S. Shikin. 1969. Relativistic effects for magnetohydrodynamic waves. *Annales de l'institut Henri Poincaré. Section A, Physique Théorique.* **11**(4), pp. 343–372.

C.-W. Shu. 2020. Essentially non-oscillatory and weighted essentially non-oscillatory schemes. *Acta Numerica.* **29**, pp. 701–762.

S. J. Smartt. 2009. Progenitors of Core-Collapse Supernovae. *Annual Review of Astronomy and Astrophysics.* **47**(1), pp. 63–106.

W. B. Sparks, D. Fraix-Burnet, F. Macchetto, and F. N. Owen. 1992. A counterjet in the elliptical galaxy M87. *Nature.* **355**(6363), pp. 804–806.

A. Spitkovsky. 2006. Time-dependent Force-free Pulsar Magnetospheres: Axisymmetric and Oblique Rotators. *The Astrophysical Journal*. **648**(1), article no: L51.

A. Stahl, M. Landreman, O. Embréus, and T. Fülöp. 2017. NORSE: A solver for the relativistic non-linear Fokker-Planck equation for electrons in a homogeneous plasma. *Computer Physics Communications*. **212**, pp. 269–279.

J. M. Stone and M. L. Norman. 1992. ZEUS-2D: A Radiation Magnetohydrodynamics Code for Astrophysical Flows in Two Space Dimensions. II. The Magnetohydrodynamic Algorithms and Tests. *Astrophysical Journal Supplement*. **80**, pp. 791–818.

J. L. Synge. 1957. *The relativistic gas*. Amsterdam: North-Holland Publishing Company, Amsterdam.

A. H. Taub. 1948. Relativistic Rankine-Hugoniot Equations. *Physical Review*. **74**(3), pp. 328–334.

T. M. Tauris and E. P. J. van den Heuvel. 2006. Formation and evolution of compact stellar X-ray sources. In: W. Lewin and M. van der Klis, eds. *Compact Stellar X-ray Sources*. Cambridge: Cambridge University Press, pp. 623–666.

J. Taylor and J. Weisberg. 1982. A new test of general relativity - Gravitational radiation and the binary pulsar PSR 1913+16. *The Astrophysical Journal*. **253**, pp. 908–920.

A. Tchekhovskoy, J. C. McKinney, and R. Narayan. 2007. WHAM: a WENO-based general relativistic numerical scheme - I. Hydrodynamics. *Monthly Notices of the Royal Astronomical Society*. **379**(2), pp. 469–497.

A. R. Thompson, J. M. Moran, and G. W. Swenson. 2017. Very-Long-Baseline Interferometry. In: ???. *Interferometry and Synthesis in Radio Astronomy*. 3rd ed. Cham: Springer International Publishing, pp. 391–483.

E. F. Toro, M. Spruce, and W. Speares. 1994. Restoration of the contact surface in the HLL-Riemann solver. *Shock Waves*. **4**(1), pp. 25–34.

E. F. Toro. 1997. *Riemann Solvers and Numerical Methods for Fluid Dynamics: A Practical Introduction*. Berlin: Springer Berlin, Heidelberg.

T. S. Tricco and D. J. Price. 2012. Constrained hyperbolic divergence cleaning for smoothed particle magnetohydrodynamics. *Journal of Computational Physics*. **231**(21), pp. 7214–7236.

T. Ushida. 1997. Theory of Force-Free electromagnetic fields. I. General theory. *Physical Review E.* **56**(2), pp. 2181–2197.

B. van Leer. 1977. Towards the ultimate conservative difference scheme. IV. A new approach to numerical convection. *Journal of Computational Physics.* **23**(3), pp. 276–299.

J. VonNeumann and R. D. Richtmyer. 1950. A Method for the Numerical Calculation of Hydrodynamic Shocks. *Journal of Applied Physics.* **21**(3), pp. 232–237.

Y. Wang and J. Zhu. 2020. A new type of increasingly high-order multi-resolution trigonometric WENO schemes for hyperbolic conservation laws and highly oscillatory problems. *Computers and Fluids.* **200**, article no: 104448.

G. M. Webb, G. P. Zank, and J. F. McKenzie. 1987. Relativistic oblique magnetohydrodynamic shocks. *Cambridge University Press.* **37**(1), pp. 117–141.

C. J. White, J. M. Stone, and C. F. Gammie. 2016. An Extension of the Athena++ Code Framework for GRMHD Based on Advanced Riemann Solvers and Staggered-mesh Constrained Transport. *The Astrophysical Journal Supplement Series.* **225**(2), article no: 22.

S. Woosley. 1993. Gamma-Ray Bursts from Stellar Mass Accretion Disks around Black Holes. *The Astrophysical Journal.* **405**, pp. 273–277.

S. Woosley and T. Janka. 2005. The physics of core-collapse supernovae. *Nature Physics.* **1**(3), pp. 147–154.

S. Woosley and J. Bloom. 2006. The Supernova-Gamma-Ray Burst Connection. *Annual Review of Astronomy and Astrophysics.* **44**(1), pp. 507–556.

X.-B. Wu, F. Wang, X. Fan, W. Yi, W. Zuo, F. Bian, L. Jiang, I. D. McGreer, R. Wang, J. Yang, *et al.* 2015. An ultraluminous quasar with a twelve-billion-solar-mass black hole at redshift 6.30. *Nature.* **518**(7540), pp. 512–515.

W. Xiaoshuai and Z. Yuxin. 2015. A high-resolution hybrid scheme for hyperbolic conservation laws. *International Journal for Numerical Methods in Fluids.* **78**(3), pp. 162–187.

C. Xu, Z.-w. Li, and Y.-z. Ge. 1985. A numerical model for Type II supernovae — The collapse stage. *Chinese Astronomy and Astrophysics.* **9**(2), pp. 154–158.

W. Xu and W. Wu. 2018. An Improved Third-Order WENO-Z Scheme. *Journal of Scientific Computing.* **75**(3), pp. 1808–1841.

A. L. Zachary, A. Malagoli, and P. Colella. 1994. A Higher-Order Godunov Method for Multidimensional Ideal Magnetohydrodynamics. *SIAM Journal of Scientific Computing.* **15**, pp. 263–284.

O. Zanotti, F. Fambri, and M. Dumbser. 2015. Solving the relativistic magnetohydrodynamics equations with ADER discontinuous Galerkin methods, a posteriori subcell limiting and adaptive mesh refinement. *Monthly Notices of the Royal Astronomical Society.* **452**(3), pp. 3010–3029.

O. Zanotti and M. Dumbser. 2015. A high order special relativistic hydrodynamic and magnetohydrodynamic code with space-time adaptive mesh refinement. *Computer Physics Communications.* **188**, pp. 110–127.

Y.-z. Zhang, Y.-y. Fu, Y.-h. Wei, C.-m. Zhang, S.-h. Yu, Y.-y. Pan, Y.-q. Guo, and D.-h. Wang. 2016. Spin-down of Pulsars, and Their Electromagnetic and Gravitational Wave Radiations. *Chinese Astronomy and Astrophysics.* **40**(2), pp. 210–219.

X.-H. Zhao, K.-H. Kwek, J.-B. Li, and K.-L. Huang. 1993. Chaotic and Resonant Streamlines in the ABC Flow. *SIAM Journal on Applied Mathematics.* **53**(1), pp. 71–77.